



HAL
open science

**Modelling the effects of surface roughness and a forest
litter layer on passive microwave observations:
application to soil moisture retrieval by the SMOS
mission**

Heather Lawrence

► **To cite this version:**

Heather Lawrence. Modelling the effects of surface roughness and a forest litter layer on passive microwave observations: application to soil moisture retrieval by the SMOS mission. Continental interfaces, environment. Université Sciences et Technologies - Bordeaux I, 2010. English. NNT : . tel-01024075

HAL Id: tel-01024075

<https://theses.hal.science/tel-01024075>

Submitted on 17 Jul 2014

HAL is a multi-disciplinary open access archive for the deposit and dissemination of scientific research documents, whether they are published or not. The documents may come from teaching and research institutions in France or abroad, or from public or private research centers.

L'archive ouverte pluridisciplinaire **HAL**, est destinée au dépôt et à la diffusion de documents scientifiques de niveau recherche, publiés ou non, émanant des établissements d'enseignement et de recherche français ou étrangers, des laboratoires publics ou privés.

N° d'ordre : 4207

THÈSE
PRESENTÉE A
L'UNIVERSITÉ BORDEAUX I
ÉCOLE DOCTORALE DES SCIENCES PHYSIQUES ET DE L'INGÉNIEUR

Par Heather LAWRENCE

POUR OBTENIR LE GRADE DE

DOCTEUR

SPÉCIALITÉ : Électronique

**MODÉLISATION DE L'EFFET DE LA RUGOSITÉ DE SURFACE ET
DE LA LITIÈRE DES COUVERTS NATURELS SUR LES
OBSERVATIONS MICRO-ONDES PASSIVES - APPLICATION AU
SUIVI GLOBAL DE L'HUMIDITÉ DU SOL PAR LA MISSION SMOS**

Soutenue le : **15 décembre 2010**

Après avis de :

Mme. Thuy LE TOAN
Mme. Jacqueline BOUTIN

Rapporteur
Rapporteur

Devant la commission d'examen formée de :

M. Yann KERR
M. Francis GROUSSET
M. Jean-Pierre LAGOUARDE
M. Philippe PAILLOU
M. Jean-Pierre WIGNERON
M. François DEMONTOUX

Examineur
Examineur
Examineur
Examineur
Directeur de Thèse
Co-Directeur de Thèse

Titre :

Modélisation de l'effet de la rugosité de surface et de la litière des couverts naturels sur les observations micro-ondes passives : application au suivi global de l'humidité du sol par la mission SMOS

Résumé :

Dans le cadre de la mission spatiale SMOS (Soil Moisture and Ocean Salinity), nous présentons dans cette thèse une nouvelle approche numérique de modélisation du calcul de l'émissivité et du coefficient bi-statique de systèmes forestiers sol-litière en Bande L. Le système sol-litière est représenté par deux couches diélectriques 3D comportant des interfaces rugueuses, une démarche qui n'apparaît pas actuellement dans la littérature. Nous validons notre approche pour une seule couche en comparant les simulations de l'émissivité avec celles produites par la méthode des moments et des données expérimentales. A partir de ce nouveau modèle, nous évaluons la sensibilité de l'émissivité du système sol-litière en fonction de l'humidité et de la rugosité de la litière. Ce nouveau modèle permettra de créer une base de données synthétiques d'émissivités calculées en fonction de nombreux paramètres qui contribuera à améliorer la prise en compte de la litière dans l'algorithme d'inversion des données de la mission spatiale SMOS.

Mots clés : radiométrie micro ondes des forêts, émissivité des structures sol litière, Modélisation numérique par éléments finis, rugosité du sol, litière des forêts, HFSS, IEM, SMOSREX, Coefficient de rétro diffusion, Coefficient bi-statique, mission SMOS

Title:

Modelling the effects of surface roughness and a forest litter layer on passive microwave observations: application to soil moisture retrieval by the SMOS mission

Abstract:

In the context of the SMOS (Soil Moisture and Ocean Salinity) mission, we present a new numerical modelling approach for calculating the emissivity and bistatic scattering coefficient of the soil-litter system found in forests, at L-band. The soil-litter system is modelled as two 3-dimensional dielectric layers, each with a randomly rough surface, which to our knowledge has not previously been achieved. We investigate the validity of the approach for a single layer by comparing emissivity simulations with results of Method of Moments simulations, and experimental data. We then use the approach to evaluate the sensitivity of the soil-litter system as a function of moisture content and the roughness of the litter layer. The numerical modelling approach which has been developed will allow us in the future to create a synthetic database of the emissivity of the soil-litter system as a function of numerous parameters, which will contribute to validating and improving the inversion algorithm used by the SMOS mission to retrieve soil moisture over forests.

Key Words: microwave forest radiometry, soil-litter emissivity, FEM numerical modelling, soil roughness, forest litter, HFSS, IEM, SMOSREX, backscattering coefficient, bistatic scattering coefficient, SMOS mission

Acknowledgements

The work of this thesis was made possible by the joint financial support of the Aquitaine Region and the Centre Nationale d'Etudes Spatiales (CNES), to whom go my grateful thanks. Many people also supported me directly during my PhD, particularly in the IMS and INRA-EPHYSE laboratories in Bordeaux. I would like to thank in particular the following people:

- François DEMONTOUX for all his help and support as my PhD co-director, always willing to give me time and help when required, and to send emails and make phone calls on my behalf. I also remember especially the occasional practical joke, the wide-ranging discussions over coffee (or tea) breaks, and the banter when France were playing England, all of which provided a relaxed working environment
- Jean-Pierre WIGNERON, my PhD director, for always making time to see me when I needed help, for his constantly invaluable input and advice, and teaching, for his sense of humour and for his kindness and support during the occasional stresses of the last three years.
- The SMOS team led by Yann KERR in CESBIO laboratory, Toulouse, for making this work possible under the SMOS umbrella. I would like to thank in particular Arnaud MIALON for his help in providing and explaining data and his collaboration on the SMOSREX 2009 soil-litter experimental campaign
- Philippe PAILLOU for the very helpful discussions around numerical modelling and radar scattering, and for his advice and input in planning the work at the early stages

My thanks go also to Liang Chen and T.D. Wu, for answering my questions by email and providing me with the AIEM model, to Marc Crapeau for kindly talking me through matlab programming one Friday afternoon, and to Alain Kruszewski for driving me the 2 hours to the SMOSREX site and back in the cold and sometimes rainy winter and for his help on the SMOSREX 2009 campaign. I would like to thank all members of INRA-EPHYSE and IMS-MCM laboratories for their support and camaraderie over the years, and would particularly like to thank the INRA “non-permanents” for the wonderful lab community they provided.

Many thanks also to my two thesis reviewers Jacqueline BOUTIN, and Thuy LE TOAN, for evaluating my work, for putting up with the short time limit we had to give and for all their helpful suggestions and corrections, and also to all members of the jury for their insightful comments and helpful discussion during the viva and afterwards.

Lastly, to all my friends and family, near or far, thank you for your love and support, in particular to: Guilherme Bontorin, Priscilla Boyer, Jérémie Brusimi, Faith Gischler, Luc Gischler, Jennifer Grant, Marie Guillot, Mena Hatchman, Stephanie Hayes, Emilie Hobday, Julien Lahoudere, Amanda Lawrence, Carol Lawrence, Hazel Lawrence, Peter Lawrence, Virginie Moreaux, Damien Parent, Tovo Rabemanantsoa, Jean-Charles Samalans, Sylvain Schnee, Alex Soudant, Katharina Spannraft, Kat Vyce, and Nathalie Yauschew-Raguenes, to name but a few of those who have greatly enriched this 3-year journey.

For my Father

Contents

1. Introduction	2
2. Background Theory	6
2.1 Passive and Active Remote Sensing.....	6
2.2 Electromagnetism.....	6
2.2.1 Maxwell's Equations.....	7
2.2.2 The Wave Equation.....	9
2.2.3 Plane Waves and Polarisation	10
2.2.4 A Superposition of Waves.....	11
2.2.5 The Poynting Vector.....	13
2.2.6 Waves at boundaries.....	13
2.2.6.1 Reflection and Transmission coefficients for H and V polarization	14
2.2.6.2 Total Reflection and the Brewster Angle	15
2.2.6.3 Wave Propagation in a lossy medium	15
2.2.7 Layered media	18
2.2.8 Antenna Radiation.....	18
2.2.8.1 Radiation from current sources: the Hertzian Dipole	18
2.2.8.2 Radiation from aperture sources.....	19
2.3 Dielectric Properties of Mixtures: Effective Media	22
2.3.1 Physical mixing formulas	23
2.3.2 The Semi-empirical Refractive Mixing Formula	24
2.4 Radiation	25
2.4.1 Important Quantities in Radiation and their definitions	26

2.4.2	Thermal Radiation.....	27
2.4.2.1	Black Body Radiation.....	28
2.4.2.2	Non-black body Radiation and Emissivity.....	30
2.4.3	Radiative Transfer.....	32
2.4.3.1	The Radiative Transfer Equation.....	33
2.4.3.2	The Simplified Radiative Transfer Equation.....	34
2.5	Passive Microwave Remote Sensing of Land.....	35
2.5.1	Emission of Bare Soil Surfaces.....	36
2.5.1.1	The soil dielectric permittivity constant in the microwave region.....	36
2.5.1.2	Non-uniform Temperature and Dielectric profiles.....	38
2.5.1.3	Rough Surface Scattering and Emission.....	40
2.5.2	Modelling the emission of the ground covered by vegetation.....	46
2.5.3	Note.....	47
3.	Modelling the Emission of the Soil-Litter system.....	50
3.1	Microwave Emission of Soil: modelling the effects of a rough surface.....	50
3.1.1	A Semi-Empirical model for soil emission at L-Band.....	52
3.1.1.1	Q-h Model Formulation.....	52
3.1.1.2	Model Development.....	53
3.1.1.3	Comparing semi-empirical models to theoretical models.....	55
3.1.2	Analytical Models.....	56
3.1.2.1	General Approach.....	56
3.1.2.2	Different Analytical Models.....	57
3.1.3	Numerical Models.....	62
3.1.3.1	Methodology.....	63
3.1.3.2	Numerical Methods.....	67
3.1.3.3	Selection of the appropriate numerical approach.....	82

3.1.3.4	Validation of Numerical Methods.....	83
3.1.3.5	Problems of current interest.....	84
3.2	Modelling the contribution of the litter layer to forest emission at L-band.....	85
3.2.1	The Forest structure.....	85
3.2.2	Remote Sensing of Forests.....	88
3.2.2.1	Experimental data.....	88
3.2.2.2	Theoretical Models.....	88
3.2.3	Discussion.....	94
3.3	Choice of approach for modelling the soil-litter L-band emission in this thesis.....	96
4.	The Numerical FEM Approach developed for Calculating the L-band Scattering and Emission of the Soil-Litter system found in Forests.....	102
4.1	Model Description.....	102
4.1.1	Ansoft's HFSS software.....	102
4.1.2	Calculating the scattering and emission of forest multilayer structures using a numerical FEM approach.....	103
4.1.2.1	Building the structure.....	105
4.1.2.2	HFSS Simulations.....	107
4.1.2.3	Analysing Results calculated by HFSS.....	111
4.1.3	Note.....	112
4.2	A sensitivity analysis to set model parameters.....	112
4.2.1	Model Parameters and calculation conditions.....	113
4.2.2	Method and Results.....	116
4.2.2.1	Number of Rough Surfaces.....	116
4.2.2.2	Integration step, s.....	128
4.2.2.3	Type of incident beam.....	134

4.2.2.4	Surface size.....	139
4.2.2.5	Calculation Cost	142
4.2.3	Conclusions: Values determined for model parameters	143
5.	Validation of the Numerical FEM Approach for a Single Layer	146
5.1	Comparison with Fresnel for a flat surface	146
5.1.1	HFSS calculation set up.....	146
5.1.2	Results and Conclusions.....	147
5.2	Comparison with the Method of Moments for a rough surface.....	149
5.2.1	Method of Moments data.....	149
5.2.2	Method.....	150
5.2.3	Results	151
5.2.4	Conclusion.....	155
5.3	Comparison between the numerical approach, experimental data and the AIEM model....	156
5.3.1	SMOSREX 2006 dataset	156
5.3.2	Method.....	162
5.3.3	Results and Discussion	163
5.3.4	Conclusions	170
6.	Emissivity of the Soil-Litter system: comparison with Experimental Data and the Schwank Model.....	172
6.1	The Bray 2009 Experimental campaign and the Schwank model predictions	172
6.2	Method.....	174

6.3	Results and Discussion.....	178
6.4	Conclusions and Perspectives.....	182
7.	Conclusions	186
8.	Perspectives.....	190
9.	Appendix A : Résumé en Français.....	194
10.	Appendix B: Publication.....	204

List of Symbols and Abbreviations

α : attenuation constant, a measure of the attenuation of an electromagnetic wave as it travels through a lossy medium

AIEM: Advanced Integral Equation Method

β' : phase constant, a measure of the change of phase experienced by an electromagnetic wave when it enters a lossy medium

B: Magnetic Field

c: speed of an electromagnetic wave

c_0 : speed of an electromagnetic wave in a vacuum, equal to $3 \times 10^8 \text{ ms}^{-1}$

D: Electric displacement field

ϵ_p : emissivity at polarisation p

ϵ_N : emissivity calculated by averaging the scattered electric field over N surfaces

ϵ : electric permittivity of a material

ϵ_0 : electric permittivity of a vacuum, equal to $8.85 \times 10^{-12} \text{ F/m}$

ϵ_r : the relative permittivity (electric permittivity relative to that of a vacuum)

E: Electric Field

f: frequency of an electromagnetic wave

F_f : spectral flux density at frequency f

F: radiative flux density

FEM: Finite Element Method

FDTD: Finite Difference Time Domain Method

γ : propagation constant, a measure of the change in phase and magnitude of a wave as it enters a lossy medium

g: the beamwidth of a tapered wave

h: Planck's constant, equal to $6.26 \times 10^{-34} \text{ Js}^{-1}$

H: magnetising field

HFSS: High Frequency Software Simulator, electromagnetic modelling software used in this PhD

I: electric current

I_f : specific intensity, or brightness, of a radiated beam

IEM: Integral Equation Method

J: surface current density (current per unit area)

k: the wave number of an electromagnetic wave

k_b : Boltzmann constant, equal to $1.381 \times 10^{-23} \text{ JK}^{-1}$

KA: Kirchoff Approximation

λ : wavelength of an electromagnetic wave

λ_0 : wavelength of an electromagnetic wave in a vacuum

L: size of the rough surface, also equal to the width of the calculation area

L_c : autocorrelation length of a rough surface

L-MEB: L-Band Microwave Emission of the Biosphere model

m: rough surface slope, equal to σ/L_c

m_g : gravimetric soil moisture content

m_v : volumetric soil moisture content

μ : magnetic permeability of a material

μ : the direction of propagation $\cos\theta$

μ_0 : magnetic permeability of a vacuum, equal to $4\pi \times 10^{-7} \text{ H/m}$

μ_r : the relative permeability (magnetic permeability relative to that of a vacuum)

MoM: Method of Moments

n: refractive index of a wave

N: number of simulations performed for a given roughness condition

p: penetration depth of a medium

P: power

ρ : the volume charge density

$\rho(x',y')$: autocorrelation function of a rough surface

ρ_{xy} : degree of coherence of a wave, where the symbols x and y refer to the wave's components

ρ_b : soil bulk density

ρ_w : density of water

R_p : Reflection coefficient for a wave of polarisation p

RTE: Radiative Transfer Equation

σ : the standard deviation of surface heights of a rough surface, also used for a material's conductivity

σ_N : the bistatic scattering coefficient calculated by averaging the electric field over N surfaces

σ_{sb} : Stephan-Boltzmann constant

σ_{pq}^0 : bistatic scattering coefficient at polarisation p of the incident beam and polarisation q of the scattered beam

σ^0 : backscattering coefficient

s: the step in angles (θ_s, ϕ_s) at which the scattered field is calculated, equivalent to the integration step for the emissivity calculation

S: Poynting vector

SMOS: Soil Moisture and Ocean Salinity mission

SMOSREX: Surface Monitoring Of the Soil Reservoir EXperiment

θ : angle of incidence for scattering problems, equivalent to the angle of emission

θ_T : angle of transmission when a wave encounters a boundary

θ_c : critical angle, for incident angles greater than or equal to this value total reflection occurs

θ_B : Brewster angle: the incident angle at which total transmission occurs for a V polarised wave

(θ_s, ϕ_s) : scattering angle

τ : optical depth of a medium

T_p : Transmission coefficient for a wave of polarization p

Γ : reflectivity

T: transmissivity

T: temperature

T_{eff} : effective temperature of a medium

$T_B(\theta, \phi)$: Brightness temperature at angle (θ, ϕ)

u_f : spectral energy density (at frequency f)

$u(T)$: energy density of a radiated beam

ω : angular frequency of an electromagnetic wave, also used for a medium's single scattering albedo

$W(z)$: temperature weighting function for each layer in the soil

CHAPTER 1. INTRODUCTION

1. Introduction

Remote sensing is the collection of information about objects from a distance. As a discipline it first became possible with the advent of balloons (1900), and later airplanes, providing a platform for regarding the environment. In 1960 the first satellite weather image was taken with NASA's TIROS mission, heralding the start of remote sensing as a tool for observing the environment.

Remote Sensing of the environment via satellite or airplane allows us to obtain geophysical information over large regions. The satellite or airplane provides a platform at a distance, from which a signal from the environment can be measured, usually an electromagnetic wave. This signal must be propagated between the object and the observer unambiguously and without serious loss. Ideally propagation should be in a straight line with no attenuation (from vegetation cover, or the atmosphere for example), in other words through a transparent, homogeneous medium. An interaction must also exist between the sensing wave and the object, in order to provide the observer with information about the object.

Remote Sensing of the environment combines many disciplines, principally electromagnetic theory and environmental studies. In order to obtain useful information from remote sensing observations we must understand the electromagnetic theory describing the processes involved in the propagation and interactions of electromagnetic waves as well as how the observed objects interact with these waves. This must be coupled with an understanding of key environmental and geophysical properties and how they affect such interactions. Often this means understanding the electromagnetic properties of the object and how they depend on its physical properties. For example a key electromagnetic property is the dielectric permittivity constant which can be linked to properties such as moisture content, material content, temperature, etc. Also an object's shape can affect its interaction with electromagnetic waves.

Environmental variables that can be measured by remote sensing include physical variables such as vegetation and ground structure and global variables such as the Earth's water content, salinity, and temperature.

The work of this PhD thesis was carried out in the context of the European Space Agency's (ESA's) Soil Moisture and Ocean Salinity (SMOS) mission (Y. Kerr et al 2001), a remote sensing satellite mission. The SMOS mission was launched in November 2009 with the objective of retrieving the soil moisture over land and the salinity over oceans on a global scale, from microwave radiometric measurements of the Earth's thermal radiation. The Earth's thermal emission is very sensitive to these two variables in the L-band microwave region and the mission was conceived in order to provide a way to measure globally these two variables, which had not previously been done.

Surface soil moisture is a key variable in the hydrologic cycle. Both water and energy fluxes at the surface/atmosphere interface depend strongly on soil moisture and surface soil moisture drives evaporation, infiltration and runoff while soil moisture in the vadose zone (the top part of the soil which is unsaturated by water) governs the rate of water uptake by the vegetation. Global soil moisture is an important input variable for numerical weather forecasting and climate models, such as the European Centre for Medium-range Weather Forecasts' (ECMWF's) Numerical Weather Prediction (NWP) model.

The SMOS satellite carries an interferometric radiometer which measures the Earth's natural thermal emission, at L-band. This band was chosen because at higher frequencies the vegetation cover is not transparent enough to allow us to measure the soil signal and at lower frequencies we are not able to obtain a very good resolution of the image taken by the satellite. The frequency at which the SMOS satellite radiometer takes measurements is 1.4 GHz, since this is the L-band frequency designated by the International Telecommunication Union for passive remote sensing measurements. Note that volume effects cannot be entirely neglected at this frequency: in general the Earth's emission includes mainly contributions from the surface (on average the first 3-5cm) at this frequency but for low soil moisture conditions the emission also includes contributions from much lower depths.

These measurements are taken at a mixture of the two polarisations H and V, from which the pure H and V components can be calculated and at angles in the range of 0° to 50°. A retrieval algorithm is then applied to the measurements in order to retrieve soil moisture. This algorithm models emission using the forward model and then uses an iterative approach, obtaining values of soil moisture and surface parameters which minimise a cost function computed from the sum of the square weighted differences between measured and modelled emission. The forward model is the so-called L-band Microwave Emission of the Biosphere (LMEB) model (Wigneron et al 2003, 2007). This model is the result of an extensive review of current knowledge of microwave emission of various land cover types with the objective of being accurate while remaining simple enough for operational use at a global scale, and allowing developments to be incorporated as they occur.

Other factors affecting microwave emission include surface roughness, topography, soil texture, land cover and vegetation type. All these factors are constant with time and so can be estimated or calibrated from other information such as soil maps, data taken in the optical domain, digital elevation maps, etc. Only vegetation cover is retrieved simultaneously to soil moisture, making use of multi-angular, dual-polarisation measurements.

For the work of this thesis we concentrate on soil moisture retrieval over forests. The ground emission in forests is affected by the vegetation above the ground which consists of a tree, or canopy, layer and a litter layer of organic debris covering the forest floor. The canopy acts as a semi-transparent layer which attenuates the ground emission and this can be modelled simply by the τ - ω model, with two

variables, the optical depth τ and the scattering albedo ω , determining the attenuation. However the litter layer is much denser and has a tendency to absorb and hold water which means that, besides attenuating the ground emission, it adds an emission of its own to the signal which is very strong under high moisture conditions. In addition both the ground and the litter layer often have rough surfaces, which affect the overall emission. The litter layer effectively masks the ground signal (Grant 2007, 2009) making it difficult to retrieve soil moisture. This effect has not been studied in any great depth and has not been well accounted for in the L-MEB model and so although soil moisture retrieval is performed over forests in the SMOS mission its accuracy has yet to be determined and is expected to be poor.

The motivation of this PhD thesis is to improve the L-MEB model over forests by studying in greater depth the contribution of emission from the forest floor, including the soil and litter layers, to the signal. In order to do this we aim to develop a modelling approach which allows us to calculate the emission of the soil and litter layers in forests, incorporating surface roughness of both the soil and litter layers as well as parameters relating to both layers. The advantage of a modelling approach over an experimental one is that we can better control many different parameters that effect the emission. Once developed and validated, the model can be used to create a large database of the emission of the soil-litter system, as a function of numerous parameters. Analysing results in this database, we hope to infer a simple model which can be incorporated into the L-MEB forward model to better account for the effect of a litter layer in forest emission.

The work of this PhD was to develop and validate the model to be used for modelling the soil-litter layers. Such a model requires at least two layers and surface roughness and there is currently no numerical (exact) model available for this. Although generating the database is not part of this thesis, the model must be developed with this end goal in mind.

In the following chapters we present first the background theory including the physics relevant to remote sensing of the environment and the theory for the microwave emission of forests. Secondly we present a review of the methods currently used to model the bare soil layer, and secondly methods for modelling the litter layer. The main challenge in modelling the soil layer is in modelling the surface roughness and so we concentrate mainly on this in the soil layer section. Next we present the model developed in the work of this thesis and validate it against other models and experimental data. We finish with a conclusions and perspectives section.

CHAPTER 2. BACKGROUND THEORY

2. Background Theory

In this section we present the background theory relevant to this thesis. The information presented is mainly based on the volumes by Ulaby et al (1985a,b and c) but also on the remote sensing lecture course by C. Matzler (2007), and the volumes by C. Matzler et al (2006) and Chukhlantsev (2006).

We begin with the context of active and passive remote sensing of the environment, two distinct areas of research that are nevertheless theoretically linked. We then present a summary of the physical theories of electromagnetism and thermal radiation, on which active and passive remote sensing respectively are based. We then present the background theory for passive microwave remote sensing of land. In this section we focus in particular on modelling the bare ground emission as well as the emission of the ground covered by vegetation, topics which are key to this thesis.

2.1 Passive and Active Remote Sensing

Methods for observing the environment by remote sensing can be divided in two distinct categories: active and passive. In active methods an artificially created electromagnetic wave is sent to the object to be sensed and the returned signal analysed. In passive methods it is the environment's natural thermal emission that is detected and analysed. Thus for the active case we focus on scattering from the material and in the passive case we focus on emission. The theory behind active remote sensing is based on the theory of electromagnetism whereas the theory behind passive remote sensing is based on radiation theory. In the following sections we present these two theories, focusing on areas that are important for remote sensing. As we will see electromagnetic theory relating to scattering can be linked to the concept of emission found in thermal radiation, by Peake's theorem (1959): we can calculate an object's emission by integrating the scattering resulting from an incident wave. Thus, although experimentally passive and active remote sensing techniques each provide different information about an object, theoretically we can calculate one from the other. In this thesis we are interested in the emission of soil-litter systems. However in theoretical modelling approaches it is usual to calculate the emission from the scattering, including the approach we develop and apply. We will therefore present the theory behind both electromagnetic scattering and thermal radiation as both are relevant to this thesis.

2.2 Electromagnetism

The theory of electromagnetism was formulated by Maxwell. It describes the behaviour of magnetic and electric fields for a given system of electric currents and charges. It is a macroscopic theory and so does not consider the microscopic processes in a medium in the presence of an electromagnetic field. Electric and magnetic properties of a specific medium are described by three macroscopic quantities: the magnetic permeability, μ , the conductivity σ and the permittivity ϵ . Electromagnetic theory rests on

Maxwell's four equations. These four equations are very powerful since they are simple, yet fully describe an electromagnetic field problem: all electromagnetic theory can be derived from them.

2.2.1 Maxwell's Equations

Maxwell's four equations can be expressed in differential or integral form. In differential form they can be written as:

$$\nabla \cdot \bar{D} = \rho \quad (2.1a)$$

$$\nabla \cdot \bar{B} = 0 \quad (2.1b)$$

$$\nabla \times \bar{E} = -\frac{\partial \bar{B}}{\partial t} \quad (2.1c)$$

$$\nabla \times \bar{H} = \frac{\partial \bar{D}}{\partial t} + \bar{J} \quad (2.1d)$$

where:

$$\bar{D} = \epsilon \bar{E} \quad (2.2)$$

$$\bar{B} = \mu \bar{H} \quad (2.3)$$

$$\bar{J} = \sigma \bar{E} \text{ (Ohm's law)} \quad (2.4)$$

and the electromagnetic quantities are:

E: the electric field

B: the magnetic field

D: the electric displacement field

H: the magnetising field

ϵ : the electric permittivity

ρ : the volume charge density

σ : the conductivity

J: the surface current density (current per unit area).

ε and μ can be expressed as functions of the vacuum permittivity ε_0 and the vacuum permeability μ_0 as follows:

$$\varepsilon = \varepsilon_r \varepsilon_0 \quad (2.5)$$

$$\mu = \mu_r \mu_0 \quad (2.6)$$

where ε_r and μ_r are respectively the relative electric permittivity and magnetic permeability of the material. Both ε and μ and equivalently ε_r and μ_r are usually complex and are often written as:

$$\varepsilon = \varepsilon' + i\varepsilon'' = (\varepsilon_r' + i\varepsilon_r'')\varepsilon_0 \quad (2.7)$$

$$\mu = \mu' + i\mu'' = (\mu_r' + i\mu_r'')\mu_0 \quad (2.8)$$

Note that in this thesis we deal with non-magnetic media, i.e. $\mu_r = 1$.

Maxwell's equations can be written in their integral form as:

$$\oiint_{\partial V} \vec{E} \cdot d\vec{A} = 0 \quad (2.9a)$$

$$\oiint_{\partial V} \vec{B} \cdot d\vec{A} = 0 \quad (2.9b)$$

$$\oint_{\partial S} \vec{E} \cdot d\vec{l} = -\frac{\partial \Phi_{B,S}}{\partial t} \quad (2.9c)$$

$$\oint_{\partial S} \vec{B} \cdot d\vec{l} = \mu_0 \vec{I}_S + \mu_0 \varepsilon_0 \frac{\partial \Phi_{E,S}}{\partial t} \quad (2.9d)$$

The left-hand sides of (2.9a) and (2.9b) are the integration of respectively the electric field and magnetic field over a closed surface ∂V , of area A and bounding volume V . The left-hand sides of (2.9c) and (2.9d) are the integration of respectively the electric field and magnetic fields over closed line dS of length l bounding area S . $\Phi_{B,S}$ is the magnetic flux through area S and $\Phi_{E,S}$ is the electric flux through area S , given by:

$$\Phi_{B,S} = \iint_S \vec{B} \cdot d\vec{A} \quad (2.10a)$$

$$\Phi_{E,S} = \iint_S \vec{E} \cdot d\vec{A} \quad (2.10b)$$

For the work of this thesis, we develop a numerical modelling approach to calculate the emission of the forest soil-litter system. Numerical modelling approaches such as the one used in this thesis solve Maxwell's equations for finite spaces. This is what makes them exact, since Maxwell's equations are exact and complete. As will be covered in more detail in section 3.1.3, numerical modelling

techniques can be divided into two types: those that solve Maxwell's equations in their differential form and those that solve them in their integral form.

2.2.2 The Wave Equation

For active remote sensing we are interested in the scattering of electromagnetic waves. We now consider, therefore, the concept of electromagnetic waves, which may be derived from Maxwell's equations. Maxwell's theory permits the existence of electromagnetic fields in space even without the presence of charge or current sources. This is because a changing magnetic field creates a changing electric field and vice versa. We can therefore visualise an electromagnetic wave propagating through space with oscillating electric and magnetic fields which are dependent on each other. In order to formally describe such waves we combine Maxwell's equations (grad x (2.1c)) to obtain two wave equations, which, for a non-conductor ($\sigma=0$), are given by:

$$\nabla^2 \mathbf{E} - \frac{\mu_r \epsilon_r}{c_0^2} \frac{\partial^2 \mathbf{E}}{\partial t^2} = 0 \quad (2.11a)$$

$$\nabla^2 \mathbf{B} - \frac{\mu_r \epsilon_r}{c_0^2} \frac{\partial^2 \mathbf{B}}{\partial t^2} = 0 \quad (2.11b)$$

For:

$$c_0 = (\epsilon_0 \mu_0)^{1/2} \quad (2.12)$$

Electromagnetic waves propagate with phase velocity c given by:

$$c = c_0 / \sqrt{\epsilon_r \mu_r} \quad (2.13)$$

where c_0 is the speed of an electromagnetic wave in a vacuum equal to $3 \times 10^8 \text{ms}^{-1}$.

It further follows from Maxwell's equations that a wave's electric and magnetic fields must always be perpendicular; hence if the electric field oscillates in the x direction, the magnetic field oscillates in the y or z direction. The magnitudes of the E and B fields are also related by:

$$B_0 = E_0 / c. \quad (2.14)$$

For this reason we usually only consider the electric or magnetic fields in waves since the other can be derived afterwards.

2.2.3 Plane Waves and Polarisation

There are numerous possible solutions to the wave equation and correspondingly numerous types of wave, of which the most basic form is the plane wave. In remote sensing we deal extensively with plane waves since antennas emit waves that may be considered plane far from the emitting antenna and also the earth's thermal radiation may be considered plane when measured at a distance far from the ground.

A plane wave propagating in an arbitrary direction given by the wavevector \mathbf{k} can be described by the following equations:

$$E(\mathbf{r}, t) = E_0 \exp(i\mathbf{k} \cdot \mathbf{r} - \omega t) \quad (2.15a)$$

$$H(\mathbf{r}, t) = H_0 \exp(i\mathbf{k} \cdot \mathbf{r} - \omega t) \quad (2.15b)$$

where ω is the phase velocity. Note we take the real part in the above equations but it is common practice to write wave equations in complex form and the real part is implied. A wave is considered to be plane when its electric field remains in the same plane with respect to its propagation.

Substituting these wave equations into Maxwell's equations (2.1a) and (2.1b) we find that \mathbf{k} is perpendicular to both \mathbf{H} and \mathbf{E} as follows: $\nabla \cdot \mathbf{H} = i\mathbf{k} \cdot \mathbf{H} = 0$ and $\nabla \cdot \mathbf{E} = i\mathbf{k} \cdot \mathbf{E} = 0$.

Since the electric and magnetic fields must also be perpendicular these two fields form a plane orthogonal to the direction of propagation, called the polarisation plane.

Inserting the above equations into the wave equation we deduce the following relationship:

$$\frac{\omega}{k} = \frac{1}{\sqrt{\epsilon\mu}} = \frac{1}{c} \quad (2.16)$$

ω is calculated as $2\pi/\lambda$, where λ is the wavelength. This equation for k is the dispersion relation of electromagnetic waves in unbounded space.

A wave is linearly polarised if its electric and magnetic fields oscillate in one direction only. However all waves can be rewritten as the sum of their components in the 2 orthogonal polarisations. In particular, a wave incident on a plane boundary at angle θ_i has an electric field which can be decomposed into two directions: the direction orthogonal to the boundary plane and the direction parallel to this plane:

$$\mathbf{E} = \mathbf{E}_\perp + \mathbf{E}_\parallel \quad (2.17)$$

The orthogonal component is also known as the vertical component (V) and the parallel component is also known as the horizontal component (H). Horizontal and Vertical polarisations are not intrinsic to a plane wave but rather depend on the wave's orientation relative to a boundary. A horizontally polarised wave has an electric field only in the H direction and a vertically polarised wave has an electric field in the V direction only, relative to the boundary.

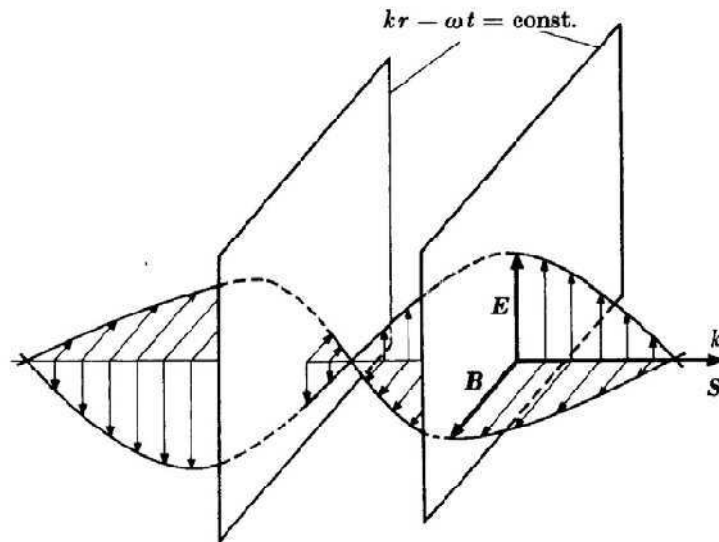


Figure 2.1: One period of a plane EM wave with linear polarization (direction of the E field is constant). The horizontal axis is the phase $kr - \omega t$ with the propagation path, r .

In remote sensing we usually consider waves that are either H or V polarised: in active remote sensing we direct these polarised beams at the environment and also measure the reflections and passive emissions at both H and V polarisation (for example the SMOS satellite measures emission at a mixture of H and V polarisation and the H and V components are then calculated from this measurement). This provides us with two sets of measurements instead of one, and allows us to better retrieve environmental parameters.

2.2.4 A Superposition of Waves

Previously we have considered plane waves of a single frequency, known as *monochromatic* waves. Signals transmitted from single frequency or multifrequency transmitters are of this type. A wave that is not monochromatic but essentially behaves like one is said to be quasi-monochromatic.

Electromagnetic signals emitted by physical objects, irregular terrains or inhomogeneous media usually cover a wide range of frequencies and consist of a superposition of many statistically independent waves. There is no correlation between the component waves of this type of signal which is said to be *incoherent* or *unpolarised*.

To identify the *state of polarisation* or *degree of coherence* of a wave, Born and Wolf (1964) and others (Ko 1962, Kraus and Carver 1973) introduced the following relationship:

$$\rho_{xy} = \frac{\langle E_x E_y^* \rangle}{\left(\langle |E_x|^2 \rangle \langle |E_y|^2 \rangle \right)^{1/2}} \quad (2.18)$$

ρ_{xy} is equal to 1 when the wave is completely polarised and 0 when the wave is completely unpolarised. ρ_{xy} between these two values is said to be partially polarised or partially coherent.

The concept of coherence more generally describes all properties of the correlation between physical quantities of a wave. When considering the addition of two waves with electric field vectors E_1 and E_2 we calculate their coherence from:

$$\rho_{12} = \frac{\langle E_1 E_2^* \rangle}{\left(\langle |E_1|^2 \rangle \langle |E_2|^2 \rangle \right)^{1/2}} \quad (2.19)$$

Often the concept of coherence refers to the amplitudes of two waves relative to each other: two waves are said to be *coherent* if they have a constant phase relative to each other. Note that if two waves add incoherently the power of the resultant wave is the algebraic sum of the powers of its components. For example, let us consider two beams E_1 and E_2 which are combined to form a beam E_1+E_2 . The power of this combined beam is then proportional to:

$$|E_1 + E_2|^2 = |E_1|^2 + |E_2|^2 + 2\langle E_1 E_2^* \rangle \quad (2.20)$$

If the beams are incoherent the third term on the right-hand side of (2.20) is equal to zero thus the amplitude of the resultant wave is the algebraic sum of the amplitudes of its components. However if the waves are coherent this term is not zero and we have what is called coherent effects. This means we see peaks and troughs in the amplitude of the combined beam, depending on whether the two components add in phase or out of phase. In radiometry because the emission is natural it is on the whole incoherent. However, in scattering coherent effects are more often seen since the beam measured is artificially created and therefore monochromatic and also multiple reflections occur which lead to coherence effects.

The concept of a coherent and an incoherent beam is important when considering rough surface scattering, as will be described in section 2.5.1.3.

2.2.5 The Poynting Vector

We now consider the energy carried by an electromagnetic wave, which can be calculated from the Poynting vector. The complex Poynting vector, \mathbf{S} , is defined as:

$$\mathbf{S} = \mathbf{E} \times \mathbf{H} \quad (2.21)$$

The Poynting vector is perpendicular to the electric and magnetic fields and so is in the direction of propagation. It represents the energy flux, or the power per unit area of the wave. A wave's energy is therefore always transferred in the direction of propagation and the amount of energy transferred by a wave per unit area and per unit time is given by $\frac{1}{2}$ times the real part of \mathbf{S} . Since the magnitude of the electric and magnetic fields are related by (2.14) the energy of a plane wave is thus proportional to the square of the electric field, or the square of the magnetic field.

It is important to note this because in the field of scattering, we often measure how much energy is scattered in different directions.

2.2.6 Waves at boundaries

So far we have considered the basics of electromagnetic theory (Maxwell's equations) and the properties of electromagnetic waves. We turn now to the scattering of electromagnetic waves at a boundary, which is important for the work of this thesis, since our numerical approach calculates the scattering of an electromagnetic wave off the boundary of the soil-litter system.

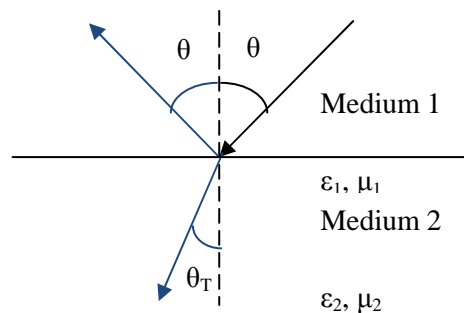


Figure 2.2: Reflection and transmission of an electromagnetic wave at a plane boundary

When a wave approaches a boundary, that is to say a change in the electromagnetic properties of the medium through which it propagates, there are certain rules governing its behaviour. The electric field, \mathbf{E} , perpendicular to the boundary must be the same either side of the boundary and the magnetic field, \mathbf{H} , parallel to the boundary must be conserved. This leads to some of the wave being transmitted, at angle to the normal, θ_T , and some of the wave being reflected, at angle θ to the normal, see Figure 2.2

for example. In sections 2.2.6.1 - 2.2.6.3 we consider the amplitudes and behaviour of the transmitted and reflected beams.

2.2.6.1 Reflection and Transmission coefficients for H and V polarization

The fraction of the wave that is reflected and the fraction transmitted can be calculated by the following Fresnel formulas, which are derived directly from the boundary conditions:

$$R_h = \frac{Z_2 \cos \theta - Z_1 \cos \theta_T}{Z_2 \cos \theta + Z_1 \cos \theta_T} \quad (2.22)$$

$$R_v = \frac{Z_2 \cos \theta_T - Z_1 \cos \theta}{Z_2 \cos \theta_T + Z_1 \cos \theta} \quad (2.23)$$

$$T_h = \frac{2Z_2 \cos \theta}{Z_2 \cos \theta + Z_1 \cos \theta_T} \quad (2.24)$$

$$T_v = \frac{2Z_2 \cos \theta}{Z_2 \cos \theta_T + Z_1 \cos \theta} \quad (2.25)$$

where Z , the material impedance, is the electric field divided by the magnetic field, equal to:

$$Z = \frac{\underline{E}}{\underline{H}} = \sqrt{\frac{\underline{\mu}}{\underline{\epsilon}_{eq}}} = \frac{-i\underline{\mu}\omega}{\underline{k}} \quad (2.26)$$

The reflectivity, Γ , and transmissivity, T , are the square of respectively the reflection coefficient and the transmission coefficient. The reflectivity is the fraction of the incident power that is reflected and the transmissivity is the fraction of incident power that is transmitted. From energy conservation we have:

$$\Gamma + T = 1 \quad (2.27)$$

The reflection and transmission coefficients are the fractions of the incident wave amplitude reflected and transmitted respectively.

The angle of transmission θ_T can be calculated from the incident angle θ as follows:

$$\sin \theta_T = \frac{k_1 \sin \theta}{k_2} \quad (2.28)$$

where k_1 is the wavenumber in medium 1 and k_2 the wavenumber in medium 2. This relationship is known as Snell's law since it was originally found by Snell, and can also be derived from the boundary conditions.

2.2.6.2 Total Reflection and the Brewster Angle

Two phenomena of interest relating to plane wave reflection and transmission across a plane boundary between lossless media are total reflection and total transmission. These two can be derived from Snell's law.

Total reflection occurs when a wave is incident from a more optically dense to a less optically dense medium ($k_1 > k_2$) and the incident angle is greater than the critical angle θ_c , such that:

$$\sin\theta_c = \frac{k_2}{k_1} \quad (2.29)$$

Inserting this value into Snell's law we find that $\cos\theta_2$ is entirely imaginary for $\theta_1 \geq \theta_c$ and thus the wave is completely reflected; no average energy can be transmitted into the lower medium. This phenomenon is true for both H and V polarised waves.

Total transmission occurs for V polarised waves at an incident angle equal to the Brewster angle, θ_B , where:

$$\tan\theta_B = \left(\frac{\epsilon_2}{\epsilon_1}\right)^{1/2} \quad (2.30)$$

This follows directly from Snell's law if we let $R=0$.

This effect can be understood qualitatively by considering electric dipoles in the medium. The incident field is absorbed by the medium and then reradiated by oscillating electric dipoles at the interface. The dipoles oscillate in the polarisation direction of the transmitted wave, the same oscillation producing the reflected beam. However dipoles cannot radiate any energy along their direction of oscillation. Therefore when the direction of the refracted beam is perpendicular to the direction of the reflected beam, as is the case at the Brewster angle, the dipoles cannot radiate any energy in the reflected direction and total transmission occurs.

2.2.6.3 Wave Propagation in a lossy medium

If medium 2 in figure 2.2 has a relative permittivity constant with a non-zero imaginary part, then the transmitted wave experiences a loss in energy as it travels through this medium, associated with the

imaginary part of the permittivity. To illustrate this, let us consider a wave propagating in the z direction through an isotropic medium with complex relative permittivity ϵ_r and complex relative permeability μ_r . Inserting (2.16) into (2.15a) (and setting $\mu_r=1$) we find that the electric field can be expressed as:

$$\underline{E}_x = |E_x| e^{-\gamma z} \quad (2.31a)$$

$$\underline{E}_y = |E_y| e^{-\gamma z} \quad (2.31b)$$

$$\underline{E}_z = |E_z| e^{-\gamma z} \quad (2.31c)$$

The electric and magnetic fields are both perpendicular to each other and to the direction of travel of the wave. Let us therefore take the E field to be entirely in the y direction and the H field in the x direction.

γ is the propagation constant and is complex since it depends on ϵ_r and μ_r , which are both complex. It can be written as:

$$\underline{\gamma} = \alpha + i\beta' \quad (2.32)$$

where α is the attenuation constant and β' is the phase constant. Thus a wave travelling in a lossy medium, i.e. one with non-zero values of ϵ_r'' and/or μ_r'' , will be attenuated by a factor of $e^{-\alpha}$. Figure 2.3 shows a representation of this. A wave passing from a vacuum to a medium will also undergo a phase change of $+\beta'$.

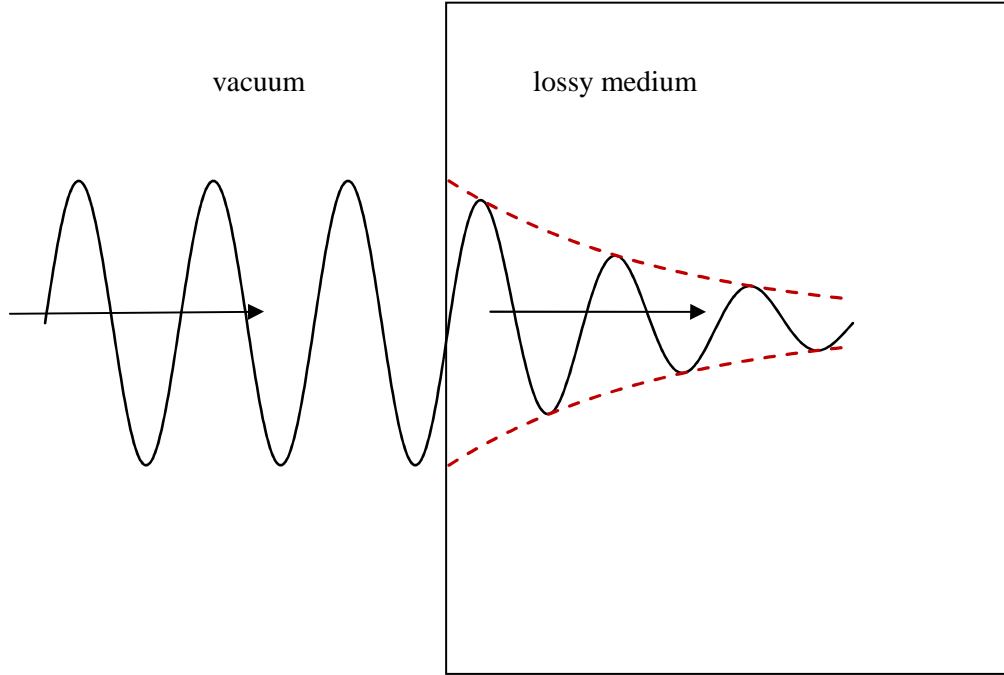


Figure 2.3: the amplitude of a wave passing from a vacuum to a lossy medium. The wave's magnitude is attenuated exponentially in the lossy medium. Note that the phase change is not shown

From Maxwell's equations we find that α and β' depend on the medium permittivity and permeability as follows:

$$\beta' = \beta_0 \sqrt{|\mu_r' \epsilon_r' - \mu_r'' \epsilon_r''| \left[\frac{1 + \sqrt{1 + \tan^2 \delta}}{2} \right]} \quad (2.33)$$

$$\alpha = \beta_0 \sqrt{|\mu_r' \epsilon_r' - \mu_r'' \epsilon_r''| \left[\frac{-1 + \sqrt{1 + \tan^2 \delta}}{2} \right]} = \frac{1}{p} \quad (2.34)$$

Where β_0 and $\tan \delta$ are given by:

$$\beta_0 = \frac{2\pi}{\lambda_0} \quad (2.35)$$

$$\tan \delta = \frac{\mu_r' \epsilon_r' + \mu_r'' \epsilon_r''}{\mu_r' \epsilon_r' - \mu_r'' \epsilon_r''} \quad (2.36)$$

p is the penetration depth, the distance the wave must travel through the medium to be attenuated by a factor of $1/e$. The penetration depth is an important idea for emission in electromagnetism, since it turns out that the ground emits thermal emission from a depth related to the penetration depth (see section 2.5.1.2)

2.2.7 Layered media

Plane boundary reflection and transmission can be generalised to a multilayer case. This is done by evaluating the fields within each layer and then applying a matrix technique to sum the effects of all layers. The current models which include the litter layer in forest scattering and emission use this type of technique since the soil and forest litter make up a two layer system. However this technique only applies to plane boundaries, where the surfaces are flat.

2.2.8 Antenna Radiation

In the previous sections we considered the properties and behaviour of electromagnetic waves. Now we will consider how these waves may be created, by antennas. This is not directly relevant to the work of this thesis which involves numerical modelling in which we consider the scattering of a wave, but not its creation, but the theory of antenna radiation leads to the important concepts such as the near and far field, which will be important later for numerical modelling.

The radiation of an antenna, or the launching of a free space wave, may be viewed in two different ways: as radiation from current sources or as radiation from apertures. These lead to different approaches for calculating the radiated electromagnetic field. The theory for antenna radiation is also relevant to emitting objects since they can be modelled as antenna.

2.2.8.1 Radiation from current sources: the Hertzian Dipole

The short dipole or Hertzian dipole has a length l which is much less than the wavelength. The fields E and H at a distance Q are induced by the current I across the dipole, which we can assume to be uniform. A linear antenna may be regarded as a series of a large number of short antennas and the field due to the linear antenna can then be calculated by integrating the fields induced by all elements, including magnitude and phase.

We assume the current in the short dipole to be sinusoidal:

$$I = I_0 e^{-i\omega t} \quad (2.37)$$

The fields E and H induced by the antenna can be calculated from the vector potential A , to be:

$$E_r = \frac{I_0 l \eta}{4\pi} e^{ikr} \left(\frac{2}{r^2} + \frac{2i}{kr^3} \right) \cos \theta \quad (2.38a)$$

$$E_\theta = \frac{I_0 l \eta}{4\pi} e^{ikr} \left(\frac{-ik}{r} + \frac{1}{r^2} + \frac{i}{kr^3} \right) \sin \theta \quad (2.38b)$$

$$H_{\phi} = \frac{I_0 l}{4\pi} e^{ikr} \left(\frac{-ik}{r} + \frac{1}{r^2} \right) \sin \theta \quad (2.38c)$$

where $\eta = \sqrt{\frac{\mu}{\epsilon}}$, and E_r and E_{θ} are the components of the electric field in the r and θ direction respectively, in spherical polar coordinates, and H_{ϕ} is the component of the H field in the ϕ direction.

It is important to note that at large distances, $kr \gg 1$, the $1/r$ term is much larger than the $1/r^2$ and $1/r^3$ terms in the above equations. Thus the fields reduce to:

$$E_{\theta} = \frac{-ikI_0 l \eta}{4\pi r} \sin \theta e^{ikr} \quad (2.39a)$$

$$H_{\phi} = \frac{-ikI_0 l}{4\pi r} e^{ikr} \sin \theta = \frac{E_{\theta}}{\eta} \quad (2.39b)$$

and E_r is negligible. This is known as the “far field region” and we see that in this region the fields produced by the Hertzian dipole are similar to uniform plane waves

2.2.8.2 Radiation from aperture sources

In this case the radiated field is related to the field distribution across the aperture, which becomes the radiation source. There are two types of formulation: the scalar formulation based on Kirchoff’s work and the vector formulation based on Maxwell’s equations. The latter is theoretically superior but more difficult and so is used mostly for apertures whose dimensions are less than or comparable to the wavelength, making the scalar approach inapplicable. In this section we will only consider the simpler scalar approach.

a) Scalar Approach

Let us consider an aperture in the plane (x_a, y_a) of length d and either an observation plane (x, y) at a fixed distance z from the aperture or an observation sphere at fixed radius $r=R$ from the centre of the aperture, as shown in Figure 2.4:

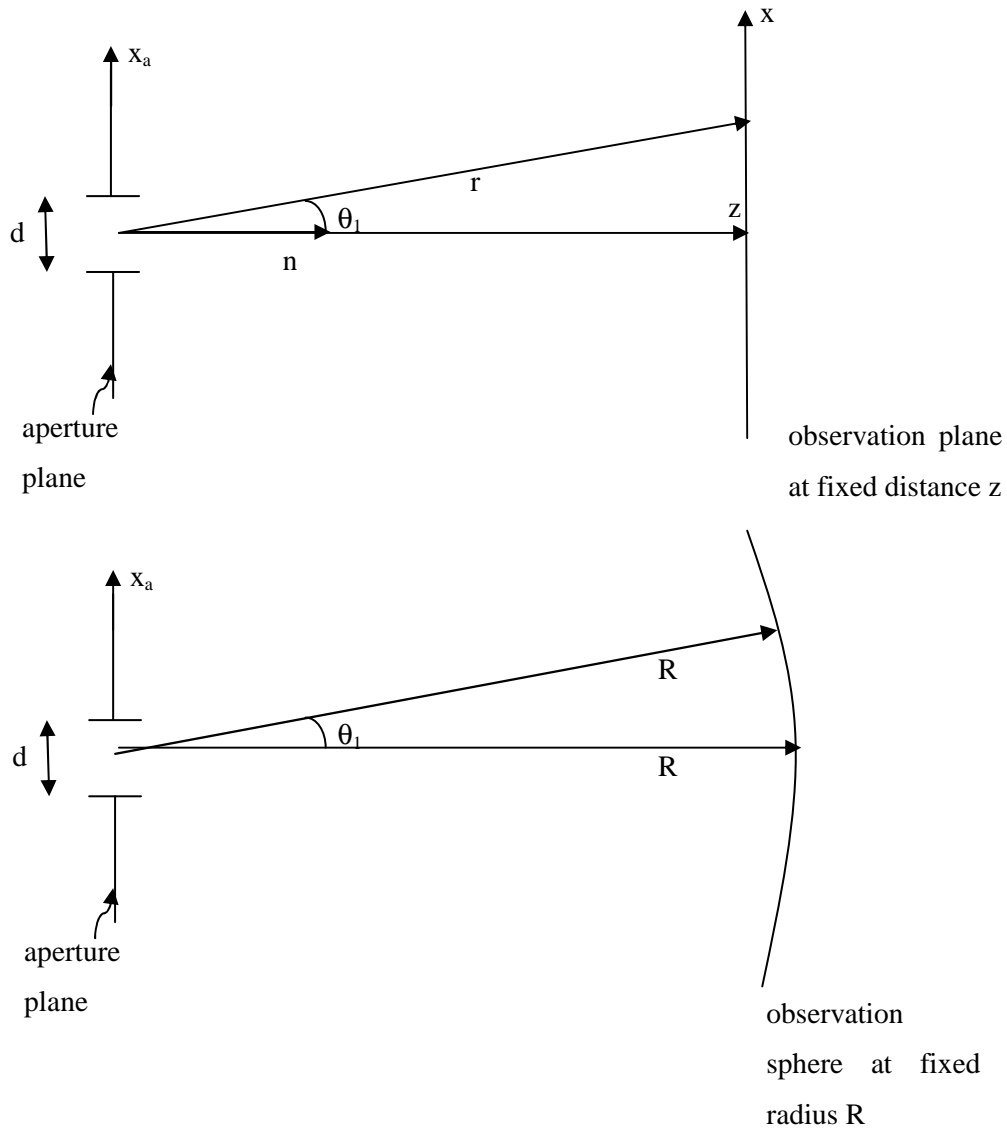


Figure 2.4: Far-zone observation regions: (a) plane at a fixed distance, and (b) sphere at a fixed radius $r=R$

Starting with Green's theorem and the Helmholtz wave equation and applying the Kirchoff boundary conditions we can derive a formula relating the field at a distance (x,y,z) from the aperture to the field distribution across the aperture $E_a(x_a,y_a)$:

$$E(x, y, z) = \frac{1}{4\pi} \iint_{\text{aperture}} E_a(x_a, y_a) \frac{e^{iks}}{s} \left[\left(\frac{1}{s} - ik \right) \cos \theta_1 - ik \cos \theta_2 \right] dx_a dy_a \quad (2.40)$$

where θ_1 is the angle between the normal to the aperture, \hat{n} , and the observation point and θ_2 is the angle between \hat{n} and the direction of the incident wave illuminating the aperture. s is the vector defining the direction of propagation of the wave.

This integral is known as the *Fresnel-Kirchoff diffraction integral*. We can use approximations to simplify the computation of the integral, namely the Fresnel and Fraunhofer approximations. These approximations explain the important concepts of the near field and far field zone and the intermediate Fresnel zone.

a1) Near Field zone

The immediate vicinity of the aperture is called the near-field region. In this region no approximations may be applied to solve the Fresnel-Kirchoff diffraction integral. Furthermore the integral itself may not be valid in this region because the Kirchoff boundary conditions applied in its derivation are not valid and so vector diffraction theory should be used.

a2) Fresnel Region

In the Fresnel region, intermediate between the near field and far field, the assumption is made that the distance z from the aperture to the observation plane is much larger than the longest linear dimension of the aperture (i.e. aperture length l). Since the aperture is much smaller than the wavelength for the scalar approach to be applicable the distance z is much larger than the wavelength. The following approximations can therefore be applied:

$$\left(\frac{1}{s} - ik\right) \approx -ik \quad (2.41a)$$

$$\cos\theta_1 \approx \cos\theta \quad (2.41b)$$

$$\frac{e^{iks}}{s} \approx \frac{e^{iks}}{r} \quad (2.41c)$$

We also replace $s = [z^2 + (x-x_a)^2 + (y-y_a)^2]^{1/2}$ by the first two terms of its binomial expansion;

$$s \approx z \left[1 + \frac{1}{2} \left(\frac{x-x_a}{z} \right)^2 + \frac{1}{2} \left(\frac{y-y_a}{z} \right)^2 \right] \quad (2.42)$$

This latter approximation is called the Fresnel approximation.

Substituting these approximations into the Fresnel-Kirchoff diffraction integral we obtain:

$$E(x, y, z) = \frac{-i(1+\cos\theta)}{2\lambda} \frac{e^{ikz}}{r} \exp \left[\frac{ik}{2z} (x^2 + y^2) \right] \times h(x, y, z) \quad (2.43)$$

$$\text{where } h(x, y, z) = \int_{-\infty}^{\infty} E_a(x_a, y_a) \exp \left[\frac{ik}{2z} (x^2 + y^2) \right] \exp \left[\frac{-ik}{2z} (xx_a + yy_a) \right] dx_a dy_a \quad (2.44)$$

a3) Fraunhofer, far-field, region

If the observation point is far enough away such that:

$$R \gg \left(\frac{k}{2}\right)(x_a^2 + y_a^2)_{max} \quad (2.45)$$

then $\exp\left[\left(\frac{ik}{2R}\right)(x_a^2 + y_a^2)_{max}\right] \approx 1$ over the aperture and we have:

$$E(x, y, z) = \frac{-ie^{ikR}}{\lambda R} h(\theta, \phi) \quad (2.46)$$

where:

$$h(\theta, \phi) = \iint_{-\infty}^{\infty} E_a(x_a, y_a) \exp[-iks \sin\theta(x_a \cos\phi + y_a \sin\phi)] dx_a dy_a \quad (2.47)$$

In practice these equations are used for the Fraunhofer conditions:

$$R \gg \frac{2d^2}{\lambda} \quad (2.48)$$

which is known as the far-field condition, and is obtained by requiring:

$$\left(\frac{k}{2R}\right)(x_a^2 + y_a^2)_{max} \ll \frac{\pi}{8} \quad (2.49)$$

and choosing the origin to be the midpoint of the longest dimension of the aperture.

So we see that when objects emit electromagnetic radiation the emitted fields have a different form near and far from the receiver. When radiation is measured by a satellite borne detector it is the far field that is measured. This is important for our numerical model since Maxwell's equations are solved in the near field but we require the far field value. In this case a near to far field transformation is applied to the solution, by treating the external surfaces as aperture antennas and calculating the field that would be emitted by such antennas. The far field value is calculated on a sphere at a distance R from the surface. The value given to R must be large enough to satisfy (2.48), so that the electric field is calculated in the far field region.

2.3 Dielectric Properties of Mixtures: Effective Media

In this section we consider the electromagnetic properties of materials that determine their interactions with electromagnetic waves. The macroscopic electromagnetic properties of materials are the relative electric permittivity, ϵ_r , the relative magnetic permeability, μ_r , and the conductivity σ . In remote sensing we consider only the permittivity since environmental media is non-magnetic. For homogeneous media, i.e. a media with only one component evenly distributed, the values of ϵ_r have been measured and tabulated. However most natural substances, including soil and litter, are

inhomogeneous mixtures, combining many different components. Furthermore the amounts and distribution of the components vary, and so such media do not have a universal value of the permittivity. Instead we must find a way to calculate their electromagnetic properties as a function of the electromagnetic properties of their components, and their physical properties (including e.g. component percentage, component shape, etc).

An inhomogeneous medium consisting of a mixture of many components that are smaller than the sensing wavelength can be modelled as homogeneous medium with an effective permittivity constant. The value of this constant depends on the permittivities of the components. A large number of effective medium theories exist that allow us to calculate the permittivity of mixtures, appropriate for different types of mixture. In this section we present some of the main ones. These formulae are applied to calculate the dielectric permittivity constant of environmental media including soil and litter as a function of parameters including notably water content for microwave frequencies. The dielectric permittivity constant is the main parameter that effects emission.

2.3.1 Physical mixing formulas

Let us assume a host medium of permittivity ϵ_1 with embedded particles of permittivity ϵ_2 and volume fraction v_f .

When an electric field is applied to a dielectric object, this object becomes polarised with polarisation density P , creating an ‘induced’ electric field due to the polarised object. The electric displacement due to the polarised object is equal to P . The total electric displacement, D , has components due to both the applied electric field and the polarised object, which is expressed mathematically as:

$$D_i = P_i + \epsilon_0 E_i \quad (2.50)$$

where E_i is the electric field applied to object i , and D_i is the resultant displacement current D field due to the applied and induced electric fields.

We also have the following relationship:

$$\langle D_i \rangle = \epsilon_i \epsilon_0 \langle E_i \rangle \quad (2.51)$$

where ϵ_i is the relative permittivity of object i .

Equally we can rewrite the total displacement current D as a function of the effective relative permittivity of the medium, ϵ_r :

$$\langle D \rangle = \epsilon_r \epsilon_0 \langle E \rangle \quad (2.52)$$

where D and E are summations of the D and E fields in the host media and the inclusion, weighted by the volume fraction of each:

$$\langle D \rangle = (1 - v_f) \langle D_1 \rangle + v_f \langle D_2 \rangle \quad (2.53)$$

and
$$\langle E \rangle = (1 - v_f) \langle E_1 \rangle + v_f \langle E_2 \rangle \quad (2.54)$$

Rearranging equations (2.50) – (2.54), we can rewrite the effective permeativity ϵ_r as a function of the permittivity of each components i , ϵ_i , the volume fraction v_f and the polarisation of each component. The component's polarisation P_i depends on its shape and dielectric properties (its dielectric permittivity constant).

A number of different equations have been derived for particles of different shape including, spheres, ellipsoids, etc.

One of the main equations is the Maxwell-Garnett mixing formula, for an ellipsoid shaped component i of volume fraction v_f in a host h , given by:

$$\epsilon = \epsilon_h \frac{\epsilon_i (1 + 2v_f) - \epsilon_h (2v_f - 2)}{\epsilon_h (2 + v_f) + \epsilon_i (1 - v_f)} \quad (2.55)$$

where ϵ_i is the relative permittivity constant of the component i , and ϵ_h is the relative permittivity constant of the host.

2.3.2 The Semi-empirical Refractive Mixing Formula

In some cases there is a lack of sufficiently accurate information on the shape of particles in a mixture and so there is a need for practical semi empirical formulas for certain materials. One of the most important is the *refractive mixing formula*. In this model the refractive indexes of the components are combined in a linear fashion with their volume fractions determining their weighting. This gives an effective refractive index of the mixture, n , of:

$$n = \sum_{i=1}^N v_{fi} n_i \quad (2.56)$$

where v_{fi} is the volume fraction of component i , n_i is its refractive index and N is the total number of components.

Note that:

$$\sum_{i=1}^N v_{fi} = 1 \quad (2.57)$$

Since for non-magnetic media $\epsilon = n^2$ and $\epsilon_i = n_i^2$, (2.56) can be rewritten as:

$$\epsilon^{0.5} = \sum_{i=1}^N v_{fi} \epsilon_i^{0.5} . \quad (2.58)$$

The physical basis for this model comes from the fact that the real part of a material's refractive index is proportional to the propagation time of waves travelling through the material. Then if we consider a wave propagating successively through three different materials, as shown in Figure 2.5, we find that propagation time can be added linearly with equation (2.59):

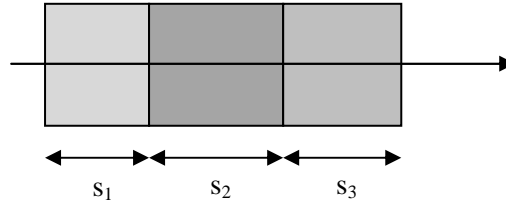


Figure 2.5: propagation of a beam through a mixture whose components are arranged linearly

$$t = \frac{1}{c_0} (n'_1 s_1 + n'_2 s_2 + n'_3 s_3) = \frac{n' s}{c_0} \quad (2.59)$$

where n' is given by:

$$n' = n'_1 v_{f1} + n'_2 v_{f2} + n'_3 v_{f3} \quad (2.60)$$

for volume fractions v_{f1} , v_{f2} and v_{f3} .

The same reasoning applies to n'' which is proportional to the wave absorption.

A model such as this where we imagine the wave travelling successful through one particle then another implies that the particle size is larger than the wavelength. Nevertheless this model is also used in situations where particles are smaller than the wavelength.

2.4 Radiation

In this section, we present the theory of electromagnetic radiation, which forms the basis for passive remote sensing of the environment. All material media (gases, liquids, solids and plasma) radiate electromagnetic energy due to their temperature, known as “thermal” emission. When a medium emits

thermal energy its temperature falls and when it absorbs thermal radiation its temperature increases. At “thermal equilibrium”, ie constant temperature, these two processes are balanced.

Up to this point we have considered electromagnetic radiation as waves, taking into account both their amplitude and phase. In order to understand the Earth’s thermal emission we must now consider radiation as photons, in particle form, considering only their amplitude or energy. We must therefore consider radiation as an incoherent, quasi-monochromatic, beam. The propagation and development of such a beam in a homogeneous medium is described by the *theory of radiative transfer*. Since we consider only incoherent radiation, this is an approximation to reality since we discount coherent effects which can occur. However it is a good approximation, provided the media considered are not dense and we do not have a large number of reflections, which lead to large coherent effects.

In this section we will first define some important radiometric quantities, and then describe firstly thermal radiation and then important aspects of radiative transfer theory.

2.4.1 Important Quantities in Radiation and their definitions

The following terms are used often in radiation theory:

1. Radiance or Specific Intensity, I_f , (sometimes also called Brightness):

This is the measure of the radiative power of a beam at a given polarisation, frequency, f , position and travelling in a given direction. It is defined as:

$$dP = I_f(r, n(\theta, \phi)) \cdot df \cdot \cos\theta \cdot d\Omega \quad (2.61)$$

where dP is the infinitesimal power at position (r, θ, ϕ) , in the frequency range $(f, f+df)$, crossing a given area dA , within the solid angle $d\Omega$, and travelling in a given direction defined by unit vector $n(\theta, \phi)$.

2. Spectral Flux density, F_f , and Radiative flux density, F

The Spectral Flux Density is the radiance integrated over all directions, as follows:

$$F_f = \int_{4\pi} I_f(r, \hat{n}) \hat{n} d\Omega \quad (2.62)$$

Hence the spectral flux density is a measure of the total power per unit area travelling all directions, at a given frequency and position.

3. The radiative flux density is the Spectral flux density integrated over all frequencies:

$$F = \int_0^{\infty} F_f df \quad (2.63)$$

The radiative flux density is therefore the total power of all radiation, at all frequencies and travelling in all directions, per unit area, at a given point.

4. Mean Intensity and spectral energy density, u_f

The energy density of a ray (the total energy propagated and absorbed per unit volume traversed) is given by:

$$du_f = \frac{I_f}{c} d\Omega df \quad (2.64)$$

2.4.2 Thermal Radiation

Radiation theory is based on Quantum theory. Atomic gases radiate electromagnetic energy at discrete frequencies, or wavelengths, giving them *line spectra*. Quantum theory describes atoms as having discrete energy levels and explains their emission as occurring when an atomic electron transfers from one energy level to another, whose discrete frequency corresponds to the discrete energy difference between levels in the atom. This comes from Planck's quantum theory which is based on the assumption that emitted radiation occurs only in discrete quanta.

Emission by an atom or particle is caused by a collision with another atom or particle. The probability of this happening increases with particle density and kinetic energy. Since temperature is a measure of kinetic energy it follows that the intensity of the radiated energy increases with the temperature of the emitter.

Molecules have vibrational and rotational modes corresponding to a set of allowable energy levels. This increases the number of lines in spectra of molecular gases compared to atomic gases since it increases the number of possible changes in energy levels. Because of this, sometimes molecular gas spectra contain lines that are so close together it is difficult to resolve them into discrete frequencies.

As gases become liquids and solids the interaction between particles increases and the radiation spectrum becomes more complicated. The radiation spectrum becomes effectively continuous and the body can be said to radiate at all frequencies.

Theoretically we divide emitting bodies up into two categories: black bodies and non-black bodies. A black body is a perfect emitter and is an entirely theoretical concept since such a body cannot exist in nature. However the concept of a black body is important because we are able to derive exact equations for its emission. This gives us a standard against which to measure the emission of all other

bodies (non-black bodies), since they will all emit less radiation than a black body. In section 2.4.2.1 we present the theory of black body radiation and in section 2.4.2.2 we present the theory of non black body radiation.

2.4.2.1 Black Body Radiation

A black body is a perfect emitter, as already stated, and also a perfect absorber: it absorbs all the energy it receives at all frequencies. At thermal equilibrium (constant temperature T) a black body will emit photons with spectral brightness B_f at frequency f . Photons follow the Bose-Einstein statistics and so their spectral brightness is given by the Planck function:

$$I_f = \frac{2hf^3}{c^2(\exp(hf/k_bT) - 1)} \quad (2.65)$$

where h is the Planck constant equal to $6.626 \times 10^{-34} \text{ Js}^{-1}$, k_b is the Boltzmann constant equal to $1.381 \times 10^{-23} \text{ JK}^{-1}$, and c is the speed of the emitted radiation (the speed of light in a vacuum).

Alternatively the brightness can be expressed as a function of the wavelength as follows:

$$I_\lambda = \frac{2hc^2}{\lambda^5(\exp(hc/\lambda k_bT) - 1)} \quad (2.66)$$

This radiance is isotropic and un-polarized. We see from (2.65) that the intensity of black body emission depends only on the frequency and temperature and is independent of any properties of the body. This concept of black body emission is important because it serves as a reference for all other types of emitters: we measure non-black body emission as a function of the equivalent black body emission at the same temperature.

Figure 2.6 shows the variation of the brightness of black body emission with frequency, at difference temperatures.

The radiated power per unit area is given by:

$$dP = dA \cdot u(T) \cdot c/4 \quad (2.67)$$

Where $u(T)$ is the energy density (an integration of the spectral energy density over all frequencies, i.e. the total energy density summed over all frequencies), found to be:

$$u(T) = \frac{8\pi^5(k_B T)^4}{15(hc)^3} \quad (2.68)$$

Therefore:

$$dP = dA \cdot \sigma_{sb} \cdot T^4 \quad (2.69)$$

where σ_{sb} is the Stefan-Boltzmann constant given by

$$\sigma_{sb} = \frac{2\pi^5 k_b^4}{15h^3 c^2} \quad (2.70)$$

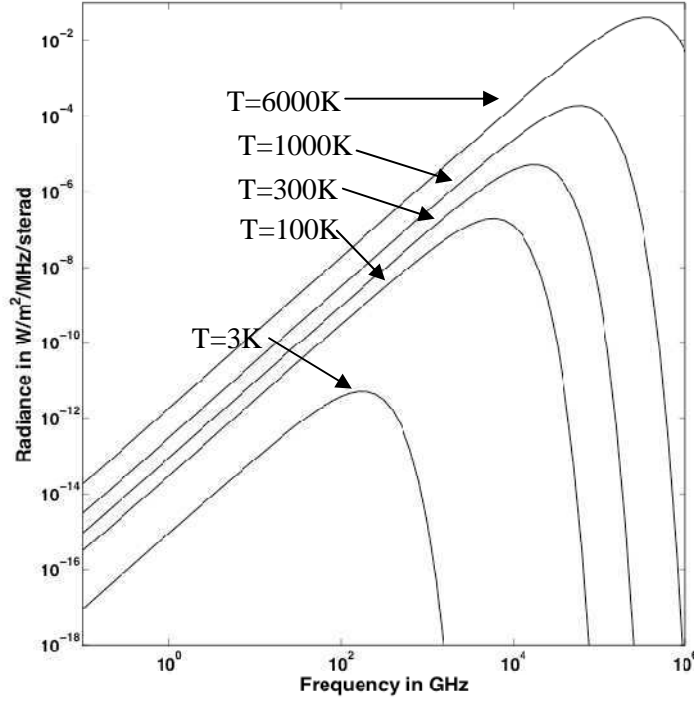


Figure 2.6: the variation of the brightness of black body emission at different temperatures.

From Figure 2.6 we note that the peak frequency increases with temperature. This relationship is expressed mathematically as follows:

The peak spectral brightness I_f occurs at frequency f_m , where:

$f_m = 5.87 \times 10^{10} \text{ HzK}^{-1} T$ and the equivalent maximum I_f is:

$$I_f(f_m) = c_1 T^3 \quad (2.71)$$

for $c_1 = 1.37 \times 10^{-19} \text{ Wm}^{-2} \text{sr}^{-1} \text{Hz}^{-1} \text{K}^{-3}$ (2.72)

Note that the maximum brightness per wavelength does not occur at the same frequency. The wavelength at which we have the maximum value of I_λ is given by:

$$\lambda_m T = 2.879 \times 10^{-3} \text{ mK} \quad (2.73)$$

This is known as the Wien displacement law. The equivalent value of I_λ is

$$I_\lambda(\lambda_m) = c_2 T^5 \quad (2.74)$$

for constant c_2 .

Figure 2.6 also shows that the total energy emitted increases with temperature. This is expressed by the Stephan-Boltzmann law. Integrating I_f over all frequencies we obtain:

$$I = \sigma_{sb} T^4 \quad (2.75)$$

for the Stephan-Boltzmann constant $\sigma_{sb} = 5.673 \times 10^{-8} \text{ Wm}^{-2} \text{ K}^{-4} \text{ sr}^{-1}$. So we see that total brightness varies with T^4 .

a) Wien Radiation Law (High Frequency Limit)

For high frequencies such that $hf/k_b T \gg 1$, (2.65) can be approximated to:

$$I_f = \frac{2h}{c^2} f^3 e^{-hf/k_b T} \quad (2.76)$$

which is known as the Wien radiation law.

b) Rayleigh-Jeans Law

The Rayleigh-Jeans law is the counterpart to the Wien Radiation law at low frequencies. For $hf/k_b T \ll 1$ (2.65) can be approximated to:

$$I_f = \frac{2k_b T}{\lambda^2} \quad (2.77)$$

This result is very useful for microwave radiometry since it is valid in the microwave region. The deviation of (2.77) from Planck's law is less than 1% provided:

$$\lambda T > 0.77 \text{ mK} \quad (2.78)$$

For $f=1.4\text{GHz}$ this is true for temperatures above 3.59K, ie all temperatures.

2.4.2.2 Non-black body Radiation and Emissivity

So far we have considered the theoretical concept of a black body. Let us now consider real bodies or non-black bodies, also known as grey bodies. Real bodies emit less radiation than a black body and do

not necessarily absorb all incident energy. From (2.77) we find that in the microwave region, the brightness of a black body over a bandwidth Δf is:

$$I_{bb} = \frac{2k_b T}{\lambda^2} \Delta f \quad (2.79)$$

For a grey body we define a radiometric temperature so that its brightness, I_{gb} , can assume a form similar to that of a blackbody. This temperature is known as the brightness temperature, or T_B , and is defined such that:

$$I_{gb} = \frac{2k_b}{\lambda^2} T_B(\theta, \phi) \Delta f \quad (2.80)$$

or:

$$T_B(\theta, \phi) = \frac{I_{gb} \lambda^2}{2k \Delta f} \quad (2.81)$$

The ratio between the grey body brightness temperature and the equivalent brightness temperature of a black body at the same temperature is known as the *emissivity*, e . This can be expressed as follows:

$$e(\theta, \phi) = \frac{I_{gb}(\theta, \phi)}{I_{bb}} = \frac{T_B(\theta, \phi)}{T} \quad (2.82)$$

In microwave radiometry we measure the brightness temperatures of grey bodies such as vegetation and soil, which is directly related to the absolute temperature of the body and its emissivity. The emissivity depends on the properties of the body and it is usually this value that we wish to determine.

The emissivity of an object is the fraction of the object's total energy that is emitted. If an electromagnetic wave is incident on an object in thermal equilibrium the energy absorbed by the wave must be equal to the energy emitted. If we consider the Earth's surface, all energy transmitted by a plane wave is absorbed and thus the emissivity is equal to the transmissivity of the surface, defined earlier by the Fresnel equations. This transmissivity is equal to 1 minus the reflectivity, which means we can express the emissivity as:

$$e(\theta, \phi) = 1 - \Gamma(\theta, \phi) \quad (2.83)$$

Thus the ground's thermal emission can be directly related to the reflection of a plane wave travelling through medium 1 and incident upon a boundary with medium 2 at angle θ_1 .

For a flat surface the ground emissivity can therefore be calculated from the Fresnel equations as follows:

$$e_H = 1 - \left| \frac{\cos \theta - \sqrt{\epsilon} \cos \theta_T}{\cos \theta + \sqrt{\epsilon} \cos \theta_T} \right|^2 \quad (2.84)$$

$$e_V = 1 - \left| \frac{\sqrt{\epsilon} \cos \theta - \cos \theta_T}{\sqrt{\epsilon} \cos \theta + \cos \theta_T} \right|^2 \quad (2.85)$$

θ_T is the angle of transmission in medium 2 and is related to θ by Snell's law as:

$$\cos \theta_T = \sqrt{1 - \frac{\lambda_2^2 \sin^2 \theta}{\lambda_1^2}}. \text{ Therefore we have:}$$

$$e_H = 1 - \left| \frac{\lambda_1 \cos \theta - \sqrt{\epsilon(\lambda_1^2 - \lambda_2^2 \sin^2 \theta)}}{\lambda_1 \cos \theta + \sqrt{\epsilon(\lambda_1^2 - \lambda_2^2 \sin^2 \theta)}} \right|^2 \quad (2.86)$$

$$e_V = 1 - \left| \frac{\lambda_1 \sqrt{\epsilon} \cos \theta - \sqrt{(\lambda_1^2 - \lambda_2^2 \sin^2 \theta)}}{\lambda_1 \sqrt{\epsilon} \cos \theta + \sqrt{(\lambda_1^2 - \lambda_2^2 \sin^2 \theta)}} \right|^2 \quad (2.87)$$

The concept of emissivity and brightness temperature, which have been presented in this section, are key concepts both in microwave radiometry and for this thesis. Microwave radiometers, including the SMOS radiometer, measure the brightness temperature of the Earth which depends on the emissivity and temperature. The emissivity depends principally on the dielectric permittivity constant which is highly sensitive to moisture content in the microwave region. Thus we are able to retrieve soil moisture from microwave radiometer measurements.

In this thesis we aim to model the emissivity of the soil-litter forest system. In order to do this we calculate firstly the reflectivity and then apply (2.83).

2.4.3 Radiative Transfer

In radiative transfer we consider an incoherent, quasi-monochromatic beam of radiative power as it propagates and develops in a complex medium. Radiative transfer theory describes how the radiation field changes from point to point and for different directions under a given illumination or source distribution.

In Radiative Transfer theory the following assumptions are made:

- the scenario is stationary
- different rays interact incoherently because their phases are mostly uncorrelated
- Local Thermodynamic Equilibrium is usually assumed

- Geometrical Optics (GO) is assumed valid when finding a selected ray path on a macroscopic scale

Deviations from these assumptions may require special treatments.

2.4.3.1 The Radiative Transfer Equation

In this section we consider what happens when the emitted radiation travels through other, potentially emitting, media. When this radiation passes through a homogeneous medium its specific intensity, I , is reduced by scattering and absorption and simultaneously increased by the emission of the medium through which it travels. The overall change in brightness is expressed mathematically for the geometry shown in Figure 2.7 by the Radiative Transfer Equation (RTE).

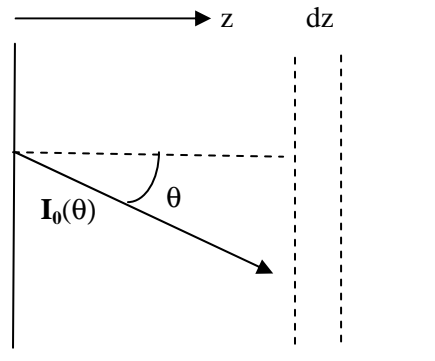


Figure 2.7: radiation travelling at angle θ to the z direction through an emitting medium

The Radiative Transfer Equation in its most general form, for polarisations H and V, is:

$$\mu \cdot dI_V(\mu, z) / dz = \alpha_a \frac{2k_B}{\lambda^2} T(z) - \alpha_{e,V}(\mu) \cdot I_V(\mu, z) + \int_{-1}^1 [(v(\mu), v'(\mu')) \cdot I_V(\mu', z) + (v(\mu), h'(\mu')) \cdot I_H(\mu', z)] d\mu' \quad (2.88a)$$

$$\mu \cdot dI_H(\mu, z) / dz = \alpha_a \frac{2k_B}{\lambda^2} T(z) - \alpha_{e,H}(\mu) \cdot I_H(\mu, z) + \int_{-1}^1 [(h(\mu), v'(\mu')) \cdot I_V(\mu', z) + (h(\mu), h'(\mu')) \cdot I_H(\mu', z)] d\mu' \quad (2.88b)$$

for directions $\mu = \cos\theta$ and $\mu' = \cos\theta'$.

(2.88a) and (2.88b) contain the following three terms:

1. The emission term $\alpha_a \frac{2k_B}{\lambda^2} T(z)$. This term accounts for the emission of the medium through which the wave travels. α_a is the *absorption coefficient* of the medium and $T(z)$ is the temperature of the medium at position z .

2. The extinction term $\alpha_{e,v}(\mu) \cdot I_V(\mu, z)$ or $\alpha_{e,h}(\mu) \cdot I_H(\mu, z)$, which accounts for energy loss due to absorption and scattering. $\alpha_{e,p}(\mu)$ is the extinction coefficient of the medium which depends on the direction, μ , and polarisation, p , of the incident beam. The extinction coefficient can be written as a sum of the absorption coefficient, α_a , and scattering coefficient, α_s , which account for energy loss to due absorption and scattering respectively, ie:

$$\alpha_e = \alpha_a + \alpha_s \quad (2.89)$$

3. The source term from scattering $\int_{-1}^1 [(v(\mu), v'(\mu')) \cdot I_V(\mu', z) + (v(\mu), h'(\mu')) \cdot I_H(\mu', z)] d\mu'$ or $\int_{-1}^1 [(h(\mu), v'(\mu')) \cdot I_V(\mu', z) + (h(\mu), h'(\mu')) \cdot I_H(\mu', z)] d\mu'$. This term accounts for scattered energy being redirected into the direction of observation by a second scattering event. $(p(\mu), p'(\mu'))$ represents the fraction of the incident wave at polarisation p travelling in direction μ scattered into direction μ' with polarisation p' . The four possible combinations for the different polarisations make up a matrix known as the phase matrix, P .

So we see a medium's ability to absorb and add radiative energy depends on its absorption and scattering coefficients, α_a and α_s . In practice however a medium is defined in radiative transfer theory by its single scattering albedo ω and optical depth τ which are defined as:

$$\omega = \frac{\alpha_s}{\alpha_e} \quad (2.90)$$

$$\tau = \alpha_e \cdot d \quad (2.91)$$

for a medium of depth d .

There is no formal solution to this equation. However when evaluating the radiative transfer equation we can often neglect the third term which allows us to evaluate this equation, leading to the simplified radiative transfer equations.

2.4.3.2 The Simplified Radiative Transfer Equation

Neglecting the scattering source term in the RTE gives us the following, which is of identical form for H and V polarisation:

$$\mu \frac{dI}{dz} = \alpha_a \cdot \frac{2k_B}{\lambda^2} \cdot T - \alpha_e \cdot I \quad (2.92)$$

We can rewrite this in terms of Brightness temperature T_B , applying (2.82) and (2.79), as:

$$\mu \frac{dT_B}{dz} = \alpha_a \cdot T - \alpha_e \cdot T_B \quad (2.93)$$

If we assume that α_a , α_e and T are constants we can integrate (2.93) from $z'=z$ to $z=0$ to obtain:

$$T_B(z) = T_B(0) \exp\left(\frac{-z \cdot \alpha_e}{\mu}\right) + \int_0^z \left(\alpha_a \cdot T \cdot \frac{dz'}{\mu}\right) \cdot \exp\left[-(z-z') \cdot \frac{\alpha_e}{\mu}\right] \quad (2.94)$$

The first term in this equation calculates the original brightness temperature reduced along the path z by an exponential factor, corresponding to total loss due to absorption and scattering. The second term sums the emission of each layer of the medium from 0 to z , which each emit thermal radiation $\alpha_a \cdot T \cdot dz'/\mu$ which is attenuated along the path it must travel by the same exponential factor.

Integrating the second term gives the following equation:

$$T_B(z) = T_B(0) \cdot \exp\left[\frac{-z \cdot \alpha_e}{\mu}\right] + \frac{\alpha_a}{\alpha_e} \left[1 - \exp\left(-\frac{z \cdot \alpha_e}{\mu}\right)\right] \cdot T \quad (2.95)$$

$$\text{or } T_B(z) = T_B(0) \cdot \gamma + (1 - \omega) \cdot (1 - \gamma) \cdot T \quad (2.96)$$

for $\gamma = \exp\left[\frac{-\tau}{\mu}\right]$ and $1 - \omega = \frac{\alpha_a}{\alpha_e}$.

2.5 Passive Microwave Remote Sensing of Land

Satellite-borne microwave radiometers have been providing information about atmospheric and oceanic parameters for some time. However this is not the case for land parameters since the spatial resolution of most satellites – typically of the order of 10km - is more compatible with spatial variations of oceanic and atmospheric parameters than land parameters and also because mechanisms for microwave emission from land surfaces and volumes are not as well understood, as they are more complicated.

Nevertheless, an extensive body of research has been collected over the last few decades in the form of experimental data and theoretical models. In this section we present this theory, related to emission of soil and vegetation, which is most relevant to this thesis.

Microwave remote sensing's main application is monitoring the water content and temperature of the land. As we have seen, the Earth's thermal radiation depends on its temperature and emissivity. The emissivity and reflectivity of the Earth is directly related to the dielectric permittivity content which depends strongly on water content in the microwave region.

In the following sections we consider first the emission the bare ground and then the emission of the ground covered by vegetation.

2.5.1 Emission of Bare Soil Surfaces

The simplest representation of the bare soil surface is a homogeneous isothermal soil medium with a plane air-soil boundary. This allows us to calculate the soil brightness temperature measured at angle θ and polarisation p as follows:

$$T_B(\theta, p) = e(\theta, p)T_s = [1 - \Gamma(\theta, p)]T_s \quad (2.97)$$

where e is the soil emissivity, T_s the soil temperature and Γ is the soil reflectivity calculated from its permittivity using the Fresnel equations.

(2.97) coupled with (2.86) and (2.87) shows that the soil's brightness temperature is determined by the dielectric permittivity constant and soil temperature. In order to understand the emission of the bare soil we must therefore understand how the soil's dielectric permittivity constant is related to soil physical parameters. This is broached in section 2.5.1.1. Also, in reality the soil is often neither homogeneous nor isothermal and its surface is not flat. The effects of these three issues therefore need to be understood and accounted for. In section 2.5.1.2 we consider the effects of a temperature profile and a rough surface on the emission.

2.5.1.1 The soil dielectric permittivity constant in the microwave region

Soils are a mixture of mineral matter, salts, organic matter, soil colloids, water containing dissolved salts, organic matter and gases, and air filling the empty voids. One of the most important structural features of a soil is its grain size (granulometric) composition or the relative content of particles of different sizes within the soil per unit volume or soil mass. It is usual to classify different soil types based on their granular composition. However there are several different classifications of soil grading that are used in soil science, geology, mining and agriculture. The classification of the US department of agriculture is often used in remote sensing and classifies the following soil particles based on their size: 1) sand: particles with a size of more than 0.05mm, 2) clay: particles with a size of 0.002 – 0.05 mm and 3)silt: particles with a size of less than 0.002mm. Thus we consider the bulk soil material (not including water and air) to be made up of sand, clay and silt. The amount of sand, clay and soil

fractions in a soil, which are expressed in percents by weight, is known as the soil texture. Different soils are grouped together into types based on their textures.

The overall soil moisture content can be defined by two different variables: the relative gravimetric soil moisture content, m_g , and the volumetric soil moisture content, m_v . The relative gravimetric soil moisture content, m_g , is defined as:

$$m_g = \frac{w_w - w_d}{w_d} \quad (2.98)$$

where w_w and w_d are respectively the wet and dry weights of the soil sample. The volumetric soil moisture m_v is defined as:

$$m_v = \frac{V_w}{V_s} = m_g \frac{\rho_b}{\rho_w} \quad (2.99)$$

where V_w is the volume of the water in the soil, V_s is the volume of the soil, ρ_b is the soil bulk density and ρ_w is the density of water (equal to approximately 1g/cm^3 at room temperature).

The value of m_v , given by (2.99) is the value of soil moisture that is retrieved from microwave radiometric measurements by the SMOS mission.

Since in the microwave band the dimensions of soil particles are small, the concept of an effective permittivity may be used for describing the propagation of electromagnetic waves in such a medium. Electromagnetically a soil consists of three components: air, bulk soil (containing sand, silt and clay), and water. Moisture is further divided into bound and free water. Bound water is the water absorbed by the surface of soil particles and kept there by chemical and physical-chemical forces, forming a film around a particle with a thickness of several molecular layers. Free water is considered to be liquid water subject only to the gravitational force and located in macro voids and cracks. Bound water interacts with an electromagnetic wave in a manner different to free water due to the high intensity of the forces physical and physical-chemical forces acting on it. This is why electromagnetically bound and free water are considered separately.

The complex permittivity constants of bound and free water are each functions of the electromagnetic frequency, the physical temperature T and the salinity S . Hence the permittivity of soil is generally a function of: 1) f , T and S , 2) the total volumetric water content m_v , 3) the relative fractions of bound and free water, related to soil surface area per unit volume, 4) the bulk soil density, ρ_b , 5) the shape of the soil particles, and 6) the shape of water inclusions. The main factor influencing the permittivity of soil in the microwave region is the water content and it is thanks to this relationship that soil moisture can be retrieved from microwave radiometric observations of soil emission. For example for a clayey

or sandy bare soil with a flat surface and at a temperature of around 300K, a change in volumetric soil moisture of about 1% leads to a change in measured brightness temperature of about 3K (Chukhlantsev 2006). Thus the measured brightness temperature of a bare soil is highly sensitive to soil moisture in the microwave region. The soil texture (or soil type) also influences the dielectric permittivity constant because this influences in particular the fraction of bound and free water in the soil. For example the quantity of bound water is low for sand (about 2-3%) and high for clay, amounting to about 30-40% of dry weight for heavy clays.

The dielectric permittivity constant of soil is the main factor determining its emission. Therefore relating the soil dielectric permittivity to its physical parameters is essential for retrieving soil moisture from remote sensing data. Because of this, numerous experiments have been conducted in order to investigate the dielectric behavior of soil-water mixtures in the microwave region (e.g. Wang and Schmugge 1980, Mironov et al 2004, 2009, Demontoux et al 2008). Currently the main models that are used to relate soil moisture to the soil permittivity are the model proposed by Dobson et al(1985), the model proposed by Mironov et al (2004) and the empirical model proposed by Wang and Schmugge (1980). The SMOS mission uses the Dobson model which gives good except for dry sandy soils, when the approach developed by Matzler (1998) is used, which accounts for the behavior of dry desert sand. The Mironov model has been developed recently and improves on the Dobson model, particularly in relation to the dielectric permittivity constant's temperature dependence (J.P. Wigneron et al 2010, Mironov et al 2009). We therefore chose to use this model for the work of this thesis. In our numerical approach the soil is represented as a dielectric layer whose permittivity constant is calculated as a function of soil moisture, temperature and soil type (clay content) using the Mironov model.

2.5.1.2 Non-uniform Temperature and Dielectric profiles

The soil emission is directly related to soil temperature, as shown by (2.97). However this equation assumes that the soil is isothermal and in reality the soil temperature usually varies with depth. Theoretically we consider the soil to be made up of many emitting layers, each dependent on the temperature and moisture of that layer. The width of each layer can then be made infinitesimally small. The net intensity of the soil emission is a superposition of intensities emitted at various depths. The emission from each layer is attenuated by the wet soil layers above. Deeper surfaces contribute less to the overall intensity because their emission is attenuated more by the above soil (Choudhury et al 1982). Thus the surface contributes the most, followed by each of the layers below in turn.

In a homogeneous medium, 63% of the emitted energy comes from a layer extending from the surface to a depth of $p \cos \theta_2$, where p is the penetration depth and θ_2 the refraction angle in the medium. There is an 87% contribution by a layer twice as thick and a 95% contribution by a layer 3 times as thick.

The penetration depth in the soil varies between approximately λ for soil moisture of $\approx 0.04 \text{ g/cm}^3$ and 0.1λ for very wet soil, which for the SMOS mission frequency of 1.4 GHz is equivalent to about 2.1cm for very wet soil and 21cm for a very dry soil. Therefore when considering the effect of temperatures and dielectric permittivities varying with depth, so called volume effects, on emission it is important to remember that only uniformities at a depth of up to about $2p - 3p$ (up to about 40 – 60cm for the SMOS mission) affect the emission, because contribution by deeper layers is relatively small.

The brightness temperature of the soil can be calculated from radiative transfer theory as the sum of the emission of each layer. This emission can be calculated by modeling the soil as an effective isothermal medium with an effective temperature T_{eff} , given by:

$$T_{\text{eff}} = \int_0^{\infty} T_s(z)W(z)dz \quad (2.100)$$

where $T_s(z)$ is the soil temperature at depth z , and $W(z)$ is a temperature weighting function of the contribution of each soil layer. $W(z)$ depends only on the soil dielectric profile and is given by:

$$W(z) = \alpha(z) \exp \left[- \int_0^z \alpha(z') dz' \right] \quad (2.101)$$

where:

$$\alpha(z) = \left(\frac{4\pi}{\lambda} \right) \frac{\epsilon_r''(z)}{2(\epsilon_r'(z))^{0.5}} \quad (2.102)$$

$W(z)$ decreases rapidly with depth for wet soils and more slowly for dryer soils.

However this model requires a detailed vertical profile of soil moisture and temperature, which is not usually available.

Several methods have therefore been developed to estimate T_{eff} as accurately as possible from a minimum number of measurements. The most simple method is to take the surface or air temperature to be T_{eff} . However this approximation is only considered to be valid at frequencies higher than 10 GHz, where the penetration depth is low. Choudhury et al (1982) developed an approximation for T_{eff} as a linear function of soil temperature measured at two different depths. This was improved on for L-band measurements by Wigneron et al (2001) by taking into account the influence of soil moisture on the penetration depth: the dryer the soil the deeper the contribution. Holmes et al (2006) developed a new parameterization which further takes into account the effect of the dielectric depth profile on the

attenuation of the emission. De Rosnay et al (2006) compared these three approaches to the SMOSREX 2006 dataset, where detailed soil moisture depth profiles had been continuously taken, along with bare soil microwave radiometer measurements, over the course of two years. Results showed that the parameterization by Choudhury et al (1982) was only suitable for short time periods (weeks) where the soil moisture does not greatly vary. The model by Wigneron et al had better agreement and the model by Holmes et al still better agreement.

2.5.1.3 Rough Surface Scattering and Emission

In this section we consider the effects of a rough surface on the ground emission. A plane wave incident upon a perfectly flat surface of a homogeneous medium will be reflected coherently, entirely in the specular direction θ , as shown in Figure 2.8 below:

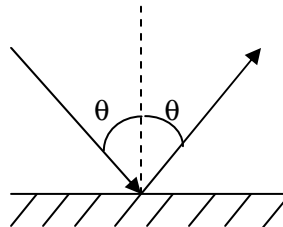


Figure 2.8: Specular reflection off a planar surface

The amount of energy reflected can be calculated by the Fresnel equations.

In the case of a slightly rough surface, with height irregularities of the order of the wavelength or larger the incident wave will be scattered in many different directions. Part of the reflected power will be in the specular direction and will maintain the phase coherence characteristic of reflection off a plane surface. This part is called the coherent component. The rest of the reflected power is phase incoherent, called the diffuse or non-coherent component. Part of the diffuse scattering component will maintain the same polarisation as the incident beam and part will be polarised in the orthogonal state. Figure 2.9, illustrates this.



Figure 2.9: Diffuse reflection of a rough surface

The coherent part decreases and the non-coherent part increases with surfaces of higher roughness. The contribution of the coherent part of the bistatic scattering coefficient to the emissivity is larger than the contribution from the non-coherent part, so the emissivity increases with surface roughness. Note that Shi et al (2002) suggested an exception to this around the Brewster angle. Using an analytical modelling technique, they found that the emissivity decreased with roughness around the Brewster angle, because the non-coherent contribution was more significant around this angle. However this effect has so far not been observed experimentally (this is covered in more depth in section 3.1.2.2c).

In the presence of a rough surface, the radiation emitted by the surface will be transmitted across the boundary in many different directions. Consequently the brightness temperature is composed of contributions that are incident upon the surface from below along many different directions.

The reflectivity and emissivity of a rough surface cannot be calculated using the Fresnel equations. A vast body of research has been dedicated to calculating the reflectivity and emissivity of a rough surface, a nontrivial problem. We will present this research topic in detail in the next chapter but first in sections a) - d) we will introduce the basic concepts of rough surface scattering and emission theory. We start by defining a rough surface mathematically, in section a), then define the bistatic scattering coefficient, a measure of the reflection of a rough surface, and finally define the concepts of a smooth surface and a very rough surface.

a) Statistical Definition of a Rough surface

A natural rough surface can be modelled as a random statistical process. This conveniently provides us with a measure of the *degree of roughness* of a surface, or quite simply its *roughness*, using 3 statistical parameters. These parameters are: the surface autocorrelation function, the autocorrelation length, L_c , and the standard deviation of surface heights, σ .

a1) Standard Deviation of Surface height, σ

Let us consider a surface in the x-y plane whose height at point (x,y) is z(x,y) above the x-y plane. For a statistically representative segment of the surface, of widths L_x and L_y in the x and y directions respectively, the surface mean height can then be calculated from:

$$\bar{z} = \frac{1}{L_x L_y} \int_{-L_x/2}^{L_x/2} \int_{-L_y/2}^{L_y/2} z(x, y) dx dy \quad (2.103)$$

The standard deviation can be calculated as follows:

$$\sigma = (z^2 - \bar{z}^2) \quad (2.104)$$

where z^2 is calculated from:

$$z^2 = \frac{1}{L_x L_y} \int_{-L_x/2}^{L_x/2} \int_{-L_y/2}^{L_y/2} z^2(x, y) dx dy \quad (2.105)$$

In practice surface profiles are digitized into discrete values $z_{ij}(x_i, y_j)$ at appropriate spacing Δx and Δy . A rule of thumb is that the spacing should be chosen to be less than or equal to 0.1λ (2.14cm for $f=1.4\text{GHz}$). For the same spacing and number of points, N , in the x and y direction, the standard deviation can be calculated from:

$$\sigma = \left[\frac{1}{(N-1)^2} \left(\sum_{i=1}^N \sum_{j=1}^N (z_{ij}^2) - \left(\sum_{i=1}^N \sum_{j=1}^N z_{ij} \right)^2 \right) \right]^{1/2} \quad (2.106)$$

a2) Surface autocorrelation function and length

The normalised autocorrelation function is defined as:

$$\rho(x', y') = \frac{\int_{-L_x/2}^{L_x/2} \int_{-L_y/2}^{L_y/2} z(x, y) z(x+x', y+y') dx dy}{\int_{-L_x/2}^{L_x/2} \int_{-L_y/2}^{L_y/2} (z(x, y))^2 dx dy} \quad (2.107)$$

and is a measure of the similarity between the height z at a point x and at a point x' distant from x . For the discrete surface profile we have a normalised autocorrelation function for discrete displacement $x' = (k-1)\Delta x, y' = (l-1)\Delta y$ of:

$$\rho(x', y') = \frac{\sum_{i=1}^{N+1-k} \sum_{j=1}^{N+1-l} z_{ij} z_{(i+k-1)(j+l-1)}}{\sum_{i=1}^N \sum_{j=1}^N z_{ij}^2} \quad (2.108)$$

The autocorrelation length L_c is defined as the length for which the autocorrelation function falls by $1/e$, ie $\rho(L_c) = 1/e$. This value provides a reference for estimating the statistical independence of two points on the surface: if their distance apart is greater than L_c they may be considered (approximately) statistically independent of one another. For a smooth surface L_c is infinity since every point is correlated with every other point on the surface with a correlation coefficient of 1.

Broadly speaking σ is a measure of how rough the surface is in the vertical direction and L_c is a measure of the roughness in the horizontal direction. Another rough surface value which is sometimes useful is the surface slope, m , equal to the ratio of σ/L_c . High slope values indicate a highly rough surface and low values of the slope indicate a smooth surface.

Rough soil surfaces are generally considered to have autocorrelation functions of the following form:

$$\rho(r) = \exp \left[- \left(\frac{\sqrt{x^2 + y^2}}{L_c} \right)^n \right] \quad (2.109)$$

where n determines the form of the autocorrelation function: for the special cases of exponential and gaussian autocorrelation functions it is equal to 1 and 2 respectively. Traditionally a Gaussian autocorrelation coefficient was assumed for rough bare soil surfaces however natural surfaces have recently been shown to have autocorrelation functions closer to exponential than gaussian.

b) Bistatic Scattering Coefficient

Since we have diffuse scattering with rough surfaces it is helpful at this point to define a more general expression for scattering: the bistatic scattering coefficient, $\sigma_{pq}^0(\theta, \phi; \theta_s, \phi_s)$. This term is defined as the fraction of the power incident upon the surface at angle (θ, ϕ) and at polarisation p that is scattered in the direction (θ_s, ϕ_s) with polarisation q . If p and q are the same, either H or V, it is called the vertically or horizontally polarised scattering coefficient, and if p and q are different it is called the cross-polarised scattering coefficient (note $\sigma_{HV}^0 = \sigma_{VH}^0$).

For a beam incident at angle (θ, ϕ) across an area A_{eff} of a surface, scattered to a point at a distance R and angle (θ_s, ϕ_s) from the surface, $\sigma_{pq}^0(\theta, \phi; \theta_s, \phi_s)$ measured at a distance R is given by:

$$\sigma_{pq}^0(\theta_s, \phi_s; \theta, \phi) = \frac{4\pi R^2 |E_p^s(\theta_s, \phi_s)|^2}{A_{\text{eff}} |E_q^i(\theta, \phi)|^2} \quad (2.110)$$

where $E_p^s(\theta_s, \phi_s)$ is the reflected Electric field of polarization p and $E_q^i(\theta, \phi)$ is the incident electric field of polarization q .

The backscattering coefficient is the bistatic scattering coefficient for the monostatic case of $(\theta_s, \phi_s) = (\theta, \phi + \pi)$ i.e. the reflection angle is equal to the incident angle.

Applying Kirchoff's radiation law to the rough-surface case, Peake (1959) developed expressions for the polarised emissivity $e_p(\theta, \phi)$ of polarisation p and measured at an angle (θ, ϕ) in terms of the bistatic scattering coefficient as follows:

$$e_p(\theta, \phi) = 1 - \Gamma_p(\theta, \phi), \quad (2.111)$$

where $\Gamma_r(\theta, \phi)$ is the reflectivity at polarization r , given by:

$$\Gamma_p(\theta, \phi) = \frac{1}{4\pi} \iint_{\text{upper hemisphere}} \frac{1}{\cos \theta} \left[\sigma_{pp}^0(\theta_s, \phi_s; \theta, \phi) + \sigma_{pq}^0(\theta_s, \phi_s; \theta, \phi) \right] \sin \theta_s d\theta_s d\phi_s. \quad (2.112)$$

Thus the emissivity can be calculated by integrating the bistatic scattering coefficient over half space. This integration reduces to the Fresnel reflectivity for the case of a smooth surface.

Note that equation (2.111) follows from energy conservation considerations. This is important for numerical calculations of emissivity since it is usual to calculate the emissivity from the reflectivity, applying (2.110), (2.111) and (2.112). This approach is only valid if the numerical solution satisfies energy conservation. It is usual to use energy conservation as a check that a numerical approach is accurate but it is particularly important for emissivity calculations, since the calculations themselves are based on energy conservation via equation (2.111).

Note that the bistatic scattering coefficient and backscattering coefficients are usually measured and calculated in dB:

$$\sigma_{dB}^0 = 10 \log_{10} \sigma^0 \quad (2.113)$$

Almost all theoretical models that calculate the emissivity of a rough surface, including the approach developed in this thesis, do this by first calculating the bistatic scattering coefficient at all points in the hemisphere above the rough surface and then applying (2.111) and (2.112)

c) Smooth surface criteria

So far we have discussed the emission of a flat and smooth surface without really thinking about at what point a surface is still considered to behave as a smooth surface and at what point it may be considered to behave as a rough surface.

When discussing a smooth surface we usually mean one that obeys Fresnel's laws of reflection and transmission. Experimentally this can mean different things depending on whether we measure the emission or scattering of a surface. For the emission case the emissivity must follow the law $e = 1 - \Gamma$, where Γ is the Fresnel reflectivity, for the surface to be smooth. For the scattering case the backscattering coefficient must decay rapidly with increasing θ , e.g. a drop of at least 40dB from nadir to 10° .

Theoretically we can apply the Rayleigh or the Fraunhofer criterion. The former states that the surface may be considered smooth if two reflected rays have a phase difference of no more than $\pi/2$. This leads to following condition on the standard deviation of surface heights:

$$\sigma < \frac{\lambda}{8 \cos \theta} \quad (2.114)$$

This condition provides a first order classifier of surface roughness but we require a more accurate condition in the microwave region where the wavelength is of the order of the standard deviation of surface heights. This can be provided by the Fraunhofer definition for the far field distance of an antenna, leading to:

$$\sigma < \frac{\lambda}{32 \cos \theta} \quad (2.115)$$

This criterion is more consistent with experimental observations.

d) Perfectly Rough Surface

It is of interest to consider the theoretical case of a perfectly smooth surface and its behaviour. This allows us to consider the emissivity of the extremes of a perfectly smooth and perfectly rough surface, and then we expect the behaviour of all other rough surfaces to fall in between.

A perfectly rough surface is known as the Lambertian surface after Lambert's law which states that the angle variation of $\sigma_{pq}^0(\theta, \phi; \theta_s, \phi_s)$ depends only on the product $\cos \theta \cos \theta_s$, ie:

$$\sigma_{pp}^0(\theta, \phi; \theta_s, \phi_s) + \sigma_{pq}^0(\theta, \phi; \theta_s, \phi_s) = \sigma_0^0 \cos \theta \cos \theta_s \quad (2.116)$$

where σ_0^0 is a constant depending on the dielectric properties of the surface. The corresponding emissivity is:

$$e_p(\theta, \phi) = 1 - \frac{\sigma_0^0}{4} \quad (2.117)$$

which is polarization and angle dependent.

Thus the bistatic scattering coefficient varies proportionally to $\cos \theta_s$ and its magnitude depends on the incident angle (its cosine).

The emissivity of a perfectly smooth surface depends on the dielectric properties, the polarization and the angle. However the emissivity of a perfectly rough surface is independent of all properties except the dielectric surface properties. In between the two extreme cases the emissivity is related to the angle, polarisation and both the geometric and dielectric properties of the surface.

2.5.2 Modelling the emission of the ground covered by vegetation

In this section we consider the emission of soil covered by vegetation, including trees, shrubs, grass, and crops. The emission of soil covered by a vegetation layer can be modelled by the simplified Radiative Transfer Equations. For example let us consider the setup shown in Figure 2.10.

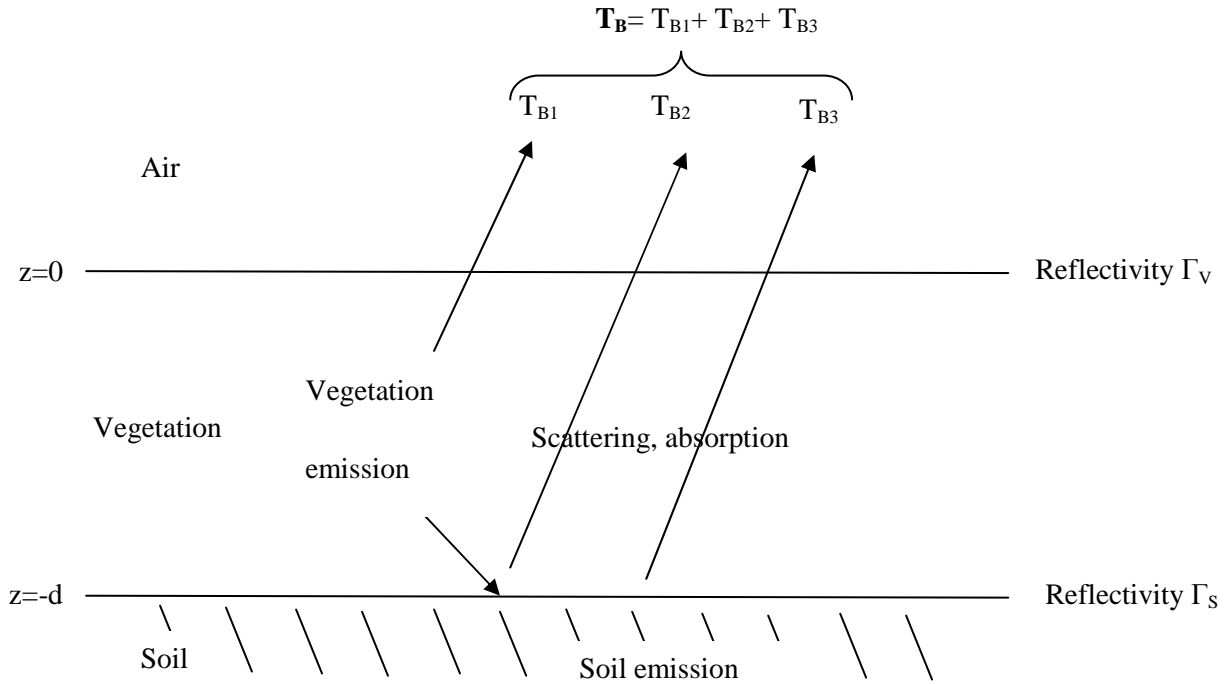


Figure 2.10: Emission of soil covered by a vegetation layer

The emission from a soil-vegetation structure has three components: the emission of the vegetation layer, the emission of the soil layer attenuated by the vegetation and vegetation emission emitted downwards and reflected back up by the soil-vegetation boundary. We have designated these three components T_{B1} , T_{B2} and T_{B3} respectively. Unless we consider tropical forests, vegetation is usually not very dense and so its permittivity is close to that of air, i.e. $\Gamma_V \approx 0$. Therefore we assume no reflections off the vegetation-air boundary.

Let us call the vegetation emission T_B^* . From (2.96) T_B^* is given by:

$$T_B^* = (1 - \omega) \cdot (1 - \gamma) \cdot T_V \quad (2.118)$$

where T_V is the temperature of the vegetation.

Assuming isotropic emission by the vegetation, T_B^* has the same value just above the vegetation-soil interface and just under the vegetation-air interface.

Assuming no reflection at the vegetation-air boundary, T_{B1} can be approximated to T_B^* , i.e.:

$$T_{B1} \approx T_B^* = (1-\omega) \cdot (1-\gamma) \cdot T_V \quad (2.119)$$

We deduce, similarly, expressions for T_{B2} and T_{B3} , as:

$$T_{B2} = T_B^* \cdot \Gamma_S \cdot \gamma \quad (2.120)$$

$$T_{B3} = (1-\Gamma_S) \cdot T_S \cdot \gamma \quad (2.121)$$

Combining these three components we have an overall emitted brightness temperature, T_{Bp} , at polarisation p, of:

$$T_{Bp} = (1-\omega) \cdot (1-\gamma) \cdot (1+\Gamma_{sp} \cdot \gamma) \cdot T_V + (1-\Gamma_{sp}) \cdot \gamma \cdot T_s \quad (2.122)$$

γ can be replaced by $\gamma = \exp(-\tau/\mu)$, rewriting T_{Bp} in terms of the coefficients τ and ω .

For this reason the model is often known as the τ - ω model.

This equation is frequently used for interpreting microwave radiometry measurements over vegetation covers, including crop fields, grasslands and forests. The values of τ and ω are to be determined experimentally, and attempted to be fitted to vegetation characteristics. The τ - ω model is used by SMOS in the L-MEB model for retrieving soil moisture over vegetation covered ground. τ and soil moisture are retrieved simultaneously from multiangular data.

In deriving this equation we have neglected the scattering source term in the full RTE. This is a good assumption at low frequencies (high wavelength) of no more than several GHz. Since SMOS measures at 1.4 GHz this equation can be considered valid.

2.5.3 Note

In section 2.5 we have presented the main concepts behind remote sensing of land. In the next two chapters we consider in more depth modelling the emission of the soil and the influence of a forest litter layer on the soil emission, since the aim of this PhD is to model the soil-litter system.

CHAPTER 3. MODELLING THE EMISSION OF THE SOIL- LITTER SYSTEM

3. Modelling the Emission of the Soil-Litter system

In this chapter we present a review of methods that have been used to calculate the scattering and emission of soil and litter layers. Firstly, in section 3.1 we present a review of models to calculate the bare soil scattering and emission, which take into account in particular the effects of a randomly rough surface on emission. Secondly, in section 3.2 we present models that take into account the effects of a litter layer on the forest ground emission. Finally in section 3.3, we discuss the choice of modelling approach for the work of this PhD.

3.1 Microwave Emission of Soil: modelling the effects of a rough surface

In this section we consider modelling the scattering and emission of a rough soil surface. This subject has been studied for several decades and a vast body of knowledge has been collected, and many different modelling techniques developed. In this chapter we present and review the different approaches currently used to model the scattering and emission of rough surfaces. In general the rough surface is represented as a dielectric of a known permittivity value. This value can be calculated from the soil moisture by applying models such as the model developed by Dobson et al (1985) or the model presented by Mironov et al (2004), which are algebraic, or an experimentally determined relationship. The models discussed in this section can in general also be used to study any medium that can be represented as a dielectric with a single homogeneous permittivity, and a rough surface. In this chapter we focus on the main methods currently used to calculate rough surface scattering and emission, presenting in detail those that are particularly relevant to this thesis. Note that in theoretical modelling approaches we consider scattering and emission together. This is because the two are theoretically linked. In general theoretical modelling approaches have been developed firstly to calculate scattering and then the emissivity can be calculated from one minus the reflectivity, where the reflectivity is calculate by integrating the bistatic scattering coefficient over halfspace.

There are typically three main scientific approaches to modelling rough surface scattering and emission: the analytical approach, semi-empirical approach and the numerical approach. Analytical and numerical approaches are theoretical whilst semi-empirical approaches have a physical basis but are essentially constructed from experimental data. These types of approach are more general than for the problem of rough surface scattering and emission. When modelling any complicated process in remote sensing (one that cannot be solved analytically without making assumptions) we can apply a semi-empirical, analytical or numerical approach.

Analytical approaches are based on a physical description of wave scattering off a rough surface (with emission calculated from the bistatic scattering coefficient using equations (2.110) – (2.112)). We wish to calculate the value of the scattered electric field in (2.110) for a given roughness condition

(given values of σ , L_c , and autocorrelation function). Due to the complexity of rough surfaces a general solution cannot be found and so we make assumptions in order to obtain an analytical solution. The solution that we obtain is then only valid under conditions where the approximations and/or assumptions are valid. Outside of these conditions the analytical model produces inaccurate results.

Once an analytical approach has been developed and shown to be valid, most of the research done focuses on testing and extending their regions of validity. In the case of rough surface scattering and emission there are many different analytical models each with their own regions of validity. Historically the main models are the Kirchoff approximation (geometric optics and physical optics models) (Ulaby et al 1985, vol II 12-4) and the small perturbation method (SPM)(Ulaby et al 1985, vol II 12-5). Currently the model most often used is the Integral Equation Model (IEM) (Fung et al 1992, Fung et al 1994) and the updated version, the Advanced Integral Equation Model (AIEM)(Chen et al 2003, T.D. Wu et al 2004), since it has a wide validity region. Analytical models such as these are very complicated but are nevertheless simpler and faster than numerical models, as they tend to be algebraic. The inputs of analytical models are generally the values of σ , L_c , the form of the autocorrelation function and the permittivity ϵ .

The semi-empirical approach consists of very simple equations, whose form has some physical basis, and which contain variables whose values are fitted experimentally. The advantage of semi-empirical theories is the simplicity of the equation or equations involved. They can also be quite accurate providing enough work is done to fit the parameters over different conditions. The disadvantage is that the parameters fitted experimentally are not usually valid under experimental conditions other than those for which they were fitted. Development work for these approaches involves further experiments to fit parameters for a wider range of conditions. The aim is to fit over many different conditions and then gradually find a relationship between them.

Inputs for such models tend to be experimentally determined parameters which intrinsically include a measure of how rough a surface is and other possible affecting factors not already accounted for such as soil dielectric inhomogeneities. In satellite remote sensing missions these parameters can be either simultaneously retrieved or measured beforehand for the different roughness conditions, the former being the approach most often adopted.

Numerical modelling methods solve directly Maxwell's equations for rough surface scattering. The input is the rough surface itself: a rough surface is constructed on a computer and then Maxwell's equations solved for wave scattering off this surface. This type of modelling therefore does not produce an analytical equation as an output but rather results of the emission or scattering of a particular surface, called a deterministic surface. In these models we reconstruct the physical situation and calculate exactly the "results" that would be obtained for that situation: in essence we perform an experiment on a computer, the advantage being that we can better control the various parameters

which affect the results. The input can either be the rough surface itself or more usually values of σ , L_c and the autocorrelation function. In the latter case we construct many different surfaces and average over the ensemble in order to compute emission and scattering for these rough surface conditions. The advantage of numerical methods over other modelling methods is that they are exact, and so the most accurate, but their main disadvantage is that they can be time consuming and require larger memory than other methods. Historically this type of method has been used principally to validate other methods (analytical, empirical, and semi-empirical), since calculation time made it unsuitable for everyday use. However with advances in computing these methods are used more and more frequently for scientific studies.

In the following sections we present firstly the semi-empirical method most often used, secondly the main analytical methods, and finally a detailed review of numerical methods. We present numerical methods in the most detail since we chose to use a numerical modelling approach for the work of this thesis. (The reasons for this choice are presented in chapter 5.) Note that the theoretical approaches are presented here in the context of calculating scattering and emission of a soil medium. However they apply equally to any medium that can be represented as a dielectric of homogeneous permittivity constant. This includes the forest litter layer (which is addressed in chapter 5) and other rough surfaces found in remote sensing including the ocean.

3.1.1 A Semi-Empirical model for soil emission at L-Band

In this section we present the main semi empirical approach currently used for rough surface emission at L-band, known as the Q-h model (Choudhury et al 1979 and Wang et al 1981), including the model's formulation and subsequent development.

3.1.1.1 Q-h Model Formulation

The Q-h model is based on two roughness parameters: the roughness height h_s and a polarization mixing parameter Q_s , both of which can be retrieved from brightness temperature measurements. The h parameter was introduced by Choudhury et al (1979) and the Q parameter by Wang et al (1981). This model based on these two parameters is known as the Q-h model and has been developed and modified over the years to account for experimental observations made. The reflectivity is calculated from a modified Fresnel reflection formula incorporating h and Q , which has been found to be appropriate for most applications. In the latest version of the semi-empirical model, the polarized soil reflectivity $R_p(\theta)$ is given by:

$$R_p(\theta) = [(1 - Q_s)R_p^*(\theta) + Q_sR_s^*(\theta)]\exp(-h_s \cos^N(\theta)) \quad (3.1)$$

Where p and q represent the polarization, which can be either h or v , R_p is the polarized specular reflectivity (calculated from θ and dielectric permittivity ϵ using the Fresnel equations) and N_s is an exponent. The corresponding emissivity is:

$$e_p(\theta) = 1 - R_p(\theta) \quad (3.2)$$

$$e_p(\theta) = 1 - \{[(1 - Q_s)R_p^*(\theta) + Q_sR_s^*(\theta)]\exp(-h_s \cos^{N_s}(\theta))\} \quad (3.3)$$

An additional factor $N_s(\theta)$ appears in this model. In the equation suggested by Choudhury this was equal to 2. Later experiments however (Wang et al (1983) and Wigneron et al (2001)) indicated a value of 0 to be more appropriate and so this was replaced with the variable $N_s(\theta)$ whose value and its dependence on polarization and angle was to be determined. Escorihuela et al (2004) demonstrated that N depends strongly on polarisation.

The physical basis for this formula is that surface roughness reduces coherent reflectivity due to dispersion of the incident wave by the rough surface. This dispersion increases with roughness. Thus the h parameter accounts for this effect. Incoherent reflectivity also increases with surface roughness (from zero at a smooth surface) but this effect is not accounted for in this model; it is assumed to be negligible. An exception has been suggested by Shi et al (2002), using the analytical AIEM formula, who found that at angles around 50° the emissivity decreased, which they explained by the increase in the non-coherent component at around the Brewster angle, where coherent scattering is negligible. This Q - h semi-empirical formula would be incorrect in this case. However this has not yet been observed experimentally.

The second main effect of a rough surface on emission is depolarization, accounted for by the Q parameter.

This model is useful for soil moisture retrieval studies. However the dependence of h and Q on roughness statistical parameters (σ, L_c , autocorrelation function, surface slope) is still unclear.

3.1.1.2 Model Development

Early experimental data of rough surface emission was acquired by Choudhury et al (1979), Wang et al (1981) and Mo et al (1987) but was not large enough to allow for the development of the model over a large validity range. A large dataset (PORTOS-93) of bare soil rough surface emission at L-band was acquired (Wigneron et al 2001) over the whole range of roughness values found in agricultural fields and a large range of soil moisture and temperature conditions. This showed that Q_s and N_s could be set to zero, ie no theta dependence and no depolarization. This conclusion for $N=0$ was in agreement with findings of Wang et al (1983) who also showed that N could be set to zero for $\theta = 10$ to 60° and at three frequencies (1.4, 5 and 10.7 GHz). Mo and Schmugge (1987) also considered

that N could be set to zero for L and C bands. In a more recent study for rather smooth soil Escorihuela et al (2004) showed that values of N should be different for each polarization with $N \approx 1$ for H polarization and $N \approx 0$ for V polarization. This result has yet to be generalized to a larger roughness range.

Considering that $Q_S=0$ at L-Band is also in agreement with most published experimental datasets, including Mo and Schmugge (1987), Njoku and Entekhabi (1996) and Wegmuller and Matzler (1999). Wang et al (1983) found that Q_S was very strongly frequency dependent with very small values obtained at L-Band, with varying values at different soil types including 0, 0.01 0.12. Prigent et al (2000) also found that Q was frequency dependent, increasing with frequency.

Setting $N_S=0$ and $Q_S=0$, we obtain:

$$e_p = 1 - R_p(\theta) = 1 - [R_p^*(\theta)\exp(-h_s)] \quad (3.4)$$

The roughness parameter h_s was retrieved in the PORTOS-93 experiment for angles $\theta=0 - 40^\circ$. This parameter accounts for both “geometric roughness” effects and “dielectric roughness” effects. h_s was therefore linked to the slope ($m=\sigma/L_C$) and surface soil moisture w_s and the equation with the best fit to measurements was found to be:

$$h_s = A(w_s)^B(\sigma/L_C)^C \quad (3.5)$$

with best fit parameters $A=0.5761$, $B=-0.3475$ and $C=0.4230$. Mo and Schmugge (1987) also found h_s to be linked to the slope. Without considering a soil moisture dependence for h_s the following fit was found (Wigneron et al 2001):

$$h_s = A(\sigma/L_C)^C \quad (3.6)$$

with best fit parameters $A=1.3972$ and $C=0.5879$. For this fit the range of rms error and bias were respectively approximately 8 – 10K and 0 – 2K. The dependence on soil moisture can be considered to account for the soil’s “dielectric roughness” as this originates from the effect of the soil drying inhomogeneously.

Recent results from the SMOSREX 2006 campaign of L-Band measurements taken over a year for bare soil at a range of angles, roughness conditions, soil moisture and temperatures (Escorihuela et al 2004) confirm general soil moisture dependence of h_s . Preliminary results show a linear dependence instead of an exponential was preferable for h_s .

A link between h_s and physical parameters such as σ , L_c and soil moisture has been attempted, as described above, but this has limited success because the model is too simple and the reality much more complicated than considered above.

Wigneron et al (2010) re-analysed the PORTOS-93 dataset (which was presented in an earlier paper) which included experimental data over a large range of roughness conditions. The authors confirmed that QR could be set to zero and further found that considering N_R to depend on polarization (two separate values N_{RH} and N_{RV}) improved the model accuracy. They also related parameters H_R and the difference between N_{RH} and N_{RV} ($N_{RH} - N_{RV}$) to the standard deviation of surface height as follows:

$$H_R = \left(\frac{0.9437\sigma}{0.8865 + 2.2913\sigma} \right)^6 \quad R^2 = 0.93 \quad (3.7)$$

$$N_{RH} - N_{RV} = -0.0361\sigma + 2.24 \quad R^2 = 0.44 \quad (3.8)$$

Also the following linear relationship was suggested between N_{RH} and N_{RV} :

$$N_{RV} = 0.686N_{RH} - 1.167 \quad R^2 = 0.59 \quad (3.9)$$

Note that R^2 is the coefficient of determination which provides a measure for how close the fit is to the experimental data: a value close to 1 indicates a good fit and a value close to 0 indicates a poor fit.

3.1.1.3 Comparing semi-empirical models to theoretical models

It is worth noting the differences between the semi-empirical approach to rough surface emission and theoretical modelling approaches and thus the problems encountered when comparing the two. When modelling rough surfaces we consider them to have homogeneous characteristics, i.e. surface roughness is the same in both x and y directions and soil moisture is homogeneously spread inside the ground, providing a dielectric constant that is homogeneous across and under the surface. However the reality is more complex. For example let us consider a ploughed soil. After heavy rainfall the surface will be homogeneously wet and will have a homogeneous roughness. If a sunny period follows however the ground will not dry out in a homogeneous manner: large emerging clods dry out more rapidly than hollows within the field. This may lead to a large spatial variation in soil moisture content at the surface and within the soil at a spatial scale of about 1m. There is also soil moisture non-uniformity at a lower spatial scale of a few cm from the surface of the clods drying more quickly than the inside. The roughness is no longer isotropic due to the clods created by the drying process. Under dry conditions we must also consider volume effects in the soil, since the emission is no longer only produced by the surface but by soil up to a depth of 10cm at low frequencies. In this case, the soil emission results from both geometric roughness and “dielectric roughness” from soil moisture heterogeneities.

Current theoretical surface scattering models, both analytical and numerical, should therefore be limited to cases where the soil can be considered homogeneous, namely very wet soil or very dry

conditions. Rough surface models should be extended to include heterogeneities if we wish to use them accurately for the case of dry soils. On the other hand semi-empirical models, such as the Q-H model, are based mainly on experiments and so already take into account implicitly both the surface effects and the heterogeneous volume effects for dry soils. This difference in current physical and semi empirical models makes it hard to make comparisons between them.

3.1.2 Analytical Models

In this section we present different analytical models for the calculation of rough surface scattering and emission. Firstly we present the general approach and then the main models.

3.1.2.1 General Approach

In analytical methods, the emissivity and bistatic scattering coefficient are computed from the scattered electric field in the far-field region, E_s , applying formulas (2.110) – (2.112).

In order to calculate E_s the Stratton-Chu formula is used which expresses the scattered field in the far zone in terms of tangential surface fields, as follows:

$$\vec{E}_s = K\hat{n}_s \times \oint_{\Sigma} [\hat{n} \times \vec{E} - \eta_s \hat{n}_s \times (\hat{n} \times \vec{H})] \exp(-ik_s \vec{r} \cdot \hat{n}_s) d\Sigma \quad (3.10)$$

where $d\Sigma$ is an infinitesimal element on the rough surface, n is the normal to the rough surface at point $d\Sigma$, n_s is the normal to surface s of the far field sphere on which we calculate E_s , and E and H are the electromagnetic fields at $d\Sigma$ on the rough surface. The geometry relating to this integral is shown in Figure 3.1 below.

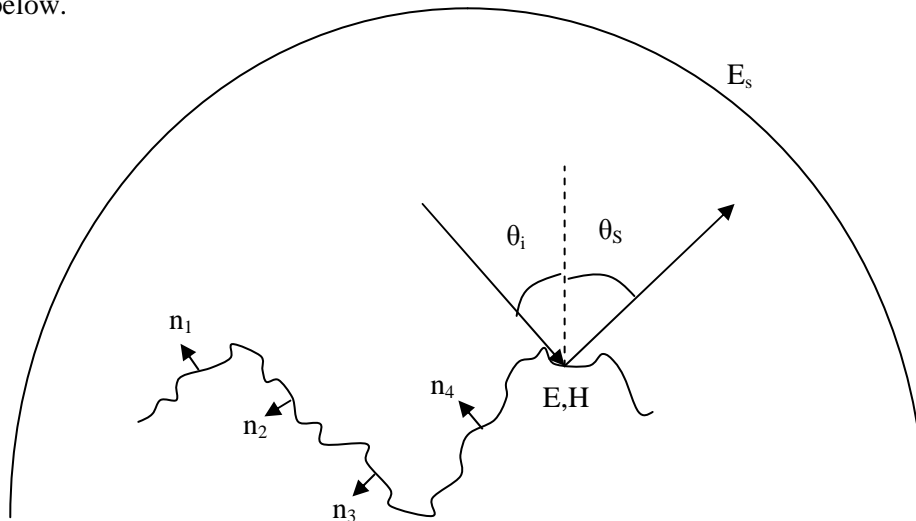


Figure 3.1: The scattered field in the far field region, E_s , may be expressed in terms of the surface fields E and H

3.1.2.2 Different Analytical Models

The different analytical models make assumptions which allow us to calculate the surface fields ($n \times E$) and ($n \times H$), for the rough surface case (neglecting volume effects). The standard models are:

- The Small Perturbation Method (SPM) for slightly rough surfaces
- The Kirchoff approximation for surfaces of gentle curvature. This includes the Physical Optics (PO) and Geometric Optics (GO) models for different conditions

The Integral Equation Model (IEM) takes the Kirchoff approximation and extends its range of validity to include a wide range of roughness conditions. It is currently the analytical model with the largest validity range and is therefore the most commonly used.

In the following we present briefly the standard models, including their main ideas and their validity regions and then present the Integral Equation Model (IEM) and its updated version the Advanced Integral Equation Model (AIEM), detailing its general formulation as well as a summary of the research done to extend and improve the model, and finally the results of AIEM simulations.

a) Small Perturbation Method (SPM)

For this method (Ulaby et al 1985 vol. II 12-5) to be valid the standard deviation of surface heights, σ , must be less than about 5% of the electromagnetic wavelength. Note that in this case σ refers to the value obtained when only frequency components responsible for scattering at a certain wavelength are included in the rough surface profile. A further condition is that the average surface slope should be of the same order of magnitude as the wave number times the standard deviation of surface heights, σ . No precise validity conditions have been obtained for this method but the following provides a guideline:

$$k\sigma < 0.3 \quad (3.11)$$

$$\sqrt{2} \sigma / L_C < 0.3 \quad (3.12)$$

b) Kirchoff Approximation

The basic assumption of the Kirchoff approximation (Ulaby et al 1985 vol. II 12-4) is that plane-boundary reflection occurs at every point on the surface. In other words each part of the surface may be looked at locally as an inclined plane. For this to be valid the curvature of the surface must be gentle, ie small slope (high L_C , low σ). Mathematically this is expressed in the following validity conditions for the Kirchoff approximation:

$$kL_C > 6 \quad (3.13)$$

$$L_c^2 > 2.76\sigma\lambda \quad (3.14)$$

where λ is the wavelength and k the wavenumber.

The Kirchoff approximation is employed by both the Physical Optics model and the Geometric Optics model but with a different interpretation in each case (leading to different validity regions):

b1) Physical Optics (PO) Model

In the Physical Optics model we assume that each point on the surface behaves like an *infinite* plane centred on that point (see Figure 3.2 below).

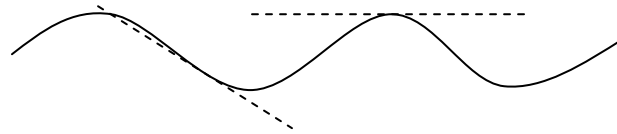


Figure 3.2: Each surface point behaves like an infinite plane

We can then apply the Fresnel equations for an infinite plane boundary reflection in order to obtain expressions for $n \times E$ and $n \times H$.

This assumption is valid for small or medium values of σ , as well as small slope for the Kirchoff approximation. This leads to the following validity conditions for surfaces of gaussian autocorrelation function:

$$\left. \begin{array}{l} L_c > 2-3 \lambda \\ \sigma < 0.5 \lambda \end{array} \right\} \text{Low slope and low to medium } \sigma$$

b2) Geometric Optics (GO) Model

This model is also based on the Kirchoff assumption but instead of infinite planes we consider the surface to be composed of many finite facets, as shown in Figure 3.3:



Figure 3.3: The rough surface is represented by many small facets

This method uses the stationary phase method requires the arc of each point on the surface to be greater than the wavelength. This imposes the condition of $\sigma \gg \lambda$.

It is also preferable that L_c be greater than λ .

This model takes into account only the non-coherent component in the specular direction. Therefore this works best with high roughness. This model also does not include shadowing or multiple reflections.

c) The Integral Equation Model (IEM)

The Integral Equation Method (IEM) is based on the Kirchoff approximation with modifications made to correct for inaccuracies for roughness conditions outside its validity range. This model assumes that each part of the surface reflects/emits in the same way, ie it assumes a homogeneous permittivity across the surface. Shadowing of incident and scattered intensities is not included, as the Kirchoff approximation is applied. However a corrective term can be added.

The main assumptions for the original IEM analytical model are the following (Chen et al 2003):

1. The local angle in the Fresnel coefficients are approximated to either the incident angle for slightly rough surfaces or to the specular angle for rough surfaces.
2. Edge diffraction terms are excluded.
3. The absolute phase terms in the surface Green's function and its gradient, which are needed for computing the complementary field coefficients, are set to zero.

However recent work has removed assumption 3 and reduced the effect of assumption 1 somewhat.

IEM reduces to Geometric Optics model in the high frequency limit and to the SPM model for low frequency.

c1) IEM formulation

The reflectivity can be written as the sum of the coherent component, $R_p^{\text{coh}}(\theta)$, and the noncoherent component, $R_p^{\text{non}}(\theta)$:

$$R_p(\theta) = R_p^{\text{non}}(\theta) + R_p^{\text{coh}}(\theta) \quad (3.15)$$

The coherent component is approximated to the flat surface reflectivity (calculated from the Fresnel equations) reduced by an exponential factor, as follows:

$$R_p^{\text{coh}}(\theta) = R_p^*(\theta) \exp [-(4\pi\sigma \cos \theta/\lambda)^2] \quad (3.16)$$

where σ is the standard deviation of surface heights. Thus the coherent of the bistatic scattering coefficient is not calculated by IEM but incorporated into the reflectivity by (3.16). Note that the accuracy of this coherent term is unknown.

The non-coherent reflectivity is calculated from the bistatic scattering coefficient, σ° , by applying equation (2.110), which is in turn calculated from the tangential surface fields by applying the Stratton Chu integral equation (3.10).

An estimate of the tangential fields is formed from a sum of Kirchoff and complimentary terms, as shown in (3.17):

$$\hat{n} \times E = (\hat{n} \times E)^K + (\hat{n} \times E)^C \quad (3.17)$$

$(\hat{n} \times E)^K$ is the Kirchoff component of the tangential surface Electric field and $(\hat{n} \times E)^C$ is its complementary component.

The Kirchoff term accounts for large scale roughness effects while the complementary term corrects for inaccuracies in the Kirchoff approximation and accounts for the small scale effects. The complementary term is expressed as a function of complementary field coefficients (F_{qp}) that can be computed from a spectral representation of the Green's function G and its gradients ∇G . The Kirchoff term is expressed as a function of the Kirchoff field coefficients f_{qp} . Field coefficients are computed for all polarisation combinations, ie HV, VH, HH and VV. F_{qp} and f_{qp} can be expressed as functions of the Fresnel coefficients.

Inserting these field coefficients back into the Stratton-Chu integral, we obtain a Kirchoff component and a complimentary component of the scattered field as well as a cross term. The bistatic scattering coefficient, σ° , which is calculated from the scattered electric field, can therefore be expressed as follows:

$$\sigma^\circ = \sigma^K + \sigma^C + \sigma^{KC} \quad (3.18)$$

where σ^K is the Kirchoff term, σ^C is the complementary term and σ^{KC} is the cross term.

For weak-to-moderate roughness conditions σ° can also be rewritten as a sum of single and multiple scattering terms.

The IEM model is entirely algebraic which makes it faster to compute than numerical methods. The updated AIEM has been formulated for surfaces of either gaussian or exponential autocorrelation function.

c2) Development of IEM to AIEM

The IEM model has been developed to remove some of the approximations made and thus improve its accuracy. This was particularly important in order to compute the emissivity since an accurate value of reflectivity is required for energy conservation and thus equation (2.111) to be valid.

As a first step Chen et al (2000) included all phase terms in G and ∇G for multiple scattering terms whilst continuing to set them to zero for single scattering terms. In a second step Chen et al (2003) then reformulated IEM to also include these phase terms for single scattering, allowing the calculation of emissivity. This version of IEM was renamed the Advanced Integral Equation Model (AIEM) and it included the same Kirchoff term as before but the complementary term now contained 8 terms and the cross term contained 64 terms. The formulation remained algebraic. These two steps removed the third assumption in IEM, producing a model of higher accuracy but with longer computation time. However computation time remained significantly lower than for numerical models.

IEM was further improved by Wu et al (2001) with the introduction of a “transition function”. In the original IEM the Fresnel coefficient, needed in the calculation of f_{qp} and F_{qp} , was evaluated at either the incident angle (θ_i) for low roughness or the specular angle (θ_{sp}) for high roughness. However it was unclear what the conditions for these two regions were or what to do for medium roughness conditions, in between these two regions. Wu et al (2001) therefore proposed a transition function to connect and smooth these two approximations. In doing this the Fresnel coefficient of either $R_p(\theta_i)$ for low roughness or $R_p(\theta_{sp})$, were replaced by $R_p(T)$:

$$R_p(T) = R_p(\theta_i) + [R_p(\theta_{sp}) - R_p(\theta_i)]Y_p \quad (3.19)$$

where Y_p is the transition function with a value ranging from 0 to 1. It is calculated as a function of S_{qp} , which is the ratio of the complementary term to the total scattering coefficient, given by:

$$S_{qp} = \frac{\sigma_{qp}^c}{\sigma_{qp}^o} \quad (3.20)$$

This transition function was validated against numerical Method of Moments simulations (Chen et al 2001) and experimental data (Fung and Chen 2004) and incorporated into AIEM.

c3) AIEM simulations of soil emission

AIEM has mostly been used for calculating the backscattering coefficient (Chen et al 2000, Fung et al 2004, Wu et al 2004). Since recent improvements in accuracy, as described in the previous section, studies have also been performed on rough surface soil emission. Two studies (Liou et al 2001 & Shi et al 2002) have evaluated AIEM simulations of soil emission at L-Band for both gaussian and exponential autocorrelation functions. These studies showed that roughness effects differ strongly at different incident angles and polarizations. As roughness increases, emission was found to increase at H polarization and decrease at V polarization. This latter is a new and surprising result since emissivity is considered to generally increase with roughness, which forms the basis for the semi empirical Q-h model. Shi et al explained the result by the increase in the non-coherent component being larger than the reduction in the coherent component at angles around the Brewster angle and at

V polarization. This is because the coherent component of a flat surface is negligible at this Brewster angle and at V polarization. This result strongly impacts the ratio of reflectivity at V and H polarization (R_V/R_H).

Shi et al (2002) developed a new parameterized model of the surface reflectivity, based on AIEM data, that accounted for these new results. This model was designed to be able to invert soil parameters from L-Band measurements.

It is important to bear in mind that the IEM model accounts for surface effects but not volume effects and should therefore only be used for rather wet soils where surface effects are dominant. In addition the IEM model assumes the permittivity is homogeneous across the surface which is more likely to be true for very wet or very dry surfaces. Comparisons between AIEM and experimental data confirm this limitation to wet soils, for example reasonable agreement was found to be limited to wet soils for the backscattering coefficient (Zribi et al 2005).

Shi et al 2005 developed a parameteric model based on an AIEM study for rough surface emission as a function of surface slope, polarization and frequency (for frequencies larger than about 3 GHz). Comparison with AIEM showed a maximum error of 10^{-3} of this model. This result is interesting as it demonstrates the importance of the rough surface slope as a measure of surface roughness.

3.1.3 Numerical Models

Numerical methods calculate exactly the emission or scattering of rough soil surfaces by solving Maxwell's equations. This makes them more complex and more computationally costly (require longer computation time and higher memory) than analytical methods but they are exact and are not limited to certain ranges of roughness.

In this section we will first present the general methodology for calculating the bistatic scattering coefficient and emissivity of an infinite rough surface by a numerical method. We further detail important considerations relating to this, which include determination of the surface size and incident beam to be used in numerical calculations. Secondly we present the different numerical methods which can be used in such a calculation. In particular we present the *Method of Moments (MoM)*, which is currently the most popular numerical method used to study rough surface scattering and emission, and in the latter category we present the *Finite Difference Time Domain method (FDTD)* and the *Finite Element Method (FEM)*. We then detail the choice of numerical method to be used for different applications, validating a numerical method, and finally the research performed to data in this field. We finish with a discussion of the choice of method for solving this problem.

3.1.3.1 Methodology

a) Procedure

In reality a soil surface, as “seen” by a radar or radiometer, can be considered to be infinite in size. However it is not possible to model this numerically. Instead, calculations are performed for N different rough surfaces each of discrete size L (or $L \times L$ for 3D surfaces) and each with the same autocorrelation functions and values of σ and L_c . Using a numerical method, such as those presented in section 3.1.3.2, the electric field scattered off each rough surface is calculated in the far field region, $E_{r,j}^s(\theta_s, \phi_s)$ at distance R from the surface and as a function of position (θ_s, ϕ_s) , when a beam is incident upon the surface of a given dielectric permittivity.

We then calculate the bistatic scattering coefficient, for incident polarization t and reflected polarization r , σ_{pq}^0 , from the reflected electric field in the far field region, averaged over all N surfaces. The bistatic scattering coefficient is then calculated from (2.110), summing the scattered electric field over all rough surfaces as follows:

$$\sigma_{pq}^0(\theta_s, \phi_s; \theta, \phi) = \frac{4\pi R^2}{A_{\text{eff}} |E_q^i(\theta, \phi)|^2} \frac{1}{N} \sum_{j=1}^N |E_{p,j}^s(\theta_s, \phi_s)|^2, \quad (3.21)$$

where (θ, ϕ) is the angle of the incident wave, (θ_s, ϕ_s) is the angle of the reflected wave, N is the number of surfaces to be averaged over, A_{eff} is the effective area of the surface illuminated and E_t^i is the incident electric field with polarization t ,

The bistatic scattering coefficient calculated by (3.21) contains both coherent and non-coherent components. The coherent component is given by:

$$\sigma_{pq}^0(\theta_s, \phi_s; \theta, \phi)_{\text{coh}} = \frac{4\pi R^2}{A_{\text{eff}} |E_q^i(\theta, \phi)|^2} \frac{1}{N^2} \left| \sum_{j=1}^N E_{p,j}^s(\theta_s, \phi_s) \right|^2 \quad (3.22)$$

Therefore the non-coherent component can be isolated as follows:

$$\sigma_{pq}^0(\theta_s, \phi_s; \theta, \phi)_{\text{noncoh}} = \frac{4\pi R^2}{NA_{\text{eff}} |E_q^i(\theta, \phi)|^2} \left[\sum_{j=1}^N |E_{p,j}^s(\theta_s, \phi_s)|^2 - \frac{1}{N} \left| \sum_{j=1}^N E_{p,j}^s(\theta_s, \phi_s) \right|^2 \right]. \quad (3.23)$$

The emissivity can be calculated from the bistatic scattering coefficient applying equations (2.111) – (2.112).

The procedure of averaging over many surfaces allows us to approach the bistatic scattering coefficient and/or emissivity of an infinite rough soil surface. As the ensemble size increases results

should converge. The number of rough surfaces, N , must be chosen so that we have convergence. However, in order to obtain convergence towards a solution which is accurate the surface size must be carefully chosen, as will be explained further in the following section.

The averaging procedure can be done “by hand”, as for this thesis. In this case the rough surfaces are created by hand prior to numerical calculation and also the procedure of recovering the scattered electric fields for each surface and applying (3.23) and (2.111) – (2.112) to the ensemble is done by hand post-calculation. However this process can be time consuming. The Monte Carlo method is therefore often employed, coupled with a numerical method, to automatically average the deterministic scattered fields of individual surfaces over an ensemble of surfaces.

For any numerical study of rough surface scattering and emission, the size of the surface, and the incident beam must be chosen with care. In sections b) and c) we explain how this can be done.

b) Surface Size, L

The physical meaning of limiting surface size is limiting the coherent interaction of waves hence the larger the better. However since the number of unknowns is directly related to surface size the larger the surface the longer the computation (CPU) time and memory. Note that we refer to the calculation time and memory combined as the *calculation costs*. A compromise must therefore be reached.

For each individual surface simulated, the surface size must be large enough compared to the autocorrelation length so that it represents the statistical problem. An empirical rule is that for Gaussian surfaces a size of 10 correlation lengths is enough (Saillard & Sentenac 2001).

The surface should also be large enough to be considered macroscopic in comparison to the wavelength; normally 10λ is considered sufficient. Smaller surfaces may yield acceptable results with a greater number of realizations but important interactions between long wavelength components may be neglected. For example, Zhou et al (2004) found that a surface size of $8\lambda \times 8\lambda$ is sufficient.

c) Incident beam and Avoiding Edge Effects

In practice, source and receiver antenna are far from the ground surface and the incident field can be approximated locally to a plane wave. However for numerical scattering we must use a finite surface and in this case a plane incident wave would lead to an edge effect on the sides of the calculation area, or sidelobes, which would reduce the accuracy of the computed scattered field. In order to avoid these problems, calculations are usually performed with tapered incident waves which have zero amplitude at the edges of the surface. Alternatively a window function, of usually Gaussian form, can be applied after the scattering of plane waves (e.g. Chen & Bai 1990, Axeline and Fung 1978, Ceraldi et al 2005, Inan & Ertuk 2006, Fung et al 1994, Zhou et al 2001) to reduce the contributions of edge scattering to

the far field calculation. Other methods include periodic boundary conditions or resistive regions at the edges of the surface.

Often the tapered incident wave is of Gaussian form however this poses a problem as a gaussian wave is “non-Maxwellian”, ie it is not a solution to Maxwell’s equations. One other problem with the Gaussian incident wave is that the illuminated area spreads with incident angle, increasing computational time. Alternatively a Gaussian spectrum of plane waves can be used. This maintains the tapering effect at the edges and yet since it consists entirely of plane waves it is a solution to Maxwell’s equations. However this type of wave increases calculation time since it requires numerical integration. Another popular tapered wave involving a summation of plane waves was proposed by Thorsos et al (1988) for the 2D scattering case. This wave, whilst not being an exact solution to Maxwell’s wave equation, is closer than a purely Gaussian beam and, since it does not involve numerical integration, the calculation time is not increased as much as for the integration of plane waves. It can be considered to be a compromise between the Maxwellian integration of plane waves and the faster, simpler Gaussian beam. The Thorsos taper is however limited at grazing angles, as analysed and discussed by Toporkov et al (1999) and Marchand and Brown (1999). Most of the work on the above mentioned incident beams has focused on the 2D scattering case. For the 3D emissivity case it may be desirable to have an incident beam that is not an integral thus reducing computation time.

Braunisch et al updated the spectrum of plane wave formulation with a new formulation that included both evanescent and propagating waves with the use of a simple Gaussian plane wave spectrum. This new formulation addressed the problems of losing the dominant polarisation state and degradation of tapering at normal incidence. This produced a more reliable tapered wave with dominant polarisation state that could be used for all incidence angles, which was Maxwellian. The authors also discussed a newly encountered problem of grazing when buried objects are present (scattering of buried objects into the edges).

The tapered wave and window function contain a factor “g” which controls the beam-width of the wave. This then becomes one of the parameters that must be decided for numerical calculation. Its value must be large enough to illuminate the majority of the rough surface, such that the solution is accurate, and small enough to diminish the edge effects (ie the wave must be negligible at the edges). It is a compromise between resolution and stability; we must sample the bistatic scattering coefficient enough such that we maintain the form and not too much so that we obtain oscillations due to edge effects. The choice of g depends on the wavelength, the roughness and the size of the rough surface as well as the desired resolution of the bistatic scattering coefficient (Axeline & Fung et al 1978). It also depends on incident angle. Different authors have suggested different conditions for the choice of g.

The value of g to be used in simulations depends in general on: surface roughness (Axline and Fung 1978), wavelength (Axline and Fung 1978), surface size, L , and incident angle. The beamwidth must be large enough so that enough of the rough surface interacts with the wave but small enough so that edge effects are negligible. For smaller surfaces we require a smaller beamwidth, thus we usually consider restriction on the size of g as a function of L . The beamwidth size varies with angle, so we must consider the angle to be used. The area of the surface that must be illuminated in order to obtain accurate calculations of the scattered field depends on the surface roughness and also the wavelength.

Axline and Fung (1978) drew the general conclusion that smaller g should be used for a rougher surface or the same surfaces with smaller λ . In some papers, g was chosen so that the wave amplitude was negligible at the edges of the surface, in some cases falling by 10^{-6} its maximum amplitude at the edge (Franceschetti et al 2000, Inan & Ertuk et al 2006, Axline and Fung 1978) and in some cases 10^{-3} its maximum amplitude (Fung et al 1994, Devayya et al 1992), equivalent to g of less than $L/7.43$ and $L/5.25$, respectively for a Gaussian incident beam on a 1D surface, where L is the length of the calculation area. Other authors have suggested the empirical condition that g must be less than $L/4$, which is often used.

Setting a maximum value of g is important for the reduction of edge effects and also for the calculation of the bistatic scattering coefficient, which requires the effective surface area to be calculable. However g must also be large enough to illuminate enough of the rough surface so that the bistatic scattering coefficient is calculated accurately. This means that, in order to maintain the previous condition, the rough surface itself must be large enough. L is already limited by conditions based on wavelength and autocorrelation length but we may require additional conditions when applying a tapered incident beam.

A minimum value of g can be obtained by considering spreading of the beam with angle. For example the following condition has been suggested for the Thorsos beam (Thorsos 1988):

$$g \gg \frac{1}{k \cos \theta_i} \quad (3.24)$$

where k is the wavenumber. This means that minimum g varies from 0.16λ at 0° to 0.92λ at 90° , which is not very meaningful since these values are very small. Tsang (1994a) suggested g in the range $(L/10, L/4)$ whose actual value depended on incidence angle, but this cannot be used for grazing angles approaching 90° . Kapp et al (1999) suggested:

$$g > \frac{A}{k(\frac{\pi}{2} - \theta_i) \cos \theta_i} \quad (3.25)$$

where A is some constant. Toporkov et al (1999) further suggested a value of 9.4 for this constant. However this condition is not very meaningful for small angles. For example we have a minimum g of 0.95λ at 0° .

Ye and Jin (2005) suggested the following condition for the Thorsos taper, which was found by imposing a minimum error in the Helmholtz equation (a simplified version of the wave equation based on the assumption that the wave's dependence on time and space can be separated) of 10^{-4} :

$$g_{\min} = \frac{6}{(\cos \theta_i)^{1.5}} \quad (3.26)$$

This leads to a minimum g of 6λ at 0° incidence, 11.6λ at 50° and 83λ at 80° incidence. However we note that this condition was based on limiting errors arising from the non-Maxwellian nature of the Thorsos taper at non-zero incidence, not on sufficient sampling of the rough surface.

Marchand and Brown (1999) suggested the values between $g > 10\lambda$ and $L > 4g$, which leads to a minimum L of 40λ .

It must be noted that these conditions have all been derived and proposed for the case of 2D scattering. Authors of numerical emissivity calculations have adopted the $L > 4g$ condition and the Thorsos taper.

3.1.3.2 Numerical Methods

Thus far we have considered the general methodology of all numerical methods when applied to the problem of rough surface scattering and emission. In this section we now consider the different numerical methods that may be applied including their formulations and differences. A numerical method solves Maxwell's equations over a finite region by: (1) discretizing the region into a "mesh", (2) solving the equations for each discrete element and then (3) regrouping the solutions of each element into a global solution. The mesh is then continuously refined to smaller and smaller elements until the solution converge.

In this section we present different numerical methods currently used to calculate the electric field scattered off rough surfaces, concentrating only on the main methods. Most of the literature concentrates on the surface case (i.e. a single homogeneous dielectric layer with a rough surface) but numerical methods can be extended to include volume effects including multilayer structures, some more easily than others. This is important for the work of this thesis since the aim is to develop a method for modelling the L-band emission of the two layer soil-litter system.

The ways in which numerical methods solve Maxwell's equations can be used to classify the models into broadly speaking three different categories: (a) those based on approximations; (b) those that solve integral equations and (c) those that solve differential equations. Methods in the first category

solve an approximation of Maxwell's equations and the other two categories solve Maxwell's equations directly in either their differential or integral form.

Methods solving differential equations require a volume mesh whereas those solving integral equations require a surface mesh.

All numerical methods are approximate but some can be considered to be numerically exact. A method is numerically stable if the error, due to perturbations such as rounding error, remains small as the degrees of freedom (number of unknowns) increase.

a) Integral Equation Methods (Boundary Integral Methods)

In these methods the scattering of EM waves off a rough surface is approached as a boundary problem. We consider two homogeneous media separated by a boundary. Maxwell's equations are solved in their integral form to find the unknown surface current induced by the incident field. The scattered field created by the surface current can then be found: see Figure 3.4 for an illustration of this.

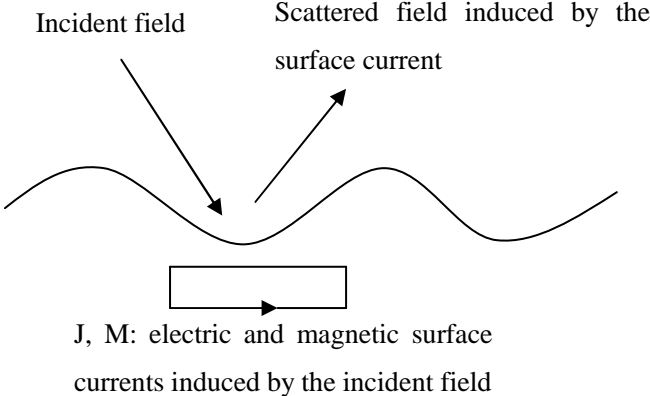
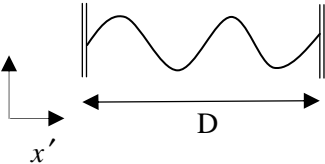


Figure 3.4: The incident field induces electric and magnetic currents in the surface, which in turn induced a scattered wave

The integral equations are formulated using either Green's functions or elementary solutions to Maxwell's equations for an infinitesimal source. As an example let us consider a perfectly conducting 1-dimensional surface:

The surface is divided into many segments of equal length, D :



The surface current for each segment i , given by $J_s^i = [\hat{n} \times H^i]$, is related to the incident field as follows:

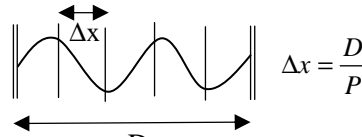
$$\int_{x_i - D/2}^{x_i + D/2} \nabla_r G_1(r, r') \times J_s^i(r') ds' = -H_{inc}^i(r) \quad (3.27)$$

where $G_1(r, r')$ is the scalar free space Green's function satisfying:

$$\Delta G_1 + k_1^2 G_1 = \delta(r - r') \quad (3.28)$$

Note that for V polarization equation (3.28) is a function of the magnetic field and not the electric field.

The segment i is divided into P sub-segments, as shown below, and equation (3.28) solved by applying an Integral Equation (IE) method such as the Method of Moments (MOM):



The different types of Integral Equation (IE) method are distinguished by choice of the functions used to discretize the integral equation (3.28) as well as iterative algorithms employed and methods used to accelerate the evaluation of the integral operators.

The Method of Moments (MoM) expands the unknown surface current as a linear combination of a set of basis functions. The integral equations are projected onto a set of field test functions. The basis functions can be considered to radiate fields which are then received by the field testing functions. This produces a dense linear system of equations:

$$\bar{Z} \cdot \bar{x} = \bar{b} \quad (3.29)$$

where Z is the moment matrix of interactions between basis functions and testing functions, b is the projection of the incident field onto the testing functions and x determines the approximate current solution. These basis and testing functions are defined on an underlying surface mesh.

The far zone scattered field $E_i(\theta)$ due to the surface current, as shown in Figure 3.5, can be written as a function of J_i , calculated by the method of moments (MoM).

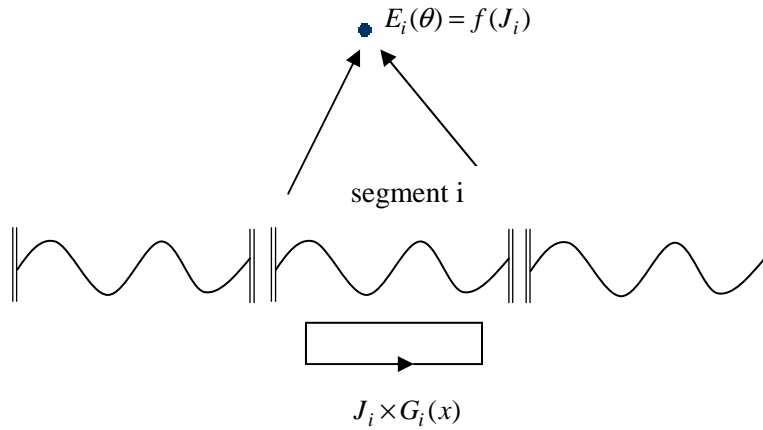


Figure 3.5: The scattered electric field in the far field region can be calculated from the surface current

At this point a Gaussian “window function” $G_i(x)$ can be introduced to remove edge effects from the last segments (see section 3.1.3.1c):

$$G_i(x) = \exp\left[-(x - x_i)^2/g^2\right] \quad (3.30)$$

The bistatic scattering coefficient at this point is calculated by summing the scattered field due to all N segments:

$$\sigma^0(\theta) = \frac{2\pi R}{gN\sqrt{\pi/2}} \sum_{i=1}^N E(x_i)E^*(x_i) \quad (3.31)$$

The parameters $g, D, \Delta x$ and N must be chosen appropriately in order to obtain good estimates of the average scattered power.

The traditional version of MOM used standard inversions to solve matrix equation (3.29) however computation time scales as N^3 where N is the number of unknowns. A lot of work has been done to reduce computation time using iterative methods, instead of standard inversions, and fast methods to speed up the process. This is addresses in the next section.

a1) Development of the Method of Moments: fast methods and iterative techniques

The method of moments is the solution of the surface integral equation. This can be solved by applying one of the following iterative techniques:

1. The Kirchoff iterative approach
2. Sparse Matrix Canonical Grid (SMCG) method
3. Steepest-descent fast multipole method (SDFMM)

One of the following fast methods can also be applied to speed up computation:

1. Fast Fourier Transform Methods
2. Fast multipole method
3. Physics based two-grid method (PBTG) meshing using 2 grids, a dense and a coarse one

Due to the geometry of a rough surface which is planar on average it has been shown that for most surfaces only short range interactions are relevant, i.e. the current at any point on the surface depends only on the geometry and incident field at this point. This of course depends on the incident angle and the rough surface statistics but is true for most surfaces. Taking advantage of this, the interaction matrix, Z , can be decomposed into a strong component Z^s and a weak component Z^w :

$$Z = Z^s + Z^w \quad (3.32)$$

Z^s is a sparse matrix whose filling ratio depends on the strong interaction radius (ρ_s) and size of the area illuminated. Z^w is a dense matrix without any property. The aim is to avoid generating and storing Z^w .

In the Sparse Matrix Canonical Grid (SMCG) method Z^w is expanded as a Taylor series about the ratio of vertical to horizontal distances:

$$Z^w = \sum_{m=0}^M Z_m^w \quad (3.33)$$

Fast Fourier Transforms are used to compute the product of each matrix Z_m^w with column vectors.

Storage memory is thus reduced from N^2 to $N \times M$, where M is the number of matrices in the Taylor series and is much smaller than N . However the rougher the surface, the longer the strong interaction radius must be. This increases the size of Z^s and rapidly increases computation time.

The steepest-descent fast multipole method (SDFMM) also divides the matrix decomposition into strong and weak interactions. This technique is designed to speed up matrix-vector products in conjugate-gradient algorithms. To compute $Z^w \cdot x$ instead of a Taylor expansion the surface currents are mapped onto a 3-dimensional grid using the fast multipole plane-wave field expansion.

The forward-backward method, also called the Method Of Multiple Interaction (MOMI) has been suggested to avoid storing large matrices. In this case Z is rewritten as:

$$Z = I - (L + U) \quad (3.34)$$

Where I is the identity matrix and L and U are lower and upper triangular matrices, respectively, with zeros on the diagonal. This leads to the expansion:

$$x = (I - U)^{-1} \left(\sum_{m=0}^{\infty} \{[(I - L)^{-1} - I][I - U]^{-1} - I\}^m \right) (I - L)^{-1} b \quad (3.35)$$

This decomposition requires a second type of integral equation and at present this method has been implemented only for perfectly conducting surfaces with MFIE. This method is called the forward backward method because for one dimensional surfaces and low grazing angles the triangular matrices describe scattering in either the forward or backward direction. However this interpretation is not valid for the case of 2-dimensional surfaces and low incident angles.

For very rough surfaces, such as when σ and L_c approach the wavelength, the MOMI fails to converge (Tran 1997). Equally for the SMCGM or SDFMM very rough surfaces if convergence were achieved it would require a large radius of strong interaction slowing the computation down considerably. A way to overcome this is to compute exactly the terms of the weak interaction matrix Z^w , for example with the original sparse matrix flat surface approach (SMFSIA). Since Z^w is a dense matrix it cannot be stored and must be recalculated for each iteration. Applying this method means that the computation time scales as N^2 but by combining with a robust iterative scheme based on the generalized minimal residual (GMRes) method (G Soriano and M Saillard 2001) very rough surface scattering can at least be solved.

b) Differential Equation Methods

In this section we present the two main differential equation methods: the Finite Element Method (FEM) and the Finite Difference Time Domain (FDTD) method. We present the former in greater detail since this is the method used in this thesis. (Reasons for this choice are given in chapter 5).

b1) Finite Element Method (FEM)

The Finite Element Method was developed originally to solve problems in structural mechanics arising during the development of airplanes in the 1940s. The basic idea was to divide a complicated structure into different mechanical elements (beams, plates, etc.) for which the deformation could be calculated and then assemble them using linking equations. The method has since been formalized mathematically and generalized to a wide number of problems including in the field of electromagnetism. It is also generally used in the field of fluid dynamics.

In this section we present the basic concepts of the finite element method applied to electromagnetic problems, including rough surface emission and scattering.

The finite element method calculates an approximate solution in a finite space, to a set of partial differential equations (PDEs), satisfying certain boundary conditions on the boundary of the finite space. In the case of electromagnetism these equations are Maxwell's equations in their differential form. The solution approach is either to eliminate the PDE completely, i.e. for the case of steady state problems, or to render it into an equivalent ordinary differential equation (ODE) (one with only one variable) which is then solved by standard techniques.

In the following we will describe the main steps to solving electromagnetic problems by the finite element method, which leads us to solve the electromagnetic fields in the calculation area. We then describe how the scattered electric field in the far field region can be calculated from this value.

Step 1: Establish the physical equations

The first step is to establish the physical equations that we wish to solve. In the case of electromagnetism this is Maxwell's equations, which are usually rewritten in terms of potentials. For example in the case of electro- and magneto- statics the equations can be rewritten in terms of scalar potentials, which are then easier to solve since they have one degree of freedom (the scalar ϕ or V) instead of three (vector H or E). Reduced scalar potentials and vector potentials can also be used, depending on the problem. In the following we consider the case of an electrostatic problem in order to illustrate the basics of the FEM approach. We consider this problem since it is simple but the concepts can also be extended the scattering of electromagnetic waves: the problem at hand.

For electrostatics we wish to solve Maxwell's first equation in terms of the electric scalar potential V :

$$\nabla \cdot \epsilon \nabla V = \rho \text{ (in 2D), where } E = -\nabla V.$$

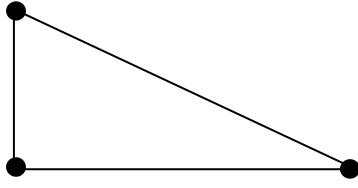
This can be rewritten as:

$$\frac{\partial}{\partial x} \left(\epsilon \frac{\partial V}{\partial x} \right) + \frac{\partial}{\partial y} \left(\epsilon \frac{\partial V}{\partial y} \right) = -\rho, \quad (3.36)$$

Step 2: Discretize the space

The second step is to solve the equations in the finite dimensional space for which we wish to find the solution, by discretization. Let us consider the domain Ω for which we wish to solve an electromagnetic problem by the Finite Element Method. The domain, or problem area, is divided into a mesh of N sub-domains of the same shape, called *elements*, and the solution found in each element. The global solution at any point in Ω is then the solution of the surrounding element at that point. In 2-dimensional problems we often consider triangular elements and in 3-dimensional problems tetrahedral elements. The points defining the elements are called "nodes" or "degrees of freedom". The solution is calculated at each node and then the solution of the element is calculated from the solution at the nodes and a function to interpolate between them. Figure 3.6 shows a triangular element with 3 and 6 nodes, or degrees of freedom.

3 nodes:



6 nodes:

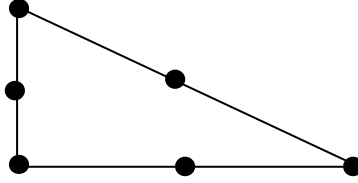


Figure 3.6: Triangular elements with 3 (left) and 6 (right) nodes

Let $U_E(x,y)$ be the approximate solution for the element and the exact solution be U . It is usual to choose polynomials for $U_E(x,y)$ eg for 3 nodes:

$$U_E(x,y) = a + bx + cy \quad (3.37)$$

An element with this solution is known as a first order element.

For 6 nodes the polynomial solution is:

$$U_E(x,y) = a + bx + cy + dx^2 + exy + fy^2 \quad (3.38)$$

A 2-dimensional element with this solution is known as a second order element. Once we know the solution at the nodes we can calculate the values for the constants a,b,c (or a,b,c,d,e,f) and we have the solution for the element. For example let us consider a triangular element with nodes 3 nodes (x_1,y_1) , (x_2,y_2) and (x_3,y_3) . (3.37) must be true on the nodes so we can write:

$$U_E(x_1,y_1) = a + bx_1 + cy_1 \quad (3.39a)$$

$$U_E(x_2,y_2) = a + bx_2 + cy_2 \quad (3.39b)$$

$$U_E(x_3,y_3) = a + bx_3 + cy_3 \quad (3.39c)$$

From these equations we can rewrite the coefficients a , b and c in terms of the solutions at the nodes and the nodal coordinates. Substituting these expressions into (3.37) and simplifying we obtain:

$$U_E(x,y) = \sum_{i=1}^3 \frac{1}{D} (p_i + q_i x + r_i y) U_E(x_i, y_i) \quad (3.40)$$

$$\text{where } = \begin{vmatrix} 1 & x_1 & y_1 \\ 1 & x_2 & y_2 \\ 1 & x_3 & y_3 \end{vmatrix}.$$

Also $p_1 = x_2 y_3 - x_3 y_2$, $q_1 = y_2 - y_3$, $r_1 = x_3 - x_2$ and the remaining terms p_2 , q_2 , r_2 , p_3 , q_3 , r_3 are obtained by cyclical permutation of the indices.

(3.40) can also be rewritten under the form:

$$U_E(x, y) = \sum_i \phi_E^i(x, y) U_E(x_i, y_i) \quad (3.41)$$

where $\phi_E^i(x, y)$ is the interpolation function or “shape function”, given by:

$$\phi_E^1(x, y) = \frac{1}{D} (p_1 + q_1x + r_1y) \quad (3.42a)$$

$$\phi_E^2(x, y) = \frac{1}{D} (p_2 + q_2x + r_2y) \quad (3.42b)$$

$$\phi_E^3(x, y) = \frac{1}{D} (p_3 + q_3x + r_3y) \quad (3.42c)$$

In doing this we ensure a continuous solution. Note that this procedure also applies for more than 3 nodes, leading to shape functions of different forms. So far, we have reformulated the problem so that each node has an associated solution and shape function. The shape function is known, but the solution unknown. The form of the shape function is chosen at the start, usually to be polynomial. The overall solution for the element (as a function of position) is written as the sum of the solution of each of its nodes multiplied by the node’s shape function. To find the solution of each element we therefore need only to find the solution at the nodes.

$\phi_E^i(x, y)$ can take various forms including linear as in the above example, in which case it is called a **form function**, and quadratic, called **basis functions**. It is usual to choose Legendre polynomials as shape functions. e.g for a 1-dimensional element with 2 nodes:

$$\phi_E^1(x) = \frac{x_2 - x}{x_2 - x_1} \quad (3.43a)$$

$$\phi_E^2(x) = \frac{x - x_1}{x_2 - x_1} \quad (3.43b)$$

Since (3.42a), (3.42b), and (3.42c) must reduce to the nodal solutions $U_E(x_i, y_i)$ when $(x, y) = (x_i, y_i)$, we observe that the following identities are true:

$$\phi_E^1(x_1, y_1) = 1 \quad \phi_E^1(x_2, y_2) = 0 \quad \phi_E^1(x_3, y_3) = 0$$

$$\phi_E^2(x_1, y_1) = 0 \quad \phi_E^2(x_2, y_2) = 1 \quad \phi_E^2(x_3, y_3) = 0$$

$$\phi_E^3(x_1, y_1) = 0 \quad \phi_E^3(x_2, y_2) = 0 \quad \phi_E^3(x_3, y_3) = 1$$

In other words a node’s shape function varies from 1 on the node itself to zero on all other nodes, implying that the effect of one node is zero on all other nodes. We also note that, in order to maintain a continuous solution the following conditions must be satisfied:

1. A node belonging to several elements must have the same value in each, as must each point on the boundary between two elements.

2. The shape function must fall to zero outside the element (so that nodes only have an effect on the element they are in).

Condition 1 can be written mathematically as follows. For any point (x,y) on the boundary between two elements E1 and E2, we have:

$$U(x,y) = U_{E1}(x,y) = U_{E1}^i \phi_{E1}^i(x,y) = U_{E2}(x,y) = U_{E2}^i \phi_{E2}^i(x,y) \quad (3.44)$$

It is important to have a continuous solution for the potential since the electromagnetic field vectors E, D, B and H must be continuous in space in order to be physical.

Step 3: Application of the weighted residual method

Thus far we have formulated the problem over the discrete domain into a set of nodal solutions and shape functions but we still have to calculate the nodal solutions. As a first step towards this we regroup the solutions of each element into a global solution and impose conditions so that this solution satisfies the original defining equation. To do both of these we can either apply a *residual method* or we can determine a *variational functional* for which stationarity is sought. The former is the method most commonly used since it is comparatively simpler and easier to understand and apply. *Galerkin's method of weighted residuals* is a particular form of a residual method and is widely used in electromagnetism. We will therefore focus on this method.

Since the solution obtained by the finite element method U_E is only approximate to the exact solution U (ie $U_E \neq U$) this introduces a “residual” in the defining equation. For example in the case of electrostatics we have a residual “R” in Maxwell’s first equation:

$$\nabla \cdot \epsilon \nabla U + \rho = R \quad (3.45)$$

In order to satisfy the original equation defining the problem, (3.36), over the domain Ω , we force R to be zero as follows:

$$\int_{\Omega} w R d\Omega = 0 \quad (3.46)$$

where w is a weighting function and Ω is the domain over which the condition is forced. We replace R by the defining equation, which in the case of an electrostatic problem is:

$$\int_{\Omega} w [\nabla \cdot \epsilon \nabla U + \rho] d\Omega = 0 \quad (3.47)$$

Applying Green’s theorem we obtain:

$$\int_{\Omega} w[\nabla \cdot \epsilon \nabla U_E + \rho] d\Omega = \oint_{S(\Omega)} w \epsilon \nabla U_E \cdot ds - \int_{\Omega} \epsilon \nabla U_E \cdot \nabla w d\Omega + \int_{\Omega} w \rho d\Omega \quad (3.48)$$

where $S(\Omega)$ is the boundary of the domain Ω and ds is an element of the boundary. This provides the governing equation that must be solved for each element. Note that the first term on the right hand side of the equation relates to the boundary conditions and the last term is called the “source term”.

In the Galerkin method, the shape functions are also used as the weighting functions. Furthermore we can integrate the above equation element by element as follows:

$$\sum_{n=1, N} \int_{\Omega} [\epsilon \nabla U_E \cdot \nabla \phi_n - \rho \phi_n] d\Omega = 0 \quad (3.49)$$

where n is a generic element and N is the number of elements in the solution domain.

Replacing U_E by the nodal solutions and shape functions, we can integrate the right-hand side of (3.48), obtaining a matrix equation for each element. For example in the electrostatic case the second term of (3.48) can be rewritten as:

$$\frac{\epsilon}{2D} \begin{bmatrix} q_1 q_1 + r_1 r_1 & q_1 q_2 + r_1 r_2 & q_1 q_3 + r_1 r_3 \\ q_1 q_2 + r_1 r_2 & q_2 q_2 + r_2 r_2 & q_2 q_3 + r_2 r_3 \\ q_1 q_3 + r_1 r_3 & q_2 q_3 + r_2 r_3 & q_3 q_3 + r_3 r_3 \end{bmatrix} \begin{bmatrix} U_1 \\ U_2 \\ U_3 \end{bmatrix}$$

This matrix is known as the “stiffness matrix”.

The third, source term can be written as: $\frac{\rho D}{6} \begin{bmatrix} 1 \\ 1 \\ 1 \end{bmatrix}$.

Summing elements therefore requires assembling all matrices into a global matrix: adding lines and columns corresponding to the numbering of the nodes in the global matrix. Our next steps are to insert boundary conditions and solve this matrix system using a linear system solving technique.

Note that the source term does not depend on unknown potentials or the location of nodes and so is assembled on the right-hand side of the matrix system.

In order to obtain a solution we must specify what happens on the boundary of the problem domain. This comes from the first term on the right hand side of (3.48). This term must be equal to zero since the numerical procedure imposes that the sum of the integrals on Ω be zero. So we require:

$$\oint_{S(\Omega)} w \epsilon \nabla U_E \cdot ds = 0 \quad (3.50)$$

There are two types of boundary conditions that ensure this: 1) the Dirichlet boundary condition where the potentials are known on the boundary and the weighting functions are set to zero for all boundary nodes where the potential is known 2) the Neumann boundary condition where the potentials are unknown on the boundary in which case $\nabla U_E \cdot ds$ is set to zero, which means that the E field is tangential to the boundary.

In order for the solution to be physical the following conditions must be fulfilled:

1. Over the exterior boundary either U_E or $\frac{\partial U_E}{\partial n}$ (or a combination of both) must be prescribed
2. If only $\frac{\partial U_E}{\partial n}$ is prescribed the solution is not unique
3. For an infinite problem the potential must be regular at infinity (i.e. the solution decays to zero at a specified rate)

We have now presented the main steps required to solving an electromagnetic problem using FEM. In order finding to apply these steps it is often practical to use different coordinate systems including the global coordinate system, a local system for each element or a natural coordinate system (in triangular elements, barycentric coordinates ζ and η).

If Legendre polynomials are chosen for the shape function, the coordinate transform from a local system (based on the two nodes) to a global system can then be performed using the same element shape functions e.g.:

$$x = U_E^1 x_1 + U_E^2 x_2 \quad (3.51)$$

As well as calculating the potential we must also calculate derivatives of the potential to obtain electromagnetic fields E, D, B and H. To simplify this process the derivative is calculated in local coordinates and then these can be transformed to global derivatives using the ‘‘Jacobian’’ which is defined as:

$$[J] = \begin{bmatrix} \frac{\partial x}{\partial \xi} & \frac{\partial y}{\partial \xi} \\ \frac{\partial x}{\partial \eta} & \frac{\partial y}{\partial \eta} \end{bmatrix} \quad (3.52)$$

where:

$$\frac{\partial x}{\partial \xi} = \frac{\partial U_E^1}{\partial \xi} x_1 + \frac{\partial U_E^2}{\partial \xi} x_2 \quad (3.53)$$

Global derivatives are written in terms of local derivatives as follows:

$$\begin{bmatrix} \frac{\partial U_E^i}{\partial x} \\ \frac{\partial U_E^i}{\partial y} \end{bmatrix} = [J]^{-1} \begin{bmatrix} \frac{\partial U_E^i}{\partial \xi} \\ \frac{\partial U_E^i}{\partial \eta} \end{bmatrix} \quad (3.54)$$

Thus solutions can be obtained for each element in its local coordinate system and the solution transformed to the global system, before collecting the element solutions into the global solution.

b.1.1) Near to Far Field Transformations

FEM computes the total electric and magnetic fields in the calculation area as shown below in Figure 3.7. The total calculated field, E_{tot} , is the sum of the incident and scattered fields, E_{inc} and E_{scatt} respectively.

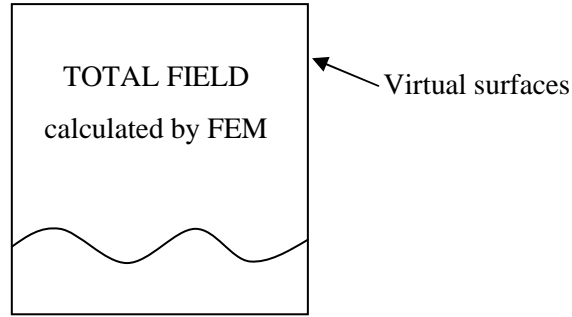


Figure 3.7: The FEM calculation area

In order to calculate the bistatic scattering coefficient and emissivity we require the scattered field in the far field region. The scattered field in the calculation area can be calculated from $E_{tot} - E_{inc}$. Once we have our scattered field in the calculation area we must perform a transformation to the far field region. In order to do this we select a surface or surfaces in the area or on the calculation area boundary to be known as the “virtual surface”. The tangential components of the scattered field are calculated on this surface (by FEM), E^S and H^S , and from these values we obtain equivalent surface currents:

$$\vec{J}^S = \hat{n} \times \vec{H}^S \quad (3.55)$$

$$\vec{M}^S = \hat{n} \times \vec{E}^S \quad (3.56)$$

Where \hat{n} is the outward normal vector on virtual surface S . The scattered far fields are then found by the transform of the currents over the free space Green’s function, as with MoM.

b2) Finite Difference Time Domain (FDTD) method

The finite difference time domain method was originally introduced in 1966 by Yee for the calculation of near-field scattering from an object in the time domain (Yee 1966). It has since been developed to

also calculate far-field quantities and the steady state solution. The method is based on approximating the derivative operators in Maxwell's equations with finite differences, i.e. ∂t becomes Δt , ∂x becomes Δx , etc. These equations are then used to calculate field values at a given time step and in a given element of space from values calculated at a previous time step.

In this section we show how Maxwell's equations are converted to finite difference forms and give conditions for acceptable time and spatial increments, as given in Fung et al (1994b).

Following Yee's notation we define a spatial increment Δ , where $\Delta = \delta x = \delta y = \delta z$, and a time step δt . Then we denote a mesh point as:

$$(i, j, k) = (i\Delta, j\Delta, k\Delta) \quad (3.57)$$

and any function in space and time as:

$$F^n(i, j, k) = F(i\Delta, j\Delta, k\Delta, n\delta t). \quad (3.58)$$

The differential operator within the curl operator of Maxwell's equations is discretized using the *central difference approximation*. Any derivative of F^n with respect to space and time is approximated as:

$$\frac{\partial}{\partial x} F^n(i, j, k) \approx \frac{F^n(i+1/2, j, k) - F^n(i-1/2, j, k)}{\Delta} \quad (3.59)$$

$$\frac{\partial}{\partial t} F^n(i, j, k) \approx \frac{F^{n+1/2}(i, j, k) - F^{n-1/2}(i, j, k)}{\delta t} \quad (3.60)$$

where x may be replaced by y or z and i exchanged for j and k in (3.59) to obtain the equivalent derivative with respect to y or z .

Applying these approximations to Maxwell's equations Yee obtained the finite difference approximate expressions of Maxwell's curl equations by positioning different field components on a unit cell, as shown in Figure 3.8.

The finite difference approximations for the y components of the E and H fields were obtained as:

$$H_y^{n+1/2}(i+1/2, j, k+1/2) = H_y^{n-1/2}(i+1/2, j, k+1/2) + \frac{\delta t}{\mu(i+1/2, j, k+1/2)\Delta} \left[E_x^n(i+1/2, j, k) - E_x^n(i+1/2, j, k+1) + E_z^n(i+1, j, k+1/2) - E_z^n(i, j, k+1/2) \right] \quad (3.61)$$

and

$$\begin{aligned}
E_y^{n+1}(i, j+1/2, k) &= \left[1 - \frac{\sigma(i, j+1/2, k)\delta t}{\epsilon(i, j+1/2, k)} \right] E_y^n(i, j+1/2, k) \\
&+ \frac{\delta t}{\epsilon(i, j+1/2, k)\Delta} \left[H_x^{n+1/2}(i, j+1/2, k+1/2) - H_x^{n+1/2}(i, j+1/2, k-1/2) \right] \\
&- \frac{\delta t}{\epsilon(i, j+1/2, k)\Delta} \left[H_x^{n+1/2}(i+1/2, j+1/2, k) - H_x^{n+1/2}(i-1/2, j+1/2, k) \right]
\end{aligned} \tag{3.62}$$

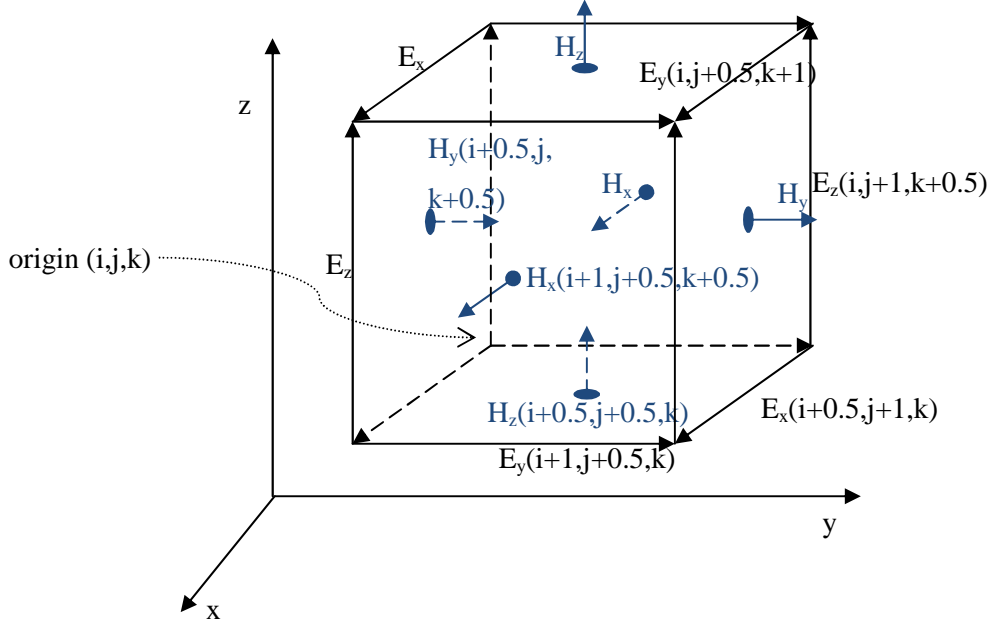


Figure 3.8: Position of the field components in a unit cell of the Yee Lattice. Vectors in blue represent magnetic, H , fields and vectors in black represent electric E fields.

Therefore the H field at a certain position and time is calculated as a function of the H field at this position in a previous time increment and also the E field in the current time step but in adjacent positions. The E field is calculated in the same way as functions of itself at a previous time and the H field in adjacent positions.

To ensure an algorithm which is stable and accurate, conditions are imposed on the spatial and temporal increments Δ and δt . According to Taflove and Umashankar (1989), $\Delta \leq \lambda/10$ is sufficient to obtain a solution with an uncertainty of less than $\pm 7\%$ in the near fields due to the approximation of the spatial derivatives. To ensure stability in the time stepping algorithm δt should satisfy the following (Fung et al 1994):

$$\delta t \leq \left[(\delta x)^{-2} + (\delta y)^{-2} + (\delta z)^{-2} \right]^{-1/2} C_{\max}^{-1} \tag{3.63}$$

where C_{\max} is the maximum phase velocity of the incident wave. For a cubic lattice where (3.63) reduces to:

$$\delta t \leq \Delta \times (\sqrt{3}C_{\max})^{-1}. \quad (3.64)$$

As with the Finite Element method, conditions must be defined on the boundaries of the calculation area that determine the behavior of the electric and magnetic fields at these boundaries. For example we can mathematically impose total reflection on the boundary, or radiation to infinity. These conditions are necessary for a numerical solution to be found. Substituting these conditions into equations (3.61) and (3.62) reduces the unknowns in the numerical equations and allows them to be solved. As with FEM, FDTD calculates the total Electromagnetic fields in the calculation area. The scattered electric field in the far field region can be calculated by defining virtual surfaces and performing a near to far field transformation, as described in section b1).

3.1.3.3 Selection of the appropriate numerical approach

We have now described several different numerical approaches which can all be used to model rough surface scattering and emission. In order to choose which method to use we must consider the required application, since each method has its advantages and disadvantages and is consequently better suited to certain problems. However, in general a method may be considered to be “better” if it has a lower calculation CPU time and memory requirement (is less “computationally costly”) and/or a higher accuracy. Usually a compromise has to be reached between these two ideals.

In discussing computational time and memory requirements of different methods it is important to understand the meaning of sparse and dense matrices. A sparse matrix is a matrix populated primarily with zeros. Physically this corresponds to loosely coupled systems such as a line of balls connected by springs. A dense matrix on the other hand is primarily populated by non-zero elements and corresponds to strongly coupled systems such as a group of balls each one connected to all of the others by springs. Computationally, sparse matrices are easily compressed and stored and specialized algorithms and data structures can be used which take advantage of their sparse nature and are therefore less computationally costly. Numerical methods which solve sparse matrices are therefore less computationally costly.

Differential operators are local and therefore lead to sparse matrices, as opposed to integral equations which lead to dense interaction matrices. This means that the FDTD and FEM methods are faster and less memory consuming than the traditional Method of Moments. A large amount of research has gone into developing fast solvers for MoM while maintaining the accuracy of the solutions obtained.

As with MoM the Finite Element Method (FEM) requires the solution of a linear system but with a sparse matrix, so that matrix-vector multiplications are less computationally costly. FEM is well suited to inhomogeneous problems with complex geometries.

MoM methods are well suited to rough surface scattering and emission problems since they use a surface mesh, making the meshing more accurate and allowing calculations to be done for much larger surfaces without greatly increasing memory requirements or calculation time. Also for differential methods error can accumulate with surface size, whereas for MOM error is size independent. However traditional MoM methods were slow because of the necessity of solving and storing dense matrices. A large amount of research has gone into developing fast solvers for MoM while maintaining the accuracy. Currently MOM-based fast solvers are considered to be the most accurate methods available for rough surface scattering and emission.

For the general inhomogeneous volume problem it is more desirable to use a volume-meshing approach such as FEM. FEM has a more flexible meshing procedure than FDTD. This makes the FEM method well suited to heterogeneous structures since the mesh shape and size can be modified as required around the object, with larger elements in homogeneous areas and smaller elements in heterogeneous zones. Alternatively the volume integral equation method can be applied for heterogeneous media.

FDTD calculates the solution as a function of time whereas FEM and MoM calculate directly the steady state solution so FDTD is better suited to problems where the temporal response is required.

FDTD is a good method for time-domain or broadband scattering results as it provides these directly. It is a straight forward method flexible enough to handle a wide range of problems.

3.1.3.4 Validation of Numerical Methods

In section 3.1.3.2 we presented the main numerical methods that can be used to calculate rough surface scattering and emission in general, and the scattering of a soil layer of homogeneous moisture content in particular. We then discussed how to select an appropriate method for the required application. Once we have selected a method to be adopted, it is important to test its validity, that is to say whether or not the calculated solution is accurate. The best known test of the validity for using numerical methods to calculate the scattering and emission of a rough soil surface is an energy check. For lossless media the sum of the Poynting vector of the scattered field above the surface and the total field below the surface must equal the Poynting vector of the incident field. However if the lower medium absorbs part of the energy performing this energy check would involve the integration of volume density which is harder to achieve.

Other tests include one based on the Lorentz reciprocity theorem which is well suited to incident plane waves but not finite incident beams.

3.1.3.5 Problems of current interest

In this section we discuss in more detail the research that has been carried out in the field of modelling electromagnetic scattering and emission of rough surfaces using numerical methods.

Historically, numerical models were developed to provide an accurate baseline against which analytical models and their validity regions could be tested and also to provide results for the cases where analytical models could not be used. Validation remains an important application of numerical methods, and studies continue to be carried out using numerical methods where methods such as the standard Kirchoff Approximation (KA) and the small perturbation method (SPM), as well as the more recent integral equation method (IEM) fail.

Before the 1990s, research was mostly done for scattering from 1-dimensional surfaces, including studying backscatter and bistatic scattering. Problems studied were also restricted to incident waves at moderate angles relative to the normal. Current research of 1-dimensional surface scattering concentrates on low-grazing angle scattering, which is harder to model.

Since the 1990s, with the increase in computational resources and improvements to the numerical methods, attention has turned to 3-dimensional scattering, usually of 2-dimensional surfaces. Investigations of scattering include studying the physical phenomena which typically occur when a rough surface is present, e.g. enhanced backscatter. There have also been studies comparing numerical predictions with experimental results. Inverse scattering is also studied as this is important for buried object detection by radar, including detection of mines for example.

With the development of 3-dimensional scattering models it has also become possible to model the emissivity and in the last ten years attention has turned to the passive case. Passive remote sensing requires greater accuracy in energy conservation than active remote sensing. This is because the relationship $e = 1 - \Gamma$ relies on energy conservation. The transmission energy must be equal to one minus the scattered energy and if these values are different we do not know whether to take the emissivity equal to one minus scattering or equal to the transmissivity. On the other hand (Zhou et al 2004) the bistatic scattering coefficient fluctuates from one realization to another because of speckle, a phenomenon where a lot of interference between waves of different phases leads to an intensity which varies randomly, and in the case of scattering a lot of realizations are required to average this out. However the emissivity is an integration of the bistatic scattering coefficient and this tends to smooth out the speckle effect; hence fewer realizations are usually required in the passive case.

Emission studies focus on accuracy for cases that are harder to model such as surfaces of exponential correlation function with high permittivity.

Research has also focused on developing the models themselves, in order to increase accuracy and reduce computation time. Much work has been done to develop the Method of Moments (MoM) model, which is well suited to the surface scattering problem and gives highly accurate results for this case. Research has focused on speeding up computation time whilst maintaining accuracy. The method of moments is currently generally considered to be a reference method for surface scattering and emission due to the high accuracy of its predictions and the application of fast solvers coupled with advances in computer capabilities has made its use practical.

The FEM and FDTD methods were originally developed to provide alternatives to the Method of Moments, which was considered more accurate, since they are faster. Both methods have been used to study the rough surface scattering: the FEM by Lou et al (1991a and 1991b) and FDTD notably by Fung et al (1994b). However they became less important for the surface scattering and emission case as developments in computational resources and also in the use of MoM, made the more accurate MoM a practical tool. To our knowledge there are no papers that present the emission of rough surfaces as calculated by the FDTD or FEM. However the FD-TD and FEM methods are still useful for respectively temporal studies and studies of heterogeneous media. In particular the FEM method can be extended to study heterogeneous media such as multiple layers with rough surfaces, dielectric gradients, and buried objects more easily than the MoM. Indeed, the approach adopted for the study of the soil-litter layer adopted in this thesis utilises an FEM modelling tool, and one of the reasons for this choice is its adaptability to multi-layer structures.

3.2 Modelling the contribution of the litter layer to forest emission at L-band

In order to explain the role the leaf litter layer plays in forest emission, and how this can be modelled, we must start with what is currently known about forest emission. In this section we present firstly the general structure of forests. Secondly, we present a background on forest emission, including experimental results and theoretical models. We then present and compare attempts that have been made to include effects of the litter layer in theoretical models for forest emission. Information on the structure of forests is mainly taken from Chukhlantsev (2006), although some information is taken from Bonan (2008).

3.2.1 The Forest structure

A third of the Earth's land surface is covered by forest (about 50 millions of square kilometres). The distribution of different types of forest over the Earth's land surface is shown in Figure 3.9:

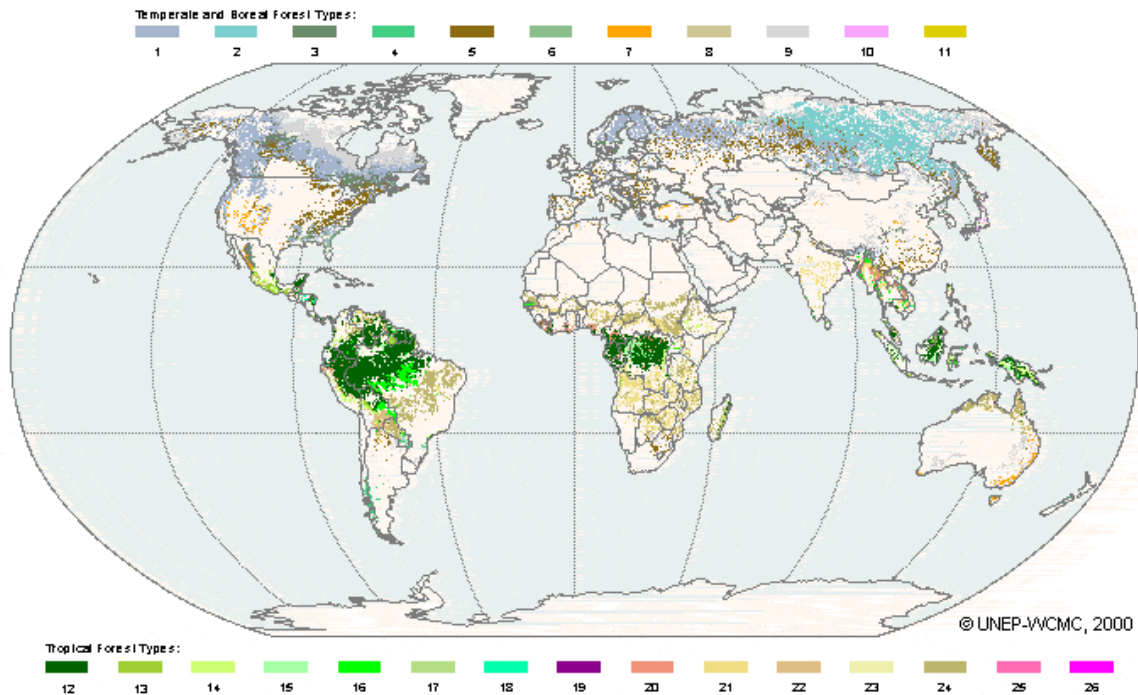


Figure 3.9: Global map of the Earth's forest cover. Different colours represent different forest types.

Boreal forests of Europe, Russia, Canada, and the USA occupy about fifteen millions of square kilometres. Tropical forests make up about 53% of the world forest store.

Forests play a key role in the global carbon and nitrogen cycles and considerably affect the energy and water balance of the biosphere. Forests exchange carbon both with the atmosphere and the ground, by mechanisms such as photosynthesis, autotrophic respiration, and litterfall. Forest-atmosphere interactions are complex and non-linear and a lot of research has gone into understanding the processes involved. Forests transfer water to the atmosphere by evapotranspiration (evaporation from the ground plus transpiration from the vegetation). Water transferred from the atmosphere to the land by precipitation is caught by forest vegetation and either held by the vegetation or funnelled down to the ground through stemflow. Water is also transferred from the soil to the forest vegetation by water uptake. Tropical forests also increase precipitation compared with pastureland. Forests have low surface albedo (the fraction of radiation reflected by a surface) and can mask the high albedo of snow allowing more heat to be absorbed by the land. However for the case of tropical forests this warming is offset by strong cooling through evapotranspiration.

A characteristic feature of forests is their stratum, or *layered*, structure. The basic components are: 1) the forest stand (including the canopy and trunks), 2) the understory layer, including the undergrowth (small trees, bushes, ferns etc) and the live soil cover, and 3) the ground, including dead litter in various stages of decomposition, and the underlying soil. The stand consists of one or more stratum formed by trees of different heights and species. The forest canopy contains elements of small size

(branches and leaves) and has a low density of $0.03 - 0.3 \text{ kg/m}^3$, a large height of 2 – 25m, and a relatively stable water (gravimetric moisture) content.

The live soil cover includes bushes, shrubs, grass, moss, and lichen. In the absence of live soil cover, a layer of dead needles, leaves, small branches and bark forms on the soil surface. This litter layer has a friable structure and dries and moistens fast. Its height varies from 0.01 to 0.07m, its mass is $0.1 - 0.6 \text{ kg/m}^2$, and its density is $5 - 30 \text{ kg/m}^3$.

Forest leaf litter is fragmented and mixed into the lower layers of the soil, usually within 1 year of falling from the trees. The reduction and mixing of leaf litter is largely done by many different soil animals ranging from microscopic nematodes to large earthworms. This decomposition process leads to distinct layers in the forest floor.

The forest ground can be divided into two layers: the forest floor and the underlying mineral soil layer. Each of these two layers can be further subdivided. The forest floor usually consists of three main layers, named L, F and H. The L layer is the previously mentioned fresh, undecomposed litter layer. Below this we have the F layer consisting of fragmented organic materials in a stage of partial decomposition. This layer contains mostly organic materials in cellular form, and fungi and bacteria are common. The H, or humus, layer consists primarily of resistant products of the decomposition process and has lower proportions of organic matter in cellular form. The lower portion of the H layer often shows an increasing proportion of inorganic mineral soil constituents, but organic components still dominate.

Below these layers we have the mineral soils, including the A_1 horizon which is a mixture of soil and the humus layer and then the pure mineral soil layers.

Temperate forests have two main types of forest floor, known as “mor” and “mull”. Mors are found in cooler climates, often with coniferous vegetation, and decomposition is slow and incomplete resulting in a thick organic layer. This is largely due to a low earthworm population resulting in little fragmentation and mixing with the underlying soil. Mulls are typically found in deciduous forests in warm temperate climates and decomposition of the forest floor is more rapid. Often the fragmentation and mixing make it difficult to distinguish between different forest floor layers. Lowland tropics have a decomposition process that is even more complete and rapid than temperate forests, resulting in little forest floor mass. Tropical forests in general have an absence of a thick forest litter layer.

3.2.2 Remote Sensing of Forests

3.2.2.1 Experimental data

Prior to 2000, remote sensing of forests at microwave frequencies was usually done using an active system since this allows us to penetrate the canopy and retrieve information about the forest parameters.

More recently the development of space projects such as the SMOS mission has stimulated interest in studies of forest emission. The SMOS mission is particularly concerned with the sensitivity to soil moisture and measuring other influencing parameters in order to remove them from the signal. Forest emission is important for SMOS since a significant fraction of land pixels is either partially or fully covered by forest (see Figure 3.9).

In recent years several ground-based radiometric measurements for deciduous and coniferous forests have been carried out (Guglielmetti 2008, Grant 2007, Santi 2007) with interesting results. These three experiments demonstrated the semi-transparency of the forest canopy at L-band frequencies which allows the sensing of the forest ground radiation. However Guglielmetti et al (2008) and Grant et al (2007) found that variations in soil moisture had a weak influence on overall emission and reasons for this were suggested to be litter effects. From the Forest Soil Moisture Experiment (FOSMEX) performed by Guglielmetti et al (2008) at a deciduous forest site, it was postulated that a large fraction of the rainwater is caught by the litter layer and funnelled through to deeper soil horizons. Under wet conditions the litter layer acts as an absorber of the underlying soil radiation and also itself emits a strong signal. It acts as an impedance matching layer, with a permittivity whose value is in between that of the soil and canopy layers. The “Bray 2004” campaign performed in a coniferous forest by Grant et al (2007) also showed generally high scene emissivities which were associated with substantial litter and understory layers.

In order to improve understanding of the electromagnetic properties of the litter layer, Demontoux et al (2008) performed laboratory measurements of the litter permittivity as a function of its moisture content. These experiments were performed for litter taken from the site of the Bray 2004 campaign, which consisted of a mixture of decomposed grass and pine needles. These measurements were taken to be complimentary to theoretical models of litter emission.

3.2.2.2 Theoretical Models

Theoretical simulations carried out using physical models add important information to our understanding of forest emission. Measurements are necessarily limited to single forests and single environmental conditions. Analytical models allow us to extend studies of forest emission to several

cases of possible forest variables, single out contributions from different forest components and carry out parametric studies at different frequencies, angles and polarizations.

In this section we firstly outline the main forest emission models that have been presented in the literature and secondly focus on the work presented in the literature to model the litter layer and include it in forest emission models.

a) Modelling Forest Microwave Emission

Theoretical models are an important attempt to understand the complexity of forest emission and in particular its dependence on many different variables. However in practice only a limited set of forest variables is available by direct measurements.

The majority of theoretical simulations have so far mostly focused on radar applications, or forest scattering. However, some physical models of emission are also available, notably Ferrazzoli et al (1996), and Karam (1997). The basic modelling approach for forest scattering and emission involves contributions from discrete forest elements and is based on radiative transfer theory. The medium is subdivided into three main regions or layers: crown, trunks and soil. The contribution of each layer may then be calculated using radiative transfer theory, as demonstrated previously in section 2.5.2. The relevant emission and absorption properties of each layer (values of τ and ω) are then calculated by electromagnetically modelling its components, which includes leaves, branches, trunks and leaf ground litter. The single elements tend to be modelled as canonical bodies, typically discs, needles, ellipsoids and cylinders and the contributions from each element are combined using algorithms which consider multiple scattering effects.

The crown is filled with scatterers representing leaves, needles, twigs, and branches. They may be positioned at different heights, depending on the properties of the tree species being modelled. Usually the scatterers are assumed to be uniformly located within the crown.

Prior to the identification of its contribution to forest emission, the litter layer was considered transparent and generally ignored in the physical models.

In the next section, as an example, we present the model proposed by Ferrazzoli et al (2006), which was later modified by Della Vecchia et al (2007) to include contributions from the forest litter.

a1) Forest Emission model without litter contributions, by Ferrazzoli et al

Figure 3.10 shows a visual representation of the model by Ferrazzoli et al (1996), without contributions from forest litter.

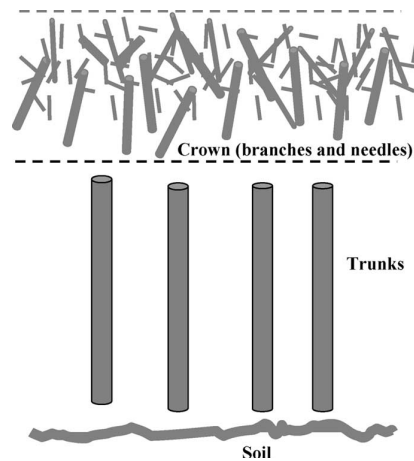


Figure 3.10: Model of the three forest layers: soil, trunks and crown

Vegetation elements were represented by cylinders of various dimensions: those representing the trunk standing upright and those in the crown of different random orientations. Bistatic scattering and extinction cross sections for each element were calculated by applying suitable Electromagnetic theory (such as the “infinite length” cylinder, Rayleigh-Gans approximation, etc.) depending on wavelength and cylinder dimensions. The canopy scattering including contributions of all elements was then computed using a multiple scattering algorithm. This same algorithm was then used to combine canopy and soil scattering. The soil was represented as a homogeneous half space with a rough interface and its scattering calculated from the Q-h semi-empirical model. Finally the emissivity of the whole system was calculated from one minus the reflectivity ($1-\Gamma$).

b) Inclusion of the litter layer

Since the recognition of the litter layer’s role in forest emission, there have been two attempts to include it in physical models of forest emission: by Della Vecchia et al (2007) and Schwank et al (2008). This topic is still very new and so we may expect further developments in the future (including the work of this thesis). Demontoux et al (2008) also proposed a simple numerical approach for modelling the soil-litter emission. In all these approaches, the litter was modelled as an effective dielectric medium with a homogeneous effective permittivity value. This permittivity value was related to physical properties of the litter layer, including notably litter moisture content. The litter can be represented as an effective medium, at L-band frequency, because the components are smaller than the wavelength. It is also worth noting that since the litter is a dense medium we expect coherent effects to be non-negligible and therefore modelling the litter layer in the same manner as the canopy layer, applying radiative transfer theory, would lead to inaccuracies.

In the next sections we present the models proposed by Della Vecchia et al (2007), Schwank et al (2008) and Demontoux et al (2008), and then briefly compare them.

b1) Model by Della Vecchia et al

Della Vecchia et al (2007) present an updated version of the forest emission model proposed by Ferrazzoli et al in (1996), including contributions from a litter layer (Della Vecchia et al 2007). In the updated version the soil layer was replaced by a two layer soil-litter system with flat surfaces, as a first step, where the litter is represented as a layer of a mixture of air and dielectric material, as shown below in Figure 3.11:

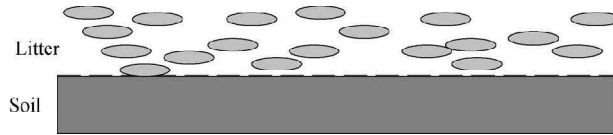


Figure 3.11: Representation of the soil and litter layers

The uniform permittivity of the litter layer was calculated from the permittivities of the respective components of dielectric material (leaves and water) and air, with the aim of finding a relationship with measurable quantities. The permittivity of the dielectric material, ϵ_{dm} , was calculated as a function of the litter moisture using the empirical formula adopted for vegetation by El-Rayes and Ulaby 1987.

The permittivity of the mixture, ϵ_{litter} , was then calculated from the semi-empirical “refractive model” for mixtures (Ulaby et al vol I) as:

$$\epsilon_{litter}^{1/2} = (1 - V_F)\epsilon_{air}^{1/2} + V_F\epsilon_{dm}^{1/2} \quad (3.65)$$

where V_F is the volume fraction of dielectric material, expressed as a function of litter biomass, litter moisture, litter layer thickness and the density of water and dry dielectric material (leaves). A ratio was later assumed between litter thickness and litter biomass of 0.5 kg/m^2 , which fits the Bray 2004 measurements.

Soil permittivity was calculated using the semi-empirical model proposed by Hallikainen et al (1985) and the reflectivity of the overall soil-litter system was then calculated using the coherent multiple reflection model described in chapter 4, pages 232-237 of Ulaby et al (1985a). Note that this is still considering flat layers. This leads to oscillations due to coherent interactions between multiple reflections which in reality are smoothed by natural variations in the layer thickness around its average value and so the trend was modified in order to eliminate oscillations and keep the asymptotic values. In order to do this an exponential function was fitted to the coherent model output (reflectivity as a function of litter biomass) such that the root mean square difference between the function and the output was minimized.

The whole soil-litter medium was reduced to an equivalent single homogeneous half space whose permittivity was computed by minimizing a cost function proportional to the root mean square differences between the Fresnel reflectivity of the half space and the reflectivity calculated from the composite soil-litter medium, considering all angles in the range of 0° to 60° with a step of 10° and both polarisations.

Finally the roughness of the equivalent half space was accounted for using the integral equation method (taken from Fung et al 1994) to calculate the bistatic scattering coefficient of the equivalent half space and combine soil and vegetation scattering.

From this model, the litter was found to behave as a matching layer between the soil and the air (or canopy). The litter layer is less dense than soil and so its permittivity is between that of soil and air which led to the litter layer reducing reflectivity in the model and increasing emissivity at the soil-canopy boundary. This was mostly evident in the real part of the equivalent half space permittivity.

Inclusion of the litter layer in the model did not affect the time variation of simulated brightness temperatures but greatly increased their absolute values (by about 20K). The model was compared to results of the Bray 2004 radiometry experiment and the increased brightness temperature due to the litter layer meant that the calculated T_B and experimental T_B were very close in absolute values. Inclusion of the litter layer in the model also led to an improved representation of the forest emissivity's sensitivity to soil moisture.

b2) Model by Schwank et al

Schwank et al (2008) proposed a physically based model for the microwave radiation of leaf litter at different moisture conditions. Like the Della Vecchia model, Schwank et al used an effective medium approach, considering the litter layer as a mixture of leaves, water and air, which each contributed to an overall effective permittivity of the litter layer. However the Schwank model considers the contributions of each of the components in a more physical way, using physical mixing formulas instead of the semi-empirical refractive index formula.

The litter is modelled as an isotropic mixture of ellipsoids embedded in air (see Figure 3.12).

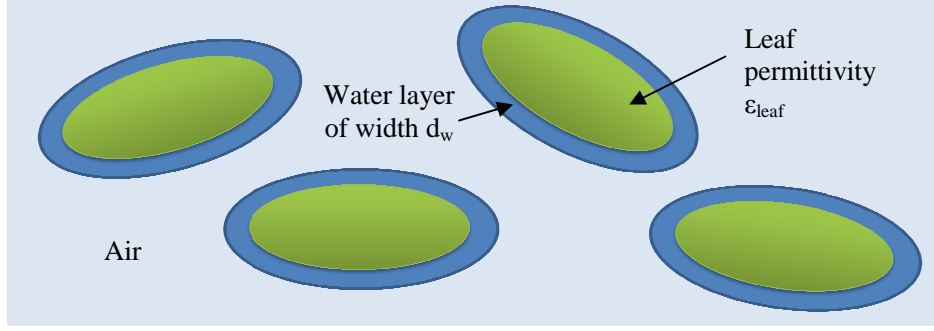


Figure 3.12: representation of the litter mixture

The ellipsoids represent the leaf surround by a layer of free water, to represent the wetting of the leaf surface, and have permittivity ϵ_{leaf} , semi axes a , b and c ($b \gg c$) and number density n . The air has permittivity $\epsilon_A=1$ and free water permittivity ϵ_w . The ellipsoid leaves are coated with water of thickness d_w . An empirical model was used to compute the temporal evolution of the density of the water column wetting the litter, $\rho_{wL}(t)$, to the precipitation rate $P(t)$ (rain intensity in mm per hour). The thickness of the free water coating is then related to $\rho_{wL}(t)$.

The leaf permittivity is modelled from the microwave dielectric model of leaves proposed by C. Matzler (1994).

The directional dependent polarizabilities of the water coated ellipsoids (Π_a , Π_b , Π_c) are averaged in accordance with the assumed isotropy. The overall effective litter permittivity is then calculated from these values as well as ϵ_A and n , using the Maxwell-Garnett mixing rule valid for depleted dielectric mixtures. The permittivity is then calculated as a function of depth, $\epsilon(z)$, and is equal to the litter permittivity for depths that fall within the litter layer and the soil permittivity at depths within the soil layer (see

Figure 3.13). Two Fermi functions are applied to smooth the transition between the air and litter layers and the litter and soil layers. $\epsilon(z)$ is therefore given by:

$$\epsilon(z) = \epsilon_A + \frac{\epsilon_L - \epsilon_A}{1 + \exp\left(-\frac{z - z_{AL}}{k_{AL}}\right)} + \frac{\epsilon_S - \epsilon_L}{1 + \exp\left(-\frac{z - z_{LS}}{k_{LS}}\right)} \quad (3.66)$$

z_{AL} is the average position of the litter-soil boundary and z_{LS} the average position of the litter-soil boundary, which two are related by $z_{LS} = z_{AL} + \langle D \rangle$, where $\langle D \rangle$ is the mean litter layer thickness. Parameters k_{AL} and k_{LS} within the two fermi functions are linked to the standard deviation of surface height of the litter and soil layers respectively, on lateral scales smaller than the Bragg limit, where the heights are considered to have a Gaussian distribution. These standard deviations were estimated to be 1cm. In this way small scale roughness of the soil and litter surfaces is accounted for.



Figure 3.13: representation of the soil and litter layers as an effective medium with an effective permittivity that varies with depth z

A coherent radiative transfer model, based on a matrix formulation of the boundary conditions at dielectric discontinuities derived from Maxwell's equations (Bass et al 1994), is applied to calculate the overall reflectivity from $\epsilon(z)$.

In order to account for large scale variations in litter depth, the reflectivity for each litter depth D_L was computed as the average reflectivity over a depth $D_L \pm \Delta D_L$.

b3) Numerical Approach proposed by Demontoux et al

In order to improve understanding of the electromagnetic properties of the litter layer, Demontoux et al (2008) performed laboratory measurements of the litter permittivity as a function of its moisture content. These experiments were performed for litter taken from the site of the Bray 2004 campaign, which consisted of a mixture of decomposed grass and pine needles. These measurements were used to derive an empirical relationship for the litter permittivity as a function of litter moisture. The authors then proposed a simple numerical model where the soil litter system was represented as two dielectric layers with flat surfaces. The soil permittivity was calculated from the soil moisture, using an empirically derived relationship and the litter permittivity was also calculated from litter moisture using an empirical relationship derived from laboratory measurements. The emission of the soil-litter system was calculated at nadir (0°).

3.2.3 Discussion

The identification of the role the litter layer plays in forest emission is an important discovery since it means that, unless we find a way to account for and remove the litter effect, we will be unable to retrieve soil moisture over forests under high moisture conditions. It is worth noting however that this may not be the case for all forests since the litter's contribution to the emission is restricted to forests with a significant litter covering (which discounts tropical forests for example) and may be restricted to certain litter types, for example with a large leaf surface area. The dependence on litter type is still to be investigated.

Theoretical models could play a key role in improving our understanding of the effect of the litter layer since if the model is complete it allows us to vary the many different parameters involved and identify the key affecting factors.

So far the only two attempts have been made to model the contribution of the litter layer to forest emission: models proposed by Della Vecchia et al (2007) and Schwank et al (2008). Both models focused on calculating the permittivity of the litter layer as a function of its physical parameters, including moisture content. Della Vecchia et al calculate this in a more semi-empirical manner and Schwank et al in a more physical manner. Della Vecchia et al calculated the emission of the soil-litter system using a coherent multiple reflection model and the rough surface of the litter layer was accounted for by representing the soil-litter medium as a single homogeneous effective medium with a rough surface, whose emission was calculated using the Q-h semi-empirical model. Schwank et al calculated the emission of the soil-litter system by representing the soil-litter system as a single medium with a permittivity varying with depth. The rough surfaces were accounted for as variations in the permittivity constant with depth. In summary, Della Vecchia et al applied an exact electromagnetic model to calculate the soil-litter emission but only took into account the litter layer roughness, and this was accounted for using an approximate method. On the other hand Schwank et al accounted for both the litter and soil rough surfaces but in an approximate manner, considering only the standard deviation of surface height and not the autocorrelation length or autocorrelation function.

The two models are therefore both approximate in the way they deal with litter and soil surface roughness, but they both provide first attempts at calculating the permittivity of the litter as a function of its physical properties. More research is required, particularly in experimental data on the litter permittivity, in order to further test the validity of these models.

A numerical modelling approach for calculating the soil-litter emission was also proposed by Demontoux et al (2008), based on the Finite Element Method. Calculations were performed for a two layer system, with soil and litter permittivities. Both layers had flat surfaces and the emissivity was calculated only at nadir (0°). The litter permittivity was calculated as a function of litter moisture from a relationship determined experimentally from laboratory measurements of litter samples taken from the Bray 2004 site (Grant et al 2007). Note that this was a first step in the model that was later developed for the work of this PhD.

3.3 Choice of approach for modelling the soil-litter L-band emission in this thesis

The objective of this thesis is to develop and validate a modelling technique that allows us to study the microwave emission of the soil-litter forest system. The modelling approach that we adopt must allow us to model all important features of the soil and litter layers as well as the measurement conditions of the SMOS mission. This includes the following features of the soil and litter layers:

1. Soil layer:
 - Temperature gradient (modelled as T_{eff})
 - Soil moisture content, which varies as a function of depth
 - Rough surface
 - Inclusions such as rocks or stones (in some cases)
2. Litter layer:
 - A dense layer of organic debris
 - Rough surface
 - Litter moisture content
 - Litter depth

In order to reproduce the measurement conditions of the SMOS mission, we must also be able to perform calculations of the emissivity for two polarisations, H and V, at all angles from 0° to 50° , and for different permittivity values covering the range of soil and litter moistures. These requirements are summarised in Figure 3.14.

As we have seen, the soil layer can be represented as a homogeneous dielectric layer with a permittivity ϵ_{soil} which can be calculated from the frequency, soil moisture content, soil texture and soil temperature. There are various algebraic models that allow us to do this, including the model developed by Mironov et al (2004). Thus the moisture content and soil texture can be accounted for in the soil's dielectric permittivity constant. The overall emission of the soil layer can then be calculated from its effective permittivity and as a function of its roughness (standard deviation of surface height, σ , autocorrelation length, L_c , and autocorrelation function) using either a semi empirical approach, a numerical method, or an analytical method, as discussed in section 3.1.2. Since volume effects are non-negligible at microwave frequencies for low soil moisture it may be important to model heterogeneous features below the soil's surface, which includes soil moisture and potentially temperature gradients and in some cases inclusion such as buried rocks can have an effect.

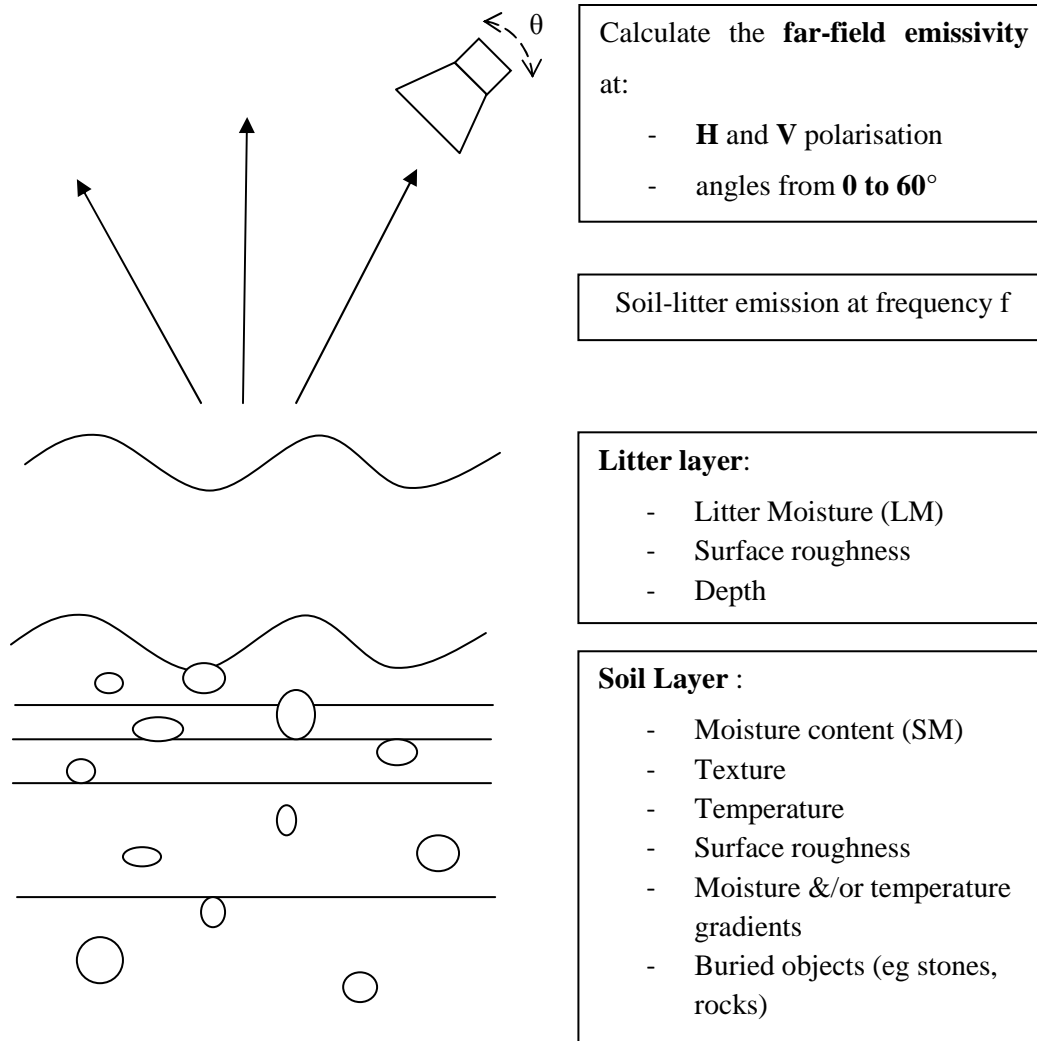


Figure 3.14: The features of the soil and litter layers and measurement conditions that must be modelled in the approach adopted

The litter may be modelled in a similar manner to the soil layer: as a homogeneous layer with an effective dielectric permittivity constant, ϵ_{litter} , which can be calculated as a function of its physical parameters using a standard mixing model such as the models used by Schwank et al (2008), or Della Vecchia et al (2007), or an empirical, experimentally determined relationship (e.g. Demontoux et al 2008), and a rough surface accounted for using one of the methods presented in chapter 4.

Thus we can model the soil-litter system as two dielectric layers, each with a rough surface. It may be important to include heterogeneous features such as moisture gradients or buried objects (rocks, stones, etc.). The emission of each dielectric layer could then be calculated as discussed in chapter 4: using the semi-empirical Q-h model, an analytical model such as IEM, or a numerical approach. However we require the combined emission of the two layers. If we chose to use one of the numerical models presented in chapter 4, we could equally calculate the emission of two layers as of one, since results are obtained by solving Maxwell's equations directly for the desire structure. If we were to

apply an analytical or semi-empirical approach, we could calculate the emission of the whole system using radiative transfer equations, or an electromagnetic approach such as those adopted by Della Vecchia et al (2007) or Schwank et al (2008). However we may lose information due to reflections between the two rough surfaces. Also we cannot model volume effects with the analytical approach and with the Q-h approach we would not be able to study the effects of σ and L_c . Furthermore we could not model heterogeneous features such as moisture gradients and inclusions using an analytical or semi-empirical method.

In this thesis we therefore chose to use a numerical approach since it is the most accurate of all the methods, and it also allows us to include all our requirements, including in particular the inclusion of heterogeneous features such as multilayers.

We now consider the choice of numerical modelling approach for this thesis. In constructing a numerical model which solves Maxwell's equations for a given structure, there are several steps which must be completed. The numerical equations of the selected method (MoM, FEM, or FDTD) must be developed and written as a code (usually in Fortran), the structure (including rough surfaces) created and meshed, boundary conditions and calculation conditions (frequency, incident beam, incident angle) defined and the numerical equations solved in the mesh.

It is possible, and even common, to write a code for each step and a code to run them together. This process is a long one and takes many years of work. Often, laboratories develop and improve such codes over time and it involves the work of many different people. The advantage of writing codes is that they can be adapted specifically to the structure to be studied, such as to the rough surface scattering case. For example some MoM based codes have been speeded up thanks to characteristics particular to rough surfaces, and the Thorsos taper (Thorsos 1988) which has been developed specifically for rough surface scattering applications can be included.

Alternatively it is possible to purchase commercial software designed to solve Maxwell's equations numerically for a number of different problems and adapt this software to the problem in hand. In this case we are able to skip the stages where the numerical equations are written and the meshing procedure is established and begin working directly on the application. We benefit from a meshing procedure, a powerful tool for creating geometric structures, and a calculating code, all of which have been optimised and are continually being updated and optimised by the software developers. This makes the process of developing the model much faster, since a lot of the work has been done for us, and we are able to generate and analyse results much sooner. The disadvantage is that we cannot develop or adapt the code for the rough surface case and we may come across limitations. However if we choose a flexible software tool, we can keep these restrictions to a minimum.

For the work of this thesis we decided to adopt the second method of developing a procedure using commercial software, in the interests of being able to apply the model more quickly. Furthermore, prior to the start of this PhD, the IMS (Integration du Matériau au Système) laboratory, where the work of this thesis was in part carried out, already owned electromagnetic software and was experienced in its use.

The IMS laboratory owns software based on the FDTD method and also software based on the FEM method, both of which can be used to model the scattering and emission of rough surfaces. In choosing which of the two to use we must consider again the afore-mentioned requirements, summarised in Figure 3.14. In addition to these factors, the model must be practical for the use of creating a database.

We chose to use the FEM software, Ansoft's HFSS© (High Frequency Structure Simulator), because it fulfils these criteria. It is based on the finite element method which is well suited to calculating a solution to Maxwell's equations for heterogeneous structures, and so can be easily extended to considering multilayer structures and even including moisture gradients and inclusions. Also, there is the possibility to vary certain parameters such as incident angle and permittivity (soil moisture) within one calculation. This will be useful when we require results of many different values of soil moisture and measurement angles for the database.

A MoM method was not adopted because whilst it is the most accurate method for calculating rough surface scattering it is not well suited to heterogeneous structures including multilayers and/or temperature and moisture gradients. The approach developed in this thesis allows us to model two dielectric layers with rough surfaces, which to date has not been done with the Method of Moments. It can also be extended to include temperature and soil moisture gradients, which has not been done with the Method of Moments.

Our general approach was to develop a method for calculating the emission of the soil-litter system and then validate it, first for the bare soil emission and secondly for the two layer soil system. This validation process is important since there are currently no results published of the rough surface emissivity and only a very few papers of the rough surface scattering, as calculated using the Finite Element Method. Furthermore there are no results of rough surface scattering and emission published using the HFSS modelling tool. Therefore it is important to validate first for a single layer with a rough surface, and secondly for the two-layer system. Note that although Ansoft's HFSS tool was used to perform numerical simulations, it forms only a part of the whole approach developed to calculate the scattering and emission of the soil-litter structure. In this thesis we will refer to this whole approach as the numerical FEM approach.

**CHAPTER 4. THE NUMERICAL FEM APPROACH DEVELOPED
FOR CALCULATING THE L-BAND SCATTERING AND
EMISSION OF THE SOIL-LITTER SYSTEM FOUND IN FORESTS**

4. The Numerical FEM Approach developed for Calculating the L-band Scattering and Emission of the Soil-Litter system found in Forests

In this section we present the numerical modelling approach developed in this thesis to calculate the scattering and emission of multilayer heterogeneous forest structures. In section 4.1 we present the approach developed and in section 4.2 we present a sensitivity study that was carried out to determine values of model parameters.

4.1 Model Description

The numerical modelling approach developed during this thesis relies on the use of Ansoft's HFSS (version 12.1) simulation software¹ which in turn solves Maxwell's equations using the Finite Element Method. At the start of this PhD, a simple HFSS modelling approach had already been developed in the IMS laboratory, to model the emission of the soil-litter system. In this approach the soil and litter media were modelled as dielectric layers with flat surfaces and the emission was calculated only at nadir (0°). For the work of this PhD, I developed this approach to include rough surfaces and to calculate both the scattering and emissivity of the soil-litter a system over the whole range of angles ($\theta=0 - 90^\circ$) and both H and V polarisation.

In the following sections we present an introduction to the HFSS software and then describe each stage in the numerical FEM approach developed to calculate the scattering and emission of multilayered forest structures. Lastly we present a perspective on how the procedure could be adapted to future applications.

4.1.1 Ansoft's HFSS software

Ansoft's HFSS software is a numerical modelling software tool that calculates the electromagnetic field using the Finite Element Method, described in section 3.1.3.2b1). The reasons for our choice of this software are given in section 3.3.

HFSS combines a 3D graphics design tool, an automatic meshing tool, a numerical solver and an application for post-calculation results analysis, all of which can be controlled in the HFSS user interface. This interface includes a number of windows and commands that allow us to set up a calculation and view and export results. The two main windows are the calculation area and the project

¹ HFSS product website : <http://www.ansoft.com/products/hf/hfss/>

manager. The calculation area shows a visual representation of the object for which we wish to perform a calculation. The object is built or imported in this window. We can then select the object or any of its faces, and apply material properties or boundary conditions to them. The project manager is where all the calculation conditions may be defined and the post-calculation results analysis may be controlled. Other windows allow us to see the progress of a calculation, including any errors which have occurred, view and export results, and view the convergence obtained during the meshing procedure.

The basic HFSS procedure is to create or import a structure, apply material properties to this structure, set calculation conditions, start the calculation and then view and export data once the calculation is finished.

4.1.2 Calculating the scattering and emission of forest multilayer structures using a numerical FEM approach

In the approach developed during this thesis, the soil and litter layers are represented as homogeneous dielectrics with randomly rough surfaces. It is also possible to extend the approach to include heterogeneous features of the two layers, such as permittivity gradients and inclusions (buried rocks or stones), but as a first step the soil and litter layers are considered to be effective media with homogeneous permittivity constants. The electric field scattered off such a structure is calculated using the Finite Element Method, by use of Ansoft's HFSS software.

The approach developed during this thesis for calculating the scattering and emission of multi-layer forest structures with rough surfaces follows the usual HFSS procedure with some developments, and involves the following stages:

1. Creating the required rough surface(s)
2. Building graphically the structure to be studied using one or more of the rough surfaces and then exporting it into a HFSS project
3. Adding extra features to the structure with HFSS, if necessary, including inclusions, temperature and moisture gradients
4. Applying calculation conditions including
 - boundary conditions
 - incident beam set up
 - optimetrics: a "sweep" different values for a given variable
 - convergence conditions necessary for the meshing procedure
 - the far field sphere on which the scattered electric field will be calculated
5. Running calculations and post-calculation results analysis

6. Exporting the calculated scattered electric field
7. Repeating all the previous stages for N different surfaces, creating N different HFSS projects and exporting N sets of results of the scattered electric field

These different stages, and the software tools used at each stage, are shown in Figure 4.1.

We present each of stage in depth in sections 4.1.2.1 to 4.1.2.3.

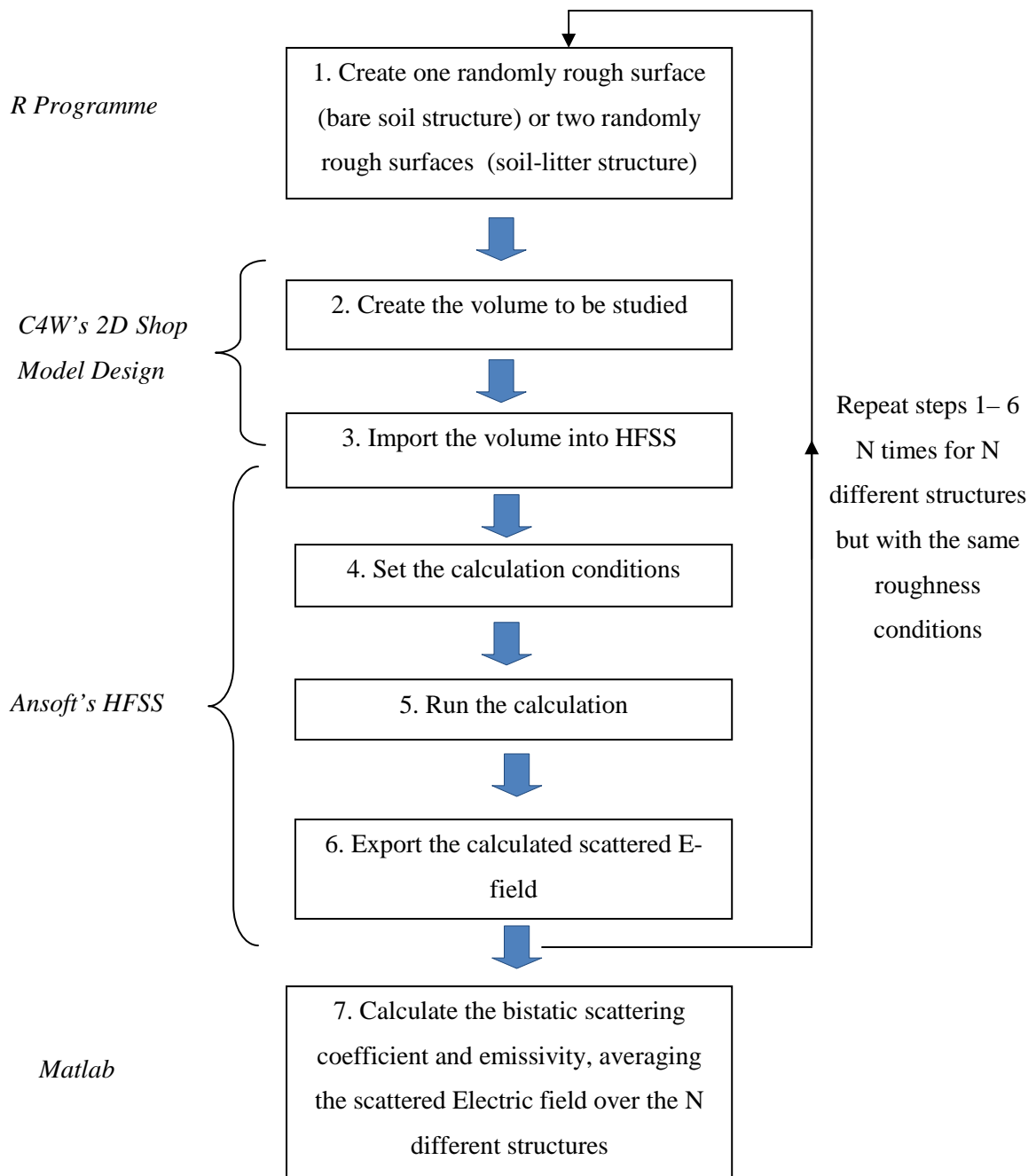


Figure 4.1: The different stages in the numerical FEM approach developed to calculate the scattering and emission of the soil-litter structure. The different programmes used for each stage are shown on the left.

4.1.2.1 Building the structure

HFSS possesses a powerful 3D graphics design tool that allows the user to build many different and complicated structures. However for this thesis we wished to create randomly rough surfaces of specific autocorrelation functions and values of σ and L_c , and this was not possible with HFSS' graphics tool. Therefore we developed a procedure for creating the desired structures elsewhere and importing them into HFSS.

A 3-dimensional layer with a rough surface is introduced into HFSS's calculation area by the following procedure. Randomly rough surfaces are generated in the form of $\{x,y,z\}$ points using the "R" statistical software©, employing in particular the "Random Fields" package. These rough surfaces have gaussian random distribution, standard deviation of surface heights, σ , and autocorrelation functions of the following form:

$$g(r) = \exp \left[- \left(\frac{\sqrt{x^2 + y^2}}{L_c} \right)^n \right] \quad (4.1)$$

L_c is the autocorrelation length and the value of n determines the form of autocorrelation function: for the special cases of exponential and gaussian autocorrelation functions it is equal to 1 and 2 respectively.

The distance between the points, known as the surface's "resolution", was set to 1cm for the work of this thesis. The size of the surface, $L \times L$, must be carefully chosen. This will be broached in the next section.

It is also possible to introduce roughness profiles measured experimentally. The rough surfaces, either those created using the statistical software, or real profiles measured experimentally, are then transformed into 3-dimensional layers: C4W's "3D Shop Model Design" © software (a graphics design tool) is used to create solid slabs out of the rough surfaces.

Figure 4.2 shows the procedure for creating volumes from the rough surfaces and then importing them into HFSS. There are three variants of the procedure, shown in columns a), b) and c). If we wish to study the rough surface only, using C4W's 3D shop model design software, we can create a volume above the rough surface, representing a vacuum. This is shown in column a) of Figure 4.2. If we wish to study the soil volume, including heterogeneities in the soil (added later in HFSS), we can create a volume below the rough surface to represent the soil, as shown in column b) of Figure 4.2. This can then be capped by a vacuum above the rough surface, by creating and importing the structure shown in column a). A multilayer structure can also be built by importing each different layer using one of the procedures shown in columns a), b) or c) as appropriate. Column c) shows the importation of a

“middle layer” in a multilayer structure: a volume with rough surfaces below and above it. In the following chapters of this thesis we concentrated only on a single homogeneous layer with a rough surface, the surface case, and so applied the procedure shown in column a).

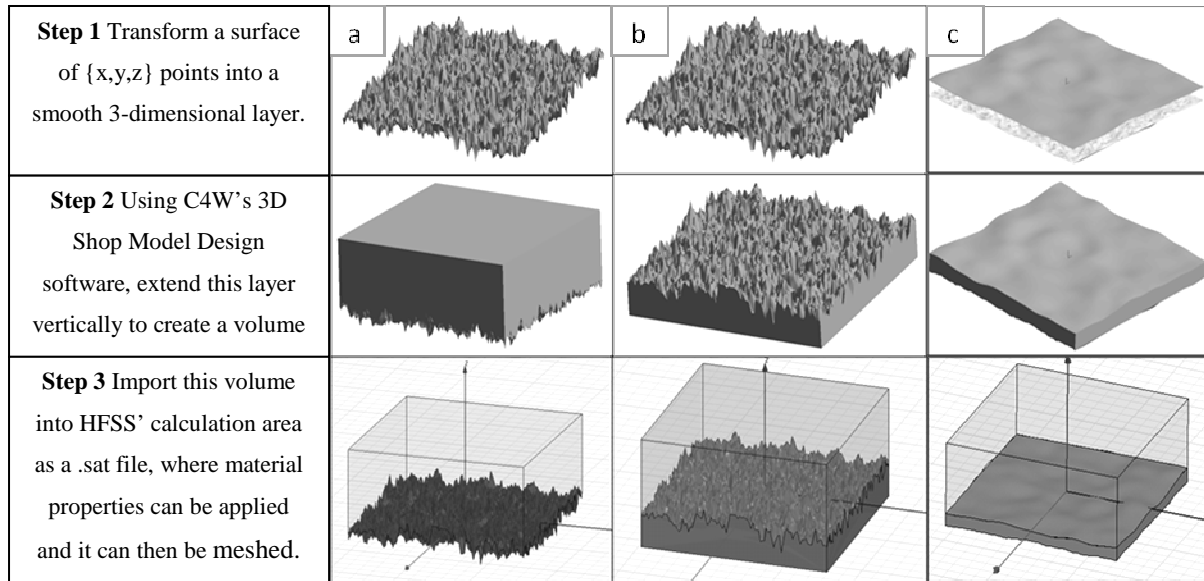


Figure 4.2: Procedure for creating a 3D structure with a rough surface. The three right-hand columns show the 3 procedures which can be adopted.

This stage of creating a volume in “3D Shop Model Design” is important because HFSS cannot perform a calculation on a surface alone. Creating such volumes proved difficult and in order to do so a powerful graphics tool was required, such as C4W's 3D Shop Model design.

Once a structure has been exported into HFSS it is possible to use HFSS' graphics tool to build some of the heterogeneous features that can be found in the soil and litter layers. For example HFSS allows us to easily build regular structures such as spheres, cubes, cylinders, spheroids etc. HFSS also allows us to apply different actions to the objects in the calculation area, such as subtracting one object from another, splitting objects and joining objects together. We can use these tools to create the heterogeneous features, for example rocks and stones found in the ground can be represented using spheroids, distributed either homogeneously or in-homogeneously below the soil-air rough surface, within the volume representing the soil. Furthermore it is possible to apply a temperature and/or soil moisture gradient to the structure in HFSS. During this PhD, calculations were not performed with these heterogeneous features, but it would be of interest to test and develop these features in future work.

4.1.2.2 HFSS Simulations

Once the structure has been built we must set up and run the calculation. We wish to calculate the resulting scattered electric field when a wave is reflected off the structure. From this we can calculate both the bistatic scattering coefficient and the emissivity. Figure 4.3 shows the set up we require. Note that we wish to calculate the scattered electric field in the far field zone on the hemisphere above the surface of the structure.

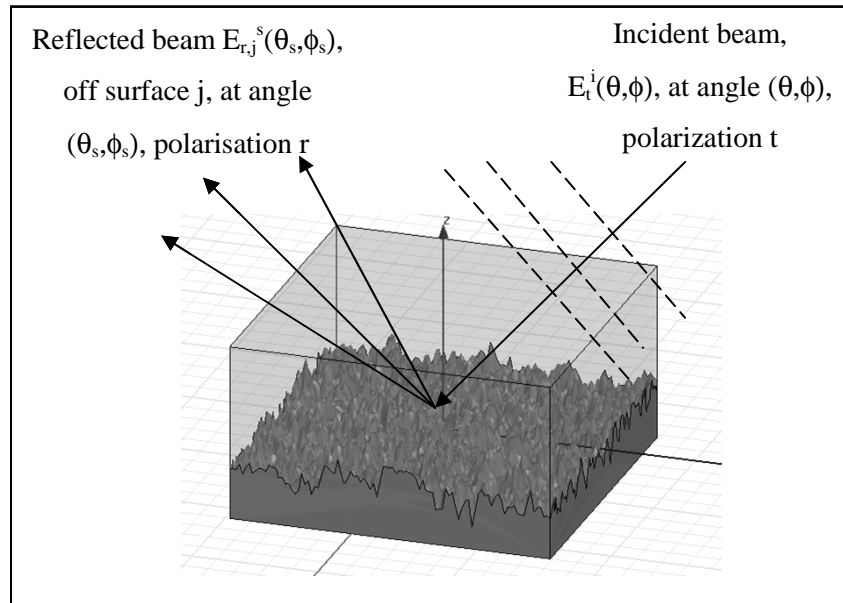


Figure 4.3: HFSS calculation setup

In order to set up this type of calculation, we must apply material properties and boundary conditions to the structure, set up the incident beam and define the calculation conditions including the frequency of the beam and the convergence conditions associated with the meshing procedure.

The first step is to apply a permittivity constant (ϵ) to the imported layer. We apply the vacuum permittivity to volumes representing a vacuum and the soil permittivity to volumes representing the soil. The soil permittivity can be calculated from models such as the models developed by Dobson et al (1985) or Mironov et al (2004) or measured directly from soil samples taken in the field. The litter dielectric permittivity constant can also be calculated or measured. Possible models for calculating this value include dielectric mixing models such as the one developed by Schwank et al (2008) or Della Vecchia et al (2007).

The next stages are described in the sections a) to e).

a) Boundary Conditions

Before performing the calculation, boundary conditions must be applied to the boundary faces of the structure. These boundary conditions describe the behaviour of the electromagnetic field at and beyond the boundaries, for example whether it is radiated to infinity, absorbed or reflected. Boundary conditions are necessary in order to obtain a numerical solution. HFSS allows us to apply a number of different boundary conditions; the two used in the work of this thesis are the “radiation condition” and the “layered impedance” condition. The former “radiates” all electromagnetic fields incident on the boundary to infinity. Note that this condition assumes a vacuum inside the boundary and so if applied to the boundary of a non-vacuum surface there will be reflections. The radiation condition is also necessary for the near to far field calculation. The “layered impedance” boundary condition acts as if there is an infinite material on the other side of the boundary. The “starting impedance” is defined by selecting a material for the layered impedance boundary condition. Note that if this is the same as the material on the inside of the boundary the Electromagnetic field is totally absorbed on the boundary. However if a different material is selected there will be reflections. In summary the radiation and layered impedance boundary conditions provide total absorption on the boundaries of the calculation area, the former on boundaries bordering a vacuum and the latter on boundaries bordering materials. The layered impedance boundary can also be used to create a change in permittivity at the boundary, as in the calculations performed for the work of this thesis.

In our calculations, a layered impedance boundary condition was applied below the structure to simulate an infinitely deep lower layer. At the top and sides of the calculation area radiation boundary conditions were applied in order to prevent reflections, as well as to provide “virtual surfaces” for the near to far field calculation.

b) Incident wave

For our calculations we required a continuous polarized incident wave, at an incident angle θ in the range of 0° to 90° , azimuth angle $\phi=0$, and polarization H or V.

The incident wave(s) are set under the “excitation” section in the project manager. Possible incident waves include a plane wave and a gaussian beam. The plane wave is the natural choice for satellite radar and radiometer applications. However a gaussian beam allows us to avoid errors due to “edge effects” (see section 3.1.3.1c)). Unfortunately the HFSS software does not allow us to vary the equations of the wave so we cannot apply the Thorsos taper (described in section 3.1.3.1c)) for this. The Gaussian beam has the form:

$$E_{q_i}^i = \exp \left[- \frac{(x - x_{\text{centre}})^2 \cos^2 \theta + (y - y_{\text{centre}})^2}{g^2} \right], \quad (4.2)$$

where (x,y) is a point on the surface, $(x_{\text{centre}},y_{\text{centre}})$ is the centre of the surface and g is a measure of the beam width.

The type of wave must be carefully chosen as well as the value of g for a Gaussian beam. This is explained in detail in the next section.

The incident angle of the beam, its polarisation (H or V), and, in the case of the gaussian beam, the value of g must all be defined.

HFSS can calculate the electromagnetic field resulting from a number of different incident angles in one calculation. This can be done in two different ways. A sweep of the angle can be included in the the wave setup, with a starting point, an ending point and a homogeneous step, for example 0, 30, 60°. Alternatively a number of different incident beams can be set up, each with a different angle. In the first case the disadvantage is that, in our experience, for complicated structures HFSS is sometimes unable to perform mesh operations with this kind of setup or is likely to take longer setting up such a calculation. In the second case the disadvantage is that exporting the data takes longer. This is because the results of each angle must be viewed and exported separately and each time a new beam is selected HFSS must recalculate the far field data. In the second case it is also important not to apply too many different waves as HFSS may then be unable to find a solution.

c) Calculation Conditions

HFSS solves Maxwell's equations by dividing the structure in the calculation area into a mesh of small elements or cells, and then solving for each cell, taking into account the boundary conditions. Once a solution has been found the mesh is refined many times, with progressively smaller cells, and a new solution obtained. With each refinement (iteration) the change in the calculated energy value, ΔE , of each solution or the change in the reflection coefficient matrix, ΔS , is obtained. A final solution is obtained by imposing a convergence criterion on ΔE or ΔS .

Before beginning calculations, criteria for a converged solution must therefore be defined, so that HFSS knows when to stop the mesh refining procedure. This includes a value of ΔE or ΔS (the change in energy or the S matrix between passes) which indicates convergence, the maximum number of iterations, the maximum refinement per pass, and the minimum number of converged passes. In all the calculations performed during the work of this thesis the minimum converged passes was set to 2 and a convergence of 0.03 (3%) in ΔE was set. A high maximum number of passes was set (around 20) so that a 3% convergence was always obtained. This allowed us to restrict errors due to the meshing approximation to approximately 3%. A maximum refinement per pass of 10% was also set.

Other calculation conditions that must be defined are the frequency and the order. For the work of this thesis, the frequency was always set to 1.4GHz since the first application of this model is the SMOS mission. However the model can be used for different frequencies as required. It is also possible to perform a frequency sweep with HFSS, where a solution is obtained for a number of different frequencies, but this was not considered in this thesis. However it could be of interest for future work.

The order gives the type of shape functions, used in the FEM calculation and can be equal to 1 or 2. An order of 2 refers to quadratic shape functions and an order of 1 refers to linear shape functions. The order also indicates the number of nodes on a cell: a higher order means more nodes. An order of 2 is more accurate but requires more CPU time and memory. In the latest version of HFSS (v12.1.1) it is possible to set a “mixed order”. This means that HFSS can use different orders on different cells: it chooses order 2 for more complex geometrical areas and order 1 for simpler geometrical areas, thus maintaining the accuracy of order 2 but reducing computational cost. In the results presented in this thesis we chose therefore to use mixed order.

All calculations presented in this thesis were performed on a 64 bit machine with 64GB of available memory.

d) Optimetrics

It is possible to vary the value of certain parameters in one calculation by defining an “optimetric”, a sweep over that parameter. The parameter is defined as a variable, which is given a starting value and then an optimetric of different values for this variable may be defined. The optimetric includes a list of all possible values. HFSS then calculates automatically a solution for each value in the optimetric, recalculating the mesh if necessary. Parameters for which an optimetric may be defined include material permittivities and dimensions of objects in the calculation area, providing changing these does not add any external faces for which boundary conditions are not defined. For the work of this thesis we were able to calculate automatically different values of soil moisture, by setting an optimetric for the soil permittivity. This feature of HFSS will also be useful for the future application of creating the final database.

e) Displaying and Exporting Results

The scattered electric field is calculated inside the area by HFSS. The electric field in the far field region, at a distance R from surface j , $E_{r,j}^s(\theta_s, \phi_s)$ is then extrapolated from this value at the virtual surfaces, a procedure which is described in section 3.1.3.3b1.1, r is the polarization of the scattered field, and θ_s and ϕ_s are the scattering angles. This is done by defining a near field sphere at a distance R from the structure. In defining this sphere we set a ‘step’ for the angles around the sphere, which sets the integration step in the emissivity calculation later on. This value must therefore be chosen to

be small enough so that errors due to discretising the integration process are minimized. This will be addressed in section 4.2. HFSS then performs a near to far field calculation from the virtual surfaces to the sphere. The value of R was set to 50m for smaller surfaces ($L=6\lambda$) and 100m for larger surfaces ($L>6\lambda$), both of which are in the Fraunhofer far field region according to the condition (2.50).

Results of the scattered electric field in the far field sphere may be viewed in HFSS as a table. These results may then be exported as .txt files.

4.1.2.3 Analysing Results calculated by HFSS

The HFSS calculation procedure described in the previous section is repeated for structures with N different rough surfaces with the same autocorrelation functions and values of σ and L_c . This gives us N HFSS projects and N sets of results of $E_{p,j}^s(\theta_s, \phi_s)$ at all angles (θ_s, ϕ_s) in the hemisphere above the rough surface. We then calculate the bistatic scattering coefficient, for incident polarization p and reflected polarization q, σ_{pq}^0 , from the reflected electric field averaged over all N surfaces. This averaging process is done in order to approach the value that would be obtained for the case of an infinitely large rough surface. The bistatic scattering coefficient is calculated from the following:

$$\sigma_{pq}^0(\theta_s, \phi_s; \theta, \phi) = \frac{4\pi R^2}{A_{\text{eff}} |E_q^i(\theta, \phi)|^2} \frac{1}{N} \sum_{j=1}^N |E_{p,j}^s(\theta_s, \phi_s)|^2 \quad (4.3)$$

where (θ, ϕ) is the angle of the incident wave, (θ_s, ϕ_s) is the angle of the reflected wave, N is the number of surfaces to be averaged over, A_{eff} is the effective area of the surface illuminated and E_q^i is the incident electric field with polarization q. For a gaussian incident beam the effective area is given by $A_{\text{eff}} = \pi g^2 / (2\cos\theta)$ and in the case of a plane wave it is simply the total area of the surface illuminated.

The bistatic scattering coefficient calculated by (4.3) contains both coherent and non-coherent components. The non-coherent component can be isolated from (3.23). The values of g and N in this equation must be carefully chosen: this will be discussed further in section 4.2. The backscattering coefficient is the bistatic scattering coefficient for the monostatic case of $(\theta_s, \phi_s) = (\theta, \phi + \pi)$ i.e. the reflection angle is equal to the incident angle. The emissivity of the surface measured at polarization p, $e_p(\theta, \phi)$ can be calculated by integrating the bistatic scattering coefficient over half space (Peake 1959), as follows. The emissivity is calculated from the reflectivity $\Gamma_p(\theta, \phi)$ using (2.83) and the reflectivity is in turn calculated from the bistatic scattering coefficient by the following:

$$\Gamma_p(\theta, \phi) = \frac{1}{4\pi} \iint_{\text{upper hemisphere}} \frac{1}{\cos\theta} \left[\sigma_{pp}^0(\theta_s, \phi_s; \theta, \phi) + \sigma_{pq}^0(\theta_s, \phi_s; \theta, \phi) \right] \sin\theta_s d\theta_s d\phi_s \quad (4.4)$$

Thus we integrate the bistatic scattering coefficient over θ_s and ϕ_s . We approximate this integral to a sum over θ_s and ϕ_s as follows:

$$\Gamma_p(\theta, \phi) = \frac{1}{4\pi} \sum_{\phi_s=0}^{\pi} \sum_{\theta_s=-\pi/2}^{\pi/2} \frac{1}{\cos\theta} \left[\sigma_{pp}^0(\theta_s, \phi_s; \theta, \phi) + \sigma_{pq}^0(\theta_s, \phi_s; \theta, \phi) \right] \sin\theta_s \Delta\theta_s \Delta\phi_s. \quad (4.5)$$

where $\Delta\theta_s$ and $\Delta\phi_s$ are the integration steps in θ_s and ϕ_s respectively. To simplify things we chose values so that $\Delta\theta_s = \Delta\phi_s = s$. (4.5) is an approximation to (4.4) that approaches (4.4) as the integration step s approaches zero. If the integration step is not small enough we could introduce errors into the emissivity calculation due to this approximation. The integration step must be carefully chosen to be small enough to prevent this: this is discussed in section 4.2.

4.1.3 Note

In this thesis we have developed a procedure to calculate the scattering and emission of multilayer forest structures with rough surfaces, as presented in the previous sections. For the work of this thesis we represent the soil and litter layers as homogeneous dielectrics but it is worth noting that heterogeneous features can also be modelled using this approach. For example, as mentioned in section 4.1.2.1, we can create structures which include temperature and soil moisture (permittivity) gradients with this approach. This will have future applications such as modelling the emission of structures with extreme temperature gradients like permafrost. Also the optimetrics feature, which allows us to vary parameters in a single calculation, was used to some extent in this PhD but it will be of great use when creating the database of the soil-litter emission, the first application of the model.

4.2 A sensitivity analysis to set model parameters

In the previous section we identified a number of model parameters that must be carefully chosen before we apply our numerical modelling approach. In order to do this, a model sensitivity analysis was performed and is presented in this section. The objective of this study was to find the value for each parameter that maximises the accuracy of the calculated emissivity for the whole range of conditions for the soil and litter layers that are found in the environment, and also for all SMOS measurement conditions, which includes angles from 0° to 50° and polarisations H and V. We also aimed to evaluate the effect of each model parameter on the calculation cost. This would allow us to verify that the values selected for the model parameters are not too costly in calculation time and memory for the required application. A secondary objective was to optimise the model, by identifying

values for parameters that have a lower associated calculation cost but produce equally accurate results.

We focused this study on parameters that are considered in the literature to most influence results of rough surface scattering (see section 3.1.3.1), and also parameters that were found to most influence results during the course of this PhD.

In the next sections, we present first the model parameters whose values we aimed to determine, and the conditions for which these values must be valid. Secondly we present the sensitivity analysis of each parameter, including method, results and discussion. Lastly we summarise the conclusions of this study, and identify values of parameters that will be used for the work of this thesis.

4.2.1 Model Parameters and calculation conditions

The model parameters whose values we aimed to determine in this study were:

1. The number of simulations performed for each rough surface, corresponding to the number of rough surfaces, N , over which we average the scattered electric field in order to obtain the bistatic scattering coefficient and the emissivity.
2. The step in the angles θ_s and ϕ_s at which the scattered electric field is calculated. This sets the step in the angles for the bistatic scattering coefficient, and is the integration step for the emissivity calculation. It is defined as the step in the θ_s and ϕ_s of the sphere for the near to far field calculation (see section 4.1.2.2e). We shall call this step s .
3. The type of incident beam
4. The size of each rough surface: $L \times L$

When modelling the scattering and emission of a rough surface using a numerical approach, we approximate a surface of infinite size to N surfaces of $L \times L$ size, as explained in section 3.1.3.1b. We must therefore determine a minimum value of N for which this approximation is valid. We must also determine the minimum value of L for which this is valid since if we perform calculations for surfaces that are too small we lose information of the long range interactions between surface points. In addition L must be large compared to the wavelength so that the surface can be considered macroscopic in its interaction with the incident beam. L must also be large compared to L_c so that the rough surface accurately represents a surface of the same roughness and infinite size. Thus the value of L must also be determined to be large enough so that we do not lose important long range interactions, the surface may be considered macroscopic, and the surface roughness of each surface is representative of the whole. Note that larger values of N and L have larger calculation costs so we cannot simply choose very high numbers. We must also determine how the values of N and L

influence the calculation costs, so that we do not choose values that have unreasonably high calculation time and memory requirements.

We chose N to range up to a high number and s down to a low number because the higher the number of surfaces the more accurate the results and the lower the integration step the more accurate the results. However it takes longer to calculate higher values of N since we require more simulations, and lower values of s require more time for the near-to far field calculations. We arbitrarily chose the values of $N=100$ for high N and $s=0.2^\circ$ for low s . We expect the results to indicate whether $N=100$ is sufficiently high and if $s=0.2^\circ$ is sufficiently low, after which we can adjust these values by performing more calculations and/or reducing the value of s below 0.2° if necessary.

For the incident beam we tested both the plane incident beam and a tapered wave. The former is the natural choice for radar and radiometer applications since the electromagnetic waves measured in the field may be considered to be plane. However with the case of finite surface size a tapered beam may be desirable in order to reduce errors due to edge effects, as discussed in section 3.1.3.1c. For the tapered beam, we chose a gaussian beam of the form of (4.2) since this is the only tapered beam option available in HFSS. For this gaussian beam, the beamwidth, g , must also be determined. We therefore tested values in the range of $g=0.1L$ to $g=0.25L$ since it has been suggested in the literature that values of g should be chosen in this range, depending on incident angle (e.g. Tsang et al 2001, Marchand and Brown 1999). In general the size of the surface is considered to be sufficient at a value of 10λ . We therefore decided to test surface sizes around this value, ranging from 12λ just above this value to 6λ just below.

The values that were considered for these parameters are summarised in Table I.

Table 4-I: Possible values for the model parameters

Parameter	Range of values
N	2 – 100 surfaces
Integration step, s	0.2, 0.5, 1 degrees
Incident beam	Plane, Gaussian $g=0.1L - 0.25L$
L	$6\lambda - 12\lambda$ (1.27m – 2.55m)

We require the chosen values for the model parameters to be valid for all conditions that we may wish to model, i.e. all conditions found in the field and for all conditions used in experimental radiometry, including all:

1. Roughness conditions: different values of the standard deviation of surface heights, σ and the autocorrelation length, L_c

2. Soil moisture conditions (dielectric permittivities of the layer with the rough surface)
3. Incident beam angles
4. Polarisation

We also require them to be valid for all possible values of the other model parameters.

We selected roughness values for σ and L_c varying between the extremes of values found in the field. Soil moisture found in the field tends to vary between approximately 5% and 50% for a saturated soil. We therefore selected 5% for the lowest value. However we selected 30% for the highest value since this corresponds to a very wet conditions and the soil permittivity does not greatly change above this value. The angle range was chosen to be that of SMOS ($\theta=0 - 50^\circ$), which also covers the usual range of radiometry measurements, the azimuth angle fixed at 0° ($\phi=0^\circ$), and both polarisations were tested.

Note that we only consider the case of a single rough surface in this study. In general we expect the parameters chosen to still be valid for multilayer structures. However further work may be required to verify the validity of some of the selected values for parameters, in the presence of multilayers and heterogeneous features (inclusions, soil moisture gradients), before the model is used to generate results for such structures.

In all calculations performed in this study, surface resolution, the distance between surface points, was chosen to be 1cm. Values in the literature that have been used in MoM emissivity studies range from approximately 0.5cm (e.g. Huang et al 2010) to 1.3cm (Zhou et al 2004). Thus we chose a value that falls within this range. However it would be of interest in future work to test the effect of this parameter on the accuracy of the results. The autocorrelation function of the rough surfaces was chosen to be exponential, since in reality rough surfaces have autocorrelation functions closer to exponential than gaussian functions. For the calculations in this study, permittivity values were calculated for a given soil moisture using the Mironov model for a soil with a clay content of 16.6% and sand content of 83.4%, as found in the field on the SMOSREX experimental site (see de Rosnay et al 2006, as well as chapter 6 of this thesis, for details of this site).

Table 4-II summarises the range of calculation conditions considered in this study.

Table 4-II: range of possible values for the calculation conditions

Condition	Range of values
σ	0.44 - 4 cm
L_c	3 – 9cm
Angle, θ	0 – 50°
Polarisation	H, V
Soil Moisture	5 – 30%

In performing this study we also consider the CPU time and memory requirements and how these depend on the values of the model parameters. The aim of this study is to evaluate the effect of each parameter on the accuracy of the results and also on the calculation costs so that we can select values that are accurate but not too costly in calculation time and memory. In the case that this involves a compromise between accuracy and calculation time we wish to evaluate this compromise.

The range of calculation conditions shown in table II presents the range over which the parameters chosen must be valid. However, it was not always necessary to test the entire range for all the conditions, in order to obtain this validity. Wherever possible we aimed to test the worst case scenario. For example if we wished to find the minimum value of N necessary to produce accurate results we tested only calculation conditions that would require the highest value of N, and so forth.

The specific conditions tested for each parameter are presented in the following sections. In all cases we considered the impact of the parameters on the emissivity and in some cases the impact on the bistatic scattering coefficient and backscattering coefficient. We considered the scattering case because although the application of the modelling approach developed is the emissivity we compare calculations of the surface scattering when we validate the model (as presented in section 5.2).

4.2.2 Method and Results

4.2.2.1 Number of Rough Surfaces

Firstly we considered the emissivity e_N and bistatic scattering coefficient σ_N of a rough surface as a function of the number of surfaces, N, over which the scattered electric field is calculated. As we average the scattered electric field over an increasing number of surfaces we expect σ_N and e_N to converge to a solution, namely the value that would be obtained for a rough surface of infinite size, or $e_{N=\infty}$ and $\sigma_{N=\infty}$. In this study we wish to evaluate the effect of N on the calculated emissivity, bistatic scattering coefficient and backscattering coefficient. We wish to observe the expected convergence with N so that later when we apply our numerical approach we can select a value of N such that

averaging over a higher number of surfaces has little effect on the results. Furthermore we wish this value to be valid for all possible calculation conditions shown in table II and all possible values of the other model parameters, shown in table I.

For the determination of this parameter, we chose to investigate only the smallest surfaces, with a size of 6λ , since we expect larger surfaces to require less averaging. We also considered only an incident gaussian beam of the smallest beamwidth $g=0.1L$. This is because this wave illuminates the smallest area of the surface and so we expect to have to average over the highest number of surfaces with this beam. Thus a value of N that is large enough for surfaces with a size of 6λ and incident beam of $g=0.1L$ will be large enough for larger surfaces and all other incident beams and we need only test these conditions. We considered surfaces of two different roughnesses:

1. $\sigma=4\text{cm}$, $L_c=3\text{cm}$
2. $\sigma=0.44\text{cm}$, $L_c=9\text{cm}$

These represent the extreme cases of very rough and very smooth (though still rough) surfaces that can be found experimentally (e.g. Wigneron et al 2010 and Mialon et al 2008).

For the rougher surface (surface 1 above) we considered only H polarisation and a value of 30% for soil moisture. We do not expect polarisation to have an effect on the number of surfaces required so we expect to find the same value for H and V polarisation. Also, if the soil moisture is high this means that the rough surface has the greatest effect on scattering since there is the largest difference in permittivity on the air-to-soil boundary. In this case the scattering profiles of each of the surfaces should vary more and we expect to have to average over a greater number of surfaces. However we performed calculations at both V and H polarisation and for both 5% and 30% soil moisture for the smoother surface (surface 2 above), to check this hypothesis.

We also used an integration step s of 1 degree since this requires the least amount of calculation time. The permittivity values were calculated using the Mironov model, to be $\epsilon_r=17.03+1.96i$ for a soil moisture of 30% and $\epsilon_r=3.54+0.24i$ for a soil moisture of 5%. These permittivity values were used throughout this study for soil moistures of 5% and 30%.

Figure 4.4 and Figure 4.5 show the results of the bistatic scattering coefficient as a function of scattering angle, for different values of N . We present results at H polarisation and for a soil moisture of 30% but results were very similar for a soil moisture of 5% and V polarisation. Figure 4.6 - Figure 4.11 show the results of the backscattering coefficient and the emissivity as a function of the number

of surfaces, N , for different angles and polarisations and for different values of surface roughness and soil moisture.

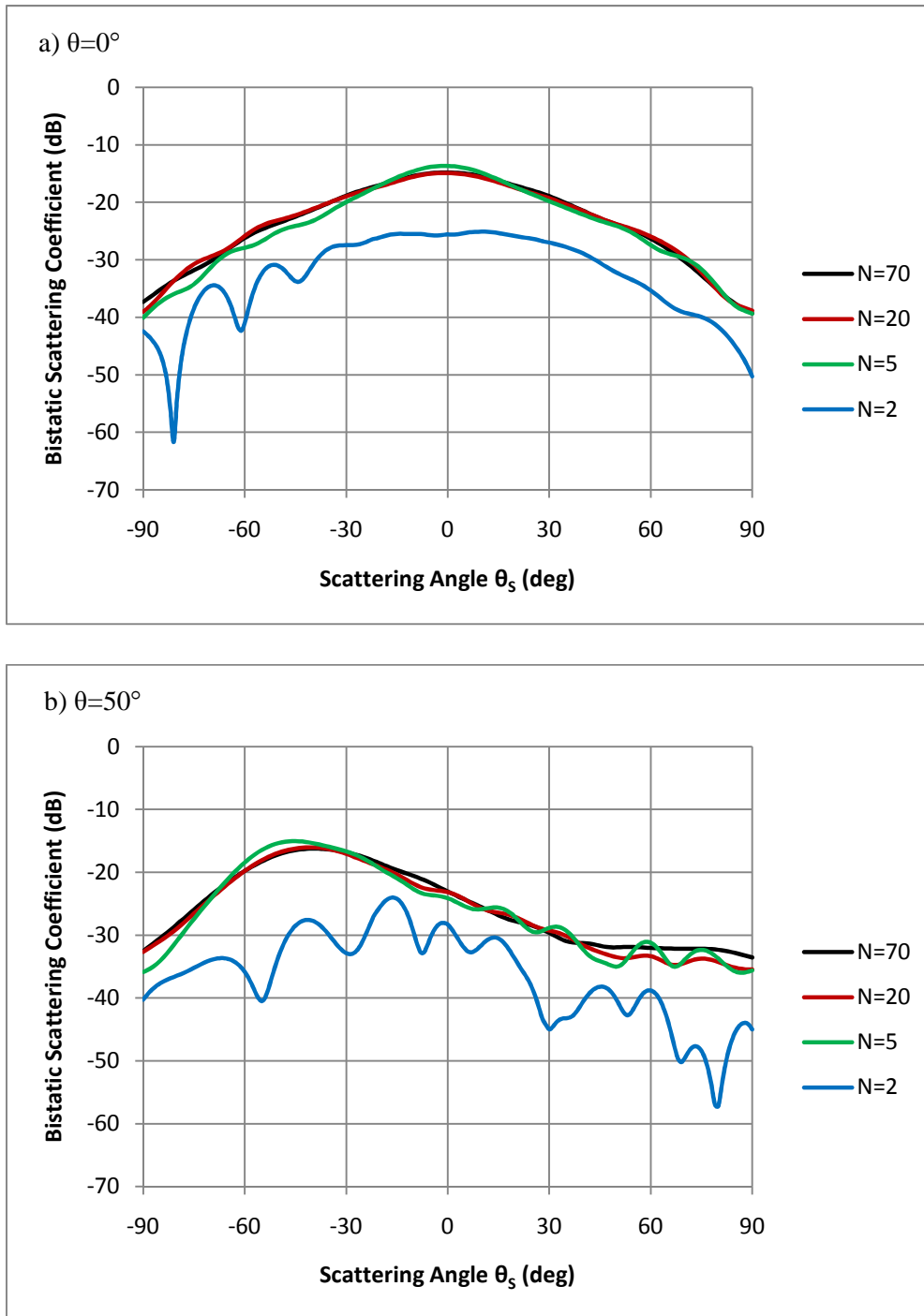


Figure 4.4: Bistatic scattering coefficient (dB) as a function of scattering angle for the smoother surface of $\sigma=0.44\text{cm}$, $L_c=9\text{cm}$, soil moisture of 30% and H polarisation. Results are shown for different values of N and for incident angles of a) $\theta=0^\circ$ and b) $\theta=50^\circ$

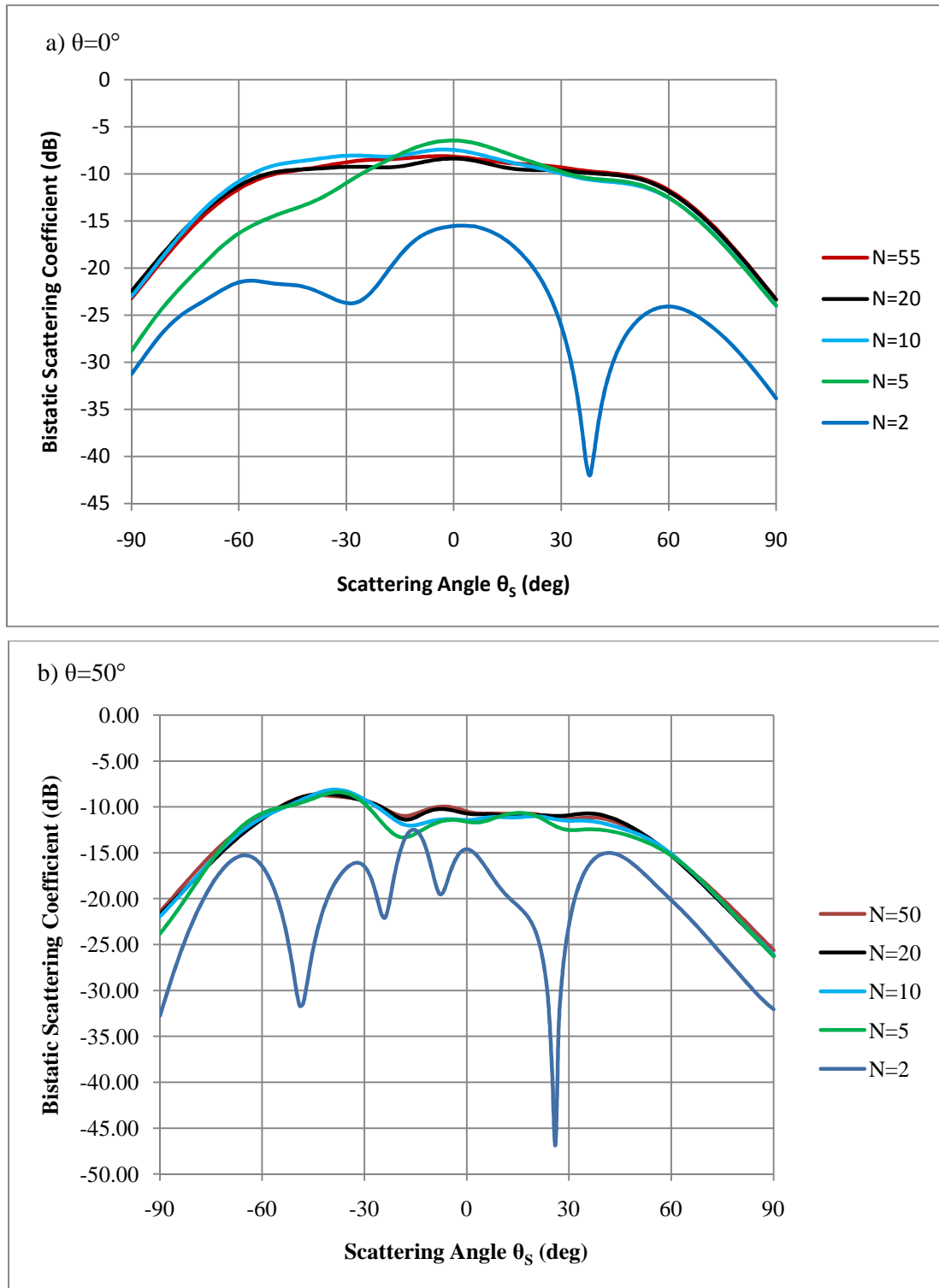


Figure 4.5: Bistatic scattering coefficient (dB) as a function of scattering angle for the rougher surface of $\sigma=4\text{cm}$, $L_c=3\text{cm}$, soil moisture of 30% and H polarisation. Results are shown for different values of N and for incident angles of a) $\theta=0^\circ$ and b) $\theta=50^\circ$

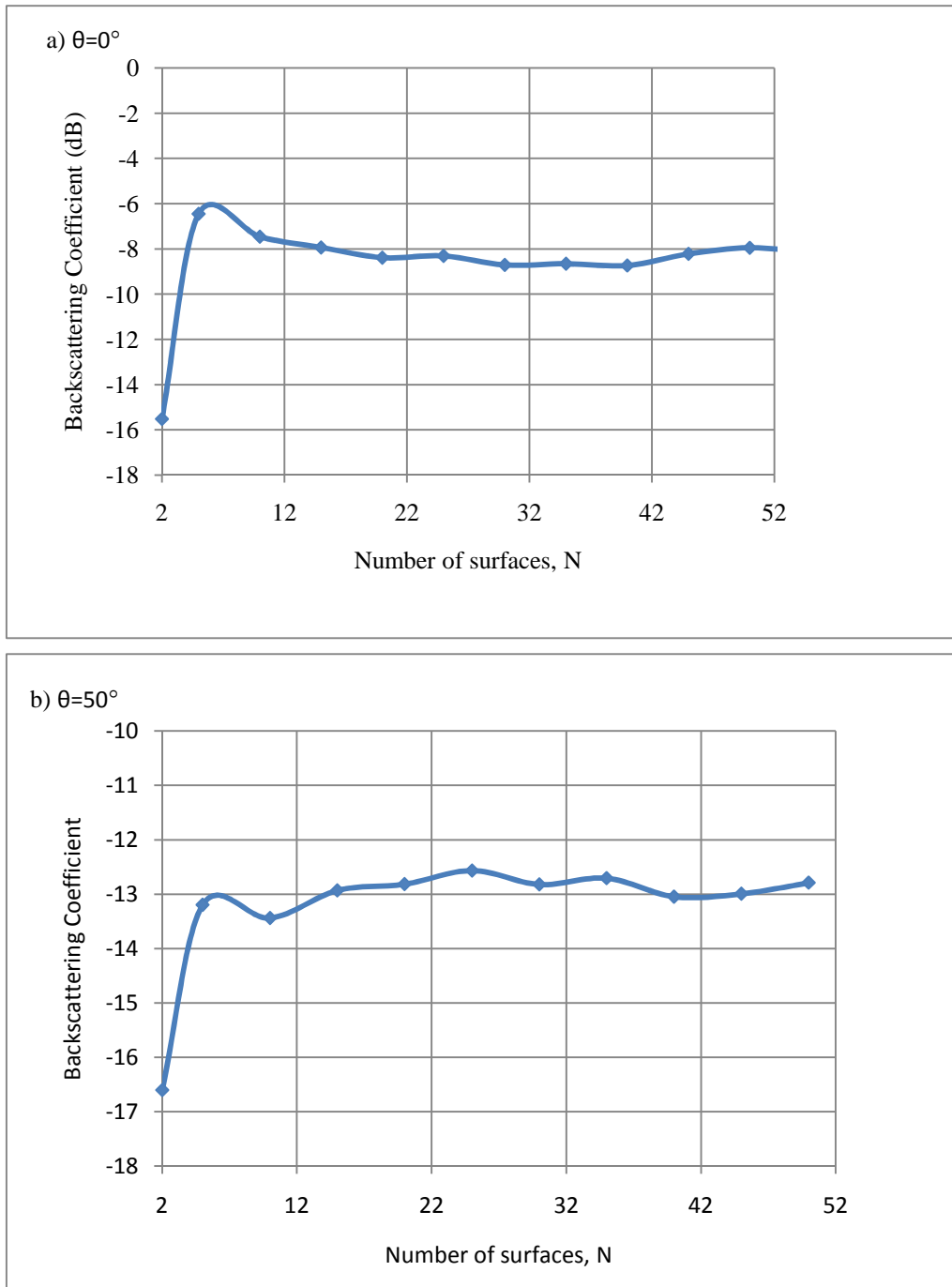


Figure 4.6: The calculated non-coherent backscattering coefficient as a function of the number of surfaces for the rougher surface of exponential autocorrelation function, $\sigma=4\text{cm}$, $L_c=3\text{cm}$ and 30% soil moisture ($\epsilon=17.03+1.96i$) at H polarization and incidence angles of a) $\theta=0^\circ$ and b) $\theta=50^\circ$

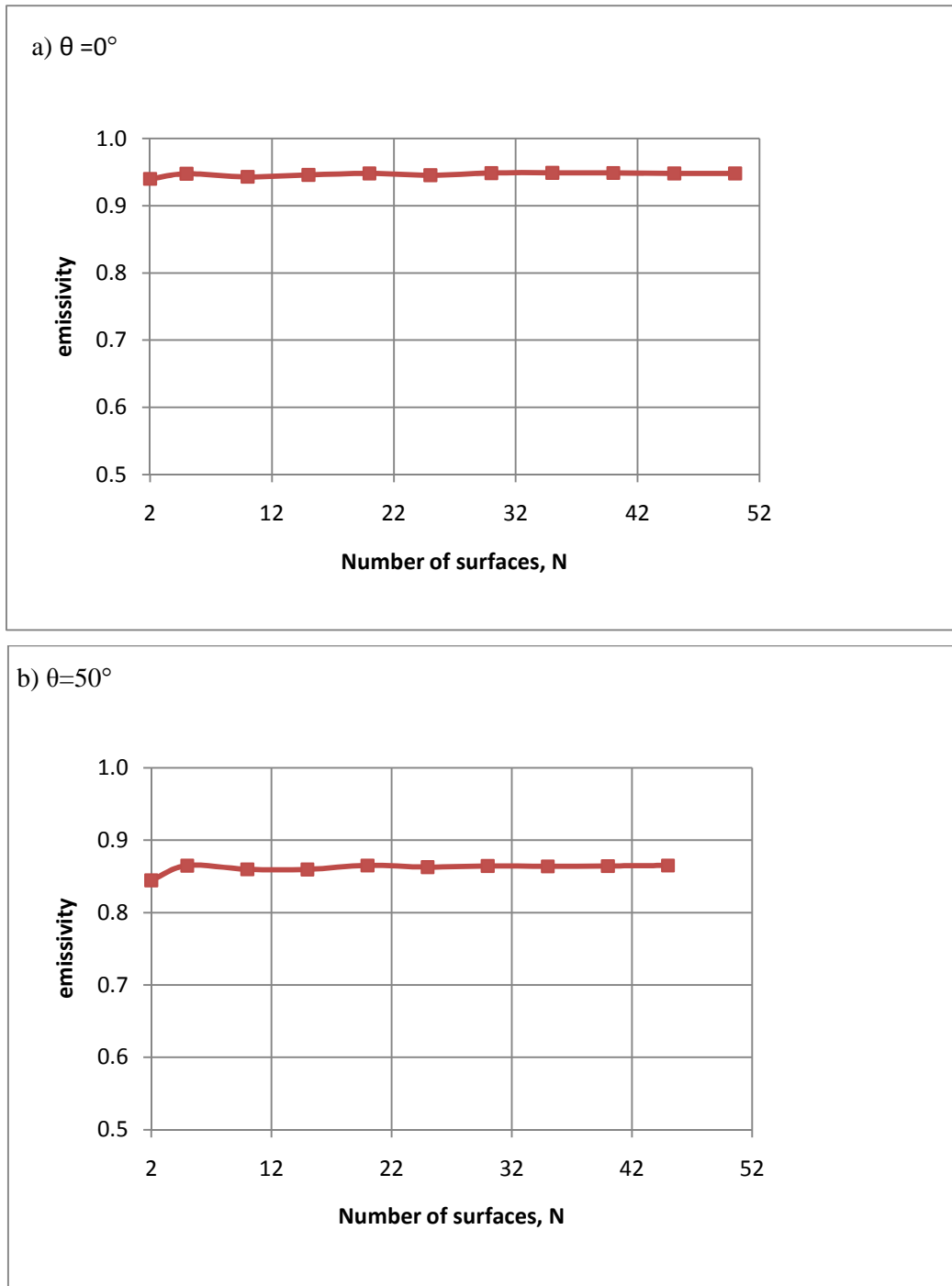


Figure 4.7: The calculated emissivity as a function of the number of surfaces for the rougher surface of exponential autocorrelation function, $\sigma=4\text{cm}$, $L_c=3\text{cm}$ and 30% soil moisture ($\epsilon=17.03+1.96i$) at H polarization and incidence angles of a) $\theta=0^\circ$ and b) $\theta=50^\circ$

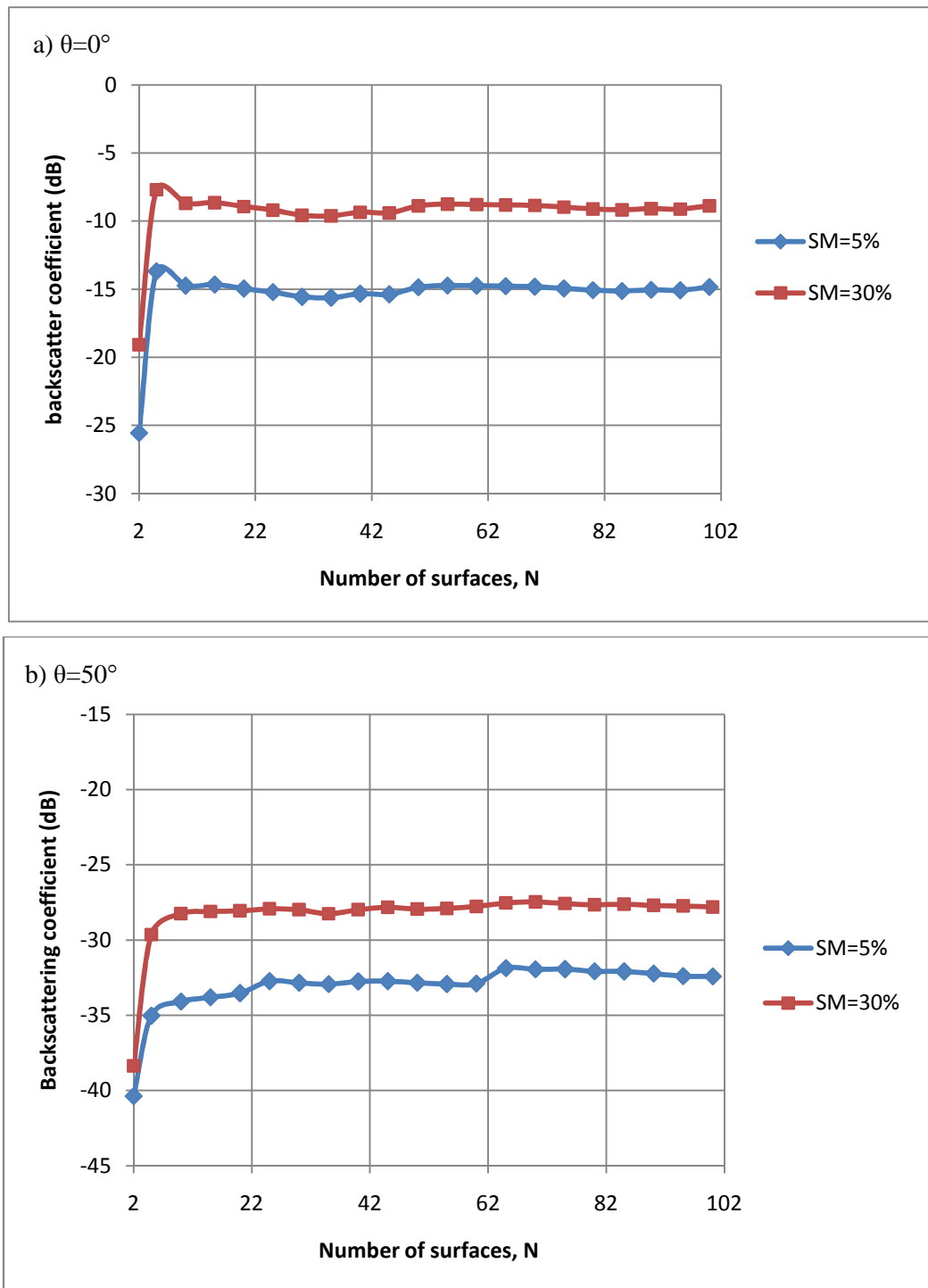


Figure 4.8: The calculated non-coherent backscattering coefficient as a function of the number of surfaces for the smoother surface of exponential autocorrelation function, $\sigma=0.44\text{cm}$, $L_c=9\text{cm}$ at H polarization, 5% and 30% soil moisture, and incidence angles of a) $\theta=0^\circ$ and b) $\theta=50^\circ$

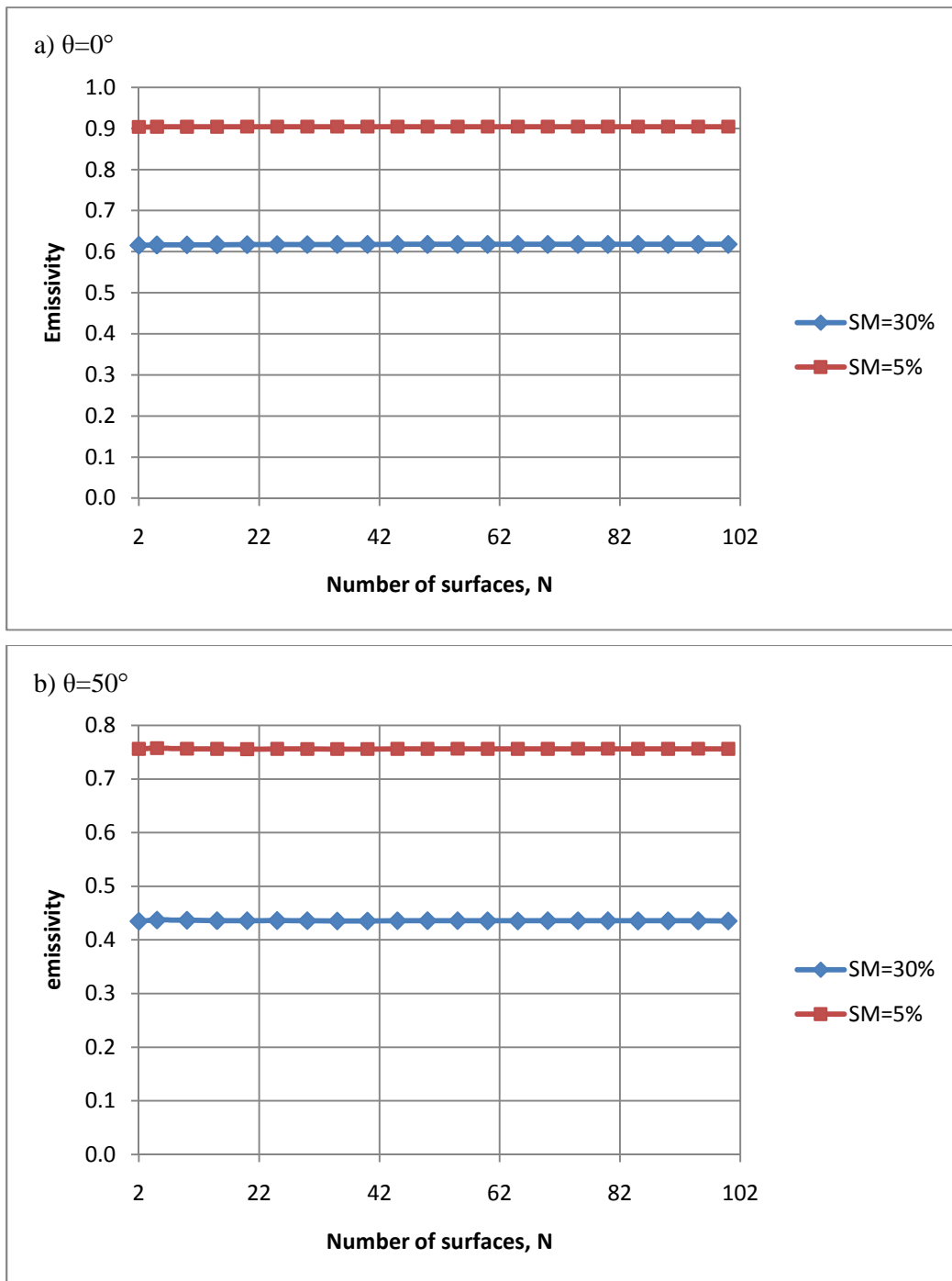


Figure 4.9: The calculated emissivity as a function of the number of surfaces for the smoother surface of exponential autocorrelation function, $\sigma=0.44\text{cm}$, $L_c=9\text{cm}$ at H polarization, 5% and 30% soil moisture, and incidence angles of a) $\theta=0^\circ$ and b) $\theta=50^\circ$

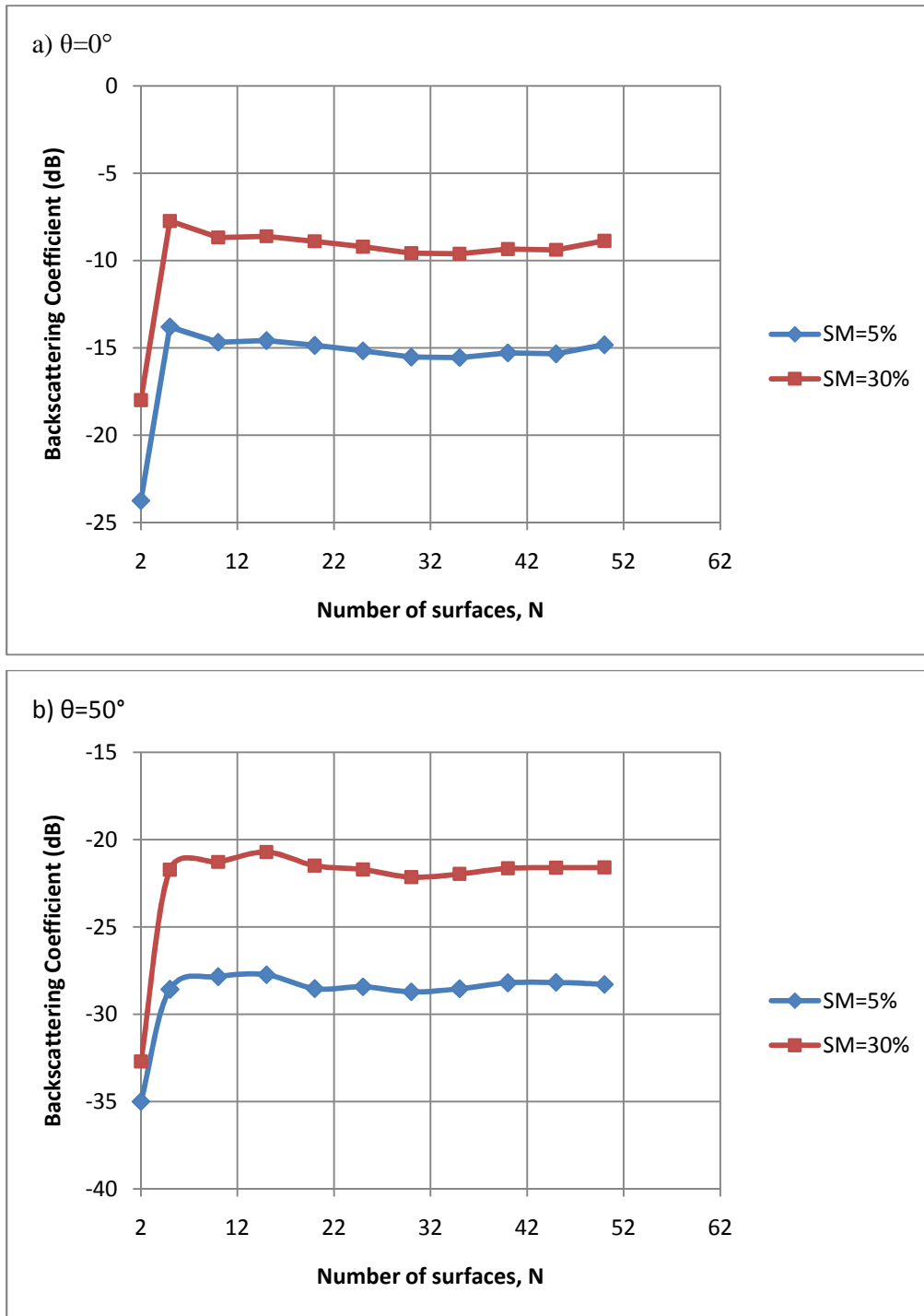


Figure 4.10: The calculated non-coherent backscattering coefficient as a function of the number of surfaces for the smoother surface of exponential autocorrelation function, $\sigma=0.44\text{cm}$, $L_c=9\text{cm}$ at V polarization, 5% and 30% soil moisture, and incidence angles of a) $\theta=0^\circ$ and b) $\theta=50^\circ$

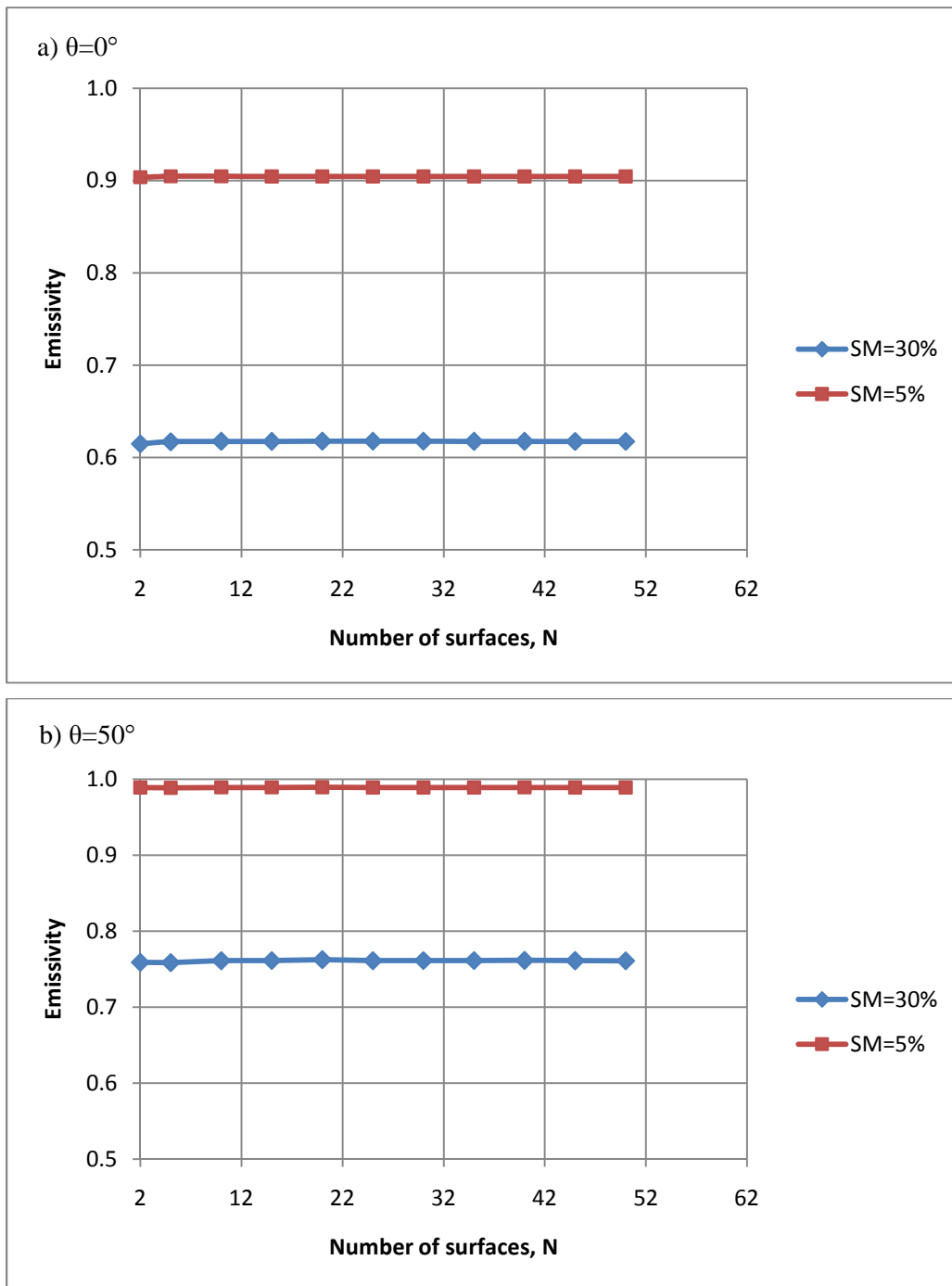


Figure 4.11: The calculated emissivity as a function of the number of surfaces for the smoother surface of exponential autocorrelation function, $\sigma=0.44\text{cm}$, $L_c=9\text{cm}$ at V polarization, 5% and 30% soil moisture, and incidence angles of a) $\theta=0^\circ$ and b) $\theta=50^\circ$

From Figure 4.6 - Figure 4.11 it is clear that the calculated result varies with N much more for the backscattering coefficient and bistatic scattering coefficient than for the emissivity. This is probably due to the fact that in integrating the emissivity any oscillations in the bistatic scattering coefficient are smoothed. In addition we do not measure emissivity in dB, and small oscillations in the absolute value of the bistatic scattering coefficient appear large in dB, when the absolute value is close to zero. These

oscillations have therefore negligible contributions to the emissivity but are significant in the bistatic scattering coefficient and the backscattering coefficient. The backscattering coefficient varies significantly, with a variation of around 10dB, at low values of N but relatively little at higher values, with a variation of no more than about 1dB for $N > 30$ surfaces. We conclude that only a very small number of surfaces are required for emissivity calculations but for the active case we require a higher number in order to avoid introducing large errors. Note that the trends are very similar for both H and V polarizations, and for both values of soil moisture, as expected.

In order to further quantify the variation produced in the results of the backscattering coefficient and emissivity for different values of N, let us first define the values, Δe , and $\Delta \sigma^0$, for the percentage error in the emissivity and backscattering coefficient (of the rougher surface) as a function of N, as:

$$\Delta e(N) = \frac{e_N - e_{N=45}}{e_{N=45}} \quad (4.6)$$

$$\Delta \sigma^0(N) = \frac{\sigma^0_N - \sigma^0_{N=50}}{\sigma^0_{N=50}} \quad (4.7)$$

$N=45$ is the highest value tested for the emissivity of the rougher surface and $N=50$ the highest value tested for the bistatic scattering and backscattering coefficients of the rougher surface. Therefore, in (4.6) and (4.7), we take $e_{N=45}$ to be the exact value of the emissivity and $\sigma^0_{N=50}$ to be the exact value of the backscattering coefficient that would be calculated for a surface of infinite size. This is an approximation but a good one as Figure 4.6 and Figure 4.7 indicate that there is a convergence with N and so we expect the values of e and σ^0 to change little for higher values of N. Note that (4.7) is calculated using linear values of the backscattering coefficients, i.e. not in dB.

Figure 4.12 shows Δe , given in percentage, as a function of the number of surfaces and Figure 4.13 shows $\Delta \sigma^0$ as a function of the number of surfaces, for a rough surface with $\sigma=4\text{cm}$, $L_c=3\text{cm}$, and 30% soil moisture.

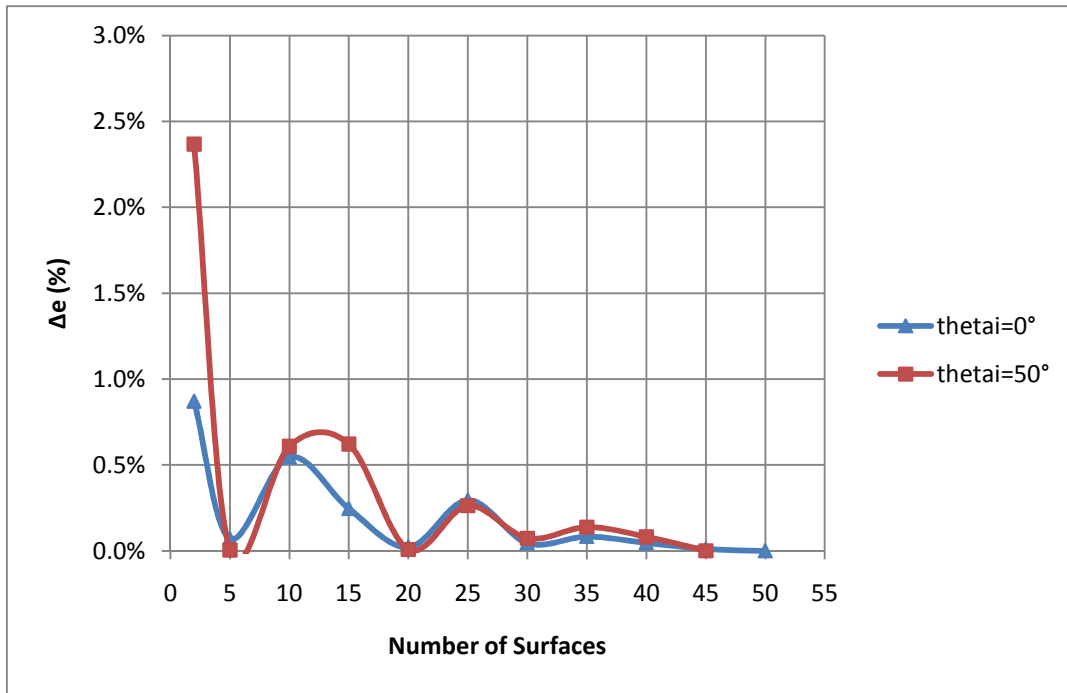


Figure 4.12: Percentage error in the emissivity due to a finite number of surfaces, $\Delta\epsilon$, as a function of the number of surfaces, N , for the rougher surface of exponential autocorrelation function, $\sigma=4\text{cm}$, $L_c=3\text{cm}$ and 30% soil moisture ($\epsilon_r=17.03+1.96i$) at H polarization and incidence angles of 0° and 50°

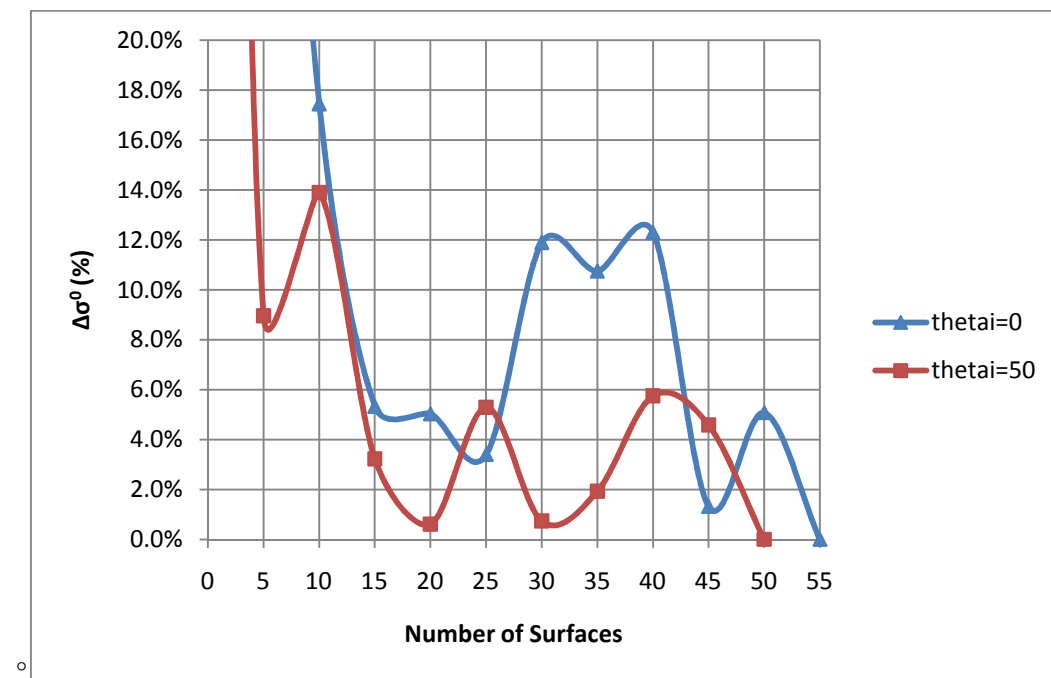


Figure 4.13: Percentage error in the linear value of the backscattering coefficient due to a finite number of surfaces, $\Delta\sigma^0$, as a function of the number of surfaces, N , for the rougher surface of exponential autocorrelation function, $\sigma=4\text{cm}$, $L_c=3\text{cm}$ and 30% soil moisture ($\epsilon_r=17.03+1.96i$) at H polarization and incidence angles of 0° and 50°

We see from Figure 4.12 that for values of $N \geq 5$ surfaces we expect the error in the emissivity due to a finite number of surfaces to be less than 1%. However Figure 4.13 shows that the backscattering coefficient (and thus the bistatic scattering coefficient) has an expected error of less than 10% in its linear value for $N \geq 15$. There seems to be an error of less than about 5% for $N \geq 50$ but we would need to perform further calculations, extending the graph beyond $N=55$, to be sure of this.

We have not performed this analysis for the case of the bistatic scattering coefficient, since the bistatic scattering coefficient also depends on θ_s and so we obtain a more accurate view of the variation of the bistatic scattering coefficient with N from Figure 4.4 and Figure 4.5. These figures show that in general the bistatic scattering coefficient (in dB) changes little for $N \geq 20$ surfaces.

In the following parts of the sensitivity analysis we consider only the emissivity since this is what interests us for SMOS applications, and therefore the purposes of this thesis. This allows us to perform calculations for a lower number of surfaces: we chose to use $N=5$ given that the result changes by less than 1% for a higher number.

However it is worth noting that the model can equally calculate the bistatic scattering coefficient so if in future work the bistatic scattering coefficient were required this analysis would now need to be extended to the active case, by performing calculations for a larger number of surfaces.

4.2.2.2 Integration step, s

For the calculation of the emissivity we approximate the integration of the bistatic scattering coefficient over θ_s and ϕ_s to a summation at discrete intervals of θ_s and ϕ_s . For simplicity we keep the intervals of θ_s and ϕ_s to be the same, and we call this interval the integration step, or s . Since the summation of the bistatic scattering coefficient is only an approximation to the integral there will be an associated error. As the value of s approaches zero this error approaches zero and the calculated emissivity approaches its true value, were a real integration to be used. However it takes longer to perform the near-to-far field transformation for smaller values of s . As with N , we therefore require an integration step which provides a sufficient accuracy (convergence) but does not require too much time for the near to far field calculation.

We performed calculations only for the smoothest surface, with $\sigma=0.44\text{cm}$, $L_c=9\text{cm}$ since smoother surfaces require a smaller integration step. This is because a smoother surface has a narrower peak in $\sigma^0(\theta_s, \phi_s)$ and therefore requires a smaller step in the angle so that this narrow beam is accurately sampled. Therefore, if we find a step which is small enough to give an accurate solution of the emissivity for the smoothest surface, it will be valid for all other rough surfaces.

We tested all possible values of s shown in table I, for the following conditions:

1. $L=6\lambda$ and $L=12\lambda$
2. Incident angles $\theta = 0^\circ, 25^\circ, 50^\circ$
3. H polarisation
4. Soil moisture content=30%
5. incident beams: plane wave, gaussian $g=0.25L$, and gaussian $g=0.1L$

From the experience gained analysing the bistatic scattering coefficients of rough surfaces during this thesis, we expect the width of the peak of $\sigma^0(\theta_s, \phi_s)$ to depend mainly on the roughness and to vary little with different polarisations and permittivity values. Therefore we did not investigate lower values of soil moisture nor V polarisation as we do not expect these variables to influence the choice of s . However it would be of interest to test this in further work.

Results for $L=6\lambda$ and different incident beams are shown in Table 4-III to Table 4-V and Figure 4.14 - Figure 4.16. Results for $L=12\lambda$ are shown in Table 4-VI to Table 4-VIII and Figure 4.17- Figure 4.19.

Table 4-III: The calculated emissivity at H polarisation, $L=6\lambda$, $g=0.1L$, and a soil moisture of 30%, for different values of theta and different integration steps

angle, θ	calculated emissivity for integration step, s			% difference in emissivity with respect to the value at $s = 0.2$ degrees	
	$s=0.2$ degrees	$s=0.5$ degrees	$s=1$ degree	$s=0.5$ degrees	$s=1$ degree
0	0.625	0.624	0.623	0.09%	0.23%
25	0.587	0.585	0.583	0.22%	0.58%
50	0.453	0.450	0.445	0.66%	1.78%

Table 4-IV: The calculated emissivity at H polarisation, $L=6\lambda$, $g=0.25L$, and a soil moisture of 30%, for different values of theta and different integration steps

angle, θ	calculated emissivity for integration step,s			% difference in emissivity with respect to the value calculated at $s = 0.2$ degrees	
	s=0.2 degrees	s=0.5 degrees	s=1 degree	s=0.5 degrees	s=1 degree
0	0.628	0.627	0.627	0.07%	0.14%
25	0.581	0.578	0.572	0.57%	1.53%
50	0.463	0.455	0.442	1.66%	4.42%

Table 4-V: The calculated emissivity at H polarisation, $L=6\lambda$, plane wave, and a soil moisture of 30%, for different values of theta and different integration steps

angle, θ	calculated emissivity for integration step,s			% difference in emissivity with respect to the value calculated at $s = 0.2$ degrees	
	s=0.2 degrees	s=0.5 degrees	s=1 degree	s=0.5 degrees	s=1 degree
0	0.639	0.638	0.638	0.07%	0.04%
25	0.596	0.591	0.582	0.57%	2.34%
50	0.476	0.464	0.444	1.66%	6.79%

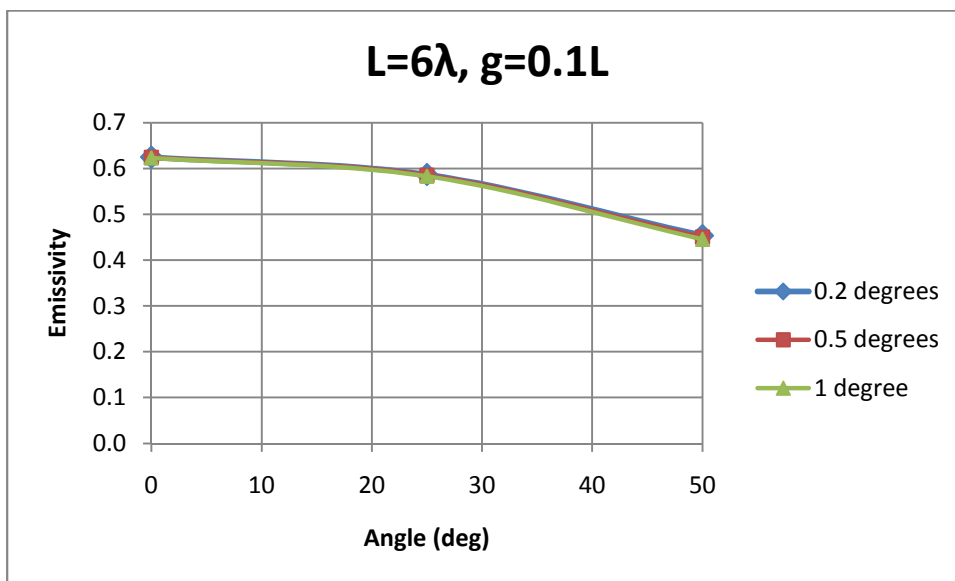


Figure 4.14: the calculated emissivity as a function of angle for different integration steps and the following conditions: H polarisation, 30% soil moisture, $L=6\lambda$, $g=0.1L$.

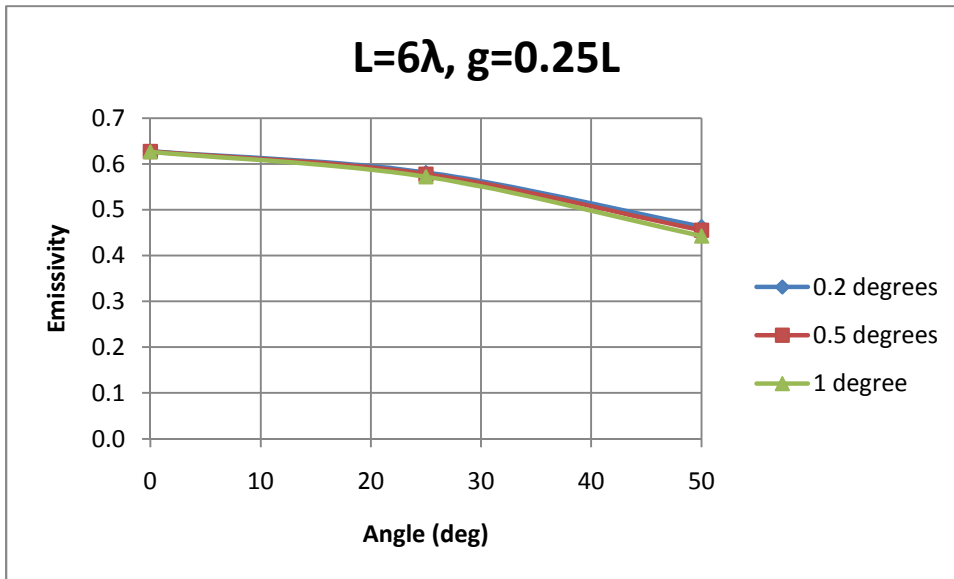


Figure 4.15: the calculated emissivity as a function of angle for different integration steps and the following conditions: H polarisation, 30% soil moisture, $L=6\lambda$, $g=0.25L$.

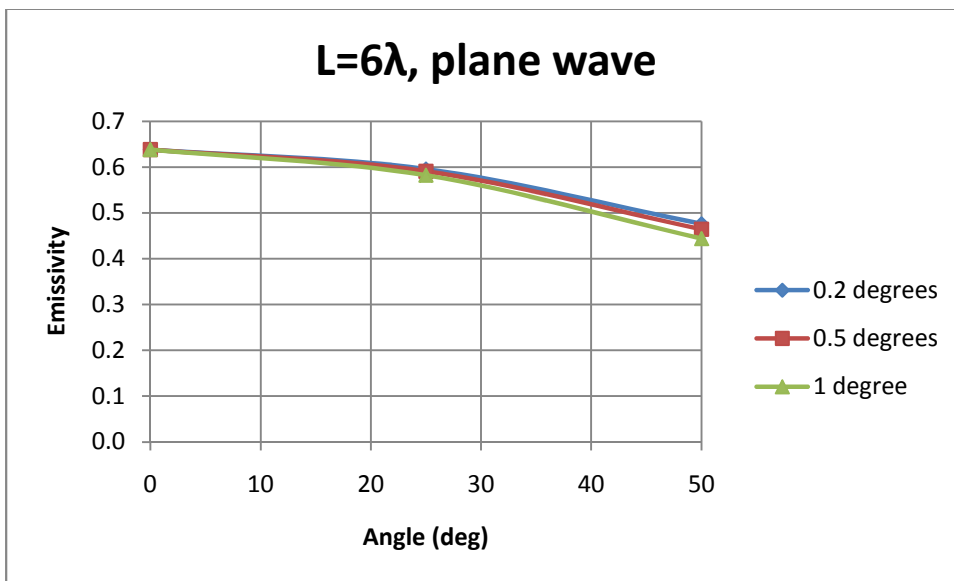


Figure 4.16: the calculated emissivity as a function of angle for different integration steps and the following conditions: H polarisation, 30% soil moisture, $L=6\lambda$, plane wave.

Table 4-VI: The calculated emissivity at H polarisation, $L=12\lambda$, $g=0.1L$, and a soil moisture of 30%, for different values of theta and different integration steps

angle, θ	calculated emissivity for integration step,s			% difference in emissivity with respect to the value calculated at s = 0.2 degrees	
	s=0.2 degrees	s=0.5 degrees	s=1 degree	s=0.5 degrees	s=1 degree
0	0.627	0.627	0.626	0.08%	0.18%
25	0.588	0.585	0.581	0.44%	1.19%
50	0.453	0.447	0.436	1.39%	3.70%

Table 4-VII: The calculated emissivity at H polarisation, $L=12\lambda$, $g=0.25L$, and a soil moisture of 30%, for different values of theta and different integration steps

angle, θ	calculated emissivity for integration step,s			% difference in emissivity with respect to the value calculated at s = 0.2 degrees	
	s=0.2 degrees	s=0.5 degrees	s=1 degree	s=0.5 degrees	s=1 degree
0	0.622	0.622	0.626	0.04%	0.58%
25	0.590	0.583	0.568	1.10%	3.73%
50	0.476	0.461	0.427	3.05%	10.17%

Table 4-VIII: The calculated emissivity at H polarisation, $L=12\lambda$, plane incident beam, and a soil moisture of 30%, for different values of theta and different integration steps

angle, θ	calculated emissivity for integration step,s			% difference in emissivity with respect to the value calculated at s = 0.2 degrees	
	s=0.2 degrees	s=0.5 degrees	s=1 degree	s=0.5 degrees	s=1 degree
0	0.633	0.634	0.443	0.11%	0.58%
25	0.599	0.588	0.572	1.68%	4.49%
50	0.503	0.480	0.443	4.47%	11.92%

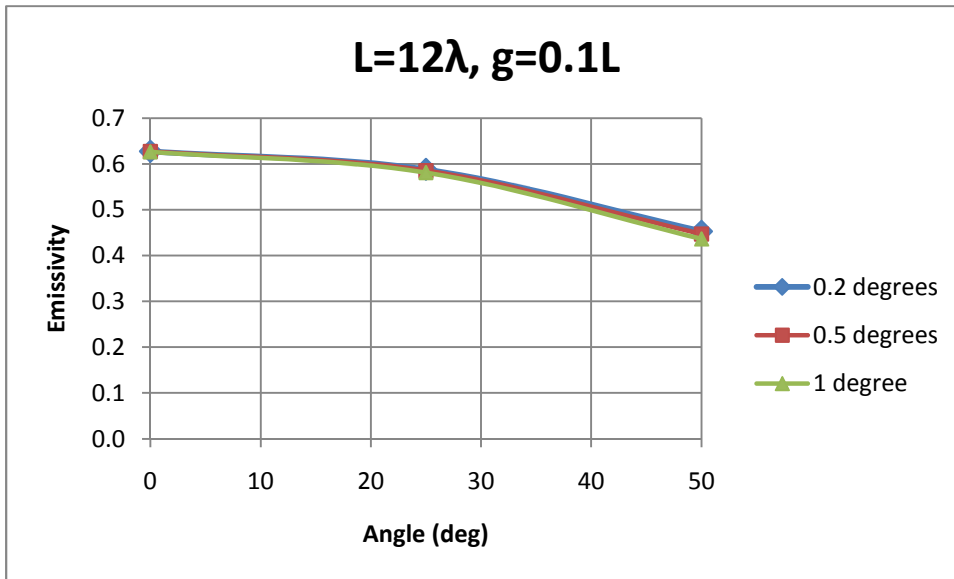


Figure 4.17: the calculated emissivity as a function of angle for different integration steps and the following conditions: H polarisation, 30% soil moisture, $L=12\lambda$, $g=0.1L$.

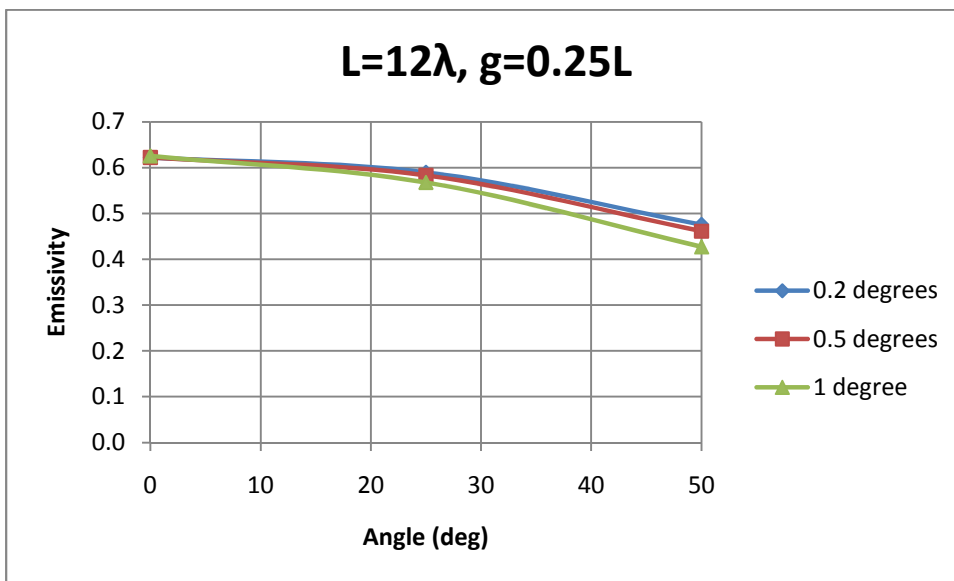


Figure 4.18: the calculated emissivity as a function of angle for different integration steps and the following conditions: H polarisation, 30% soil moisture, $L=12\lambda$, $g=0.25L$.

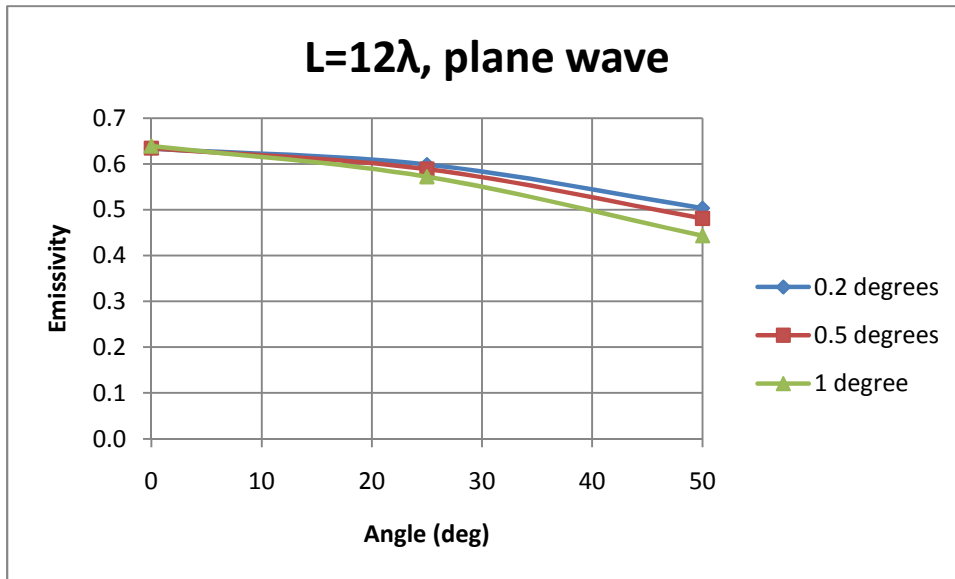


Figure 4.19: the calculated emissivity as a function of angle for different integration steps and the following conditions: H polarisation, 30% soil moisture, $L=12\lambda$, plane wave.

The results shown in Table 4-III to Table 4-VIII and Figure 4.14 - Figure 4.19 show that we require a smaller integration step for larger surfaces, higher angles and wider incident beams (a plane wave having the widest beam width, followed by $g=0.25L$ then $g=0.1L$). The worst case scenario is therefore $L=12\lambda$, with a plane incident beam, and an incident angle of 50° . Looking at the results for this case, we can state that, if we take values of $s=0.5^\circ$ or $s=1^\circ$, instead of $s=0.2^\circ$, we expect to introduce a maximum error of 4.5% and 11.9% respectively. On the other hand, if we take a surface size of 6λ we may expect a maximum error of 2.5% and 6.8% for $s=0.5^\circ$ and $s=1^\circ$ respectively. Also, if we restrict calculations to smaller angles (theta less than or equal to 25°) the largest error we can expect is 1.7% for $s=0.5^\circ$ and 4.5% for 1° . Note that these errors are approximate since we assume that the value at $s=0.2^\circ$ is exact, that is to say is equal to the value for an infinitesimal integration step. We also note that for rougher surfaces we expect the errors to be less.

Using the computer currently available in the IMS laboratory (64 bit, 64GB of available memory) it took approximately 1 hour and 30 minutes in order to calculate the near to far field approximation with $s=0.2^\circ$, approximately 30 minutes for $s=0.5^\circ$ and 10 minutes for $s=1^\circ$. Therefore wherever possible, it is better to use a step of either 0.5° or 1° .

4.2.2.3 Type of incident beam

Next we aimed to determine the type of incident beam, including the beamwidth in the case of a gaussian, to be used for calculations in this thesis. In order to do this we performed calculations for a

plane wave and gaussian beams with beamwidths of $g=0.1L$ and $g=0.25L$. Calculations were performed for the following conditions:

1. $\sigma=0.44\text{cm}$, $L_c=9\text{cm}$, representing a very smooth surface
2. a soil moisture of 30%,
3. H polarisation
4. $L=6\lambda$, $L=12\lambda$
5. Incident angles $\theta = 0^\circ, 25^\circ, 50^\circ$
6. $s=0.2^\circ$

Only the highest soil moisture was considered since at this value the rough surface has the greatest effect. For all cases considered, the integration step was taken to be 0.2° , in order to minimise additional errors. Again we only considered H polarisation since we do not expect the type of incident beam required to depend on polarisation.

We also performed calculations at $L=6\lambda$ for the case of a very rough surface, $\sigma=4\text{cm}$, $L_c=3\text{cm}$. In this case we used an integration step of $s=1^\circ$. This integration step could introduce errors into the results but we expect this to be small since we have a very rough surface of a small size. We did not test the case of $L=12\lambda$ for the very rough surface because calculation time would be very long (see section 4.2.2.5). We expect to still be able to draw good conclusions without this point, but it would be of interest to test this later.

The smoother surface is in the validity region of the analytical small perturbation model (SPM) so we can compare results obtained with this model. We did this using the AIEM model, which gives the same results as the SPM model in this region. The AIEM model used was provided by J.C. Shi and L. Chen of the University of California and CESBIO laboratory Toulouse, respectively, and is the version presented by Shi et al (2002). For interest, we also compare to Fresnel, since we expect the emissivity of any rough surface to be higher than Fresnel. Note that we do not compare results to AIEM for the rougher surface since AIEM is not valid for these roughness conditions.

Table 4-IX and Table 4-X and Figure 4.20 - Figure 4.21 show results of the emissivity as a function of angle, for the different incident beams, at H polarisation, 30% soil moisture, and roughness conditions $\sigma=0.44\text{cm}$ $L_c=9\text{cm}$ (smoother surface). Figure 4.20 and Table 4-IX show results for surface size $L=6\lambda$ and Figure 4.21 and Table 4-X present results for surface size $L=12\lambda$.

Table 4-XI and Figure 4.22 show results of the emissivity as a function of angle, for the different incident beams, at H polarisation, 30% soil moisture, roughness conditions $\sigma=4\text{cm}$ $L_c=3\text{cm}$ (very rough surface), and $L=6\lambda$.

Table 4-IX: Emissivity at H polarisation, roughness $\sigma=0.44\text{cm}$ $L_c=9\text{cm}$, different incident beams and $L=6\lambda$, compared to results from AIEM and Fresnel models

Theta	Incident beam			AIEM	Fresnel
	plane	$g=0.1L$	$g=0.25L$		
0	0.639	0.625	0.628	0.634	0.626
25	0.596	0.587	0.581	0.598	0.591
50	0.476	0.453	0.463	0.476	0.471

Table 4-X: Emissivity at H polarisation, roughness $\sigma=0.44\text{cm}$ $L_c=9\text{cm}$, different incident beams and $L=12\lambda$, compared to results from AIEM and Fresnel models

Theta	Incident beam			AIEM	Fresnel
	plane	$g=0.1L$	$g=0.25L$		
0	0.634	0.627	0.622	0.634	0.626
25	0.599	0.588	0.590	0.598	0.591
50	0.503	0.453	0.476	0.476	0.471

Table 4-XI: Emissivity at H polarisation, roughness $\sigma=4\text{cm}$ $L_c=3\text{cm}$, different incident beams and $L=6\lambda$

Theta	Incident beam		
	plane	$g=0.1L$	$g=0.25L$
0	0.945	0.948	0.944
50	0.864	0.865	0.865

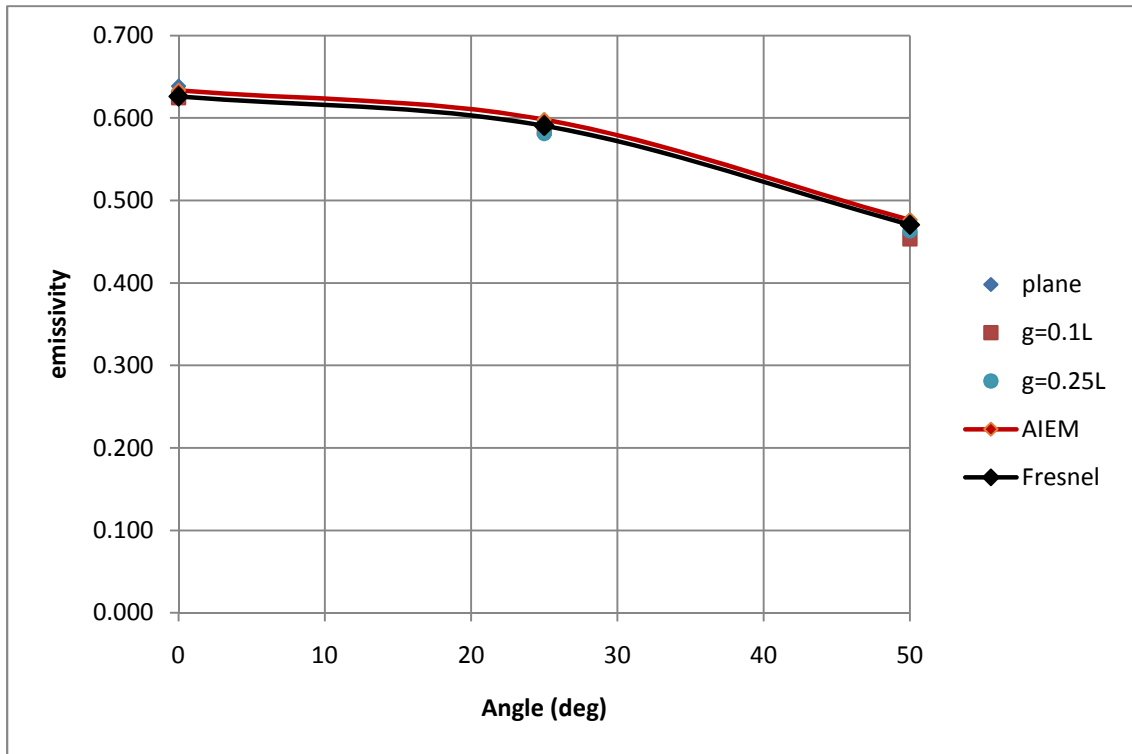


Figure 4.20: Emissivity at H polarisation, different incident beams, roughness $\sigma=0.44\text{cm}$ $L_c=9\text{cm}$, and $L=6\lambda$, compared to results from AIEM and Fresnel models

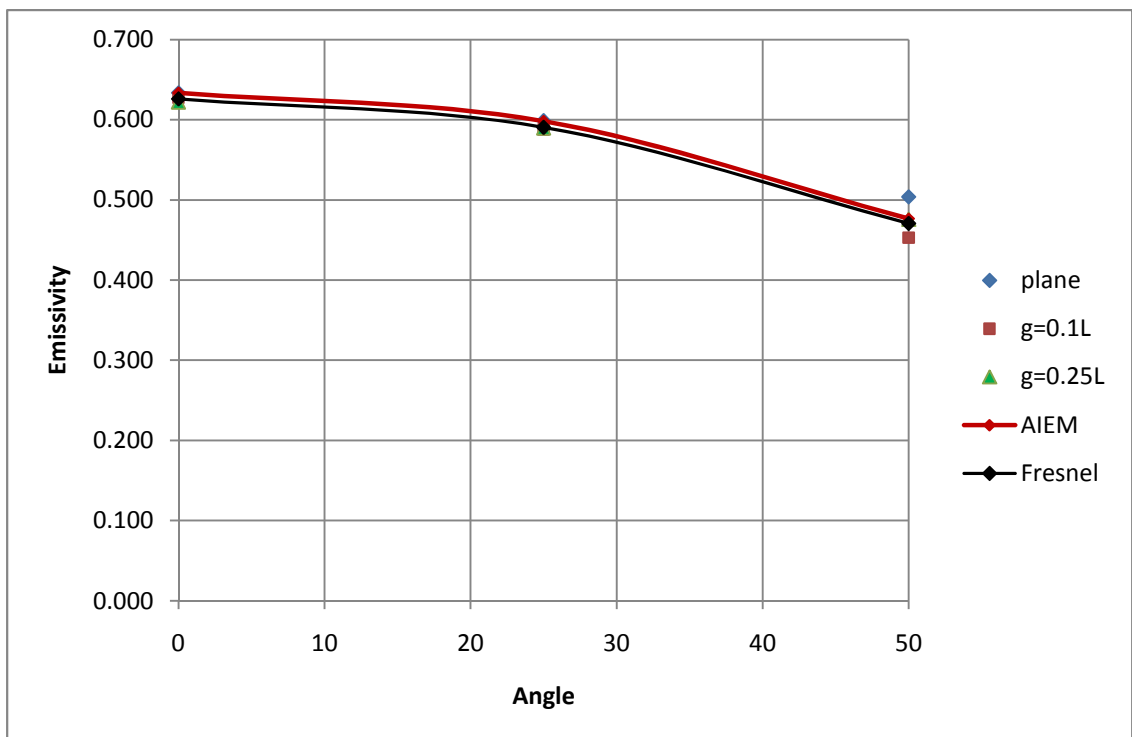


Figure 4.21: Emissivity at H polarisation, roughness $\sigma=0.44\text{cm}$ $L_c=9\text{cm}$, different incident beams and $L=12\lambda$, compared to results from AIEM and Fresnel models

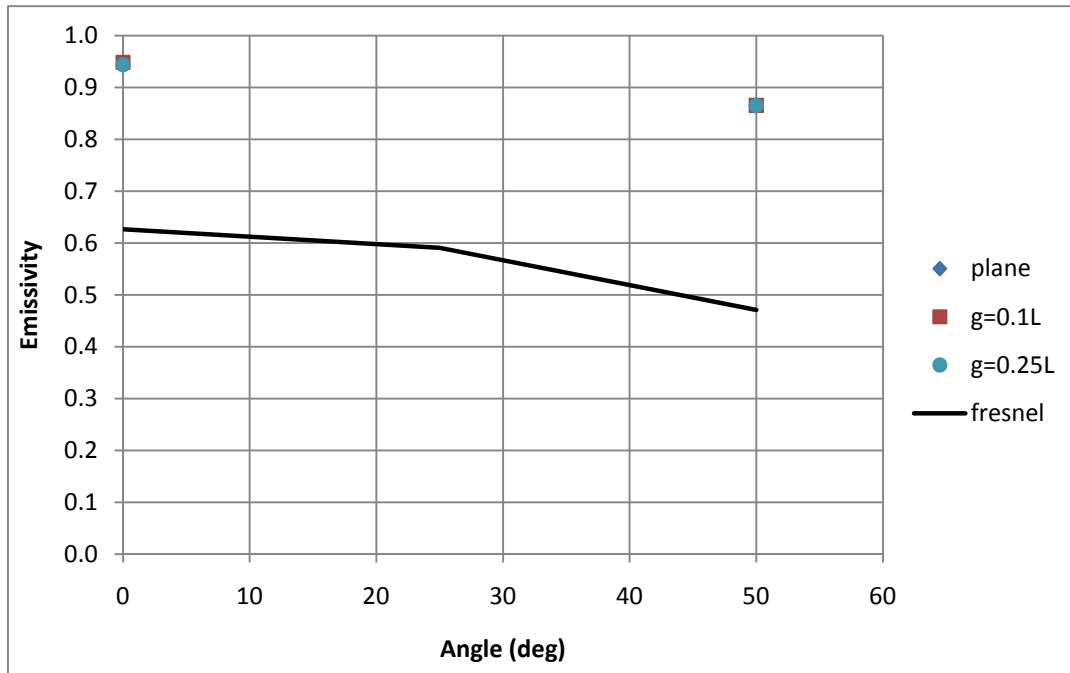


Figure 4.22: Emissivity at H polarisation, $L=6\lambda$, roughness $\sigma=4\text{cm}$ $L_c=3\text{cm}$, different incident beams, compared to results from the Fresnel models

From Table 4-IX and Table 4-X we see that in general results are closer to AIEM for the plane incident beam, followed by $g=0.25L$, then $g=0.1L$. The only exception is the point at 50° for the larger surface and a plane incident beam which is further from AIEM than the other points. This is surprising because a larger surface should produce more accurate results. Two possible reasons for this are as follows. The first is that since this is the worst case scenario for the integration step (plane beam, large angle, large surface) perhaps we need to reduce s to a value below 0.2° in order to obtain good results. A second possibility is that this result is good and it is AIEM that is inaccurate. This is possible because experimental results in the literature show that the difference between the emissivity of a rougher and smoother surface is larger for higher angles (see Wigneron et al (2010) for example) whereas the difference between AIEM and Fresnel is lower at $\theta=50^\circ$ than for $\theta=25^\circ$. On the other hand results of our model show an increase of the gap with angle, for the plane incident beam and $L=12\lambda$.

It would be interesting to investigate this further. However, for the purposes of this work we can still conclude that the plane incident beam appears to be the best choice for the emissivity calculation.

Table 4-XI and Figure 4.22 show that the incident beam that is chosen has little effect on the emissivity results for very rough surfaces and $L=6\lambda$. We estimate that this will be the case for the larger surface size also ($L=12\lambda$), since results of the smoother surface indicate that the surface size

does not affect the incident beam that gives the most accurate results. However in further work it would be interesting to verify this.

4.2.2.4 Surface size

As explained in section 3.1.3.1b, the size of the surface required depends on: the autocorrelation length, the surface roughness, and the wavelength. Firstly for larger autocorrelation lengths we require larger surfaces in order for the surface to be statistically representative of a rough surface of infinite size. Secondly in restricting surface size we lose long range scattering interactions between different points on the surface. If surfaces are rougher (higher standard deviation of surface height σ , lower L_c) these interactions are more likely to occur and so we expect the loss of these interactions to be more significant for rougher surfaces. Therefore rougher surfaces may require a larger surface size.

We performed calculations for two surface sizes, $L=6\lambda$ and $L=12\lambda$, and for two different rough surfaces: a low roughness of $\sigma=0.44\text{cm}$, $L_c=9\text{cm}$ and a high roughness of $\sigma=4\text{cm}$, $L_c=3\text{cm}$. The surface size of 12λ should be sufficient to give results of a good accuracy (10λ is considered sufficient) but since a size of 6λ will considerably reduce calculation time and memory requirements it is of interest to investigate whether results of a surface size of 6λ will be sufficiently accurate for the conditions considered in this thesis; the conditions of the SMOS mission and roughness conditions found in the field.

As well as the two surface sizes, we performed calculations for the following conditions:

1. H polarisation
2. A soil moisture of 30%
3. Incident angles $\theta=0^\circ, 25^\circ, 50^\circ$
4. Incident plane wave

We chose a value of $N=5$ for all conditions except for the very rough surface ($\sigma=4\text{cm}$, $L_c=3\text{cm}$) of large size ($L=12\lambda$) where we chose a value of $N=2$, since calculation times were very long in this case. Again we compared results to predictions of the AIEM (SPM) model and the Fresnel equations for the smoother surface.

Table 4-XII, Table 4-XIII and Figure 4.23 show the emissivity calculated using the numerical approach presented in section 4.1 for the two different surface sizes as a function of angle. Table 4-XII and Figure 4.23 present results for a low surface roughness of $\sigma=0.44\text{cm}$ and $L_c=9\text{cm}$ and Table 4-XIII presents results for a high surface roughness of $\sigma=4\text{cm}$ and $L_c=3\text{cm}$. For the low roughness condition

the integration step was set to 0.2 and for high roughness the integration step was set to 0.5, in keeping with results of section 4.2.2.2.

Table 4-XII: The emissivity at H polarisation as a function of angle, for the rough surface $\sigma=0.44\text{cm}$, $L_c=9\text{cm}$, 30% soil moisture, and different surface sizes, L , compared to results of the AIEM model and Fresnel

theta	$L=6\lambda$		$L=12\lambda$		AIEM	Fresnel
	emissivity	%error wrt AIEM	emissivity	%error wrt AIEM		
0	0.639	0.80%	0.634	0.00%	0.634	0.626
25	0.596	0.35%	0.599	0.11%	0.598	0.591
50	0.476	0.02%	0.504	5.68%	0.476	0.471
Average error		0.39%		1.93%	-	-

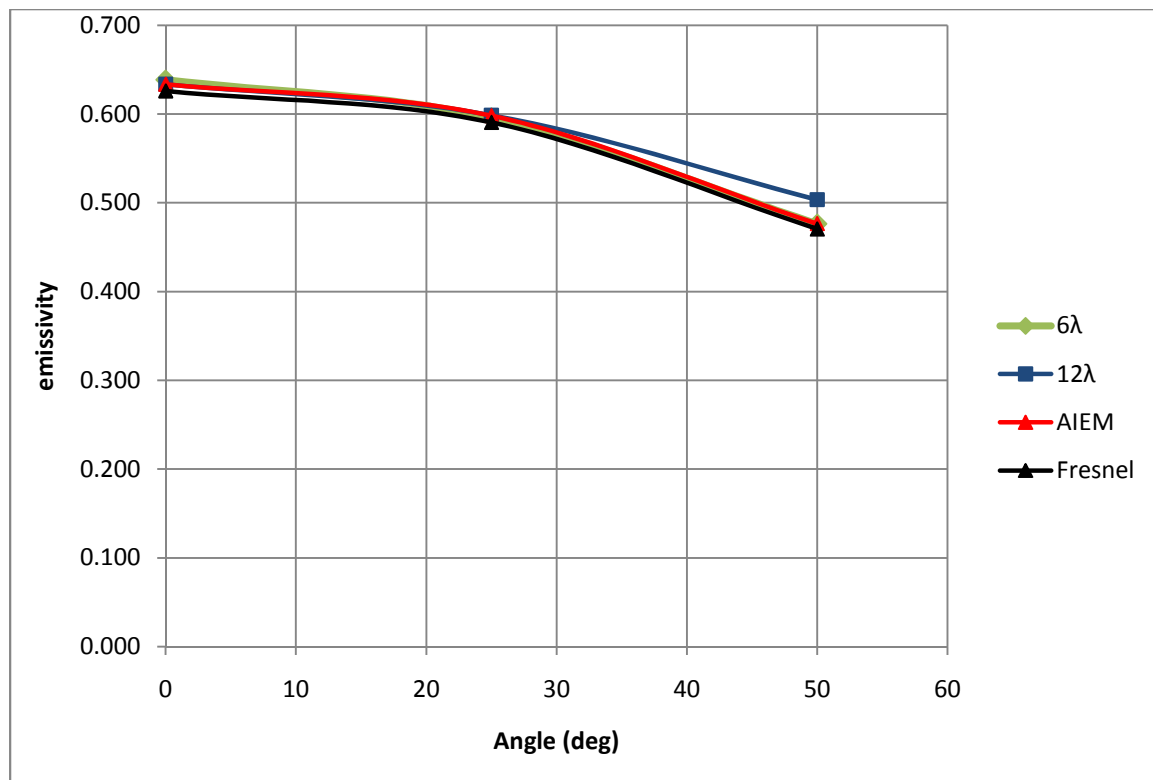


Figure 4.23: The emissivity at H polarisation as a function of angle, for the rough surface $\sigma=0.44\text{cm}$, $L_c=9\text{cm}$, 30% soil moisture, and different surface sizes, L , compared to results of the AIEM model and Fresnel

Table 4-XIII: The emissivity at H polarisation as a function of angle, for the rough surface $\sigma=4\text{cm}$, $L_c=3\text{cm}$, 30% soil moisture, and two different surface sizes, $L=6\lambda$ and $L=12\lambda$.

theta	Emissivity, $L=6\lambda$	Emissivity, $L=12\lambda$	difference
0	0.947	0.945	0.03%
50	0.864	0.870	0.69%

Table XII shows that for $\theta=0^\circ$ and 25° the higher surface produces more accurate results, as expected. However at $\theta=50^\circ$ the emissivity for $L=6\lambda$ appears to be more accurate, making the average error of $L=12\lambda$ higher than that of $L=6\lambda$. This is surprising because we know that accuracy is higher as we increase surface size so we assume that the large error for $L=12\lambda$, $\theta=50^\circ$, is either due to an integration step that is too high or is not correct due to an inaccuracy in the AIEM result, as discussed previously. Discounting the error calculated at $\theta=50^\circ$, we see that overall the higher surface produces more accurate results.

If we assume that at $L=12\lambda$ we have accurate results, then the error introduced by performing a calculation at $L=6\lambda$ is as shown in Table 4-XIV:

Table 4-XIV: errors associated with using a small surface size of $L=6\lambda$, with respect to results for a surface size of $L=12\lambda$

Theta	% error for $L=6\lambda$, w.r.t. $L=12\lambda$
0	0.80%
25	0.46%
50	5.40%
Average error:	2.22%

For low angles ($\theta=0^\circ, 25^\circ$) we see that the error produced by using a small surface size is negligible. At $\theta=50^\circ$, the error is higher, at 5.40%, demonstrating that a larger surface produces more accurate results at higher angles.

4.2.2.5 Calculation Cost

Table XIV presents the calculation CPU time and memory requirements for calculations of different surface size and roughness. We present results for the case of H polarisation and a soil moisture of 30% but we found similar figures for V polarisation and a soil moisture of 5%. We also present results for an incident gaussian beam of beamwidth $g=0.1L$ for the smoother surface and for a plane wave for the larger surface, but we found that the incident beam type also did not affect calculation cost. Note that the total number of passes, CPU time and memory are for one calculation only, and do not include the near to far field calculation. The values were averaged over several calculations. These values vary to some extent depending on the surface. Note that the calculation time and memory increase with the number of passes performed before convergence was achieved. The number of passes was around 10 – 15 for the smoother surfaces and 6 passes for the rougher surfaces. Therefore the values presented should be considered to be only an indication of the order of magnitude. Note that the CPU time also depends on the resources of the machine used for calculations. Values given in Table 4-XV were obtained on a 64 bit machine with 64 GB of available memory.

Table 4-XV: Calculation cost for surfaces of different size and roughness

Surface size, L	roughness	CPU time	Maximum Memory (GB)
6λ	$\sigma=0.44 L_c=9$	00:32:17	1.9
6λ	$\sigma=4 L_c=3$	05:11:10	15.5
12λ	$\sigma=0.44 L_c=9$	01:34:57	5.0
12λ	$\sigma=4 L_c=3$	76:14:23	31.4

Table 4-XV demonstrates that the calculation costs depend strongly on surface roughness and surface size. In particular the largest surface with the highest roughness has an extremely long calculation time. We see that, irrespective of surface roughness, doubling the surface size from 6λ to 12λ approximately doubles the memory required. However the calculation time seems to depend not only on the surface size but also on the roughness. For the smooth surface, if we increase the surface size from $L=6\lambda$ to $L=12\lambda$, we triple the calculation time but for the rough surface if we double the surface size the calculation time is 16 times longer. Thus it is much more costly in calculation time to increase the surface size of a rougher surface.

These results demonstrate the value of using a smaller surface size wherever possible and also the difficulty of modelling very rough surfaces for surface size of around 12λ or larger, with the calculation machines currently available for the work of this thesis, in the IMS laboratory.

4.2.3 Conclusions: Values determined for model parameters

Results of this study have led us to select $N=5$ for the number of rough surfaces over which we average when calculating the emissivity. However we will only use this value for calculations of the emissivity. Restricting ourselves to 5 surfaces should introduce an error of no more than 0.75% in the emissivity calculation, as shown in Figure 4.12. For the active case we will use a value of $N=20$. Figure 4.13 indicates that by not exceeding this value we introduce an error of no more than approximately 2.5%, for angles away from the specular direction. In the specular direction we will have an error of up to approximately 7.5%. The values of these errors is less certain for the scattering case than for the emissivity case since the values for the bistatic coefficient varied much more with N and so we can be less sure of the final value obtained in the scattering case. In order to quantify the errors in the bistatic scattering coefficient more accurately, more calculations would need to be performed to extend N beyond 50 for the case of a very rough surface. However, this is not necessary for the work of this thesis which focuses on applications for the SMOS mission which measures only the emissivity.

Secondly, results show that the plane wave incident beam gives the most accurate results for the case of the emissivity. We observe that results of the emissivity are more accurate for a plane beam if the surface is smoother but that the incident beam chosen has little effect on the results of the emissivity for rougher surfaces. However calculations at high roughness and for a larger surface size would be useful to confirm this. In conclusion, for the emissivity calculation we will use a plane incident beam.

Results also show that in general a surface size of $L=6\lambda$ produces accurate results for lower angles of approximately less than or equal to 30° . Above this the error due to a small surface size is no more than approximately 5.4% for a smoother surface. For a rougher surface, results did not greatly vary with surface size: the difference in the emissivity calculated for surface sizes $L=6\lambda$ and $L=12\lambda$ was observed to be no greater than 0.69% (at 50°). We chose therefore to use $L=6\lambda$ for emissivity calculations in this thesis.

For a plane incident beam, results showed that the value of the integration step had a greater influence on results for larger surface sizes. However since we will use a small surface size of $L=6\lambda$ for the work of this thesis we will use an integration step of 0.5° , which has an associated error of no more than approximately 1.66%, for the smoother surface, as shown in table V. For this value, the near to far field calculation should take no longer than 30 minutes, per calculation.

Table XV summarises the model parameters chosen for the work of this thesis.

Table 4-XVI: Summary of the values chosen for the model parameters, for the work of this thesis

Model parameter	Scattering calculation	Emission calculation
Number of rough surfaces, N	20	5
Integration step, s	1°	0.5°
Surface size, L	2.55m (=12 λ)	1.27m (=6 λ)
Incident beam	gaussian g=0.25L	Plane

**CHAPTER 5. VALIDATION OF THE NUMERICAL FEM
APPROACH FOR A SINGLE LAYER**

5. Validation of the Numerical FEM Approach for a Single Layer

It is important to demonstrate that our approach gives good results for a single layer with a rough surface representing the soil, before extending the study to the two layer soil-litter structure. This is of particular importance since there are very few studies of the finite element method presented in the literature for rough surface scattering, and none for the emissivity. In this section we aim to validate our method for the case of rough surface scattering and emission.

We begin by comparing results of our approach with the Fresnel equations for a flat surface. This is presented in section 5.1. In section 5.2 we compare results for the rough surface case with predictions of the method of moments. Lastly, in section 5.3, we compare results with experimental data. In this section we also compare results with the AIEM model, an analytical model which is valid for wet soils only (see section 3.1.2.2c). Note that the AIEM is not to validate our approach against AIEM, since the AIEM model is not considered to be accurate for all conditions. However since the AIEM model is often used to calculate rough surface emission (see for example Chen et al 2003), we compare the validity of our approach, when compared with experimental data, with the validity of the AIEM model, as a point of reference.

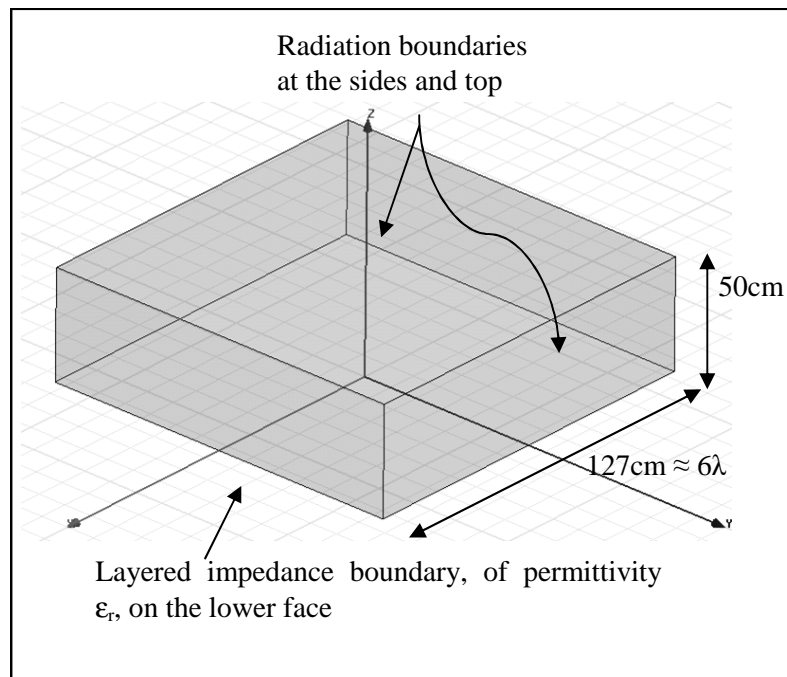
5.1 Comparison with Fresnel for a flat surface

In this section we validate the model for a flat surface by comparing results of the emissivity with predictions calculated from the Fresnel equations, which are exact for flat surfaces.

5.1.1 HFSS calculation set up

We chose two different permittivities for the ground, equivalent to low and high soil moistures. For low soil moisture we used a permittivity of $\epsilon_r=3.54+0.24i$, and for high soil moisture we used a permittivity of $\epsilon_r=17.03+1.96i$ (see p119 for an explanation of these values).

The calculation area of the HFSS project used is shown in Figure 5.1, along with a summary of its properties and the boundary conditions applied.



An incident plane wave was set up at angles from 0° to 60° , in 10° intervals ($0^\circ, 10^\circ, 20^\circ, 30^\circ, 40^\circ, 50^\circ, 60^\circ$). Calculations were performed at H and V polarisations.

5.1.2 Results and Conclusions

Results of the comparison with Fresnel are presented in Figure 5.2.

Results show a good general agreement with Fresnel for a flat surface. The maximum error for the numerical approach is approximately 0.02, at H polarisation and 50° .

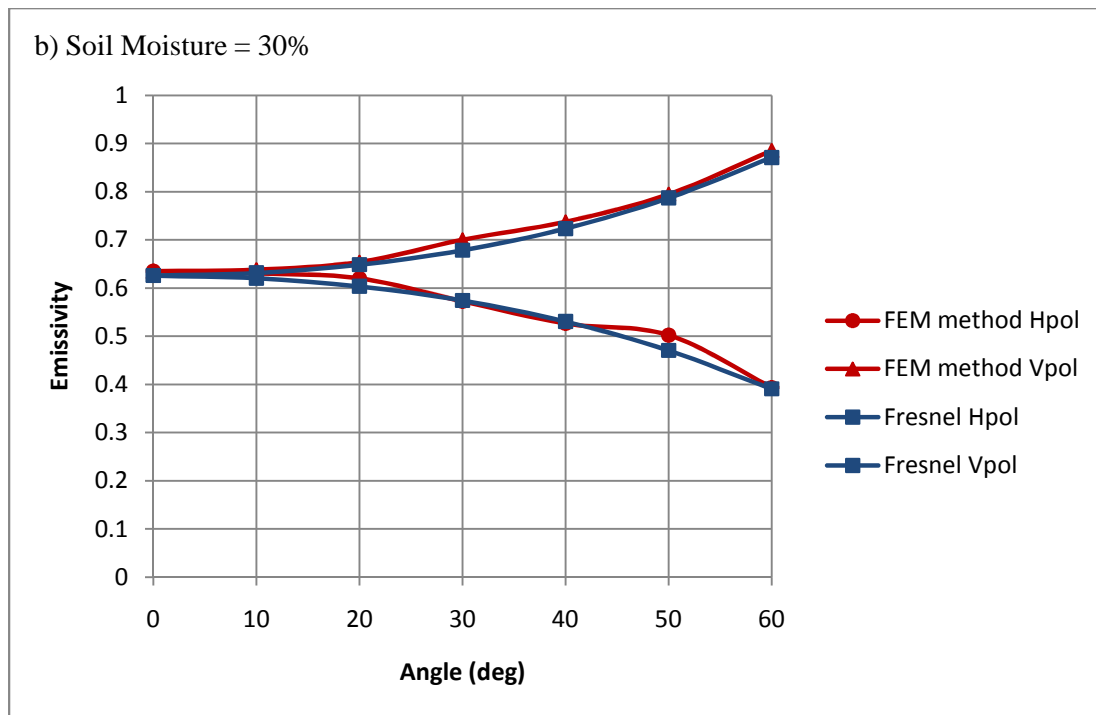
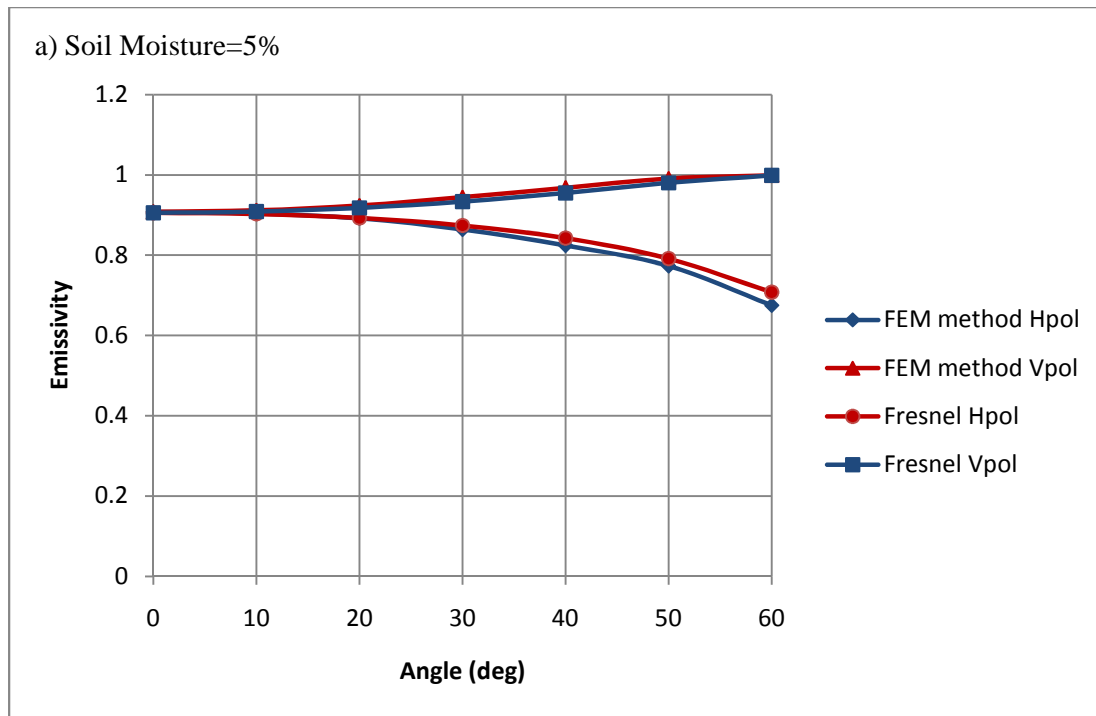


Figure 5.2: The emissivity of a flat surface, calculated using the numerical FEM approach and the Fresnel equations for H and V polarisations and: a) 5% soil moisture and b) 30% soil moisture

5.2 Comparison with the Method of Moments for a rough surface

In this section we validate our method for rough surface scattering and emission by comparing results of the bistatic scattering coefficient and emissivity with results of the Method of Moments found in the literature. The Method of Moments is the numerical model currently considered the standard model for calculating rough surface scattering and emission since it is the most accurate. It is therefore important to show that our approach produces results in agreement with MoM. Despite being interested only in emissivity calculations for the purposes of this thesis, we compare results also for the active case in order to obtain a more thorough and reliable validation of the FEM approach developed. Since the emissivity is calculated from the bistatic scattering coefficient we expect both values to be calculated accurately if the approach is valid.

The comparison was performed with results of the method of moments presented by Wu et al (2001), Ewe et al (2001a, 2001b), and Zhou et al (2004) for four different rough surfaces and permittivity values. In the following section we describe firstly conditions for these MoM calculations and secondly conditions for calculations performed with our approach, as described in section 4.1. We then present the results of the comparisons and finally the discussion and conclusions.

5.2.1 Method of Moments data

Results of the method of moments are presented by Wu et al (2001), Ewe et al (2001a, 2001b) and Zhou et al (2004) for roughness conditions and permittivity values presented in Table I.

Table 5-I: Calculation Conditions

Surface	Autocorrelation function	σ (cm)	Lc (cm)	Relative permittivity
1	gaussian	1.22	8.57	3+0.1i
2	gaussian	3.41	20.5	4+1i
3	exponential	0.4	8.4	15.57+3.71i
4	exponential	1.12	8.4	15.34+3.66i

Surfaces 1 and 2 are fairly smooth, particularly since the autocorrelation functions are gaussian which corresponds to smoother surfaces than for exponential autocorrelation functions. MoM calculations of the backscattering coefficient are presented by Wu et al (2001) for surface 1 with a low permittivity,

which is the equivalent to dry soil conditions. Results of bistatic scattering coefficient calculations, calculated by MoM, are presented by Ewe et al (2001a, 2001b) for surface 2 and also for a low permittivity value (dry soil conditions).

Zhou et al (2004) present emissivity simulations, performed by the numerical Maxwell-equation model (NMM3D), a MoM-based fast method, for surfaces 3 and 4, with high permittivity values (wet soil conditions). Surface 3 has a low roughness, and surface 4 is moderately rough.

5.2.2 Method

Calculations were performed for surfaces 1 - 4 using the numerical approach described in chapter 4, in order to compare model predictions with the Method of Moments. Since in this study we concentrate only the surface case, we set the layer thickness to zero, i.e. the structure in HFSS' calculation area consisted of a vacuum with a lower rough surface. To check the validity of this, we also tested a layer thickness of 5, 10 and 15cm but we found that this led to very little change in the calculated scattered electric field and so we chose to use zero surface thickness as calculations were faster. We applied a layered impedance boundary condition to the bottom of this rough surface, simulating an infinite dielectric layer, as described in section 4.1.2.1.

Numerical calculations were performed at 1.4 GHz and at both H and V polarizations on a 64 bit machine with 64 GB of available RAM.

A surface size of $L=2.55\text{m}$ (12λ) was used for the bistatic case and $L=1.27\text{m}$ (6λ) was used for the passive case. A gaussian incident beam with $g=0.25L$ was applied in the active case (surfaces 1 and 2) and a plane incident beam in the passive case. Calculations were performed for 20 different rough surfaces ($N=20$) for the active case and 5 different rough surfaces ($N=5$) for the active case. The conditions for the active case are in accordance with conclusions from section 4. A surface size of $L=6\lambda$ was selected to be sufficient for the emissivity case in the sensitivity study which is presented in 5.2. However the influence of the surface size on the bistatic scattering coefficient was not tested in this study and so we chose to use the larger surface, in order to avoid any potential errors due to the surface size being too small. $N=20$ was chosen for scattering calculations, in accordance with the findings of section 4.2. A gaussian beam was used for the scattering case because we expect to have errors due to edge effects to be more apparent for the scattering case than for the emissivity. The value of $g=0.25L$ was chosen for the beamwidth of this gaussian wave because this is the value most commonly adopted in the literature. The integration step was chosen to be 0.5° for the emissivity calculation and 1° for the scattering calculation.

It is usual to perform an energy conservation check for the case of rough surface emission however this was not possible since HFSS only calculates the scattered field in the upper hemisphere. Instead,

for the case of the emissivity, we performed a calculation of the reflectivity, from (4.3) and (4.5), for angles from 0 to 60°, and with a “perfect E” boundary condition replacing the “layered impedance” boundary condition on the surface. This condition ensures total reflection and so the reflectivity must be equal to unity for energy conservation to be true.

5.2.3 Results

Results for the scattering case (bistatic scattering and backscattering coefficients calculated from (4.3)) are presented in Figure 5.3 and in Figure 5.4. For surface 2 results are illustrated at H polarisation (very similar results were achieved at V polarisation). Results for the passive case are presented in Table 5-II and Table 5-III as well as in Figure 5.5 and Figure 5.6. CPU and memory requirements for each HFSS calculation (one surface only) varied from approximately 2 hours and 3 GB for surface 1 and approximately 12 hours and 15 GB for surface 4.

The energy conservation check using the perfect E boundary condition gave a reflectivity within 5% of unity for all angles. Although not conclusive, this indicates that energy conservation is good to within 5%.

Results show a good general agreement between our numerical approach and the Method of Moments, for both the active and passive case. There is a slight divergence between the two approaches for the bistatic scattering coefficient at high angles of reflection. However agreement is very good for the emissivity, the case of interest for SMOS applications. In Figure 5.5 and Figure 5.6 we note a slight increase in emissivity of about 0.05 (equivalent to ~ 15K) at H polarization as roughness increases from $\sigma=0.4$ cm to 1.12 cm. There is also a corresponding decrease in the difference between the emissivity at H and V polarizations ($e_V - e_H$). These observations are in good agreement with experimental data (e.g. Wigneron et al 2010). We conclude that whilst not as accurate as the Method of Moments, this approach provides results of adequate accuracy for scattering and good accuracy for emission, making it a good complimentary method for rough surface scattering and emission.

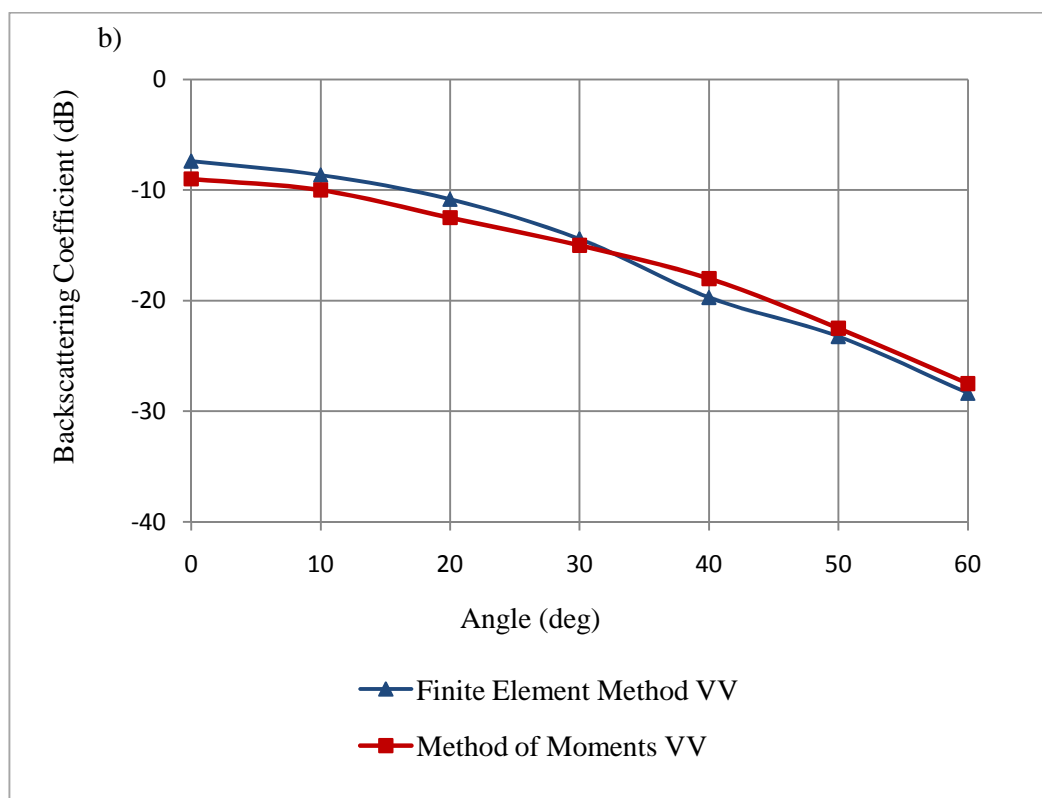
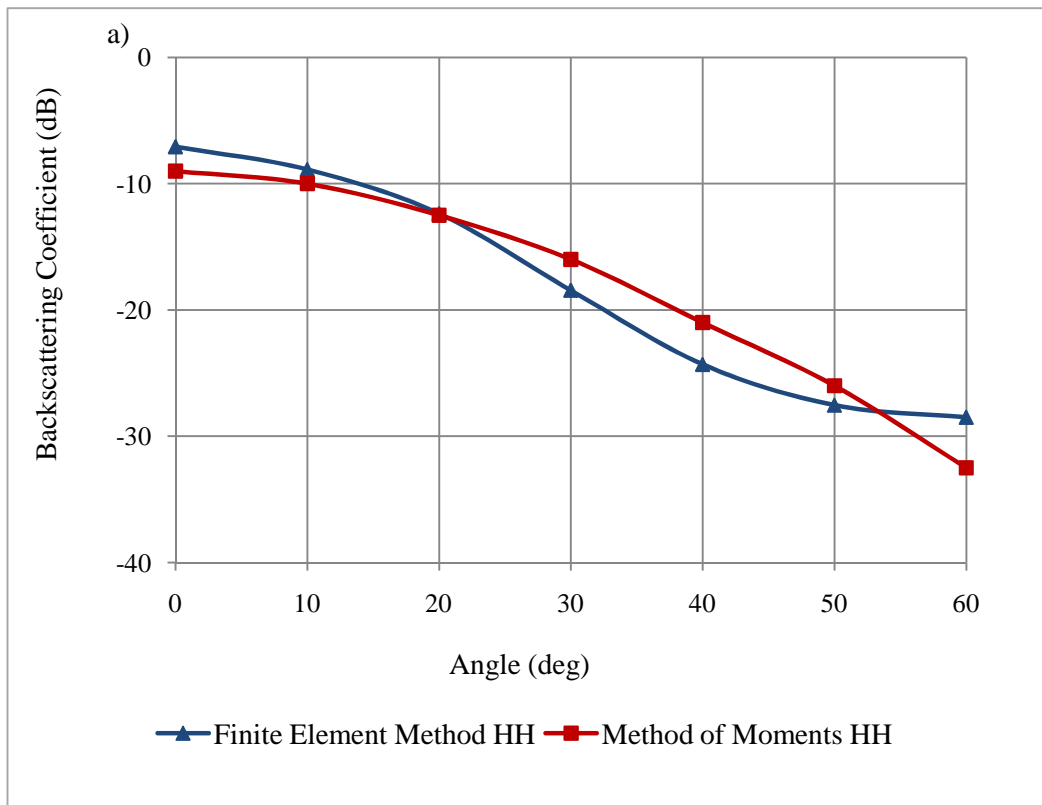


Figure 5.3: Backscattering coefficient for the Method of Moments and the Finite Element Method models, calculated at 1.4 GHz for $\epsilon_r=3+0.1i$ and $[\sigma, L_c]= [1.22cm, 8.57cm]$ at polarizations a) HH and b) VV



Figure 5.4: Bistatic scattering coefficient for the Method of Moments and the Finite Element Method models, calculated at 1.4 GHz for $\epsilon_r=4+1i$ and $[\sigma, L_c]= [3.41cm, 20.5cm]$ with an incident angle of 30° and at polarization HH

Table 5-II: Emissivities calculated by the MoM and the FEM models, at 1.4GHz, H and V polarization, for a rough surface of $\sigma=0.4cm$ and $L_c=8.4cm$, exponential autocorrelation function, and permittivity of $\epsilon_r=15.57+3.71i$

polarisation	Incident Angle (deg)	MoM Emissivity	FEM Emissivity	Difference between emissivities calculated by FEM and MoM methods
H	30	0.5891	0.5655	0.0236
H	40	0.5465	0.5608	0.0143
H	50	0.4930	0.4694	0.0236
V	30	0.6951	0.7051	0.0100
V	40	0.7397	0.7311	0.0086
V	50	0.7997	0.8075	0.0078

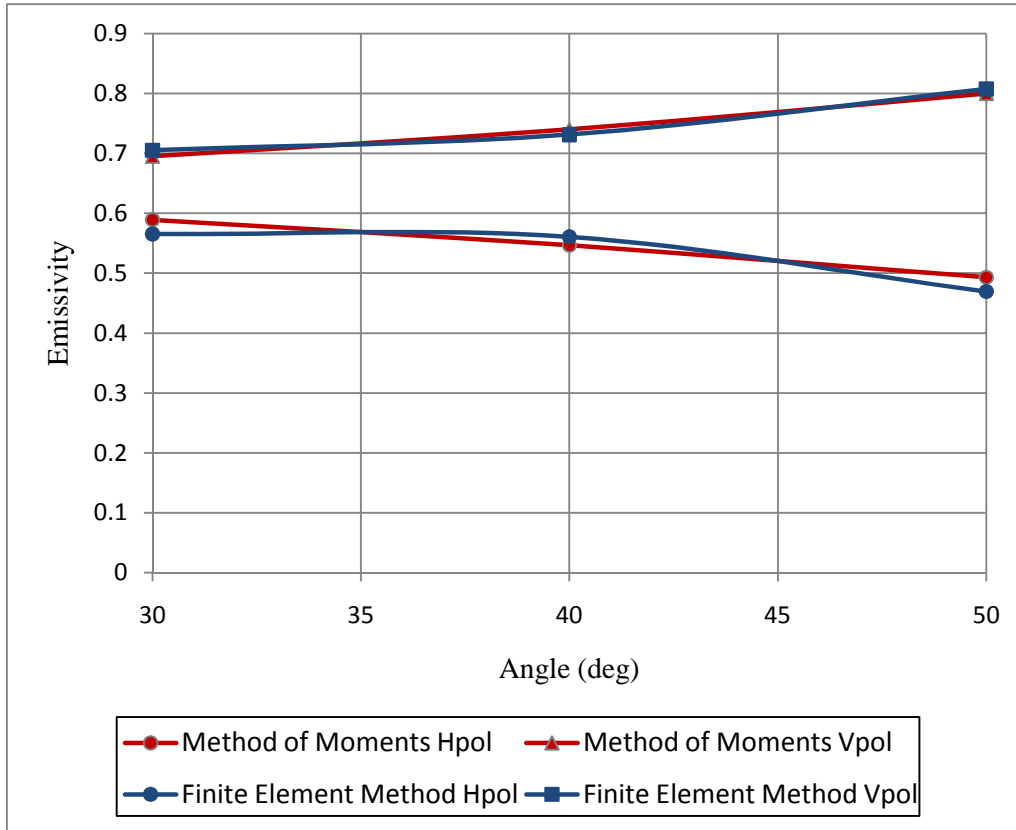


Figure 5.5: Emissivity for the MoM and the FEM models, calculated at 1.4GHz, H and V polarization, for surface of $\sigma=0.4\text{cm}$ and $L_c=8.4\text{cm}$, exponential autocorrelation function, and permittivity of $\epsilon_r=15.57+3.71i$

Table 5-III: Emissivities calculated by the MoM and the FEM models, at 1.4GHz, H and V polarization, for a rough surface of $\sigma=1.12\text{cm}$ and $L_c=8.4\text{cm}$, exponential autocorrelation function and $\epsilon_r=15.34+3.66i$

polarisation	Incident Angle (deg)	MoM Emissivity	FEM Emissivity	Difference between emissivities calculated by FEM and MoM
H	30	0.6351	0.6246	0.0105
H	40	0.5944	0.6002	0.0058
H	50	0.5338	0.5249	0.0089
V	30	0.7380	0.7252	0.0128
V	40	0.7658	0.7547	0.0111
V	50	0.8140	0.8122	0.0018

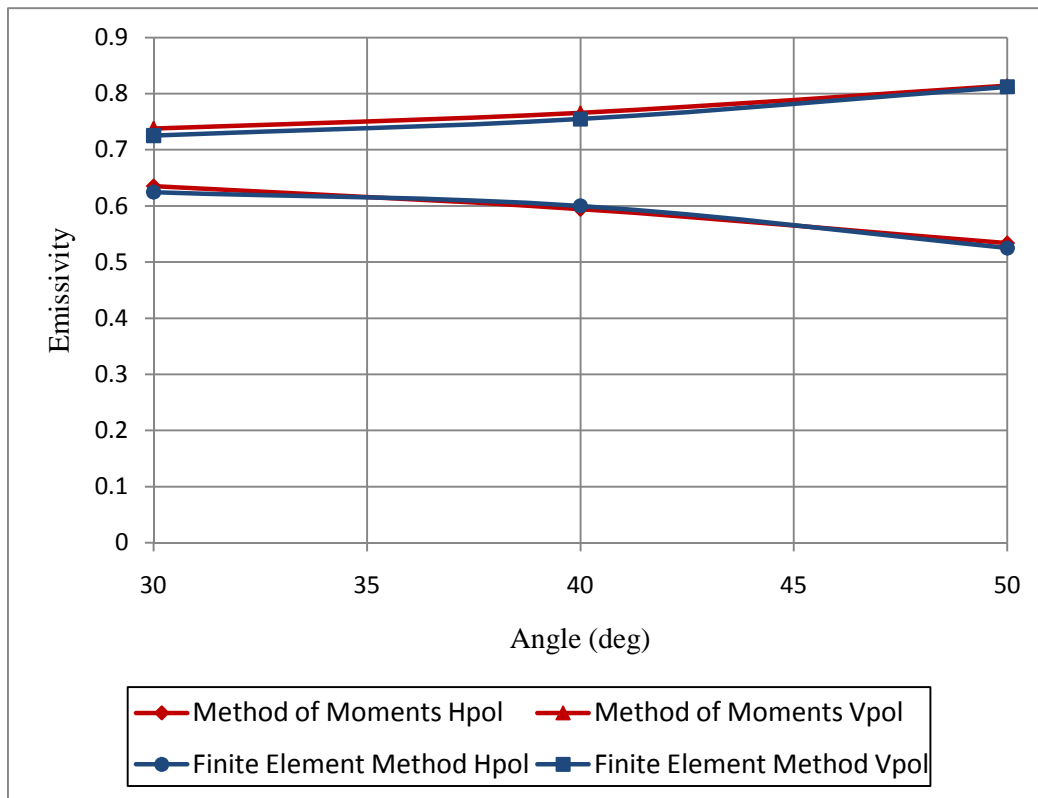


Figure 5.6: Emissivity for the MoM and the FEM models, calculated at 1.4 GHz, H and V polarization, for a surface of $\sigma=1.12\text{cm}$ and $L_c=8.4\text{cm}$, exponential autocorrelation function and $\epsilon_r=15.34+3.66i$

5.2.4 Conclusion

In this section we have compared results of rough surface scattering and emission for our numerical approach with results of the Method of Moments, a numerical method considered to be a reference in the field of rough surface scattering and emission. In particular we presented results of the emissivity of rough surfaces with exponential autocorrelation functions and also high permittivity values, which were considered difficult for the FEM simulations. Good general agreement was obtained between FEM and MoM, demonstrating that the new approach provides a good complimentary method to the Method of Moments for rough surface scattering and emission.

5.3 Comparison between the numerical approach, experimental data and the AIEM model

In this section we present a comparison between our numerical approach, the analytical AIEM approach and experimental data for the case of the emission of a bare soil layer with a rough surface. We compare rough surface emissivity predictions of the two modelling methods with experimental values for different roughness conditions and for high soil moisture. This allows us to validate our model against experimental data for the homogeneous soil layer with a rough surface. It also allows us to make a comparison with the commonly used analytical AIEM model, using the experimental data as a standard. The experimental data used in this section is taken from the SMOSREX 2006 experimental campaign (de Rosnay et al 2006a, Mialon et al 2008, Schwank et al 2010). The AIEM model was provided by L. Chen and J.C. Shi from CESBIO Laboratory, Toulouse and the University of California, respectively, and is the latest version presented by Shi et al (2002). The numerical approach is the FEM approach presented in section 4.1, with parameters determined in section 4.2

In the first section we present the SMOSREX 2006 dataset, including an initial analysis of the experimental data that allowed us to select surface roughness conditions and the soil permittivity value to be used for the comparison. Secondly we present the method and lastly we present and discuss results of the comparison between the two models and the experimental data, finishing with a conclusions section.

5.3.1 SMOSREX 2006 dataset

The experimental dataset used in this study consisted of data from the Surface Monitoring Of the Soil Reservoir EXperiment (SMOSREX) 2006 campaign (de Rosnay et al 2006a, Escorihuela et al 2007, Mialon et al 2008). A long-term dataset was acquired over the course of 2006 at the SMOSREX site near Toulouse in the south of France (43°23'N, 1°17'E, at 188m altitude), which has been in operation since January 2003. Details of the SMOSREX site including the equipment used have been presented in detail by de Rosnay et al (2006a) and Escorihuela et al (2007), and the 2006 campaign by Mialon et al (2008) and Schwank et al (2010), so here we will outline only the general method of the 2006 campaign.

On the 13th January 2006, which we shall call Day of Year (DOY) 13, the field on the SMOSREX site was ploughed to create a rough surface. It was then left to smooth out naturally over the course of the year. During this time, L-band brightness temperature measurements were taken automatically every 3 hours, at V and H polarization and at angles of 20°, 30°, 40°, 50° and 60°, using the L-band radiometer for Estimating Water In Soils (LEWIS) installed on the site. The LEWIS radiometer is mounted at the top of a 13.7m vertical tower, and measures brightness temperature at 1.4 GHz with an accuracy of \pm

0.2K and a beam-width of 13.5°. Figure 5.7 shows the LEWIS radiometer mounted on the tower at the site (left) and the soil surface being ploughed (right).



Figure 5.7: The LEWIS radiometer mounted on a tower, on the SMOSREX site, left and the soil being ploughed to create a rough surface, right.

Measurements of the soil moisture were taken throughout the year and soil temperature and weather conditions (precipitation, air temperature and humidity, wind speed and direction, atmospheric pressure, and solar and atmospheric incoming radiation) were also continuously monitored. Soil moisture was measured automatically every 30 minutes using impedance sensors (ML2 Theta probes) installed in the ground at depths of up to 90cm. Surface sensors were installed vertically in the soil, providing an integrated measurement of the soil dielectric constant (K_{TP}) at different depths. In order to address the soil moisture spatial variability, another four surface probes were placed at about 2m apart. The theta probe readings of K_{TP} were calibrated to soil moisture using gravimetric measurements of soil samples. Six soil samples were regularly taken from random locations in the field for a wide range of soil moisture conditions. Soil moisture was determined by gravimetry for each sample as follows. Samples of the soil of known volume were weighed on the site, and then removed, dried in the laboratory and weighed again. The average soil moisture of the six samples provided the gravimetric soil moisture on the site for the particular time and day that the samples were collected. These values were plotted against measurements taken on site with the probes at the same time and a straight-line relationship was obtained for impedance sensor measurements v. gravimetric soil moisture. This provided the calibration.

Soil temperature was also measured automatically every 30 minutes using thermistors at depths of 0 to 60cm. The site is equipped with a complete meteorological station that measured weather conditions, including measurements of precipitation, air temperature, atmospheric pressure, surface fluxes, wind speed and direction, infrared and solar radiation, and specific humidity every 2 minutes (averaged over 30 minutes).

In order to monitor the evolution of the surface roughness over time, 2-D profiles of the ground surface were taken on 10 different days throughout 2006, including before ploughing, and once in January 2007. To do this, a 2m needle board with 201 needles, movable in the vertical direction and with 1cm spacing between needles, was used. The needle board was placed level above the surface and the needles allowed to fall until they touched the ground. Photos were then taken of the profile created by the needle heights and these photos digitized manually and finally used to compute soil topography profiles of $f=[x_j, z_j]$ ($j=1, \dots, N$), $N=201$. For each day that this was done, 6-8 different profiles were taken in different positions on the site, both perpendicular and parallel to the furrows created by the plough. Figure 5.8 shows the needle board being used on the site (for a later experiment where the ground was covered with vegetation).



Figure 5.8: The needle board that was used to capture roughness profiles. The roughness profile is given by joining the red marks at the tops of the needles. Note that this particular profile was not taken for the 2006 campaign, but for a later campaign involving a vegetation cover. In the 2006 campaign the soil was bare.

For this study we filtered the data from the SMOSREX dataset to select measurements taken when the surface soil moisture (measured at 0 – 5cm) was relatively high. We selected a value of soil moisture close to 30% ($28\% \leq SM \leq 32\%$). A high value was chosen because the surface has the greatest impact on the emission for high moisture conditions, which places us within the validity of the AIEM model. Note that we only consider the soil moisture at a depth of 0-5cm since we consider only high soil moisture where and we consider the thermal radiation to be almost entirely emitted by the surface.

From the measurements selected, the effective soil temperature, T_{eff} , was calculated from soil temperature and moisture measurements at different depths using the method presented by Patricia de Rosnay et al (2006b). In the Microwave frequency range the bare soil polarized brightness temperature, $T_{\text{Bp}}(\theta)$, measured at angle θ and polarization p can be expressed as:

$$T_{Bp}(\theta) = e_p(\theta)T_{\text{eff}} + \Gamma_p(\theta)T_{\text{sky}} \quad (5.1)$$

where $e_p(\theta)$ is the ground emissivity, $\Gamma_p(\theta)$ is the ground reflectivity and T_{sky} is the sky radiometric temperature equal to 6.3 K. Replacing the reflectivity by one minus the emissivity (following (2.111)) and rearranging (5.1) we obtain the following relationship:

$$e_p(\theta) = \frac{T_{Bp}(\theta) - T_{\text{sky}}}{T_{\text{eff}} - T_{\text{sky}}} \quad (5.2)$$

The emissivity was therefore calculated from the selected SMOSREX measurements of T_B and T_{eff} by applying this relationship.

Roughness profiles $f(x_j, z_j)$ collected on the SMOSREX site on certain days of the year were analyzed to calculate values of σ and L_c . All measurements taken on one day were averaged (first averaging measurements taken parallel and perpendicular to the furrow) to produce a value for that day and the error estimated from the standard deviation of these measurements. Results are shown in Figure 5.9 and Figure 5.10. The error bars shown on these figures are the standard deviation in measurements taken that day.

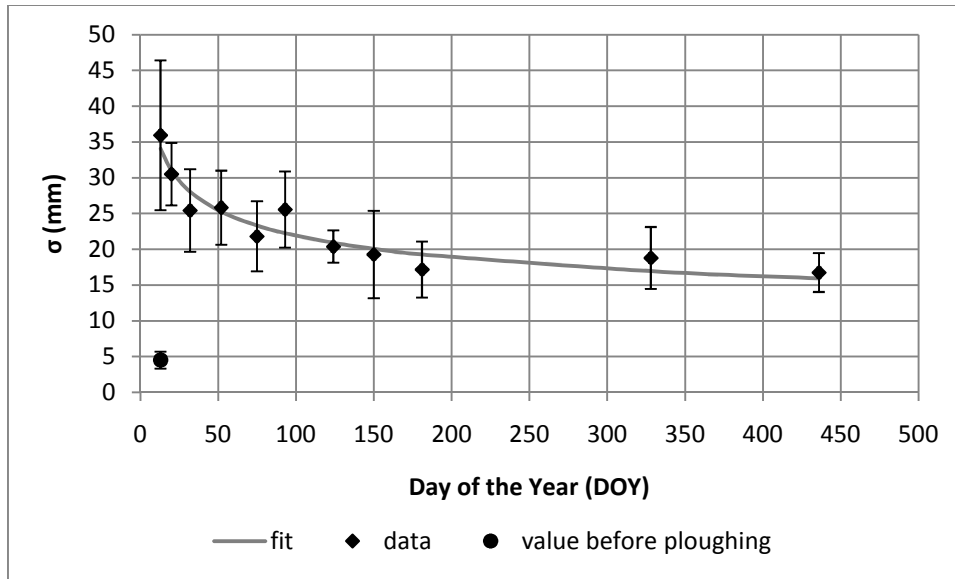


Figure 5.9: Variation of standard deviation of surface heights (σ) with time

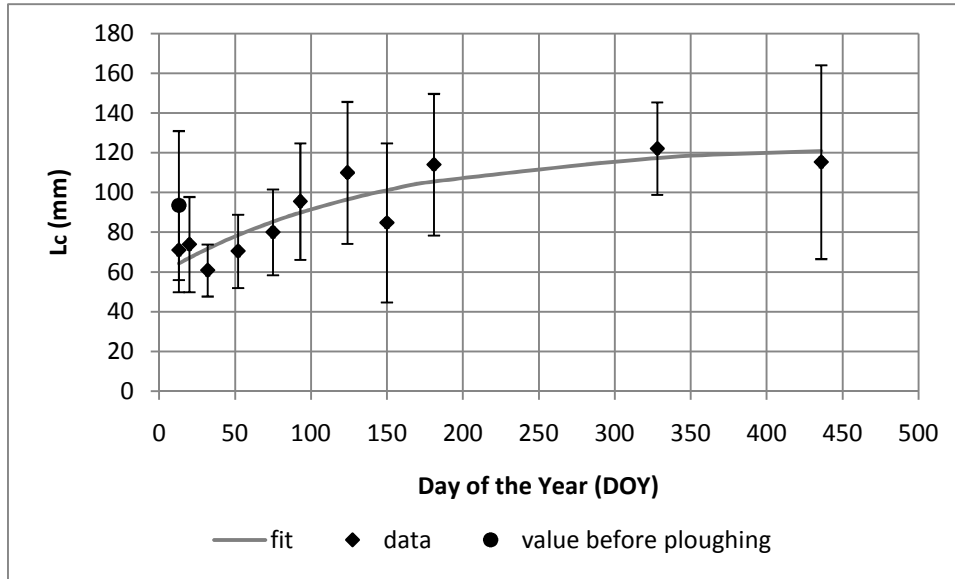


Figure 5.10: Variation of Autocorrelation length (L_c) with time

We expect the value of σ to decrease with time and L_c to increase with time in the manners shown in Figure 5.9 and Figure 5.10, that is to say quickly at first and then more slowly as time goes on. This is because the field which is very rough just after ploughing is gradually flattened over time due to weathering and also the movements of animals on the site. We expect this flattening process to be faster when the surface is rough and then slower as the surface smooths.

Equations of σ and L_c as a function of DOY (the day of the year) were fitted to these values. A power law was fit to σ and an exponential equation to L_c . The equations fitted were the following:

$$\sigma = 59.295(\text{DOY})^{-0.216} \quad R^2 = 0.906 \quad (5.3)$$

$$L_c = 65.121 \left[1 - \exp\left(-\frac{\text{DOY}}{142.640}\right) \right] + 58.693 \quad R^2 = 0.805 \quad (5.4)$$

It must be noted that the fit of L_c potentially has large inaccuracies because of the large measurement errors associated with the values. However we expect L_c to increase with time in such a manner, which lends credence to the fit.

Values of σ and L_c for the selected measurements (soil moisture of 30%) were then calculated from (5.3) and (5.4), and these values are presented in Table IV.

Table 5-IV: Roughness conditions for a soil moisture between 28% and 32% inclusively

σ (mm)	L_c (mm)	Slope σ/L_c
28	71	0.39
25	77, 78	0.32, 0.32
24	81, 82, 83	0.30, 0.29, 0.29
23	86, 87, 88	0.27, 0.26, 0.26
22	91	0.24
21	97, 98	0.22, 0.21
18	118	0.15
17	120, 121	0.14, 0.14

Three roughness values used in the comparison with the two modelling approaches were chosen from the values shown in table IV, which cover the range of values for rough surface slope in table IV. They are shown in table V.

Table 5-V: Roughness conditions selected for the comparison with the numerical approach

Surface	σ (cm)	L_c (cm)	Slope $m=\sigma/L_c$
5	1.7	12.1	0.14
6	2.3	8.7	0.26
7	2.8	7.1	0.39

These three surfaces, which we have named 5, 6 and 7 for continuity, range from a moderately rough surface (surface 5) to a very rough surface (surface 6). They therefore compliment the surfaces studied in the previous section (surfaces 3 and 4), which had a low roughness.

The emissivity at H and V polarization were calculated for surfaces 5 – 7 using both our numerical approach and the AIEM model, for incidence angles $\theta=20^\circ, 30^\circ, 40^\circ, 50^\circ, 60^\circ, \varphi=0^\circ$, exponential surface autocorrelation functions, and a soil moisture of 30%. A soil moisture of 30% was chosen since in this case surface effects dominate and this puts us in the validity region of the AIEM model. In addition at higher soil moistures. The input permittivity value equivalent to 30% soil moisture was calculated using the model developed by Mironov et al. (2009). This model requires inputs of soil moisture, soil clay content, frequency and soil temperature. The clay content for the SMOSREX site was taken to be 16.6%, as measured by Escorihuela et al (2007). The permittivity was calculated for

these values and for each temperature value measured on the SMOSREX site for days where the soil moisture was 30%. We then took the average permittivity value which was $\epsilon_r=17.03+1.96i$.

5.3.2 Method

Calculations were performed using the numerical approach and the AIEM model for roughness and permittivity conditions presented in section 5.3.1: the three different roughness conditions are shown in table V and the soil permittivity was $\epsilon_r=17.03+1.96i$.

The model parameters for the numerical approach are those selected in section 4.2. Calculations were performed for N=5 different rough surfaces with the same autocorrelation functions and values of σ and L_c and then the square of the reflected electric field averaged over all surfaces to calculate $|E_r^s(\theta_s, \phi_s)|^2$ in (4.3). This averaging process is necessary in order to approach the value that would be obtained for the case of an infinitely large rough surface, corresponding to the value calculated by the AIEM model. The emissivity was then calculated from $|E_r^s(\theta_s, \phi_s)|^2$ using (4.3), (4.5) and (2.111).

Roughness conditions are shown in table V and values of the model parameters are summarised in table VI, below.

Table 5-VI: model parameters for the numerical approach

Model Parameter	value
Surface size, L	1.27m
incident beam	Plane wave
Number of rough surfaces, N	5
Number of points on the surface	128 x 128
Integration step, s	0.5°

Currently the most commonly used model analytical model for the calculation of rough surface emission is the Integral Equation Model (IEM), or its updated version the Advanced Integral Equation Model (AIEM). This is the most widely used analytical model since it has the widest validity region. The AIEM model is limited to rather wet soils since in the AIEM model does not consider volume effects, only surface effects, and at wet soils surface effects dominate.

The version of AIEM used in this study is a code written and run in fortran. We input values of permittivity, incident angle, frequency, the standard deviation of surface heights σ of the rough surface and the surface autocorrelation length L_c . We can also choose between an exponential autocorrelation function and a gaussian autocorrelation function for the rough surface. The fortran

code was executed for roughness conditions shown in table IV, incident angles of 20 – 60°, with a step of 10°, H and V polarisation and a permittivity of $\epsilon_r=17.03+1.96i$ equivalent to 30% soil moisture.

5.3.3 Results and Discussion

Figure 5.11 - Figure 5.13 show a comparison of the emissivity as a function of measurement angle, as calculated by the numerical model, AIEM and also experimental data from the SMOSREX 2006 campaign. The six different graphs present results for the three different roughness conditions shown in table IV (surfaces 5 – 7) and H and V polarisations. Not that in some cases there are many different experimental points for one roughness condition and measurement angle. These different points correspond to measurements that were taken at different times for the same roughness and soil moisture conditions. The variation in the emissivity of these points could be due the fact that the measurements of soil moisture and surface roughness were taken by sampling and therefore somewhat inaccurately represent the roughness of the whole rough surface or the average soil moisture across the footprint. Also the soil moisture was not measured at depths of less than 5cm and for wet conditions the soil moisture profile in the region 0 to 5cm has been shown to significantly affect emission (ref Escorihuela).

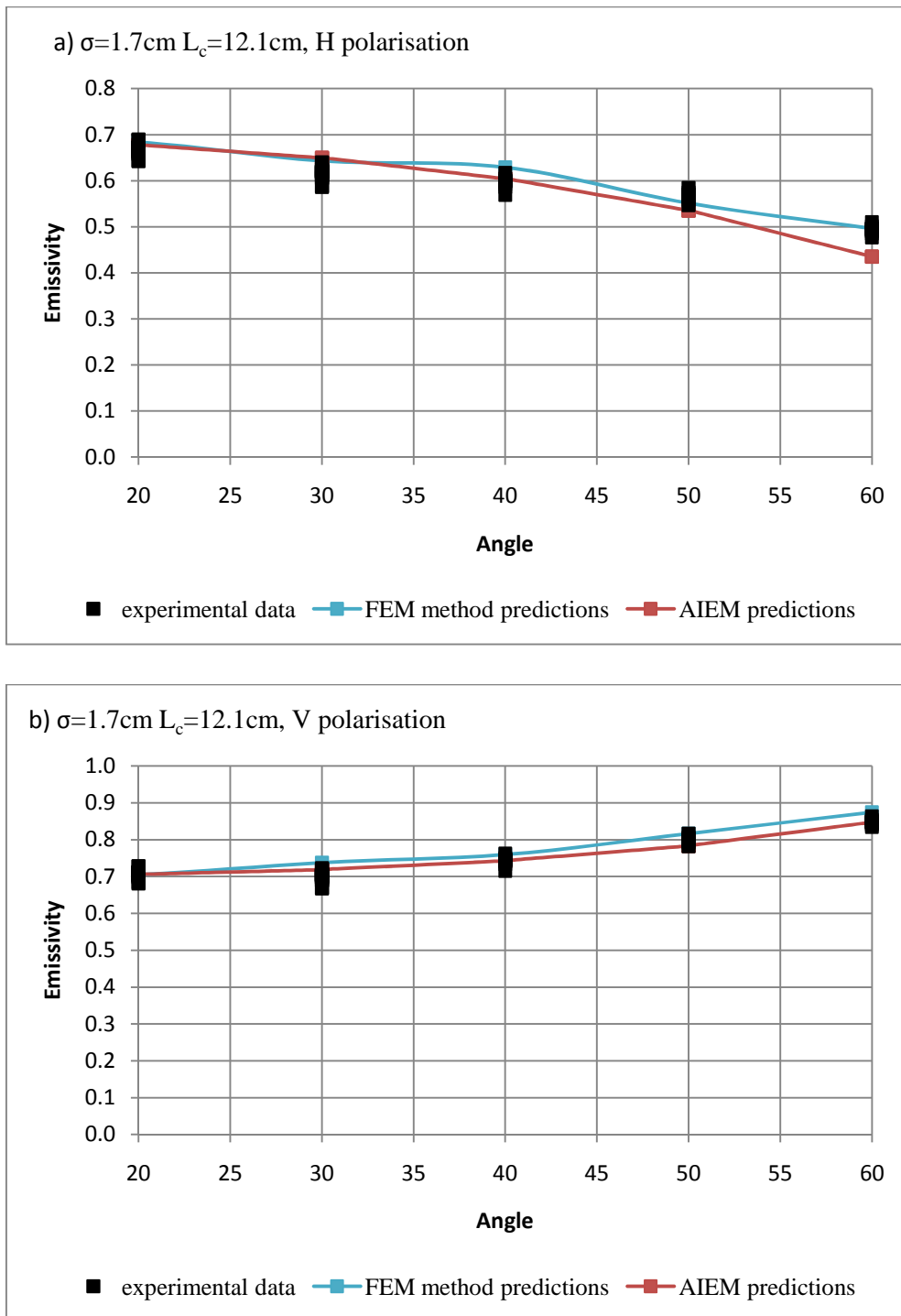


Figure 5.11: Results of the emissivity of rough surface 5, with standard deviation of surface heights $\sigma=1.7\text{cm}$, autocorrelation length $L_c=12.1\text{cm}$, a soil moisture of 30%, as calculated by AIEM and the HFSS model and as measured on the SMOSREX site, for: a) H polarization and b) V polarization.

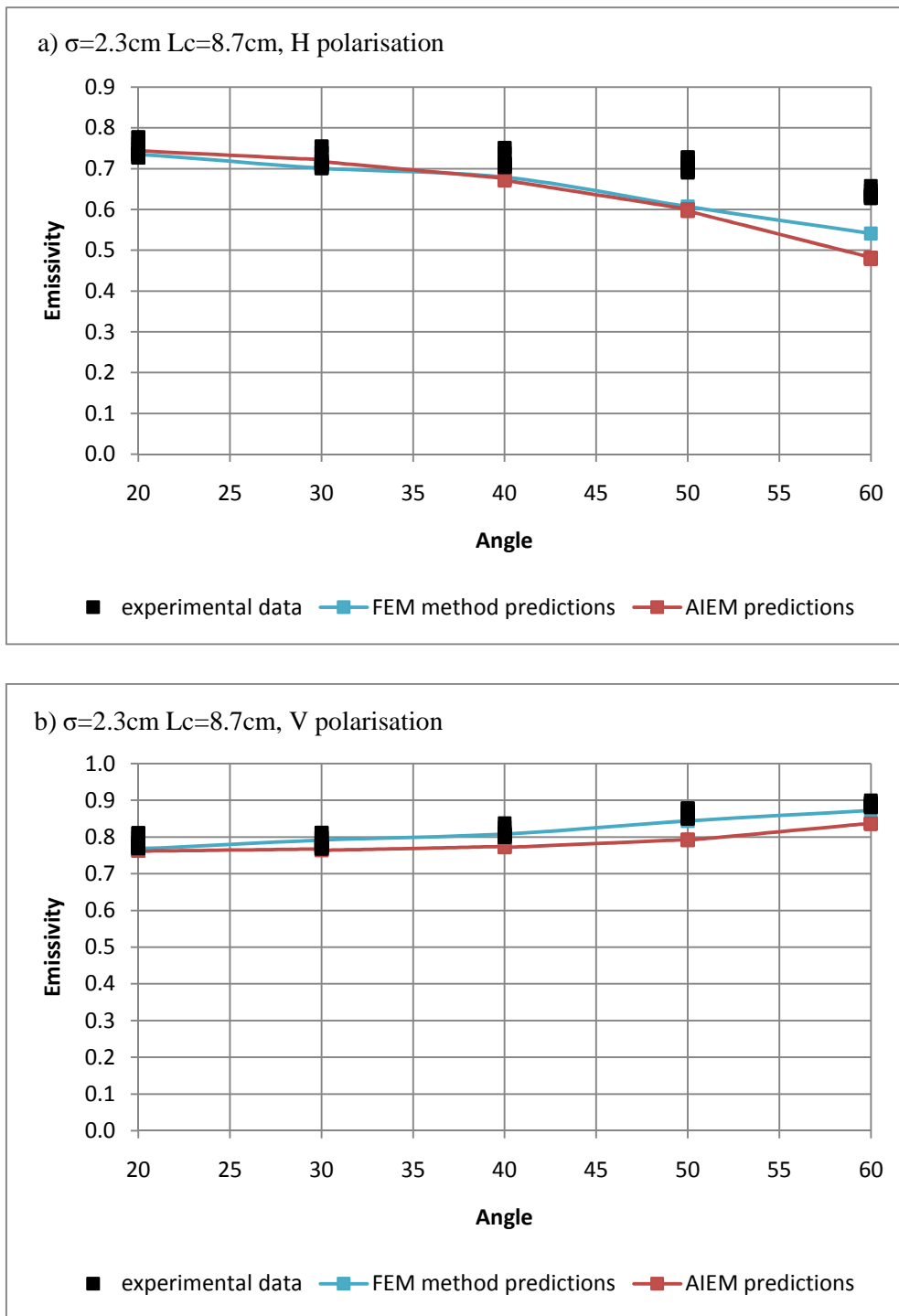


Figure 5.12: Results of the emissivity of surface 6, with standard deviation of surface heights $\sigma=2.3$ cm, autocorrelation length $L_c=8.7$ cm, a soil moisture of 30%, as calculated by AIEM and the HFSS model and as measured on the SMOSREX site, for: a) H polarization and b) V polarization.

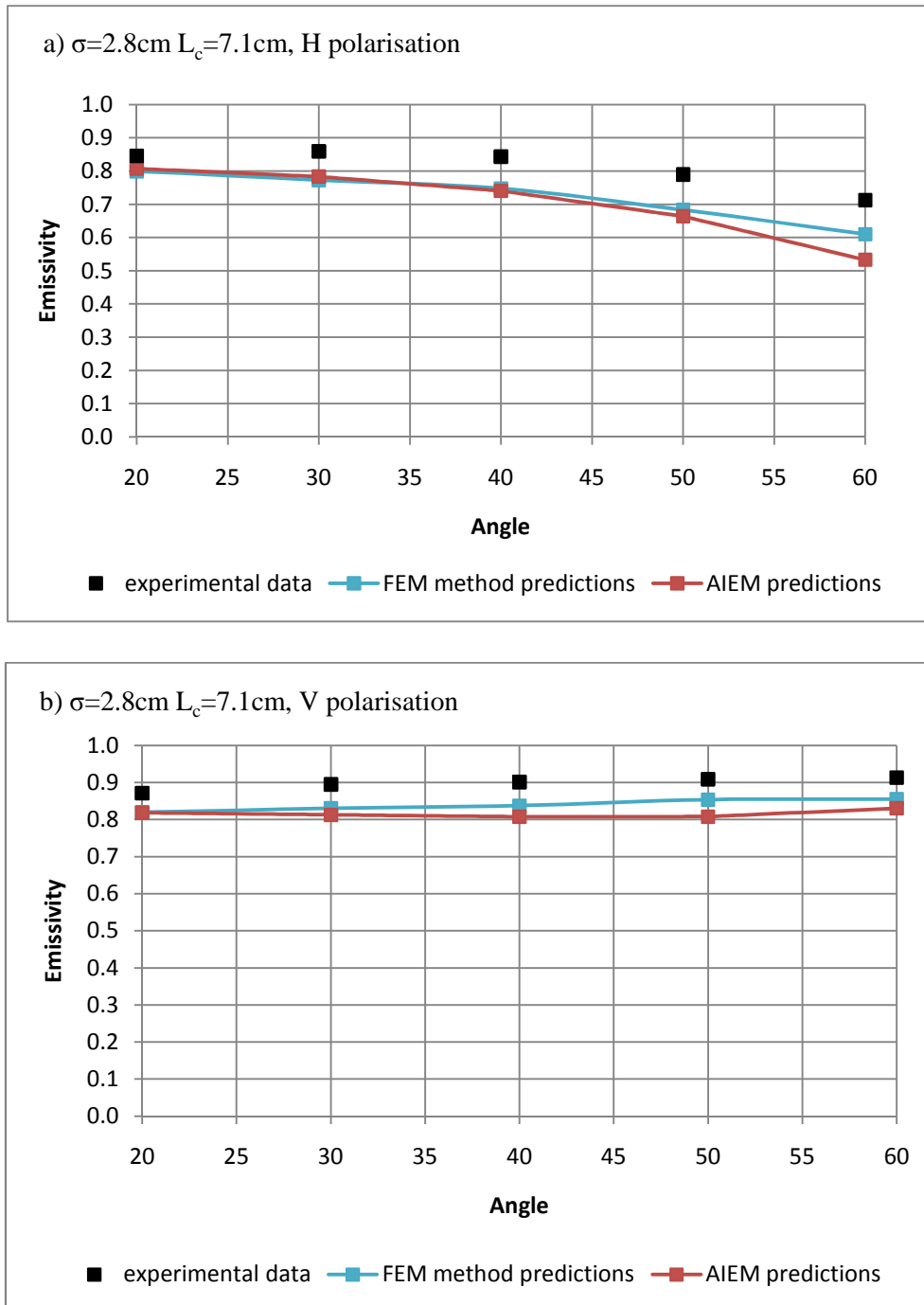
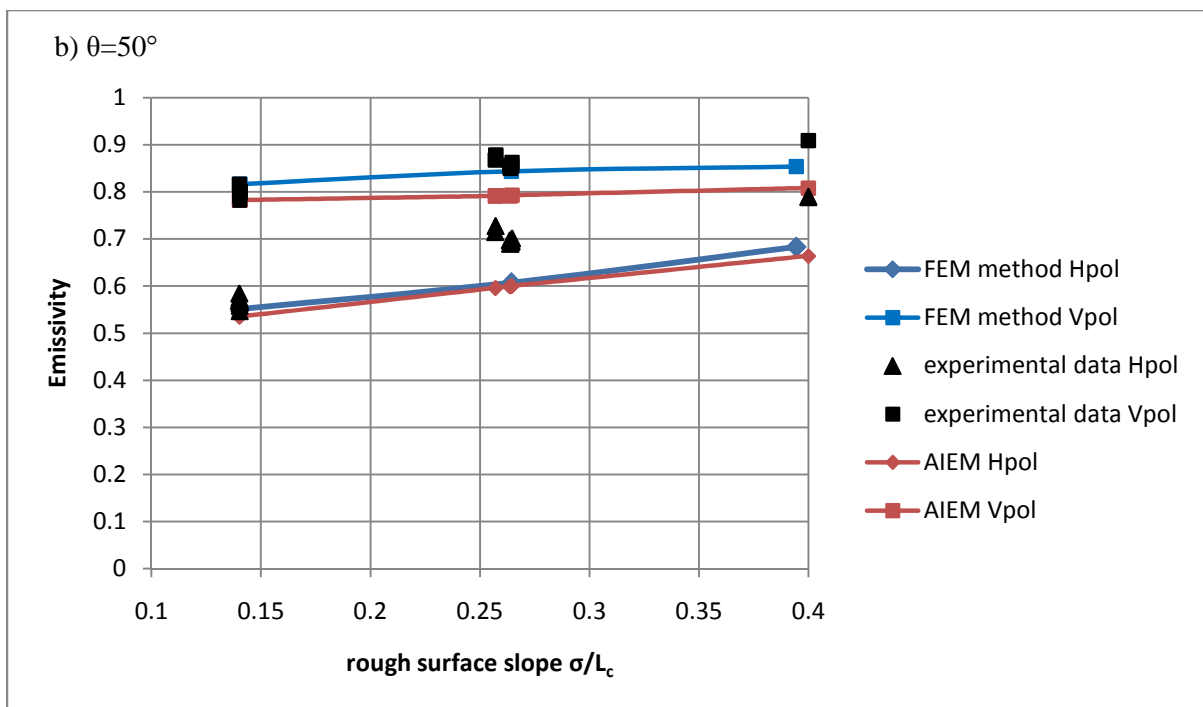
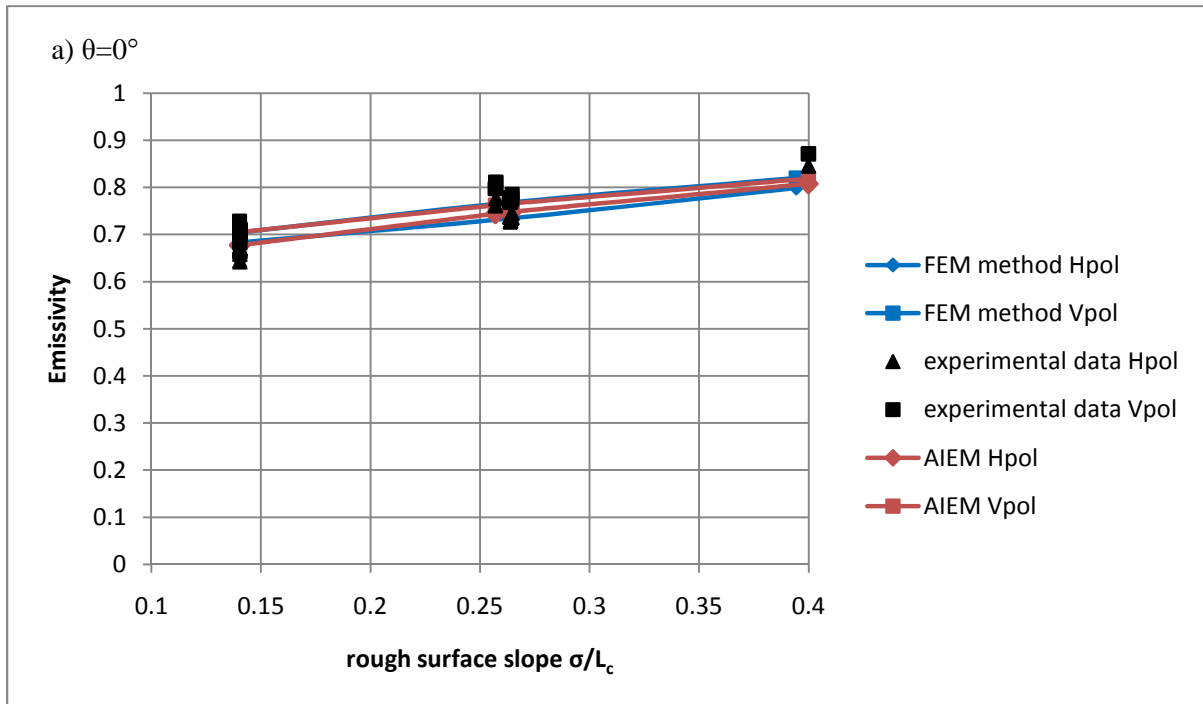


Figure 5.13: Results of the emissivity of surface 7 with standard deviation of surface heights $\sigma=2.8\text{cm}$, autocorrelation length $L_c=7.1\text{cm}$, a soil moisture of 30%, as calculated by AIEM and the HFSS model and as measured on the SMOSREX site, for: a) H polarization and b) V polarization.

Results show that both the AIEM model and the FEM approach have good agreement with the SMOSREX experimental data for surface 5, as shown in Figure 5.11. The agreement for the FEM method is better for higher angles (approximately $\geq 50^\circ$) at H polarization, as can be seen in Figure 5.11a. Agreement is good between the FEM approach and experimental data for surface 6 and at V polarisation, as shown in Figure 5.12. Agreement is less good for the AIEM approach, which predicts

values that are too low for angles above approximately 40° : there is a difference in values predicted by AIEM and experimental data of about 0.3 at 60° , at V polarisation, for surface 6, which is the equivalent of about 10K in brightness temperature. Both the AIEM model and the FEM method give similar results for surface 6 and H polarisation, which are in good agreement with experimental data for lower angles ($<40^\circ$) but are lower than the experimental data for higher angles. However at 60° the difference in emissivity is about 0.05 less for the FEM method, equivalent to about 15K in brightness temperature. For surface 7, the surface with the highest roughness, both the FEM method and the AIEM method predict emissivities that are too low. However the gap between experimental and modelled data is less for the FEM method at higher angles. For the FEM method, the difference is fairly constant for all angles, varying from 0.05 to 0.1 at H polarisation and 0.05 to 0.075 for V polarisation, in other words we observe the same trend for the FEM method as for the experimental data. However the gap between experimental and modelled data increases with angle for the AIEM model at H polarisation, varying from 0.05 at 0° to approximately 0.2 at 60° .

In order to further analyse the trends in results as a function of surface roughness, we present in Figure 5.14 the emissivity as a function of rough surface slope (σ/L_c) for the two models compared to experimental data, for polarisations H and V and at angles of a) $\theta=0^\circ$ b) $\theta=50^\circ$ and c) $\theta=60^\circ$



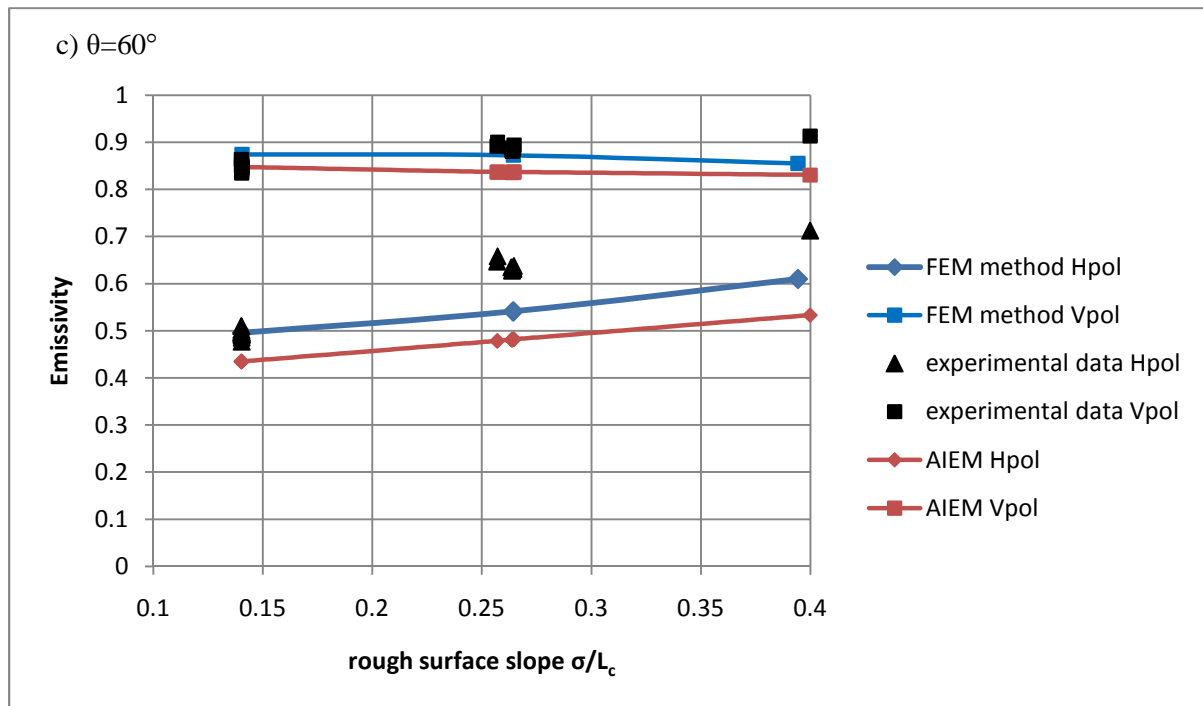


Figure 5.14: The emissivity as a function of rough surface slope calculated by the FEM and AIEM models compared to experimental data, for a soil moisture of 30%, H and V polarisation and a) $\theta=20^\circ$, b) $\theta=50^\circ$ and c) $\theta=60^\circ$.

The graphs of Figure 5.14 show that both models produce good predictions for all roughness conditions if the measurement angle is low. The AIEM model has a good agreement also for angles up to 50° if the surface has a rough surface slope of less than or equal to about 0.15. On the other hand the FEM model has a good agreement with experimental data for all angles up to 60° and a rough surface slope of less than or equal to about 0.15. At higher angles (see Figure 5.14a and b for example) and for a rough surface slope higher than 0.15, both models predict values that are too low particularly at V polarisation, but the FEM method is still overall closer to the experimental results. The difference between the experimental results and FEM model predictions at high roughness conditions could be due to the measured soil moisture and roughness values inaccurately representing the soil moisture and surface roughness across the whole field of view of the radiometer measurements. This seems likely as we see a spread in different points with the same conditions in Figure 5.11 and Figure 5.12, i.e. when we have different points of the same measured conditions the measured emissivity is not the same. This could also be due to inaccuracies in the FEM approach which we may be able to correct in future work, for example by increasing surface size or resolution.

In summary, the results presented in Figure 5.11 - Figure 5.14 show that the FEM approach has overall a better agreement with experimental data, particularly for higher angles, than AIEM. Both the FEM method and the AIEM model have a good agreement with experimental data for surfaces of moderate roughness (surface slope of about 0.15) but the FEM method makes better predictions for rougher

surfaces and at higher angles. The FEM method is still too low however for the high roughness case (high angles and H polarisation for slope=0.26 and all conditions for slope=0.39). Future work will evaluate whether these differences could be due to error in the soil moisture measurements or roughness values or due to rough surfaces being too small or having too low a resolution (number of points on the surface) in the FEM approach.

5.3.4 Conclusions

Results of this section have shown that, for all roughness conditions, we observe the same trends in the emissivity predicted by the FEM approach as with the experimental data. Results have also shown that the results of the FEM approach have an overall better agreement with experimental data than the AIEM model. In particular results are better for higher roughnesses and at higher angles. A good agreement was obtained between the FEM approach and the experimental results for a moderately rough surface. For very rough surfaces predictions of the FEM approach are lower than experimental data, but they are still closer to the experimental data than the AIEM model. We conclude then that the FEM approach gives good results for moderately rough surfaces and values that are too low for very rough surfaces but still more accurate than the AIEM approach. Further work needs to be done to determine why we have these differences between predictions of the FEM approach and experimental data at high soil roughness conditions, in particular whether this could be due to uncertainties in the soil moisture and roughness measurements or due to inaccuracies in the FEM approach such as rough surface size and/or resolution being too low.

**CHAPTER 6. EMISSIVITY OF THE SOIL-LITTER SYSTEM:
COMPARISON WITH EXPERIMENTAL DATA AND THE
SCHWANK MODEL**

6. Emissivity of the Soil-Litter system: comparison with Experimental Data and the Schwank Model

In this section we present the first results of the emissivity of the soil-litter system as calculated using the FEM approach. We model the soil and litter layers as homogeneous dielectric materials with randomly rough surfaces. As a first step in modelling the soil-litter system we consider homogeneous soil and litter layers which do not have soil moisture gradients or inclusions. The litter medium is a mixture of decomposing organic material, air and water. However since all components are smaller than the wavelength we are able to represent the litter as an effective medium of a homogeneous permittivity constant (see section 2.3). By the same reasoning, we also represent the soil layer as an effective medium with a homogeneous permittivity constant. We aim to compare the general behaviour of the emissivity of this soil-litter system, calculated by the numerical FEM approach, with results found in the literature for the emissivity of the soil-litter system. Currently very few studies of the effect of the litter layer on forest emission have been performed and only two papers present results of the emissivity of the soil-litter system. The first is an experimental paper by Grant et al (2009), in which an experimental campaign at the Bray site (Grant et al 2007) is presented, and the second is a theoretical modelling paper by Schwank et al (2008). The comparison with experimental data presented by Grant et al (2009) may also be considered a first step in validating the FEM approach for the whole soil-litter system. However the comparison with the Schwank model (2009) is a comparison only, since the model proposed by Schwank is approximate and has not yet been validated for the soil-litter system.

In the following sections we present first a summary of the studies performed by Grant et al (2009) and Schwank et al (2008), secondly the method and finally a discussion and conclusions.

6.1 The Bray 2009 Experimental campaign and the Schwank model predictions

Grant et al (2009) present experimental data taken at the Bray site in the Les Landes forest near Bordeaux, France (latitude 44°42' N, longitude 0°46' W, altitude 61 m), of the emissivity above and below the forest canopy, i.e. forest emission as a whole and emission of the soil-litter-understory layers, for different moisture conditions. This experimental data covers soil moisture conditions ranging from 15% to 30% (volumetric soil moisture), angles from 35° to 60° and H and V polarisation. The litter layer in the experimental site varied in thickness up to 10 cm and consisted of decomposing grass, pine needles, pine cones, and branches. There was also an understory layer of grass, covering the forest floor. In addition to experimental data, the authors performed simulations for the soil-litter system using a radiative transfer approach (the "Wilheit model", presented by T.T. Wilheit 1978) for flat soil and litter surfaces.

Figure 6.1, taken from Grant et al (2009), shows results of the emissivity as a function of soil moisture. The results shown in black are experimental results and include the forest emission (above canopy shown as black crosses) and the emission of the soil-litter-grass system (shown as black circles). Also shown are simulation results of the soil-litter emissivity (from a Wilheit radiative transfer model with flat surfaces) and the bare soil emissivity calculated from the Fresnel equations, which are exact for flat surfaces.

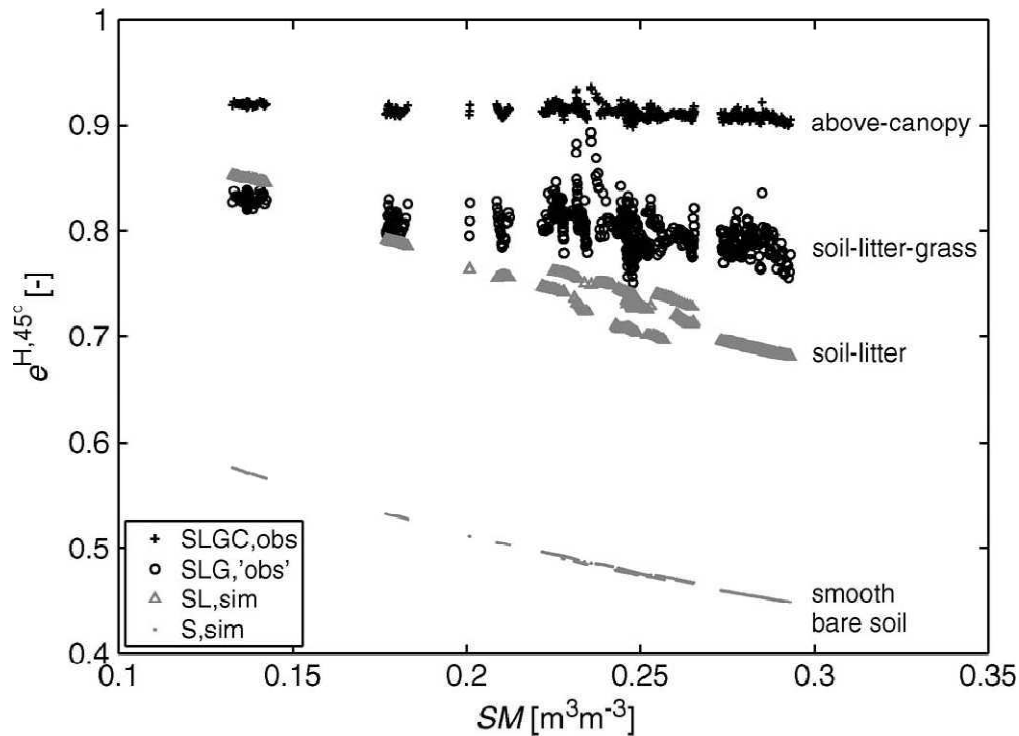


Figure 6.1: Horizontally polarized surface emissivities derived from above-canopy observations ($e_{H,45^\circ}^{SLGC,obs}$ and $e_{H,45^\circ}^{SLG,obs}$; black) and simulations ($e_{H,45^\circ}^{SL,sim}$ and $e_{H,45^\circ}^{S,sim}$; gray), plotted against volumetric soil moisture content.

The second paper by Schwank et al (2008) presents results of the reflectivity (equal to 1 minus the emissivity) calculated using a soil-litter model. This model is presented in detail in section 3.2.2.2 b2. In this model, the permittivity of the litter layer was calculated using a physical mixing formula, considering the litter to be a mixture of leaves (represented as spheroids), water and air. The soil-litter system was modelled as an effective medium with an effective permittivity $\epsilon(z)$ varying with depth z , which was equal to the litter permittivity at depths that fall within the litter medium and soil permittivity at depths that fall within the soil medium. A Fermi function was applied to smooth the transition, also accounting for small scale roughness. The roughness was estimated to have standard deviation of surface heights of 1cm for both soil and litter layers. A coherent radiative transfer model was applied to calculate the reflectivity of the soil-litter medium from the effective permittivity. Litter depth was taken to be 2cm in this model.

Results are summarised in Figure 6.2, taken from the article (Schwank et al 2008).

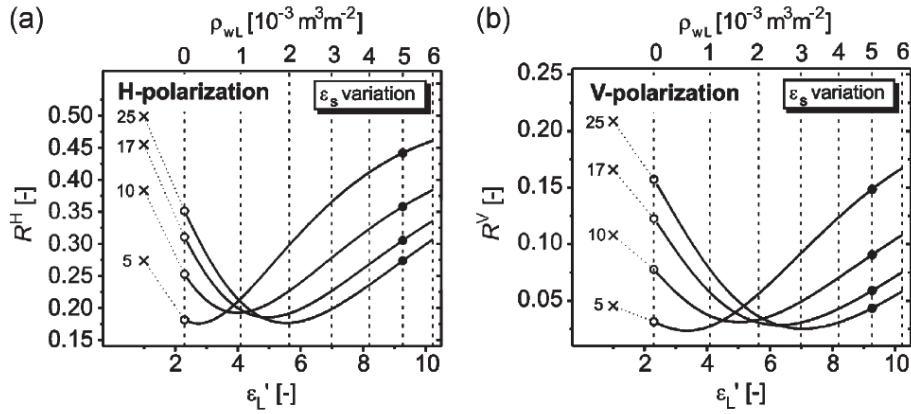


Figure 6.2: Reflectivities $R_p(\varepsilon_L, \varepsilon_S)$ of a litter–soil formation computed for litter water column density $0 \leq \rho_{wL} \leq 6 \cdot 10^{-3} \text{ m}^3 \cdot \text{m}^{-2}$, angle $\alpha = 50^\circ$, and $T = 290 \text{ K}$. Data are shown for (a) $p = H$ and (b) $p = V$ and the imaginary part of the soil permittivity $\varepsilon_S = 5, 10, 17, 25$. The crosses and the hollow and the bold dots are R_p 's for the bare soil, the drained litter condition ($\rho_{wL} = 0 \text{ m}^3 \cdot \text{m}^{-2}$), and the wettest observed litter condition ($\rho_{wL} = 5 \cdot 10^{-3} \text{ m}^3 \cdot \text{m}^{-2}$), respectively.

6.2 Method

The emissivity of the soil-litter system was calculated using the FEM approach described in section 4.1. Both soil and litter layers were represented as dielectric materials of homogeneous permittivity and with rough surfaces. In order to minimise the calculation time, the volume of the soil layer was replaced by the layered impedance boundary condition on the soil rough surface, as with calculations performed in chapter 7. The calculation area for the soil-litter system thus consisted of a litter layer with a rough surface, bordered by a vacuum above and a rough surface representing the soil layer below. Radiation boundary conditions were applied to the boundaries of the vacuum and layered impedance boundary conditions applied to the boundaries of the litter layer. The impedance boundary conditions were set to the litter permittivity at the sides of the litter layer and to the soil permittivity on the rough surface representing the soil, at the bottom of the litter layer. This is shown in

Figure 6.3.

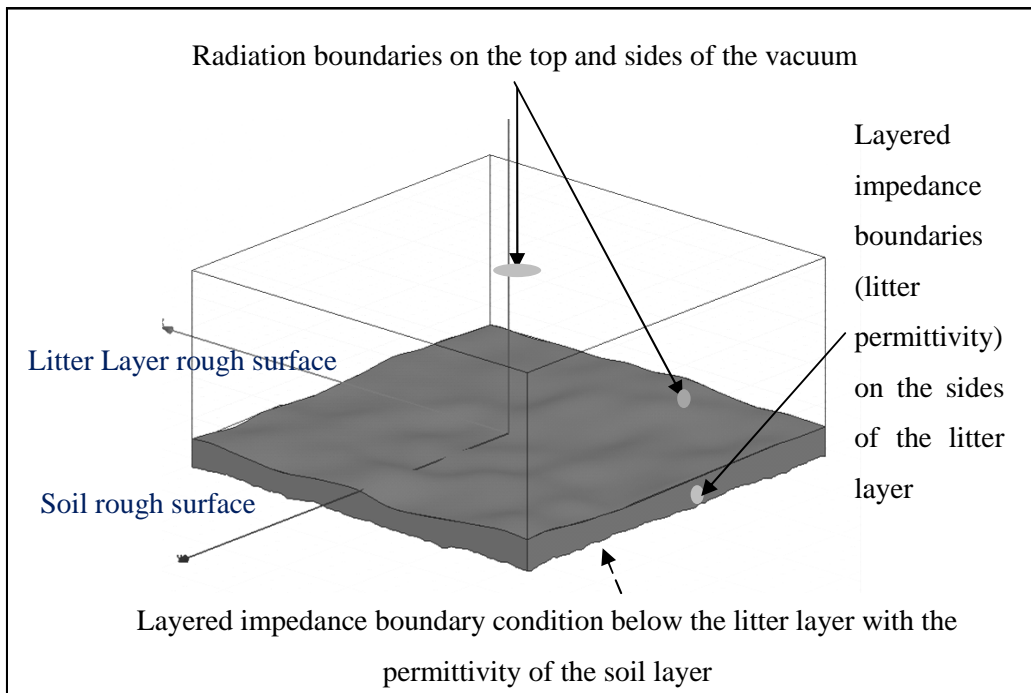


Figure 6.3: The HFSS Calculation Area in the FEM approach

The values of the model parameters were set to those chosen in section 4.2. This included 5 simulations for each soil-litter structure ($N=5$), the width of the litter and soil layers of $L \times L = 1.27\text{m} \times 1.27\text{m} (= 6\lambda \times 6\lambda)$, a plane incident beam, and an integration step of 0.5° . Note that 5 rough surfaces were created using the procedure shown in Figure 4.2 in section 4.1.2.1, for each roughness condition considered for the soil and litter layers. From these rough surfaces we created 5 different soil-litter structures for each combination of soil and litter roughness. Each of these 5 structures had soil and litter surfaces that were different from the other 4 structures, but had the same autocorrelation function, standard deviation of surface height, σ , and autocorrelation length L_c .

Calculations were performed at 1.4 GHz, both H and V polarisation and at an angle of $\phi=0^\circ$, and $\theta=40^\circ$.

Conditions for the soil and litter layers, including roughness, moisture and litter depth, were chosen to be those found in the field. Note that although we wish to compare with Schwank model we did not use the soil and litter conditions chosen by Schwank et al since we only wish to compare the general behaviour of the soil-litter emissivity and not absolute values. We chose one soil roughness and two litter roughnesses, whose values of σ and L_c are given in table I. An exponential autocorrelation function was used for the soil surface and gaussian autocorrelation functions for the litter surfaces. A low soil roughness was chosen, still within the range of rough surfaces found in the field, and an exponential autocorrelation function chosen since soil roughness profiles have been shown to be more similar to exponential autocorrelation functions than gaussian. On the other hand there is currently no available data in the literature on the roughness of the litter layer. We therefore estimated that σ and L_c

would have similar values to values of σ and L_c for a soil surface and so we chose values of relatively low surface roughness, since calculations are then faster and require less memory, but still within the range of soil roughnesses found in the field. On the other hand we chose to use gaussian autocorrelation functions since the litter tends to collect in rounded clumps, forming a profile which appears to be smoother than the soil profile and so we estimate that the litter roughness profile will be closer to a gaussian than an exponential autocorrelation function.

Table 6-I: Roughness conditions for the soil and litter surfaces

Medium	Standard deviation of surface height, σ (cm)	Autocorrelation length (cm)
Soil	0.44	9
Litter 1	0.4	12.4
Litter 2	0.8	12.4

We therefore had two different roughness combinations: the soil rough surface combined with litter 1, which we shall call soil-litter1, and the soil rough surface combined with litter 2, which we shall call soil-litter2.

We chose a litter depth of 8cm which is within the range of values found in the field. The roughness values and litter depth were chosen to be close to values observed during an experimental campaign performed at the SMOSREX site during 2009 and 2010. In this campaign the ground (with a rough surface) was covered with grass litter and the brightness temperature of the soil-litter system measured at 40°, H and V polarisation, and on different days with different moisture conditions. The litter depth and roughness values shown in Table I are also similar to values observed during the Bray 2009 campaign: the litter depth was observed to vary between 0 and 10cm during this campaign and although roughness was not measured the authors estimate it to be low on the Bray site.

Soil and litter permittivities were calculated respectively from soil and litter moisture content. Firstly we considered the soil and litter moisture to be related, so that litter moisture increases with soil moisture. We applied the following empirical relationship found by Grant et al on the Bray site, and presented by Della Vecchia et al (2007):

$$LM(\text{grav}) = SM(\text{vol}) \quad 0 < SM < 0.1 \quad (6.1a)$$

$$LM(\text{grav}) = 3.0971 * SM(\text{vol}) - 0.1817 \quad 0.1 \leq SM \leq 0.35 \quad (6.1b)$$

$$LM(\text{grav}) = 0.9 \quad SM < 0.35 \quad (6.1c)$$

where LM(grav) is the gravimetric litter moisture and SM(vol) is the volumetric soil moisture. Since in general we deal with gravimetric soil moisture, SM(grav), for the litter moisture calculations we first calculated the volumetric soil moisture SM(vol) from the gravimetric soil moisture using (2.99), which for a water density ρ_w of 1 gcm^{-3} , is given by:

$$SM(\text{vol}) = SM(\text{grav}) * \rho_s (\text{gcm}^{-3}) \quad (6.2)$$

where ρ_s is the bulk soil density, which we took to be 1.4 gcm^{-3} as measured on the SMOSREX site (see Escorihuela et al 2007).

In order to calculate the permittivity of the soil from the soil moisture SM(grav) we applied the Mironov model for a soil texture of 16.6% clay and 83.4% sand, as measured on the SMOSREX site (de Rosnay et al 2006a), and a temperature of 290K. In order to calculate the litter moisture we applied the following empirical relationship found by Demontoux et al (2008):

$$\epsilon'_{\text{litter}} = 2.3 \tanh(8(\text{LM} - 0.65)) + 5.8\text{LM} + 4.1 \quad (6.3a)$$

$$\epsilon''_{\text{litter}} = 1.25 \tanh(18(\text{LM} - 0.63)) + 1.35 \quad (6.3b)$$

Note that this relationship was determined from laboratory measurements of the permittivity constant of litter samples taken from the Bray site, where the experimental campaign by Grant et al (2009) was performed. These litter samples therefore consisted of decomposing grass, pine cones, pine needles.

The soil and litter moistures and their corresponding permittivity values are given in table II.

Table 6-II: soil and litter moistures and their corresponding permittivity values

SM(% grav)	SM(% vol)	LM(% vol)	Soil permittivity	Litter permittivity
10	14	25	5.313+0.443i	3.269+0.100i
20	28	69	10.288+1.025i	8.712+2.301i
30	42	90	16.893+1.837i	11.537+2.600i

We firstly calculated the emissivity of the soil-litter1 and soil-litter2 for the soil and litter permittivities given in table II, assuming that the litter and soil moistures are related. Thus we performed calculations for the first soil permittivity combined with the first litter permittivity, then the second soil permittivity combined with the second litter permittivity, etc. We also calculated the emissivity of the bare soil for soil permittivities shown in table II and soil roughness shown in table I. These calculations allowed us to compare results with the Bray experimental results given by Grant et al (2009). Secondly we calculated the emissivity of the soil-litter2 structure for all combinations of soil and litter permittivities shown in table II, assuming that the soil and litter moistures are not correlated.

This allowed us to observe the effects of litter moisture at fixed soil moisture and vice versa, and also to compare with results of the Schwank soil-litter model presented by Schwank et al (2008).

6.3 Results and Discussion

Figure 6.4 shows results of the emissivity of the soil-litter and bare soil systems, calculated with the FEM approach, and assuming the relationship between litter and soil moisture given by (6.1a) – (6.1c) is valid. Results are presented for H and V polarisation.

These results show a good general agreement with the experimental data reproduced in Figure 6.1, from Grant et al (2009). We see that the presence of the litter layer causes an overall increase in emissivity and we observe that the curve is generally flatter in the presence of the litter, as with the experimental results shown in Figure 6.1. This flattening of the curve indicates that the sensitivity of the emissivity to soil moisture is diminished in the presence of a litter layer, which is consistent with conclusions of Grant et al (2007, 2009). We note in Figure 6.4 the high influence of the litter surface roughness, which is a new result. When we double the litter surface standard deviation of surface heights (and also the surface slope) from the soil-litter1 to soil-litter2 structure, we observe a high increase in emissivity, particularly for H polarisation and for high soil moisture (or litter moisture).

Figure 6.5 shows the emissivity of the soil-litter2 system as a function of litter moisture, for fixed values of SM(grav) and for H and V polarisation. Results presented in this figure show that emissivity generally decreases with litter moisture, albeit with a low gradient. We also observe that at high litter moisture values the emissivity no longer depends on soil moisture: the litter layer completely masks the signal from the ground. This is consistent with conclusions from Grant et al (2007, 2009).

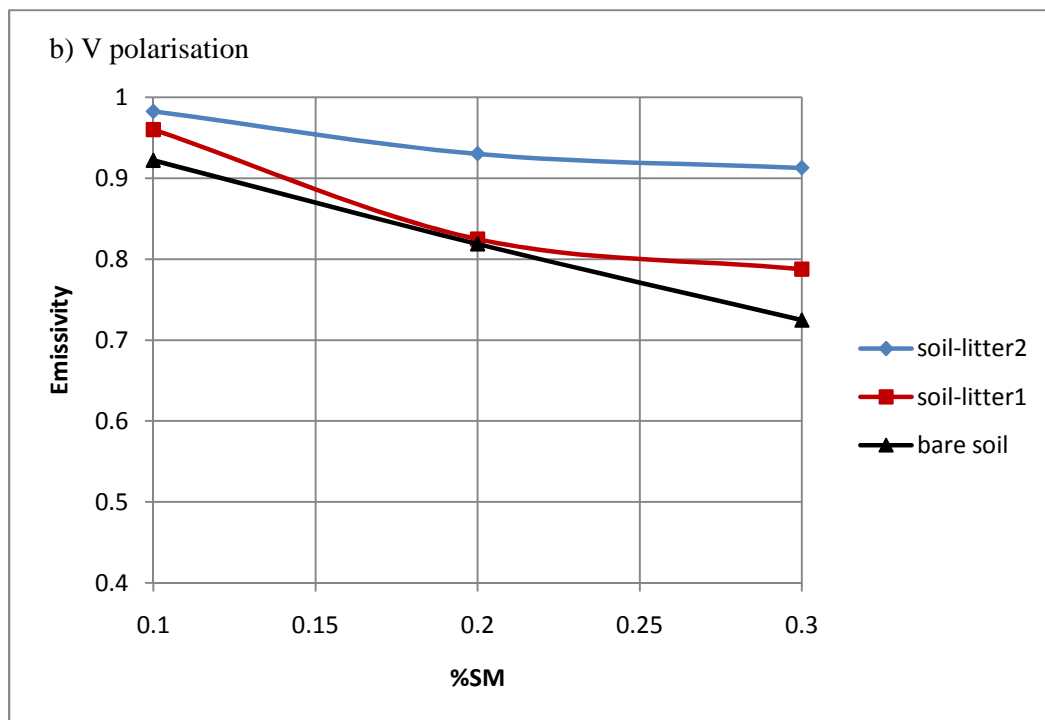
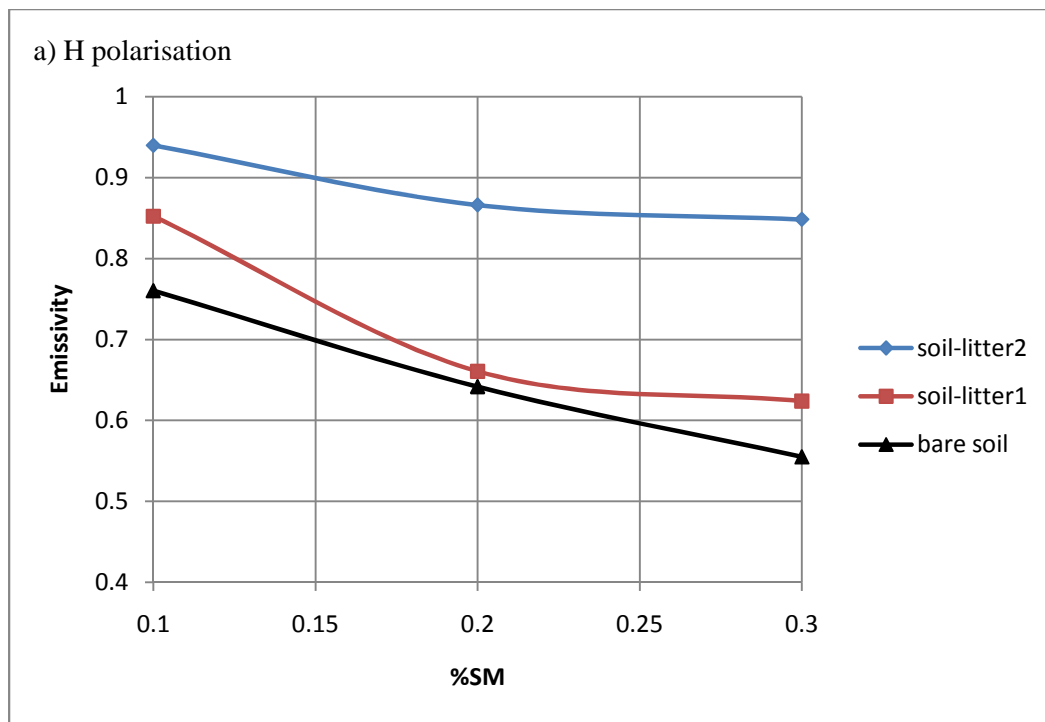


Figure 6.4: The emissivity calculated using the FEM approach at 40° for a bare soil of roughness $\sigma=0.44\text{cm}$, $L_c=9\text{cm}$, and a soil of the same roughness covered by litter layers of two different roughnesses, calculated as a function of gravimetric soil moisture content and at a) H polarisation and b) V polarisation

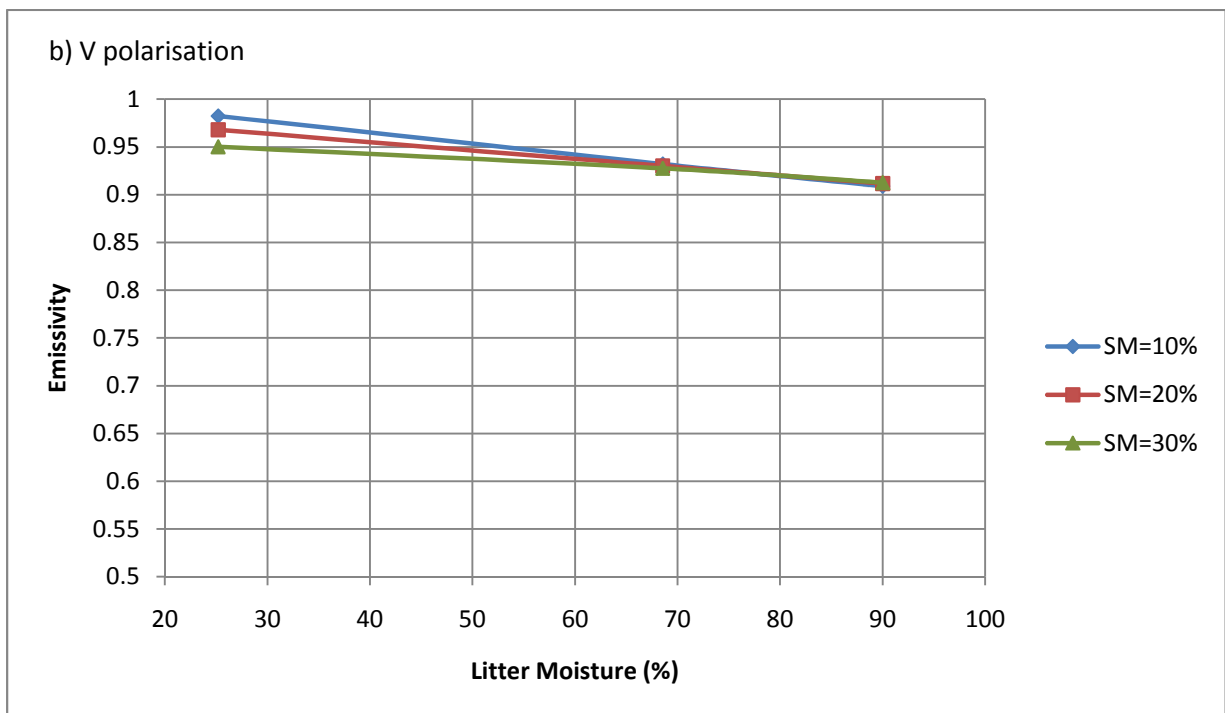
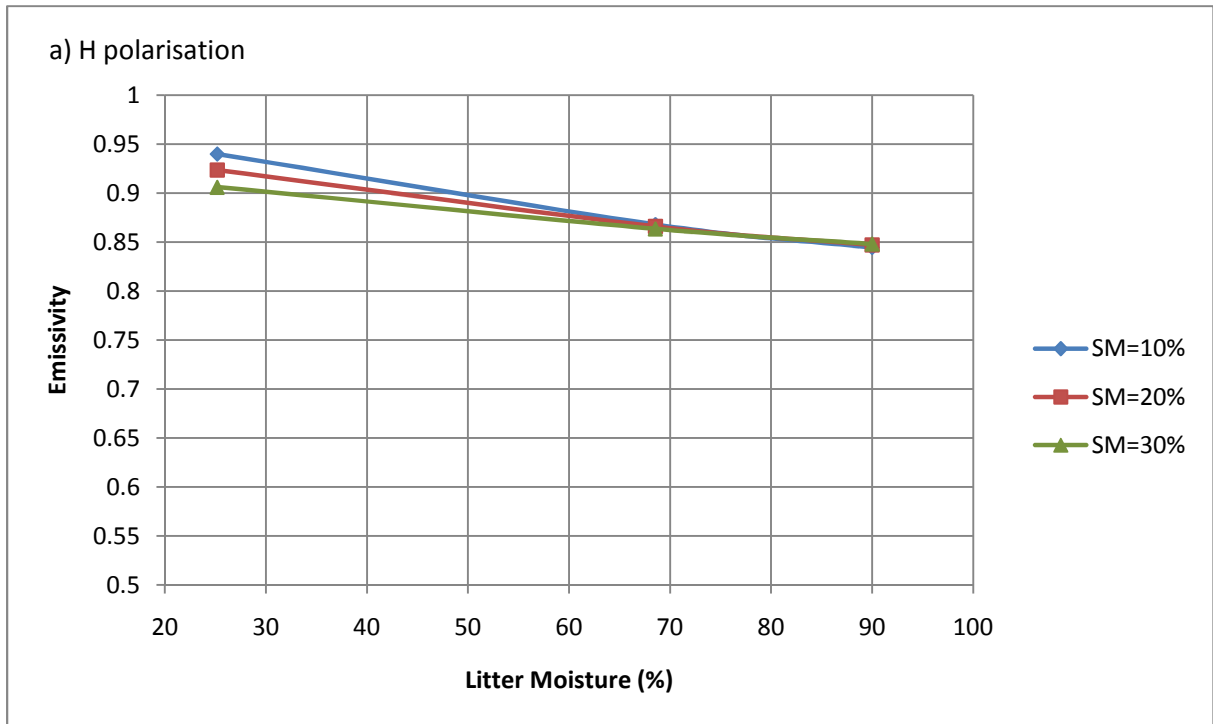


Figure 6.5: The emissivity calculated for the soil-litter system as a function of volumetric litter moisture content, calculated for fixed values of soil moisture, 40° , at a) H polarisation and b) V polarisation

Figure 6.6 shows the reflectivity as a function of the real part of the litter permittivity, for fixed values of soil permittivity. This allows us to compare with results of the Schwank model (2008) presented in Figure 6.2. Note that the points shown at $\epsilon_r'=1$ correspond to values calculated using the FEM

approach for a bare soil of roughness $\sigma=0.44\text{cm}$, $L_c=9\text{cm}$ and different soil permittivities. Again results are shown for H and V polarisation.

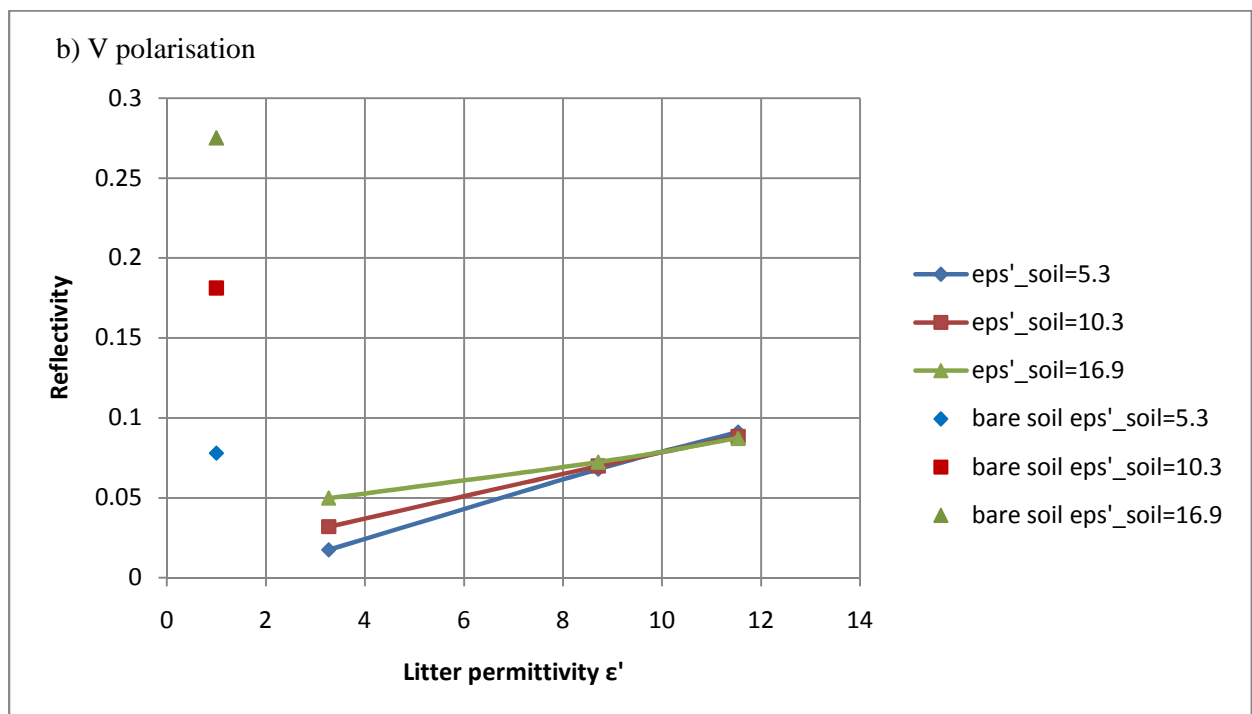
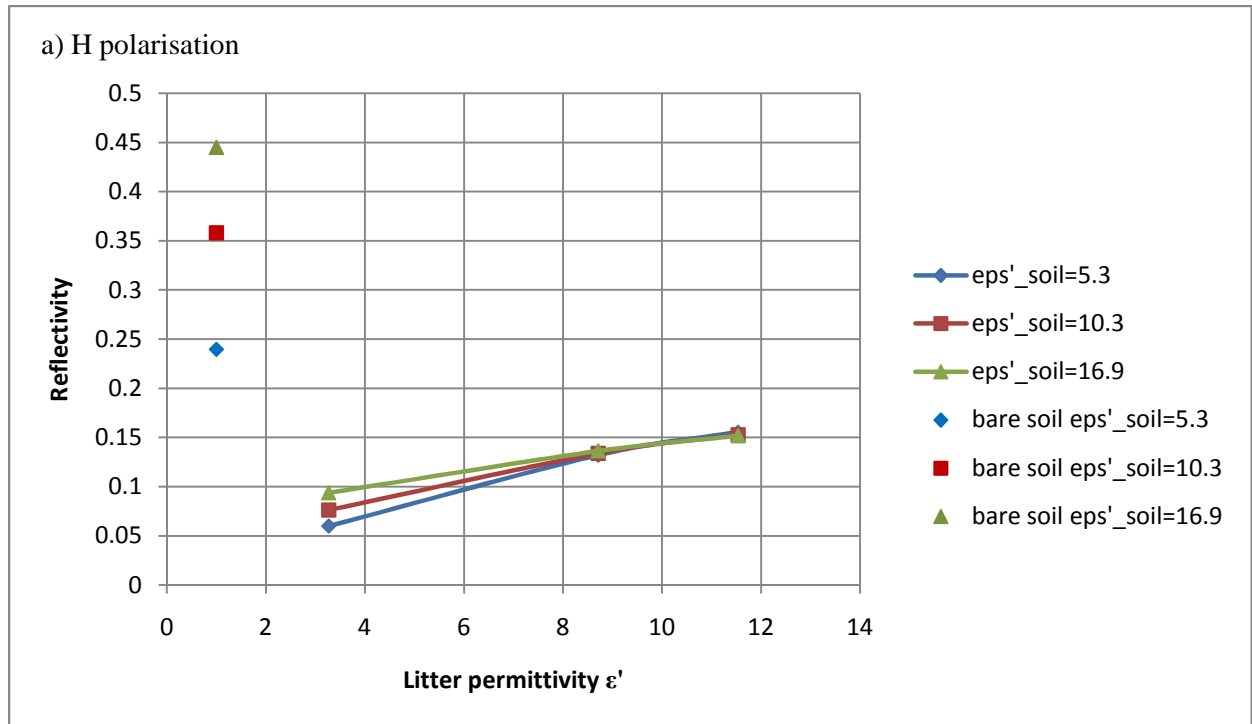


Figure 6.6: The reflectivity calculated by the FEM approach for the soil-litter system, as a function of the real part of the litter permittivity, for three different fixed values of soil permittivity (values given in table II) and for a) H polarisation and b) V polarisation.

Figure 6.6 shows that in general the soil-litter reflectivity increases with litter permittivity in a manner similar to that calculated by the Schwank model, shown in Figure 6.2. In both Figure 6.2 and Figure 6.6 we also observe that, in general, the reflectivities of the soil-litter system are lower than those of the bare soil, with the exception of the case when the soil permittivity is low and the litter permittivity high. The presence of a litter layer introduces mechanisms to both increase and decrease emission. The litter layer attenuates the soil emission which overall decreases the emission of the soil-litter system. However it also acts as an impedance-matching layer so that the soil emission is higher in the presence of the litter. Also the litter itself has an emission which adds to the overall signal. The results of Figure 6.2 and Figure 6.6 show that the overall effect of the litter layer is to increase the emission. Figure 6.6 shows that the exception to this is for low soil permittivity and high litter permittivity where the overall effect of the litter layer is to reduce the emission. In this case the litter layer's permittivity is higher than that of the soil and so it no longer acts as an impedance matching layer but rather attenuates strongly the soil emission. Also the emission of the litter layer itself is at its lowest for high moisture conditions.

A main difference between Figure 6.2 and Figure 6.6 is that at low litter moisture we observe a crossing over of the curves representing different soil moistures in Figure 6.2, which is not observed in Figure 6.6. Instead, in Figure 6.6 the curves representing different soil moistures cross at high litter permittivity, which is not observed in Figure 6.2. This crossing over represents a very low sensitivity of emission to soil moisture. It is therefore more logical that this will occur at high litter moisture, when the litter layer more effectively masks the soil, as shown in experimental data (e.g. Grant et al 2007, 2009). Therefore the FEM approach appears to model the soil-litter system more accurately than the Schwank model.

6.4 Conclusions and Perspectives

In this chapter we have presented a study of the emission of the soil-litter system as a function of soil and litter moistures, calculated by the FEM approach. We compare results with those found in the literature, in particular experimental results presented by Grant et al (2009) and the Schwank model (2008), which is not exact. Results show a good general agreement with the experimental results, validating the numerical approach for the case of the two layer soil-litter system. Results agree in general with the Schwank model. However the Schwank model predicts a low sensitivity to soil moisture for low litter moisture values whereas the FEM approach predicts a low sensitivity to soil moisture for high litter moisture values. The latter is more consistent with experimental results indicating that the FEM approach is more accurate than the Schwank model. From this study we can also conclude that the roughness of the litter layer has a large effect on the emission of the soil-litter system. To our knowledge, this is a new result since a soil-litter system with rough surfaces has not previously been studied.

Future work will further validate the FEM approach as a tool to model the emission of the soil-litter forest system by comparing results of the emissivity with experimental data over a range of soil moisture and roughness conditions. However there is currently very little data of the soil-litter emission available in the literature, and none in which the surface roughness was measured. An experimental campaign must therefore be performed for this validation. With this in mind, we carried out an experimental campaign on the SMOSREX site during 2009 and 2010, where a rough ground surface was covered with grass litter and the radiometric brightness temperatures measured at 40° and H and V polarisation for different ground moisture conditions. The ground temperature, soil and litter moistures, and soil and litter surface roughness were also monitored.

Once the modelling approach has been validated it can be used to study the effects of a number of different parameters on the soil-litter emission. The emission can be calculated at different angles and polarisations and for different surface roughnesses, soil and litter permittivities (moisture content), and litter depth. Thus we will be able to study the effect on the soil-litter emission of each of the following variables: litter depth, soil surface roughness, litter surface roughness and soil and litter moisture contents. We will be able to study the importance of the effects for angles and polarisations.

CHAPTER 7: CONCLUSIONS

7. Conclusions

During this PhD we have developed a numerical modelling approach which allows us to calculate the scattering and emission of a two-layer heterogeneous system representing the soil and litter layers in forests. This approach relies on the use of Ansoft's HFSS software, which solves Maxwell's equations using the Finite Element Method (FEM), and is therefore an exact numerical approach. In this approach, which we refer to as the numerical FEM approach, we are able to model many features of the soil-litter system including randomly rough surfaces, moisture content, and litter depth. We can calculate the bistatic scattering coefficient and emissivity of such a system at H and V polarisation, and incident angles in the range of 0 to 90°. The approach was developed in the context of the SMOS mission and so was developed for a frequency of 1.4 GHz (SMOS frequency) but it can be adapted to other frequencies. It was developed as a tool that will enable us to study in detail the emission of multilayer systems, with rough surfaces, in general and the soil-litter system in particular. To our knowledge there is currently no numerical modelling approach that allows us to model a two layer system with randomly rough surfaces, at L-band frequencies. It is important to study the emission of the soil-litter system since it is not yet well understood and has not been accurately accounted for in the inversion algorithm used to retrieve soil moisture from SMOS measurements over forests. Using the approach developed during this PhD, it is now possible to create a synthetic database of the emission of the soil-litter system at 1.4 GHz, as a function of numerous different parameters including measurement parameters such as angle and polarisation and also physical parameters of the soil and litter layers, such as the surface roughness and moisture content. Such a database will allow us to study the emission of the soil-litter system under many different conditions. This was not possible before the work of this PhD.

In this thesis we have presented the approach developed for modelling the scattering and emission of the soil-litter system and also a sensitivity study performed to set the values of the important model parameters. We then presented a validation of the approach for the case of a single homogeneous dielectric layer with a randomly rough surface (representing the bare soil). As a first step, we compared results of the scattering and emission of this system, as calculated using our numerical FEM approach, with predictions of the Method of Moments (MoM) model and also with experimental data. The Method of Moments is considered to be the most accurate method for calculating rough surface scattering and emission but cannot easily be adapted to heterogeneous or multilayer structures such as the soil-litter forest system. We compared results of the bistatic scattering coefficient, backscattering coefficient and emissivity with the Method of Moments for surfaces of low to moderate roughness and for both dry soil moisture conditions (for the bistatic scattering and backscattering coefficients) and wet soil moisture conditions (for the emissivity). Results showed a good general agreement between the Method of Moments and the new FEM approach, validating our approach for the rough surface

case and for rough surfaces of low to moderate roughness. Results showed a better agreement for the emissivity than for the active case (backscatter and bistatic scattering coefficients) indicating that our approach produces more accurate results for emissivity calculations than for scattering calculations. These results are of particular interest since, to our knowledge, the emissivity has never been calculated using the FEM method before, as it was not considered to be accurate enough. We conclude from our results however, that although the Method of Moments is a more accurate model for the case of rough surface scattering and emission, our approach is nevertheless a good complimentary method, producing results in good agreement with MoM, and has the advantage that it can be extended to model multilayer, heterogeneous media such as the soil-litter system.

As a second step in the validation of the numerical FEM approach, we compared results of the emissivity of the bare soil with a rough surface, with experimental data from the SMOSREX 2006 campaign, for high soil moisture conditions and for high to very high roughness conditions. We found that the FEM approach had a very good agreement with experimental data for high roughness conditions, at a rough surface slope of approximately 0.14, but somewhat underestimated the emissivity at very high roughness conditions, at a rough surface slope of about 0.39. In all cases, however, results of the FEM approach showed the same general trend as the experimental data. At a surface slope of around 0.26, which is already very high, our approach had a good agreement with experimental data for lower measurement angles (less than or equal to 40°) but predicted values that were up to approximately 30K too low for higher angles. However there are uncertainties in the experimental data of soil moisture measurements and roughness measurements since these were measured by taking samples in the field which may not be representative of the whole field of view. The differences between the FEM approach and experimental data at very high roughnesses may be due to these uncertainties. In addition we may be able to improve results of the FEM approach for example by increasing the size of the surfaces in the model at certain roughness conditions.

From results of the validation against the Method of Moments and experimental data, we conclude that our numerical approach is accurate for rough surfaces of a surface slope up to about 0.26 for lower angles (40° or less) and up to between 0.14 and 0.26 for angles higher than 40° . It appears that the FEM approach somewhat underestimates the emissivity of rough surfaces with higher surface slopes. However this could be due to the effects of uncertainties in soil moisture and roughness measurements on the measured emissivity values used for this validation. Future work will evaluate this and also whether results of the FEM approach can be improved, by increasing the surface size or resolution, for example. However since surface slopes of 0.14 and 0.26 are still fairly high, for now we can conclude that our method gives good results for rough surfaces in the majority of cases. As a comparison, we also compared the experimental data to predictions of the analytical IEM model, used often to calculate rough surface scattering and emission. The IEM approach is faster than our method but since it is not exact it has a limited validity region. We found that our approach had a better overall

agreement with the experimental data than the analytical IEM approach, even though we considered high soil moisture which is within the IEM validity region. In particular the FEM approach had a better agreement for high angles and high roughnesses. For example, the differences between results of the emissivity for the IEM approach and experimental data were approximately 0.2 at very high roughness and a high angle (50°), equivalent to about 60K, whereas the FEM approach only underestimated the emissivity by about 0.2, or 30K, under these same conditions.

We presented next in this thesis the first calculations of the emissivity of the soil-litter system at 1.4 GHz and H and V polarisation. We modelled the soil-litter system as two homogeneous dielectric layers each with rough surfaces: for the moment not including any further heterogeneous features such as soil moisture gradients or inclusions. We performed calculations for different soil and litter moisture conditions, one surface roughness condition for the soil layer and two surface roughness conditions for the litter layer. The soil permittivity was calculated from soil moisture using the model presented by Mironov et al (2009) and the litter permittivity was calculated from the litter moisture using a relationship found experimentally by Demontoux et al (2008). As a first step in validating the approach for the two-layer system, we compared results with experimental data presented by Grant et al (2009). Since not all input values required for the modelling approach were measured in this experimental campaign (notably surface roughness was not measured) we estimated these parameters and therefore only compared general trends of the results and not absolute values. Results of the FEM method showed a good general agreement with experimental data, predicting key features such as (in general) an increase in emission and a loss in the sensitivity of the emissivity to soil moisture, in the presence of a litter layer. Results of the FEM method also indicated that the litter roughness has a strong influence on the emission of the soil-litter system, a case that has not been studied to date. We also compared results of the FEM approach to those of an analytical model presented by Schwank (2009), which calculates the litter permittivity using a dielectric mixing model and calculates the emissivity of the soil-litter system using a coherent radiative transfer model. We concluded that the FEM approach produces similar results to the Schwank approach and in the cases where the results are different the FEM approach produces results that are more consistent with experimental data. The FEM approach better reproduces the loss in the sensitivity of forest emissivity to soil moisture at high litter moisture values, which is observed experimentally by Grant et al (2007, 2009).

CHAPTER 8: PERSPECTIVES

8. Perspectives

Since the FEM approach developed in this thesis is somewhat inaccurate for very high roughnesses further work is necessary to develop and improve its accuracy for surfaces of high roughness. In order to do this the sensitivity analysis presented in section 4.2 could be extended to further roughness conditions and also to include the surface resolution, a parameter that was not tested. In particular, a study could be performed to investigate the effect of the surface size on the calculated emissivity value for a range of roughness conditions (different values of standard deviation of surface height and autocorrelation length). In section 4.2 the surface size was tested only for very low roughness and very high roughness conditions and we found that in these cases a smaller surface size ($L=6\lambda$) was sufficient. However we expect surface size to have a high influence on the accuracy of the model and so it would be of interest to study this in more depth. In particular, we expect the surface size that is required for an accurate solution to depend on the autocorrelation length and so it would be of interest to study the effect of surface size if we fix the standard deviation of surface height and vary the autocorrelation length. Also, a study of the effect of surface resolution on emissivity for surfaces of different roughnesses could be performed. For the work of this thesis, surface resolution was fixed at 1cm (equivalent to 21 points per wavelength) since this seemed to be a good resolution when compared with values used by the Method of Moments (Zhou et al used a lower resolution of 16 points per wavelength or 1.3cm) yet did not have a heavy associated calculation cost (the lower the resolution the higher the calculation cost). However it would be of interest to evaluate the effect on the results of increasing or decreasing resolution. In particular, we expect rougher surfaces to require a higher resolution so that the surface roughness is sampled in small enough intervals to be representative of the surface profile. In these studies, it is also important to evaluate the effect of surface resolution and the width of the calculation area (size of the rough surface) on calculation cost. This will allow us to select values for the width and resolution that do not have unreasonably high calculation costs. Furthermore, studying calculation cost (CPU calculation time and memory requirements) will potentially allow us to optimise the modelling approach, by allowing us to select parameter values that lower the calculation costs whilst maintaining accuracy. We could also study whether the convergence criterion of the numerical simulations can be reduced, which would reduce calculation costs, while still maintaining accuracy of the results.

In order to develop the modelling approach further for calculations of the soil-litter system, we must further test and validate the model for a two layer system representing the soil and litter layers. In this thesis we have shown that, for low roughness conditions, the FEM approach produces results that are in agreement with experimental data in their general behaviour and main features but it is important to extend this validation to a comparison of absolute values over a range of different conditions. Since there are currently no exact modelling methods for this, this validation must be done by comparison

with experimental data. However there is currently very little data of the soil-litter emission available in the literature, and none in which the surface roughness was measured. An experimental campaign must therefore be performed for this validation. With this in mind, we carried out an experimental campaign on the SMOSREX site during 2009 and 2010, where a rough ground surface was covered with grass litter and the radiometric brightness temperatures measured at 40° and H and V polarisation for different ground moisture conditions. The ground temperature, soil and litter moistures, and soil and litter surface roughness were also monitored. It is important in future work to validate our approach against this data. In order to accurately perform this validation we would need to carry out further tests to determine some of the model parameters. In particular, we would need to test how many simulations are required, for each roughness condition, since we now have two rough surfaces in each simulation instead of one. It would also be important to verify values for the surface size and incident beam since with the inclusion of a second layer edge effects may be more significant and therefore we may now need to use larger surfaces and/or a gaussian incident beam to reduce the effects of these errors.

Once the model has been validated for a two layer system we will be able to use it to create a database of the emission of the soil-litter forest system. This will require a very large number of calculations therefore, before doing this, steps could be taken to optimise the approach used. We could aim to optimise the calculation costs as previously mentioned by studying the effects of the surface resolution on calculation costs and accuracy. Also, one of the disadvantages of our approach compared to those that have been written in code is that it is not automatic. Approaches that do not utilise software are usually automatic, making use of the Monte Carlo method to average the emissivity over a large ensemble of rough surfaces, so that we simply input all the model parameters that we wish to test (e.g. dielectric constant, roughness, incident angle, etc.) and the emissivity is calculated automatically. Since our approach uses several different software tools, it is not possible to make it entirely automatic. However perhaps it is possible to make some parts of the approach automatic. For example the process of building the structure to be studied is currently done using several different tools (R and C4W's 2D shop model design). We may be able to find one tool which creates both the rough surface and the volume to be studied in a .sat format, which can then be directly integrated into HFSS.

Once the approach has been validated for the soil-litter system it can be used to study the effects of various parameters on the emission of the soil-litter system in forests. Parameters that can be studied include soil moisture, litter moisture, litter roughness, soil roughness and litter depth. For example we can investigate whether the presence of the litter layer diminishes the effect of the rough soil surface on the signal. Studies can be performed for H and V polarisation and a range of different angles.

The FEM modelling approach developed in the work of this PhD can also be extended to applications other than L-band emission of the soil-litter system. The approach can easily be extended to any

multilayer systems with rough surfaces where the media can be represented as homogeneous dielectrics. With a little more development it would also be possible to model heterogeneous media such as trees, etc., using simple shapes like spheroids and cylinders. The model can also be extended to different frequencies, provided a study was performed of the surface size required for each frequency. The numerical Finite Element Method is particularly well suited to studies of heterogeneous media and our approach, which uses an electromagnetic modelling tool based on FEM, can also be extended to include studies of heterogeneous media. Currently, work is being done in the IMS laboratory to extend the modelling of rough surface emission to include temperature and moisture gradients for example.

The numerical FEM approach can also be used for radar applications. In this thesis we concentrate on the emissivity case since our application is the SMOS mission. However the approach developed during this PhD also allows us to calculate the bistatic scattering coefficient and so we could equally use the FEM numerical approach for radar applications, for example for ESA's current BIOMASS mission, which aims to estimate the forest biomass by use of a P-band space-borne Synthetic Aperture Radar (SAR) satellite (Le Toan 2010). In extending the approach to radar applications we would need to extend the sensitivity study used to fix model parameters (presented in section 4.2) to include the bistatic case, for example studying in more depth the number of surfaces required for each calculation of the bistatic scattering coefficient.

CHAPTER 9. APPENDIX A: RESUME EN FRANÇAIS

9. Appendix A : Résumé en Français

Ce manuscrit de thèse est composé de 8 chapitres. Le premier chapitre présente une introduction au travail en expliquant le contexte, la motivation et les objectifs de la thèse. Le contexte de ce travail de thèse est la mission spatiale SMOS (Soil Moisture and Ocean Salinity). Cette mission repose sur un satellite apportant un radiomètre interférométrique multi-angulaire qui mesure l'émission thermique microonde naturelle venant de la Terre à une fréquence de 1.4 GHz (bande L). L'objectif de la mission est de retrouver l'humidité du sol et la salinité des océans en appliquant un algorithme d'inversion sur les mesures effectuées. Cet algorithme est basé sur le modèle L-MEB (L-band Microwave Emission of the Biosphere) (Wigneron et al 2001). L'humidité du sol est une variable clé pour comprendre le cycle hydrologique. Les applications de la mesure de ce paramètre à l'échelle globale sont nombreuses, notamment pour la météo et dans le domaine agricole.

L'émission thermique des surfaces continentales est très sensible à l'humidité du sol dans le domaine microondes. Cependant d'autres paramètres ont aussi une influence non-négligeable. Il est important de prendre en compte les effets de tous ces paramètres dans l'algorithme de SMOS afin d'extraire correctement l'humidité du sol des mesures du satellite. Nous avons orienté le travail de cette thèse vers une amélioration de la compréhension des effets des paramètres forestiers. Pour comprendre l'émission d'une forêt nous considérons qu'elle peut être représentée par une structure de quatre couches diélectriques homogènes. Les couches sont le sol, une couche de litière végétale, le sous-bois qui comprend tout type de végétation plus petite que les arbres (de l'herbe,...), et la canopée qui comprend les arbres. Les effets de la canopée et du sous-bois ont été beaucoup étudiés et sont bien pris en compte dans le modèle LMEB. Cependant l'effet de la litière n'a été que très peu étudié à présent mais les études expérimentales de Grant et al (2009) indiquent que la litière a pourtant un fort effet sur l'émission pour les conditions très humides. Elle augmente notamment l'émission globale et elle diminue la sensibilité de l'émission à l'humidité du sol. L'objectif de cette thèse était de développer et de valider un modèle qui permettra d'étudier en détail l'effet de la litière sur le signal forestier. Ce modèle doit calculer l'émission du système bicouche sol-litière et doit prendre en compte les effets de tous les paramètres de ce système qui peuvent influencer son émission, tels que la rugosité de surface, les permittivités du sol et de la litière, etc. L'objectif final de ce modèle est la création d'une base de données de l'émission du système sol-litière en fonction de nombreux paramètres. Cette base de données sera utile pour valider et/ou améliorer la prise en compte de l'effet de la litière dans l'algorithme de la mission SMOS.

Dans le chapitre 4 nous présentons l'approche de modélisation développée. (Le choix de l'approche est expliqué au paragraphe 3.3.) Cette approche comprend plusieurs étapes. La première étape est la création des structures à étudier. Ceci est fait à l'aide de deux logiciels : le programme R et le

programme « 3D Shop Model Design » de la société C4W. Avec R nous créons les surfaces aléatoirement rugueuses qui ont des paramètres de rugosité σ (l'écart type des hauteurs), L_c (la longueur d'autocorrélation) et une forme de la fonction d'autocorrélation bien définis. Nous construisons ensuite des structures 3D bicouches, comportant des surfaces rugueuses, qui représentent le système sol-litière, à l'aide de « 3D Shop model design ». Nous introduisons chaque structure créée dans HFSS (High frequency Structure Simulator de la société ANSOFT) puis nous définissons des conditions de calculs, telles que les conditions de bord, les permittivités et l'onde incidente qui peut avoir la forme d'une onde plane ou d'une onde gaussienne. HFSS calcule alors le champ diffusé quand une onde électromagnétique est incidente sur la structure en résolvant les équations de Maxwell par la méthode des éléments finis. Nous calculons le champ diffusé par cette méthode pour un nombre N de structures qui ont toutes les mêmes paramètres (valeurs de permittivité, σ , L_c , etc.) mais qui ont chacun des surfaces rugueuses différentes, c.-à.d. des profils de rugosité différents mais avec un même degré de rugosité pour chaque structure. Nous calculons le champ diffusé pour des valeurs fixes de paramètres (rugosités, permittivités, épaisseur de litière) en moyennant sur les valeurs calculées pour toutes les structures différentes. A partir de cette valeur de champ diffusé nous pouvons calculer l'émissivité, en appliquant les équations (4.3), (4.5) et (2.111). Le fait de moyenner sur des structures différentes mais avec des mêmes valeurs de rugosités nous permet de s'approcher de la valeur qui serait obtenue dans la réalité pour une surface "infinie". Le nombre de structures sur lesquelles nous moyennons pour calculer l'émissivité, N, et la taille de chaque structure doivent être déterminés soigneusement. La procédure de calcul est présentée sur la Figure 4.1.

Dans la procédure de modélisation présentée dans le paragraphe 4.1 il y a une série de paramètres qui ont une influence sur la précision des résultats. Ces paramètres ont aussi un effet sur le temps et la mémoire nécessaire pour chaque calcul. Nous présentons dans le paragraphe 4.2 une étude de sensibilité qui a permis de quantifier ces effets. L'objectif de cette étude était de déterminer des valeurs pour chaque paramètre qui donneront la meilleure précision au niveau des résultats. Nous avons étudié aussi l'effet de chaque paramètre sur le « coût » de calcul (le temps et la mémoire nécessaires). Dans certains cas il sera peut être nécessaire de choisir une valeur qui sera un compromis entre le cout de calcul et la précision. Les paramètres étudiés étaient les suivants :

- le nombre de simulations (ou de surfaces différentes) pour chaque rugosité, N,
- la taille du domaine de calcul (la taille de surface dans chaque simulation), L x L,
- le pas d'intégration en angle de diffusion, s
- la forme de l'onde incidente sur chaque surface (gaussienne ou plane)

Nous avons testé l'influence de ces paramètres sur les résultats et le coût de calcul pour toute la gamme de conditions de la mission SMOS (par exemple l'humidité de sol variant de 5% à 30%, l'angle variant de 0° à 50°, etc.) et pour un grand nombre de valeurs.

Les résultats sont présentés sur les Figure 4.4 à Figure 4.23. Ces résultats montrent que nous avons besoin d'un plus grand nombre de surfaces pour les cas actifs (calcul du coefficient bi-statique et du coefficient de rétrodiffusion) que pour les cas passifs (calcul de l'émissivité). La Figure 4.12 montre qu'à partir d'une valeur de $N=5$ nous obtiendrons une valeur pour l'émissivité qui a une erreur dû au nombre fini de surfaces inférieure à 1%. Par contre la Figure 4.13 montre que 50 surfaces d'études sont nécessaire pour ne pas dépasser 5% d'erreur sur le coefficient de rétrodiffusion. Il sera nécessaire de vérifier cette conclusion en faisant plus de simulations.

Les Table 4-III à Table 4-VIII et les Figure 4.14 à Figure 4.19 montrent que le pas d'intégration, s , doit être diminué pour le calcul de l'émissivité pour les grands angles ($>25^\circ$), les ondes incidentes planes ou gaussiennes avec des largeurs importantes (supérieures à $g=0.25L$), et pour les grandes surfaces. Une valeur de $s=0.5^\circ$ paraît suffisamment petite pour les surfaces de taille $L=6\lambda$ et aussi pour les grandes surfaces ($L \leq 12\lambda$) si l'onde incidente gaussienne a une largeur inférieure à $g=0.1L$. Une valeur de $s=0.5^\circ$ est aussi suffisante dans tous les cas pour un angle de 0° . Les conditions qui nécessitent la plus petite valeur de s sont une surface de taille 12λ et une onde incidente plane. Dans ce cas si nous utilisons une valeur de $s=1^\circ$ ou de $s=0.5^\circ$ nous avons une erreur par rapport à l'émissivité obtenue avec $s=0.2^\circ$ de 4.5% et de 11.9% respectivement. Il semblerait qu'il soit alors préférable d'utiliser une valeur de $s=0.2^\circ$. Cependant les petites valeurs de s conduisent à un temps de calcul qui est plus important. Avec un ordinateur de 64Go de mémoire RAM et deux processeurs à 1.87 GHz le calcul a duré 10 minutes, 30 minutes et de 1h30 par angle pour calculer la transformation du champ proche au champ lointain pour des valeurs de $s= 1$ degré, 0.5 degré et 0.2 degré respectivement. Nous avons décidé alors de prendre une valeur de $s=0.5^\circ$ pour tous les calculs que nous ferons par la suite dans le travail de thèse parce que cela semble un bon compromis entre une bonne précision et un temps de calcul "raisonnable".

Nous avons étudié ensuite l'effet de l'onde incidente sur l'émissivité pour des surfaces peu et très rugueuses et pour des grandes et petites tailles de surface ($L=6\lambda$, $L=12\lambda$). Nous avons testé trois ondes différentes : une onde plane, une onde gaussienne avec une largeur $g=0.25L$ et une onde gaussienne avec $g=0.1L$. Pour une surface peu rugueuse nous avons comparé les résultats avec ceux produits par la méthode analytique AIEM, une méthode qui est considérée comme précise pour les surfaces rugueuses. Les résultats sont présentés en Table 4-IX à Table 4-XI et en Figure 4.20 à Figure 4.22. Table 4-IX à Table 4-XI montrent qu'en général nous obtenons des résultats plus proche de la méthode AIEM avec une onde incidente qui est plane. La seule exception est pour la plus grande surface ($L=12\lambda$) et à un angle de 50° . Ce résultat est plus éloigné de la méthode AIEM. Il y a deux

raisons possible pour cette divergence. La première est que nous avons besoin de réduire le pas d'intégration pour ce point et la seconde est que l'AIEM sous-estime l'émissivité pour ce point. La première raison est possible car nous avons montré que les surfaces plus grandes et les angles plus grands nécessitent des pas d'intégration plus petits. La deuxième est aussi possible parce que le résultat obtenu par notre méthode numérique a un meilleur accord que la méthode AIEM avec la littérature (par exemple Wigneron et al (2010)). Il sera intéressant de continuer à étudier ces points mais pour ce travail de thèse nous pouvons constater que l'onde incidente plane semble le meilleur choix car elle donne des résultats plus précis dans la plupart des cas.

Nous avons testé deux tailles de surface différentes ($L=6\lambda$ et $L=12\lambda$). L'émissivité a été calculée pour ces deux tailles, une surface peu rugueuse, des angles de 0 à 50° , une humidité du sol de 30% et en polarisation H. Les résultats sont présentés à l'aide des Table 4-XII à Table 4-XIV et de la Figure 4.23. Ces résultats montrent que pour les petits angles ($\theta \leq 30^\circ$) nous obtenons les résultats très similaires pour les deux tailles. Nous pouvons donc utiliser également une taille de surface de 6λ ou de 12λ mais il est plus avantageux d'utiliser les surfaces plus petites car ces calculs sont moins coûteux en mémoire et en temps de calcul, ce qui est montré sur la Table 4-XV. Cependant pour les angles plus grands ($\theta > 30^\circ$) une taille de 6λ introduit une erreur de 5.40% dans l'émissivité, par rapport à une taille de 12λ (voir la Table 4-XIV). Nous avons décidé toutefois de prendre une taille de 6λ pour le travail de cette thèse car cette taille permet d'obtenir une bonne précision dans la plupart des cas et une taille plus grande sera trop coûteuse en temps de calcul et en mémoire. La Table 4-XVI résume enfin la partie 4.2 en présentant les valeurs de paramètres que nous avons déterminées grâce à l'étude de sensibilité.

Le chapitre 5 présente la validation de notre méthode numérique en comparant les résultats d'un sol nu lisse avec les équations de Fresnel, et ceux d'un sol nu rugueux avec des résultats produits par la méthode des moments ainsi que des résultats expérimentaux d'une campagne de mesures SMOSREX 2006. La Figure 5.2 montre que les résultats de la méthode FEM sont en accord avec les équations de Fresnel, qui sont exacts pour les surfaces lisses. L'erreur maximale est approximativement de 0.02 et est obtenue à 50° et en polarisation H. Pour les autres angles et pour la polarisation V les erreurs sont inférieures à cette valeur.

Les Figure 5.3 à Figure 5.6 montrent la comparaison avec la méthode des moments (MoM). MoM est la méthode numérique qui est considérée comme la plus précise pour calculer l'émission et la diffusion d'une surface rugueuse. Cependant cette méthode n'est pas bien adaptée aux études des systèmes volumiques tels que le système bicouche sol-litière. Il est pourtant important de valider notre approche FEM avec la méthode des moments pour le cas d'un sol nu avant de l'appliquer aux calculs du système sol-litière. Nous avons fait des comparaisons pour le cas actif et le cas passif. Le cas passif

nous intéresse pour l'application SMOS mais nous avons aussi comparé le cas actif afin de faire une validation plus complète.

La Figure 5.3 montre la comparaison du coefficient de rétrodiffusion calculé par la méthode FEM et calculé par la méthode des moments. La Figure 5.4 montre la comparaison du coefficient bi-statique et Les Figure 5.5, Figure 5.6 ainsi que les Table 5-II et Table 5-III montrent la comparaison des calculs d'émissivité. Les résultats indiquent un bon accord entre les résultats de la méthode FEM et ceux de la méthode MoM dans tous les cas. Il y a une légère différence entre les deux approches pour le coefficient bi-statique aux grands angles de diffusion. Cependant l'accord est très bon pour le cas passif, ce qui nous intéresse le plus. Nous pouvons conclure que bien que la méthode des moments soit la méthode la plus précise pour calculer l'émission et la diffusion d'une surface rugueuse, la méthode FEM est une bonne méthode complémentaire qui a l'avantage d'être bien adaptée aux systèmes volumiques, tel que le système bi-couche sol-litière.

Les Figure 5.11, Figure 5.12 et Figure 5.13 montrent une comparaison entre les résultats de la méthode FEM et des résultats de la campagne de mesures SMOSREX 2006 pour un sol nu rugueux. Les trois figures représentent trois rugosités différentes variant d'un sol assez rugueux à un sol très rugueux. Nous comparons aussi avec des résultats produits par la méthode analytique AIEM qui est considérée précise pour des surfaces peu rugueuses et des petits angles. En comparant avec des données expérimentales, nous trouvons que dans tous les cas la méthode FEM estime mieux l'émissivité que la méthode AIEM. Nous voyons un bon accord entre la méthode FEM et les données expérimentales pour la surface assez rugueuse (l'écart type σ de 1.7cm et la longueur d'autocorrélation L_c de 12.1cm) et un bon accord pour la surface moyennement rugueuse ($\sigma = 2.3\text{cm}$, $L_c=8.7\text{cm}$) et en polarisation de V. Pour la surface moyennement rugueuse nous observons qu'en polarisation H l'accord entre la méthode FEM et les données expérimentales est bon pour les petits angles ($\theta \leq 40^\circ$) mais que la méthode FEM sous-estime l'émissivité pour les grands angles ($\theta > 40^\circ$). Nous observons aussi que la méthode FEM sous-estime l'émissivité pour la surface très rugueuse ($\sigma = 2.8\text{cm}$, $L_c = 7.1\text{cm}$) pour les deux polarisations et pour tous les angles. Cette sous-estimation peut venir soit d'une imprécision dans la méthode de modélisation soit d'une erreur de mesure dans les données de la campagne de SMOSREX 2006. Dans le premier cas, l'imprécision pourrait venir de la taille de surface que nous avons utilisé ($L=6\lambda$), qui pourrait être trop petite, ou d'un nombre de points sur la surface qui est insuffisant pour bien représenter la rugosité pour les surfaces très rugueuses. Dans le deuxième cas, l'erreur peut venir d'une mesure imprécise de l'humidité du sol ou de la rugosité. Cela semble probable car nous voyons dans la Figure 5.11 et la Figure 5.12 une diffusion verticale dans les données expérimentales alors que ses points représentent normalement les mêmes conditions (humidité de sol, rugosité etc). Nous pouvons en déduire qu'il y a des imprécisions de mesure dans les données expérimentales que nous ne voyons pas dans la Figure 5.13 car nous n'avons pas assez de points mais qui doivent certainement

exister. Pour mieux comprendre d'où vient la sous-estimation de la méthode FEM pour les fortes rugosités il sera intéressant et nécessaire de faire des études supplémentaires dans l'avenir.

Dans le chapitre 6 nous présentons les premiers résultats de calcul par la méthode FEM de l'émissivité du système sol-litière. Nous comparons dans un premier temps ces résultats avec des résultats expérimentaux obtenus sur le site du Bray en 2009 (Grant et al (2009)) et d'une méthode approximative de modélisation proposé par Schwank et al (2009). Pour la comparaison avec les données du Bray nous avons appliqué la relation empirique (6.1) qui nous permet de calculer l'humidité de la litière en fonction de l'humidité du sol, ainsi que la relation empirique (6.3) proposée par Demontoux et al (2009) qui nous permet de calculer la permittivité de la litière en fonction de son humidité. Nous présentons les résultats de l'émissivité du sol-litière, calculés avec la méthode numérique FEM, dans la Figure 6.4. Les trois courbes représentent les résultats des systèmes suivants :

« Soil-litter 1 » : sol-litière, rugosité de sol faible, rugosité de litière faible

« soil-litter 2 » : sol-litière, rugosité de sol faible (la même valeur), rugosité de litière plus forte

« bare soil » : sol nu, rugosité de sol faible (la même valeur).

Nous remarquons les mêmes tendances dans cette figure et sur les données expérimentales, présentées en Figure 6.1 . Notamment nous voyons que dans les deux cas la couche de litière augmente l'émissivité et que l'émissivité est moins sensible à l'humidité du sol quand il y a une couche de litière présente. Nous avons donc obtenu un bon accord général entre la méthode FEM et les données expérimentales pour le système sol-litière.

La Figure 6.5 présente l'émissivité du système sol-litière nommé « soil-litter 2 » en fonction de l'humidité de litière, pour des valeurs fixes de l'humidité du sol. Ces résultats montrent qu'en général l'émissivité diminue avec l'humidité de la litière avec une pente très faible. Nous observons aussi que l'émissivité perd sa sensibilité à l'humidité du sol pour les valeurs de l'humidité de la litière très élevées. La litière masque complètement le signal du sol. Ces résultats coïncident avec les conclusions de Grant et al (2007, 2009).

Dans la Figure 6.6 nous présentons les résultats qui nous permettent de comparer notre méthode FEM avec une méthode de modélisation approximative présentée par Schwank et al (2008). Nous présentons ici la réflectivité du système sol-litière, calculée par la méthode FEM, en fonction de la permittivité de la litière. Il y a trois courbes qui représentent des valeurs différentes de la permittivité du sol, et trois points qui représentent les valeurs de l'émissivité du sol nu pour les mêmes permittivités du sol. La rugosité du sol et celle de la litière sont fixes et assez basses. Nous observons que la réflectivité augmente avec la permittivité de litière de la même manière que les tendances que nous observons dans les résultats du modèle de Schwank et al, présentés en Figure 6.2. Nous

observons aussi dans les deux cas qu'en général la réflectivité du système sol-litière est plus basse que la réflectivité du sol nu, sauf quand la permittivité du sol est faible et la permittivité de la litière est forte. Il y a deux mécanismes physiques qui amènent la litière à augmenter et à la fois diminuer l'émissivité du sol. D'un côté, la litière atténue l'émission du sol, qui va diminuer l'émission globale, et aussi ajoute sa propre émission à l'émission globale qui va augmenter. La litière se comporte aussi comme une couche d'adaptation d'impédance qui augmente l'émission du sol. Les résultats de la Figure 6.2 et de la Figure 6.6 montrent que l'effet final est une augmentation de l'émission. La Figure 6.6 montre que la seule exception arrive quand la permittivité de litière est plus basse que la permittivité de sol. L'effet est alors une diminution de l'émission. Dans ces conditions la couche de litière ne peut plus être considérée comme une couche d'adaptation d'impédance et atténue fortement l'émission.

La plus grande différence entre la Figure 6.2 et la Figure 6.6 est qu'à une faible humidité de litière (faible permittivité) nous observons que les courbes de réflectivité du système sol-litière en fonction des humidités du sol se croisent sur la Figure 6.2. Contrairement à la Figure 6.6 où ce croisement est observé à une forte humidité de litière. Le croisement des courbes représente une faible sensibilité de l'émissivité à l'humidité du sol, que nous nous attendons à rencontrer lorsque la permittivité de la litière est très élevée et masque donc l'émission du sol (par exemple nous le voyons dans les données expérimentales de Grant et al 2007, 2009). La méthode FEM semble donc mieux modéliser l'émissivité du système sol-litière que le modèle de Schwank et al, qui ne modélise pas cet effet.

Dans le chapitre 7 de ce manuscrit de thèse nous présentons nos conclusions sur le travail présenté dans ce manuscrit et le chapitre 8 présente les perspectives. Au cours de cette thèse nous avons développé une approche numérique qui nous permet de calculer la diffusion et l'émission d'un système bi-couche hétérogène, représentant le système forestier sol-litière. Cette approche s'appuie sur le logiciel commercial HFSS, qui résout les équations de Maxwell par la méthode des éléments finis (FEM), et c'est donc une approche exacte. Nous avons développé l'approche FEM dans le contexte de la mission SMOS et nous avons donc orienté le développement vers des applications à 1.4 GHz et des applications d'émission. Cependant l'approche peut tout à fait être développée dans l'avenir pour les applications dans le cas actif et pour d'autres fréquences. L'approche développée nous permettra d'étudier en détail l'émission des systèmes multicouches avec surfaces rugueuses en général et le système sol-litière en particulier. Nous avons l'intention dans l'avenir d'utiliser cette approche pour créer une base de données de l'émissivité du système sol-litière en fonction de nombreux paramètres, tels que l'angle d'incidence, l'humidité du sol, etc. Une telle base de données nous permettra d'étudier l'émission du système sol-litière dans des conditions différentes ce qui n'était pas possible avant ce travail de thèse.

Pendant cette thèse nous avons présenté l'approche développée et ensuite mené une étude de sensibilité pour déterminer des paramètres importants de notre approche. Nous avons présenté par la suite une validation de l'approche pour un sol nu, en comparant avec la méthode des moments et avec des données expérimentales. Cette comparaison a montré la validité de la méthode FEM pour les surfaces peu et moyennement rugueuses (pour les rugosités à $\sigma=1.7\text{cm}$, $L_c=12.1\text{cm}$, ou moins). Nous avons observé que la méthode FEM sous-estime l'émissivité pour les surfaces très rugueuses (rugosités entre $\sigma=2.3\text{cm}$, $L_c=8.7\text{cm}$ et $\sigma=2.8\text{cm}$, $L_c=7.1\text{cm}$). Le travail futur évaluera d'où vient cette imprécision et nous espérons améliorer la méthode pour ces rugosités plus tard. Finalement nous avons présenté une étude préliminaire de l'émissivité du système sol-litière, comparant les tendances obtenues avec les jeux de données expérimentaux et de modélisation qui sont dans la littérature. Nous avons observé un bon accord entre la méthode FEM et les données expérimentales et aussi entre la méthode FEM et une autre méthode de modélisation présentée par Schwank et al (2008). Nous pourrions par la suite valider le modèle pour le système sol-litière en comparant plus précisément aux données expérimentales. Pour cela il serait nécessaire de faire une nouvelle campagne de mesures car il y a très peu de données expérimentales dans la littérature. Une campagne a déjà été faite sur le site de SMOSREX en 2009 et ces données sont en cours de traitement. Nous pourrions encore développer le modèle pour prendre en compte d'autres effets hétérogènes, tels que les inclusions ou les gradients d'humidité, ou pour l'optimiser en terme de mémoire ou de temps de calcul. Nous pourrions aussi appliquer la méthode développée au cas actif ou à d'autres fréquences, par exemple la mission BIOMASS (Le Toan 2010).

CHAPTER 10. APPENDIX B: PUBLICATION

**Article accepted by IEEE Transactions on Geoscience and Remote Sensing
letters, January 2011.**

Evaluation of a Numerical Modeling Approach based on the Finite Element Method for calculating the Rough Surface Scattering and Emission of a soil layer

Heather Lawrence, François Demontoux, Jean-Pierre Wigneron, *Senior Member, IEEE*, Philippe Paillou, Tzong-Dar Wu and Yann H. Kerr, *Senior Member, IEEE*

Abstract—We evaluate a new 3D numerical modeling approach for calculating the rough surface scattering and emission of a soil layer. The approach relies on the use of Ansoft's numerical computation software HFSS (High Frequency Structure Simulator), which solves Maxwell's equations directly using the Finite Element Method. The interest of this approach is that it can be easily extended to studies of heterogeneous media. However before being applied in this way it must first be validated for the rough surface case. In this letter we perform this validation by comparing results of rough surface scattering and emission with results of the Method of Moments (MoM), for a range of different roughnesses and permittivities and with both gaussian and exponential rough surface autocorrelation functions. Results show a good agreement between the two methods for scattering and an excellent agreement for emissivity. We illustrate the application of the new approach by calculating the emission of a two-layer system with rough surfaces, representing the soil-litter system in forests.

Index Terms— Electromagnetic scattering by rough surfaces, microwave emissivity, numerical simulation.

I. INTRODUCTION

HERE is currently great interest in numerical studies of rough surface scattering and emission, with applications

Manuscript received December 7, 2010. This work was supported jointly by the Centre National d'Études Spatiales (CNES) TOSCA and by the Aquitaine Region in France.

H. Lawrence is with the Laboratoire de l'Intégration du Matériau au Système UMR5218, University of Bordeaux 1, 33607 Pessac, France and also with the Ecologie Fonctionnelle et Physique de l'Environnement (EPHYSE) laboratory, Institut National de la Recherche Agronomique (INRA), 33883 Villenave d'Ornon, France (phone: +33-(0)5-40-00-27-08; fax: +33-(0)5-40-00-66-31; e-mail: heather.lawrence@ims-bordeaux.fr).

F. Demontoux is with the Laboratoire de l'Intégration du Matériau au Système UMR5218, University of Bordeaux 1, 33607 Pessac, France.

J.-P. Wigneron is with the Ecologie Fonctionnelle et Physique de l'Environnement (EPHYSE) laboratory, Institut National de la Recherche Agronomique (INRA), 33883 Villenave d'Ornon, France.

P. Paillou is with the Observatoire Aquitain des Sciences de l'Univers, University of Bordeaux 1, LAB-UMR 5804, 33270 Floirac, France.

T.-D.Wu is with the Department of Electrical Engineering, National Central University, Chung-Li, Taiwan 32054, R.O.C.

Y. Kerr is with the Centre d'Études Spatiales de la Biosphère (CESBIO), Toulouse Cedex 4, France.

to both passive and active microwave remote sensing of the Earth, including satellite missions such as the current SMOS mission [1] or the upcoming SMAP mission [2]. It is also of interest to extend such studies to include the scattering and emission of heterogeneous media such as forests or ice packs. Scattering and emission from these media involve rough surface effects as well as volume effects from multi-layers, or permittivity gradients, and/or inclusions such as buried rocks. Numerical studies would provide a good approach for studying the scattering or emission of these media, allowing us to control the many parameters involved.

Currently, the most widely used numerical methods for studying rough surface scattering and emission are Method of Moments (MoM)-based fast methods, e.g. [4] – [6], due to their high accuracy coupled with implementation of a fast solution method. Such methods are particularly well suited to the rough surface case, since they solve surface integral equations. However they are not well suited to studies of heterogeneous media, whose permittivity values vary horizontally or vertically (e.g. forests or ice packs) [7]. Numerical methods that utilize volume meshing, such as the Finite Element Method (FEM), on the other hand are well suited to studies of heterogeneous materials [7] but are not considered as accurate as the Method of Moments for the rough surface case.

In this letter we present a new numerical modeling approach for calculating the rough surface scattering and emission of a dielectric layer, using Ansoft's HFSS© (High Frequency Structure Simulator) (version 12.1) simulation software [8], which is based on the FEM. The advantage of HFSS as a numerical computation tool is that it allows us to vary many parameters, including the incident angle and the dielectric permittivity constants, without having to repeatedly restart simulations. The interest of the approach is that it can be extended to calculate the emissivity of heterogeneous media with rough surfaces, such as forest layers or permafrost. However before being applied in this way, it must first be validated for the rough surface case, particularly since there are very few studies of rough surface scattering calculated by FEM in the literature and none of rough surface emissivity. In this letter we aim to carry out this validation by comparing

results of the FEM approach to MoM predictions.

In section II we present the FEM approach using HFSS and in section III we present a comparison of results with MoM predictions for the rough surface case. To illustrate the interest of the FEM approach, and potential future applications, we also present results of the emissivity of a two-layer structure, representing the soil and litter layers found in forests. Concluding remarks are given in section IV.

II. MATERIALS AND METHOD

A. Numerical Modeling Approach

The FEM numerical modeling approach presented in this letter relies on the use of HFSS and comprises 3 main stages: creating many solid structures with rough surfaces and importing each of these into an HFSS project, using HFSS to calculate the electric field scattered off each structure, and finally calculating values of the bistatic scattering coefficient, backscattering coefficient and emissivity from the scattered electric field, averaging over the ensemble of rough surfaces. In this section we describe briefly the FEM and then each of the 3 stages.

1) Finite Element Method:

In FEM calculations, the structure to be studied is divided into a mesh of many small regions, called cells, and then Maxwell's equations are solved in their differential form for the electric and magnetic fields in each cell. The mesh used by the HFSS software consists of tetrahedral cells.

Once a solution has been found the mesh is refined many times, with progressively smaller cells, and a new solution obtained. With each refinement (iteration) the change in the calculated energy value, ΔE , of each solution or the change in the reflection coefficient matrix, ΔS , is obtained. A final solution is obtained by imposing a convergence criterion on ΔE or ΔS .

2) Creating structures with rough surfaces:

The 3-dimensional structure to be studied is created and imported into HFSS by the following procedure. Randomly rough surfaces are generated in the form of $\{x,y,z\}$ points using the "R" statistical software©, employing in particular the "Random Fields" package [12]. These rough surfaces have standard deviation of surface heights, σ , and autocorrelation functions of the following form:

$$\rho(r) = \exp\left[-\left(\frac{r}{L_c}\right)^n\right]. \quad (1)$$

L_c is the autocorrelation length and the value of n determines the form of the autocorrelation function: for the special cases of exponential and gaussian autocorrelation functions it is equal to 1 and 2 respectively. r is given by:

$$r^2 = x^2 + y^2. \quad (2)$$

The rough surfaces are then transformed into volumes using C4W's "3D Shop Model Design" © software [13]. Firstly the

$\{x,y,z\}$ points which form the rough surface are joined by bspline curves to create a continuous rough surface, which is then extended vertically, creating volumes above or below the surface. These volumes represent the vacuum above the rough surface and a dielectric slab below the rough surface. Note that when studying the rough surface case we do not require the dielectric slab.

3) Numerical Calculation Conditions:

Once the required structure has been created, it is imported into HFSS where permittivity constants are applied and the calculation conditions are defined. A polarized incident wave is selected, either a wave of gaussian form or a plane wave, at an incident angle θ in the range of 0° to 90° , and azimuth angle $\phi=0^\circ$. The calculation can be done for H or V polarization, for both the incident and scattered beams. An impedance boundary condition is applied below the structure to simulate an infinitely deep lower layer, preventing any reflections at the lower boundary. These are also applied at the sides of the dielectric slab, for volume studies. Radiation boundary conditions are applied at the top and sides of the vacuum area, which also prevent reflections, as well as providing "virtual surfaces" for the near to far field calculation.

The scattered electric field is calculated inside the calculation area and then the electric field in the far field region, $E_{pj}^s(\theta_s, \phi_s)$, is extrapolated from this value, at a distance R from surface j , at polarization p , and at discrete values of scattering angles θ_s and ϕ_s .

4) Data Analysis:

Numerical simulations are performed for N different rough surfaces (N different structures) with the same autocorrelation functions and values of σ and L_c . The bistatic scattering coefficient, σ_{pq}^0 , was then calculated, for incident polarization q and scattered polarization p , from the scattered electric field in the far field region, averaged over all N surfaces. This averaging process is done in order to approach the value that would be obtained for the case of an infinitely large rough surface. The bistatic scattering coefficient is calculated from the following:

$$\sigma_{pq}^0(\theta_s, \phi_s; \theta, \phi) = \frac{4\pi R^2}{A_{\text{eff}} |E_q^i(\theta, \phi)|^2} \frac{1}{N} \sum_{j=1}^N |E_{p,j}^s(\theta_s, \phi_s)|^2, \quad (3)$$

where (θ, ϕ) are incidence angles, (θ_s, ϕ_s) are angles of the scattered wave, N is the number of surfaces to be averaged over, A_{eff} is the effective area of the surface illuminated and E_q^i is the incident electric field with polarization q , which for a gaussian incident wave has the following form:

$$E_q^i = \exp\left[-\frac{(x - x_{\text{center}})^2 \cos^2 \theta + (y - y_{\text{center}})^2}{g^2}\right]. \quad (4)$$

(x,y) is a point on the surface, $(x_{\text{center}}, y_{\text{center}})$ is the center of

the surface and g is a measure of the beam width. For this type of incident wave the effective area is given by $A_{\text{eff}} = \pi g^2 / (2 \cos \theta)$ [14] and in the case of a plane wave it is simply the total area of the surface illuminated.

The bistatic scattering coefficient calculated by (3) contains both coherent and non-coherent components. The non-coherent component is isolated as follows:

$$\sigma_{\text{pq}}^0(\theta_s, \phi_s; \theta, \phi)_{\text{noncoh}} = \frac{4\pi R^2}{A_{\text{eff}} |E_q^i(\theta, \phi)|^2} \left[\frac{1}{N} \sum_{j=1}^N |E_{p,j}^s(\theta_s, \phi_s)|^2 - \frac{1}{N^2} \left| \sum_{j=1}^N E_{p,j}^s(\theta_s, \phi_s) \right|^2 \right] \quad (5)$$

The values of g and N must be carefully chosen: this is discussed further in section B. The backscattering coefficient is the bistatic scattering coefficient for the monostatic case of $(\theta_s, \phi_s) = (\theta, \phi + \pi)$ i.e. the reflection angle is equal to the incident angle. The emissivity of the surface measured at polarization p , $e_p(\theta, \phi)$ can be calculated by integrating the bistatic scattering coefficient over half space (Peake 1959), as follows [15]:

$$e_p(\theta, \phi) = 1 - \Gamma_p(\theta, \phi) \quad (6)$$

$\Gamma_p(\theta, \phi)$ is the reflectivity at polarization p given by:

$$\Gamma_p(\theta, \phi) = \frac{1}{4\pi} \iint_{\text{upper hemisphere}} \frac{1}{\cos \theta} \left[\sigma_{\text{pp}}^0(\theta_s, \phi_s; \theta, \phi) + \sigma_{\text{tp}}^0(\theta_s, \phi_s; \theta, \phi) \right] \sin \theta_s d\theta_s d\phi_s, \quad (7)$$

where σ_{pp}^0 is the like polarized bistatic scattering coefficient and σ_{tp}^0 the cross polarized bistatic scattering coefficient. Since these are calculated for discrete values of θ_s and ϕ_s , we approximate (7) to a sum over θ_s and ϕ_s . For emissivity calculations, the step in the discrete values of θ_s and ϕ_s at which the electric field is calculated must be small enough that the errors due to this approximation are negligible.

A. Numerical Calculations

A comparison between the FEM approach and MoM was performed for the rough surface case. Results of the bistatic scattering coefficient and backscattering coefficient calculated using the FEM approach were compared to MoM results presented in [9] and [10] – [11] respectively, for surfaces of gaussian autocorrelation function, low roughness values and low permittivity values (equivalent to dry soil conditions). Results of the emissivity of rough surfaces with exponential autocorrelation functions, high permittivity values (equivalent to wet soil conditions) and low to high roughness values were compared to MoM results presented in [5].

In order to illustrate the interest of the approach presented in this letter, the emissivity of a rough surface covered by a dielectric layer, also with a rough surface, was then calculated using the FEM approach. This structure represented a rough

soil surface covered by forest litter. The permittivity of the litter layer was fixed at $8.712 + 2.301i$, equivalent to a moderately wet grass litter [16] and a litter depth of 8cm was chosen. Calculations were performed for permittivity values of $5.313 + 0.443i$, $10.288 + 1.025i$ and $16.893 + 1.837i$ for the lower soil rough surface, equivalent to dry to wet soil moisture conditions. Soil roughness was fixed at a low value and calculations were performed for two litter roughnesses, at H polarization and an angle of $\theta = 40^\circ$, and $\phi = 0^\circ$.

All FEM calculations were performed at 1.4 GHz and at both H and V polarizations, on a 64 bit machine with 64 GB of available RAM. For the comparison with MoM we studied the surface case only, so the layer thickness was set to zero, i.e. the structure studied consisted of a vacuum with a lower rough surface. However it was found that results were almost unaffected by increasing the depth up to 20cm. For the soil-litter study the structure consisted of a lower rough surface covered by a dielectric layer with a rough surface and topped by a volume representing a vacuum.

The surface size L was chosen to be $12\lambda \times 12\lambda$ ($= 2.55\text{m} \times 2.55\text{m}$). This amply satisfies the specification given in [5] that surfaces must be at least $8\lambda \times 8\lambda$ in size. The surface size chosen was also much larger than the autocorrelation length, equivalent to $12L_c \times 12L_c$ or higher. The surfaces created using the R software had a resolution of 256×256 points.

We chose to use a tapered incident beam, as is common practice, in order to reduce edge effect errors, from the sides of the calculation area. We chose to use a gaussian beam, as described by (3), for its simplicity. The gaussian beam allows us to avoid errors due to edge effects but does not satisfy Maxwell's equations exactly and is therefore only considered an approximation to an electromagnetic wave. Better approximations exist but are more difficult to implement with HFSS. However the results obtained indicate that the chosen beam was adequate for the comparison presented in this paper.

The tapering parameter, g , for the incident beam must be small enough to reduce edge effects and large enough so that enough of the surface is illuminated to provide an accurate representation of the bistatic scattering coefficient. This parameter should also depend on the incident angle since higher angles lead to a spreading in the beam focal width in the x direction. Values commonly used vary from $L/10$ to $L/4$ [3]. For simplicity we chose to use the same value of g for all angles. We chose to use a high value of $L/4$ ($= 63\text{cm}$) in order to maximize the illuminated surface area since on the whole the angles considered in this paper are low, and all are far from grazing. This value may be somewhat high for the higher angles considered however the results obtained do not indicate that errors due to edge effects are significant. Calculations were performed for 20 different surfaces ($N=20$) for the scattering case since increasing calculations beyond this value led to very little change in results. Similarly calculations were performed for $N=40$ for the emissivity.

The step in θ_s and ϕ_s , was chosen to be 0.2 degrees for the emissivity calculations. To test the adequacy of this, we reduced this value to 0.1 degrees but found that this had little effect on results of the emissivity. A step of 1 degree was used

for scattering calculations.

It is usual to perform an energy conservation check for the case of rough surface emission however this was not possible since HFSS only calculates the scattered field in the upper hemisphere. Instead, we performed a calculation of the reflectivity, for angles of 30° to 50°, and with a perfect electrical reflector boundary condition (permittivity=infinity) replacing the impedance boundary condition on the rough surface. This condition ensures no transmission across the rough surface and so the reflectivity must be equal to unity for energy conservation to be true. Note that the scattered field across the whole sphere surrounding the structure was included in this calculation, including therefore any downward scattering due to edge effects, since the aim was to check that the total calculated energy was conserved.

III. RESULTS

Results of the comparison with MoM for the scattering case (bistatic scattering and backscattering coefficients calculated from (2)) are presented in Figs 1 and 2. In Fig. 2 results of the bistatic scattering coefficient are illustrated at H polarization (very similar results were achieved at V polarization). Results of the emissivity comparison with MoM are presented in Tables I and II. The final column in these tables shows the difference in brightness temperature between the two methods, $T_B(\text{FEM-MoM})$. These values are calculated from the difference in emissivity multiplied by a physical temperature of 290K. Results of the soil-litter study are shown in Fig. 3.

CPU and memory requirements for each HFSS calculation (one surface only) varied from approximately 2 hours and 3 GB for surfaces of lower roughness and approximately 12 hours and 15 GB for surfaces of higher roughness, not including CPU time for near to far field calculations which was negligible for an integration step of 1 degree (scattering calculations) and approximately 10 minutes per incident angle, for an integration step of 0.2 degrees (emissivity calculations).

The energy conservation check using the perfect E boundary condition gave a reflectivity within 0.1% of unity for all angles for the lower roughness and 1.2% of unity for the higher roughness. Although not conclusive, this indicates that energy conservation is good to within 1.2% or less.

Figs 1 and 2 show a good agreement between the new method presented in this letter and the Method of Moments, for the active case. The average difference between the two methods for the backscattering coefficient is 1.2 dB for HH polarization and 2.1 dB for VV polarization. The largest difference is 4.0 dB for HH polarization, which occurs at 60°, and 1.7 dB for VV polarization, which occurs at 40°. The average difference for the bistatic scattering coefficient is 1.4 dB, and the maximum difference occurs at 70°, and is equal to 3.5 dB for HH polarization and 6.3 dB for VV polarization.

Agreement is excellent for the emissivity, with an average difference between MoM and the FEM approach of 2.1K for the lower roughness and 2.4K for the higher roughness. The maximum difference between the two methods is 2.9K for the lower roughness and 3.6K for the higher roughness.

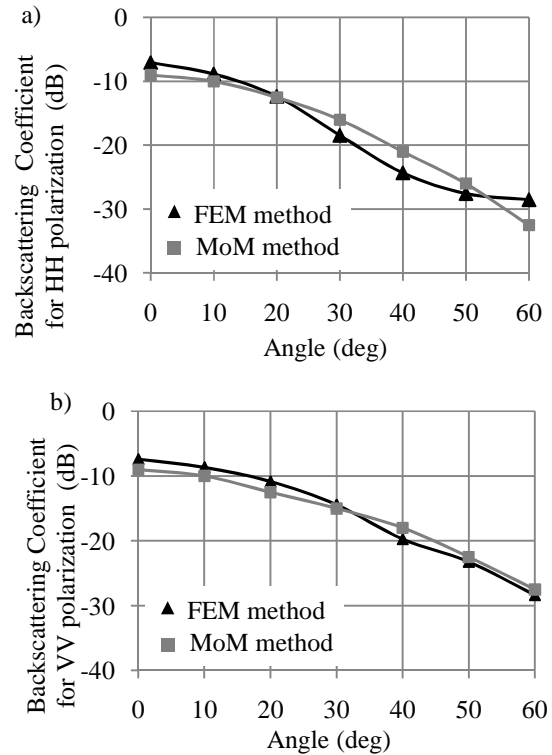


Fig. 1. Backscattering coefficient for the Method of Moments and the Finite Element Method models, calculated at 1.4 GHz for $\epsilon_r=3+0.1i$ and $[\sigma, L_c]= [1.22 \text{ cm}, 8.57 \text{ cm}]$ at polarizations a) HH and b) VV.

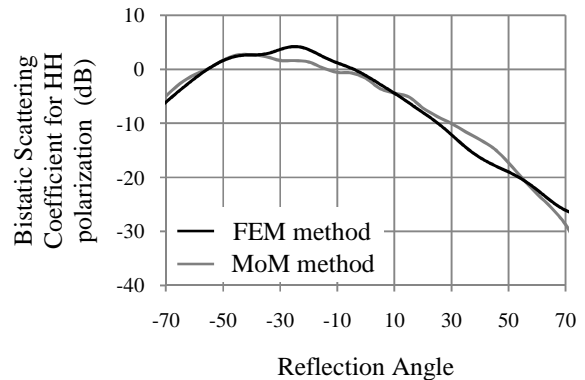


Fig. 2. Bistatic scattering coefficient for the Method of Moments and the Finite Element Method models, calculated at 1.4 GHz for $\epsilon_r=4+1i$ and $[\sigma, L_c]= [3.41 \text{ cm}, 20.5 \text{ cm}]$ with an incident angle of 30°.

TABLE I EMISSIVITY FOR THE MoM AND THE FEM MODELS, CALCULATED AT 1.4GHZ, H AND V POLARIZATION, FOR A SURFACE OF $\sigma=0.4\text{CM}$ AND $L_c=8.4\text{CM}$, EXPONENTIAL AUTOCORRELATION FUNCTION, AND PERMITTIVITY OF $\epsilon_r=15.57+3.71i$.

polarization	angle	MoM emissivity	FEM emissivity	$T_B(\text{FEM-MoM})$
H	30	0.5891	0.5920	0.8
H	40	0.5465	0.5535	2.0
H	50	0.4930	0.4987	1.6
V	30	0.6951	0.7020	2.0
V	40	0.7397	0.7467	2.0
V	50	0.7997	0.8107	3.2

TABLE II EMISSIVITY FOR THE MoM AND THE FEM MODELS, CALCULATED AT 1.4 GHz, H AND V POLARIZATION, FOR A SURFACE OF $\sigma = 1.12$ CM AND $L_c = 8.4$ CM, EXPONENTIAL AUTOCORRELATION FUNCTION AND PERMITTIVITY OF $\epsilon_r = 15.34 + 3.66i$.

polarization	angle	MoM emissivity	FEM emissivity	T_B (FEM-MoM)
H	30	0.6351	0.6296	1.6
H	40	0.5944	0.5836	3.1
H	50	0.5338	0.5365	0.8
V	30	0.7380	0.7270	3.2
V	40	0.7658	0.7726	2.0
V	50	0.8140	0.8266	3.6

We conclude that whilst not as accurate as the Method of Moments, the FEM approach provides results of good accuracy for rough surface scattering and emission, making it a good complimentary method.

Fig. 3 is an example of a calculation for a multilayer structure with rough surfaces, which illustrates the interest of the new method. We see that the presence of the second covering litter layer has a clear effect on the overall emissivity and also the effects of surface roughness of the second layer are strong.

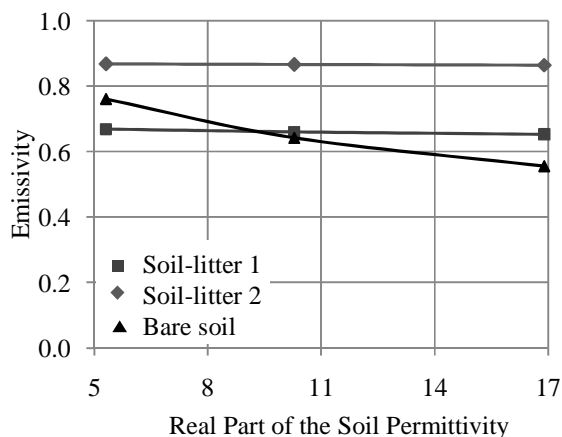


Fig. 3. Emissivity of the soil-litter forest system calculated using the Finite Element Method approach, at 1.4 GHz, H polarization, and with an incident angle $\theta = 40^\circ$ ($\phi = 0^\circ$). Litter permittivity was $8.712 + 2.301i$. Soil surface roughness was $\sigma = 0.44$ cm, $L_c = 9$ cm, with an exponential autocorrelation function and litter roughnesses were of gaussian autocorrelation function with values of: 1) soil-litter1 $\sigma = 0.4$, $L_c = 12.4$ and 2) soil-litter2 $\sigma = 0.8$, $L_c = 12.4$.

IV. CONCLUSION

An FEM approach for calculating the rough surface scattering and emission of a soil layer, using the numerical modeling tool HFSS, has been presented and results compared to MoM predictions. We obtained good agreement with MoM for rough surface scattering, and excellent agreement for rough surface emissivity. The interest of the approach is that it can be used to study the emission of heterogeneous media, which was illustrated by a calculation of the emissivity of a soil-litter structure found in forests. Future studies can focus

on this application as well as evaluating whether calculation time and memory requirements can be reduced and also whether the accuracy can be improved further by use of a less approximate tapered beam.

REFERENCES

- [1] Y.H. Kerr, P. Waldteufel, J.-P. Wigneron, J. Martinuzzi, J. Font, M. Berger, "Soil moisture retrieval from space: the Soil Moisture and Ocean Salinity (SMOS) mission," *IEEE Trans. Geosci. Remote Sens.*, vol. 39, no. 8, pp. 1729-1735, Aug. 2001.
- [2] D. Entekhabi, E.G. Njoku, P.E. O'Neill, K.H. Kellogg, W.T. Crow, W.N. Edelstein, et al. "The Soil Moisture Active Passive (SMAP) Mission," *Proc. of the IEEE*, vol. 98, no. 5, pp. 704-716, 2010.
- [3] L. Tsang, J. Kong, K.-H. Ding, C. Ao, *Scattering of Electromagnetic Waves, vol. 2 Numerical Simulations*, New York: Wiley
- [4] Q. Li, L. Tsang, J.C. Shi, C.H. Chan, "Application of Physics-Based Two Grid Method and Sparse Matrix Canonical Grid Method for Numerical Solutions of Emissivities of Soils with Rough Surfaces at Microwave Frequencies," *IEEE Trans. Geosci. Remote Sens.*, vol.38, no.4, pp.1635-1643, Jul. 2000.
- [5] L. Zhou, L. Tsang, V. Jandhyala, Q. Li, C.H. Chan, "Emissivity Simulations in Passive Microwave Remote Sensing with 3-D Numerical Solutions of Maxwell Equations," *IEEE Trans. Geosci. Remote Sens.*, vol.42, no.8, pp.1739-1748, Aug. 2004.
- [6] S. Huang, L. Tsang, E.G. Njoku, K.S. Chan, "Backscattering Coefficients, Coherent Reflectivities, and Emissivities of Randomly Rough Soil Surfaces at L-Band for SMAP Applications Based on Numerical Solutions of Maxwell Equations in Three-Dimensional Simulations," *IEEE Trans. Geosci. Remote Sens.*, vol.48, no.6, pp.2557-2568, Jun. 2010.
- [7] K.F. Warnick, W.C. Chew, "Numerical Simulation Methods for Rough Surface Scattering," *Waves in Random Media*, vol. 11, issue 1, pp R1-R30, Jan.2001
- [8] <http://www.ansoft.com/products/hf/hfss/>
- [9] T.-D. Wu, K.S. Chen, J. Shi, A.K. Fung, "A Transition Model for the Reflection Coefficient in Surface Scattering," *IEEE Trans. Geosci. Remote Sens.*, vol. 39 (9), pp. 2040-2050, Sep. 2001.
- [10] H.T. Ewe, J.T. Johnson and K.S.Chen, "A comparison study of the surface scattering models and numerical model," in *Proc. IGARSS, Sydney, Australia*, pp. 2692 - 2694, 2001.
- [11] H.T. Ewe, J.T. Johnson and K.S.Chen, "A Comparison Study of the Surface Scattering Models and Numerical Model" presentation at *IGARSS, Sydney, Australia*, July 13, 2001.
- [12] R software website: <http://www.r-project.org/>, Random Fields package: <http://cran.r-project.org/web/packages/RandomFields/RandomFields.pdf>
- [13] C4W's "3D Shop Modeldesign" product website: <http://www.3dshopmodeldesign.com/>
- [14] M. F. Chen and S. Y. Bai, "Computer simulation of wave scattering from a dielectric random surface in two dimensions - Cylindrical case," *J. Elec. Waves Appl.*, vol. 4, no. 10, pp. 963-982, 1990.
- [15] F.T. Ulaby, R.K. Moore and A.K. Fung, *Microwave Remote Sensing, Active and Passive*, vol. II. Dedham, MA: Artech House, 1985. Chapter 11-1.
- [16] F. Demontoux, B. Le Crom, G. Ruffié, J.-P. Wigneron, J. P. Grant, V. L. Mironov, and H. Lawrence, "Electromagnetic characterization of soil-litter media - Application to the simulation of the microwave emissivity of the ground surface in forests," *Eur. Phys. J.-Appl. Phys.*, vol. 44, pp. 303-315, 2008.

References

- R. M. Axline and A. K. Fung (1978), "Numerical Computation of Scattering from a Perfectly Conducting Random Surface," *IEEE Trans. Antennas Propag.*, vol. 26, no. 3, pp. 482 – 488.
- M. Bass, E. Van Stryland, R. Williams, and W. Wolfe (1995), "Optical properties of films and coatings," in *Handbook of Optics*. New York: McGraw-Hill, 1995, pt. 11, pp. 42.9–42.14.
- G.B. Bonan (2008), "Forests and Climate Change: Forcings, Feedbacks, and the Climate Benefits of Forests," *Science*, vol. 320, pp. 1444 – 1449.
- M. Born and E. Wolf (1964) *Principles of Optics*, Macmillan Company, New York 1964.
- H. Braunisch, Y. Zhang, C. O. Ao, S.-E. Shih, Y. E. Yang, K.-H. Ding, J. A. Kong, and L. Tsang (2000), "Tapered Wave with Dominant Polarization State for All Angles of Incidence," *IEEE Trans. Antennas Propag.*, vol. 48, no. 7, pp. 1086 - 1096.
- E. Ceraldi, G. Franceschetti, A. Iodice (2005), "Estimating the Soil Dielectric Constant via Scattering Measurements Along the Specular Direction," *IEEE Trans. Geosci. Remote Sensing*, vol. 43, no. 2, pp. 295-305.
- K. S. Chen, T. D. Wu, M. K. Tsay, and A. K. Fung (2000), "A note on the multiple scattering in IEM models," *IEEE Trans. Geosci. Remote Sensing*, vol. 38, pp. 249–256.
- K. S. Chen, T. D. Wu, L. Tsang, Q. Li, J. C. Shi, and A. K. Fung (2003), "Emission of rough surfaces calculated by the integral equation method with comparison to three-dimensional moment method simulations," *IEEE Trans. Geosci. Remote Sens.*, vol. 41, no. 1, pp. 90–101.
- M. F. Chen and S. Y. Bai (1990), "Computer simulation of wave scattering from a dielectric random surface in two dimensions - Cylindrical case," *J. Elec. Waves Appl.*, vol. 4, no. 10, pp. 963-982.
- B. J., Choudhury, T. J., Schmugge, A., Chang, and R. W. Newton (1979), "Effect of surface roughness on the microwave emission from soils," *Journal of Geophysical Research*, vol. 84, pp. 5699–5706.

B. J. Choudhury, T. J. Schmugge, and T. Mo (1982), “A parameterization of effective soil temperature for microwave emission,” *Journal of Geophysical Research*, vol. 87(C2), pp. 1301–1304.

A.A Chukhlantsev (2006), *Microwave Radiometry of Vegetation Canopies*, Springer 2006

P. de Rosnay, J. Calvet, Y. Kerr, J. Wigneron, F. Lemaître, M. Escorihuela, J. Sabater, K. Saleh, J. Barrié, G. Bouhours et al. (2006a), “SMOSREX: A long term field campaign experiment for soil moisture and land surface processes remote sensing,” *Remote Sens. Environ.*, vol.102 (n 3-4), pp. p377-389.

P. de Rosnay, J.-P. Wigneron, T. Holmes, and J.-C. Calvet, (2006b) “Parametrizations of the effective temperature for L-band radiometry. Inter-comparison and long term validation with SMOSREX field experiment,” C. Matzler *Thermal microwave radiation – Applications for remote sensing*, The Institution of Engineering and Technology, pp. 312 - 324.

A. Della Vecchia, P. Ferrazzoli, J.-P. Wigneron, and J. P. Grant (2007), “Modeling Forest Emissivity at L-Band and a Comparison With Multitemporal Measurements,” *IEEE Trans. Geosci. Remote Sensing Lett.*, vol. 4, no. 4, pp. 508 – 512.

F. Demontoux, B. Le Crom, G. Ruffié, J.-P. Wigneron, J.P. Grant, V.L. Mironov, and H. Lawrence (2008), “Electromagnetic characterization of soil-litter media: Application to the simulation of the microwave emissivity of the ground surface in forests,” *EPJ Applied Physics*, vol. 44, pp. 303-315.

R. Devayya and D. J. Wingham (1992), “The Numerical Calculation of Rough Surface Scattering by the Conjugate Gradient Method,” *IEEE Trans. Geosci. Remote Sensing*, vol. 30, no.3, pp. 645 – 648.

M. C. Dobson, F. T. Ulaby, M. T. Hallikainen, and M. A. El-Reyes (1985), “Microwave dielectric behavior of wet soil—Part II: Dielectric mixing models,” *IEEE Trans. Geosci. Remote Sensing*, vol. 23, pp. 35–44.

M.J. Escorihuela, Y. Kerr, J.-P. Wigneron, P. de Rosnay, J.-C. Calvet, and F. Lemaître (2004), *5th SMOS workshop*, ESA-ESRIN, Frascati, Italy, 29 November – 1 December 2004.

H.T. Ewe, J.T. Johnson and K.S.Chen, (2001a) “A comparison study of the surface scattering models and numerical model,” in *Proc. IGARSS*, Sydney, Australia, pp. 2692 – 2694.

H.T. Ewe, J.T. Johnson and K.S.Chen, (2001b) “A Comparison Study of the Surface Scattering Models and Numerical Model” presentation at *IGARSS*, Sydney, Australia, July 13, 2001.

P. Ferrazzoli and L. Guerriero (1996), “Passive microwave remote sensing of forests: A model investigation,” *IEEE Trans. Geosci. Remote Sens.*, vol. 34, no. 2, pp. 433–443.

P. Ferrazzoli, L. Guerriero, and J.-P. Wigneron (2002), “Simulating L-band emission of forests in view of future satellite applications,” *IEEE Trans. Geosci. Remote Sens.*, vol. 40, no. 12, pp. 2700–2708.

G. Franceschetti, A. Iodice, and D. Riccio (2000), “Scattering from Dielectric Random Fractal Surfaces via Method of Moments,” *IEEE Trans. Geosci. Remote Sensing*, vol. 38, no. 4, pp. 1644 – 1655.

A. K. Fung, Z. Li, and K. S. Chen (1992), “Backscattering from a randomly rough dielectric surface,” *IEEE Trans. Geosci. Remote Sens.*, vol. 30, no. 2, pp. 356–369.

A.K. Fung (1994a), *Microwave Scattering and Emission Models and Their Applications*. Norwood, MA: Artech House, 1994.

A. K. Fung, M. R. Shah, and S.Tjuatja (1994b), “Numerical Simulation of Scattering from Three-Dimensional Randomly Rough Surfaces,” *IEEE Trans. Geosci. Remote Sens.*, vol. 32, no. 5, pp.986 – 994.

A. K. Fung, and K. S. Chen (2004), “An Update on the IEM Surface Backscattering Model,” *IEEE Trans. Geosci. Remote Sens. Lett.*, vol. 1, no. 2, pp. 75–77.

J.P. Grant, J.-P. Wigneron, A.A. Van de Griend, A. Kruszewski, S. Schmidl Søbjaerg, N. Skou (2007), “A field experiment on microwave forest radiometry: L-band signal behavior for varying conditions of surface wetness,” *Remote Sens. Environ.*, vol. 109, no. 1, pp. 10–19.

J. P. Grant, A. A. Van de Griend, M. Schwank, and J.-P. Wigneron (2009), “Observations and Modeling of a Pine Forest Floor at L-Band,” *IEEE Trans. Geosci. Remote Sens.*, vol. 47, no. 7, pp. 2024-2034.

M. Guglielmetti, M. Schwank, C. Mätzler, C. Oberdörster, J. Vanderborght, and H. Flüßler (2008), “FOSMEX: Forest Soil Moisture Experiments With Microwave Radiometry,” *IEEE Trans. Geosci. Remote Sens.*, vol. 46, no. 3, pp. 727 – 735.

M. Hallikainen, F. T. Ulaby, M. Dobson, M. A. El-Rayes, and L. Wu (1985), "Microwave dielectric behavior of wet soil—Part I: Empirical models and experimental observations," *IEEE Trans. Geosci. Remote Sens.*, vol. GRS-23, no. 1, pp. 25–34.

T.R.H. Holmes, P. de Rosnay, R. de Jeu, J.-P. Wigneron, Y. Kerr, J.-C. Calvet, et al, (2006) "A new parameterization of the effective temperature for L band radiometry," *Geophysical Research Letters*, 33, L L07405.

S. Huang, L. Tsang, E.G. Njoku, K.S. Chan, (2010) "Backscattering Coefficients, Coherent Reflectivities, and Emissivities of Randomly Rough Soil Surfaces at L-Band for SMAP Applications Based on Numerical Solutions of Maxwell Equations in Three-Dimensional Simulations," *IEEE Trans. Geosci. Remote Sens.*, vol.48, no.6, pp.2557-2568.

K. Inan and V. B. Ertürk (2006), "Application of Iterative Techniques for Electromagnetic Scattering From Dielectric Random and Reentrant Rough Surfaces," *IEEE Trans. Geosci. Remote Sens.*, vol. 44, no. 11 pp 3320 – 3329.

V. Jandhyala, E. Michielssen, S. Balasubramaniam and W.C. Chew (1998), "A Combined Steepest Descent-Fast Multipole Algorithm for the Fast Analysis of Three-Dimensional Scattering by Rough Surfaces," *IEEE Trans. Geosci. Remote Sens.*, vol. 36, no. 3, pp 738-748.

D. A. Kapp and G. S. Brown (1996), "A new numerical method for rough surface scattering calculations," *IEEE Trans. Antennas Propag.* vol. 44, pp 711–721

M. A. Karam (1997), "A physical model for microwave radiometry of vegetation," *IEEE Trans. Geosci. Remote Sens.*, vol. 35, no. 4, pp. 1045 – 1058.

Y.H. Kerr, P. Waldteufel, J.-P. Wigneron, J. Martinuzzi, J. Font, and M. Berger (2001), "Soil moisture retrieval from space: the Soil Moisture and Ocean Salinity (SMOS) mission," *IEEE Trans. Geosci. Remote Sens.*, vol. 39, no. 8, pp. 1729-1735.

H.C. Ko (1962), "On the Reception of Quasi-monochromatic Partially Polarized Radio Waves," *Proc. IRE*, vol. 50, pp. 1950 – 1957.

J.D. Krauss and K.R. Carver (1973), *Electromagnetics*, McGraw-Hill, New York, 1973.

T. Le Toan, S. Quegan, M. Davidson, H. Balzter, P. Paillou, K. Papathanassiou, S. Plummer, S. Saatchi, H. Shugart, and L. Ulander (2010), "The BIOMASS Mission : Mapping global forest biomass to better understand the terrestrial carbon cycle", accepted, *Remote Sensing of the Environment*, October 2010.

Q. Li, L. Tsang, J.C. Shi, C.H. Chan, (2000) "Application of Physics-Based Two Grid Method and Sparse Matrix Canonical Grid Method for Numerical Solutions of Emissivities of Soils with Rough Surfaces at Microwave Frequencies," *IEEE Trans. Geosci. Remote Sens.*, vol.38, no.4, pp.1635-1643.

Y.-A. Liou, K.-S. Chen, and T.-D. Wu, (2001) "Reanalysis of L-band brightness predicted by the LSP/R model-for prairie grassland: incorporation of rough surface scattering," *IEEE Trans. Geosci. Remote Sens.*, vol. 39 no. 1, pp. 129 – 135.

S. H. Lou, L. Bang and C. H. Chan, (1991a), "Application of the finite element method to Monte Carlo simulations of scattering of waves by random rough surfaces: penetrable case", *Waves in Random and Complex Media*, vol. 1, no. 4, pp. 287 – 307.

S.H. Lou, L. Tsang, C.H. Chan, and A. Ishimaru (1991b), "Application of finite element method to Monte Carlo simulations of scattering of waves by random rough surfaces with the periodic boundary condition," *Journal of Electromagnetic Waves and Applications*, vol. 5, iss. 8, pp. 835 – 855.

R.T. Marchand and S. G. Brown, (1999) "On the use of finite surfaces in the numerical prediction of rough surface scattering," *IEEE Trans. Antennas Propag.* vol. 47, no. 4, pp 600–604.

C. Mätzler (1994), "Microwave (1–100 GHz) dielectric model of leaves," *IEEE Trans. Geosci. Remote Sens.*, vol. 32, no. 4, pp. 947–949.

C. Mätzler (1998), "Microwave permittivity of dry sand," *IEEE Trans. Geosci. Remote Sensing* vol. 36, pp. 317–319.

C. Matzler et al (2006), *Thermal Microwave Radiation: Applications for Remote Sensing*, The Institution of Engineering and Technology.

C. Mätzler, *Physical Principles of Remote Sensing*, Lecture course, Bern, Switzerland 2007

A. Mialon, J.-P. Wigneron, P. De Rosnay, M.J. Escorihuela and Y. Kerr (2008), "Continuous monitoring of surface roughness changes over a bare soil field using L-Band brightness temperature," *poster presentation at Microrad*, Florence, Italy.

V.L. Mironov, M.C. Dobson, V.H. Kaupp, S.A. Komarov, and V.N. Kleshchenko (2004), "Generalized refractive mixing dielectric model for moist soils," *IEEE Trans. Geosci. Remote Sensing*, vol. 42, no. 4 pp. 773 – 785.

V.L. Mironov, L.G.Kosolapova, and S.V. Fomin (2009), "Physically and Mineralogically Based Spectroscopic Dielectric Model for Moist Soils," *IEEE Trans. Geosci. Remote Sens.*, vol.47, no.7, pp.2059-2070.

T. Mo, and T.J. Schmugge (1987), "A parameterization of the effect of surface roughness on microwave emission," *IEEE Trans. Geosci. Remote Sensing*, vol. 25, pp. 47–54.

E.G. Njoku and D. Entekhabi (1996), "Passive microwave remote sensing of soil moisture," *J. Hydrol.*, vol 184, pp. 101-129.

W.H. Peake 1959, "Interaction of electromagnetic waves with some natural surfaces," *IEEE Trans. Antennas Propag.*, vol. 7, pp. 324-329.

C. Prigent, J.-P. Wigneron, W.B. Rossow, and J.R. Pardo-Carrion (2000), "Frequency and angular variations of land surface microwave emissivities: Can we estimate SSM/T and AMSU emissivities from SSM/I emissivities?" *IEEE Transactions on Geoscience and Remote Sensing*, vol. 38, pp. 2373–2386.

M Saillard and A Sentenac (2001), "Rigorous solutions for electromagnetic scattering from rough surfaces," *Waves in random media*, vol. 11, no.3, pp 103-137.

E. Santi, S. Paloscia, P. Pampaloni, and S. Pettinato (2007), "Ground-based microwave investigations of forest plots in Italy," in *Proc. Int. Geosci.Remote Sens. Symp.*, Barcelona, Spain, Jul. 23–28, 2007, pp. 1416–1419.

M. Schwank, M. Guglielmetti, C. Matzler, and H. Fluhler (2008), "Testing a New Model for the L-Band Radiation of Moist Leaf Litter", *IEEE Trans. Geosci. Remote Sens.*, vol. 46, no. 7, pp 1982-1994.

M. Schwank, I. Völksch, J.-P. Wigneron, Y. H. Kerr, A. Mialon, P. de Rosnay, and C. Mätzler (2010), "Comparison of Two Bare-Soil Reflectivity Models and Validation With L-Band Radiometer Measurements," *IEEE Trans. Geosci. Remote Sens.*, vol. 48, no. 1, pp. 325 – 337.

J. C. Shi, K. S. Chen, Q. Li, T. J. Jackson, P. E. O'Neill, and L. Tsang (2002), "A parameterized surface reflectivity model and estimation of bare surface soil moisture with L-band radiometer," *IEEE Trans. Geosci. Remote Sens.*, vol. 40, no. 12, pp. 2674–2686.

G. Soriano and M. Saillard (2001), "Scattering of electromagnetic waves from two-dimensional rough surfaces with impedance approximation," *J. Opt. Soc. Am. A*

A. Taflove, and K.R. Umashankar (1989), "Review of FD-TD Numerical modeling of electromagnetic wave scattering and radar cross-section," *Proceedings of the IEEE*, vol. 77, no. 5, pp. 682 – 699.

E. I. Thorsos (1988), "The validity of the Kirchhoff approximation for rough surface scattering using a Gaussian roughness spectrum," *J. Acoust. Soc. Am.*, vol. 83, pp. 78-92.

J. V. Toporkov, R.S. Awadallah, and G. S. Brown (1999), "Issues related to the use of a Gaussian-like incident field for low-grazing-angle scattering," *J. Opt. Soc. Am. A* vol. 16, no.1, pp 176 – 187.

P. Tran (1997), "Calculation of the scattering of electromagnetic waves from a two-dimensional perfectly conducting surface using the method of ordered multiple interaction," *Waves in Random Media*, vol.7, no. 3, pp. 295 – 302.

L. Tsang, J. Kong, K.-H. Ding, C. Ao (2001), *Scattering of Electromagnetic Waves, vol. 2 Numerical Simulations*, New York: Wiley.

F.T. Ulaby, R.K. Moore and A.K. Fung (1985), *Microwave Remote Sensing, Active and Passive, vol. I. Microwave Remote Sensing Fundamentals and Radiometry*, Dedham, MA: Artech House, 1985.

F.T. Ulaby, R.K. Moore and A.K. Fung (1985), *Microwave Remote Sensing, Active and Passive, vol. II. Radar Remote Sensing and Surface Scattering and Emission Theory*, Dedham, MA: Artech House, 1985.

F.T. Ulaby, R.K. Moore and A.K. Fung (1985), *Microwave Remote Sensing, Active and Passive, vol. III From Theory to Applications*. Dedham, MA: Artech House, 1985.

J.R. Wang, and T.J. Schmugge (1980), "An Empirical Model for the Complex Dielectric Permittivity of Soils as a Function of Water Content," *IEEE Trans. Geosci. Remote Sensing*, vol 18, pp. 288-295.

J.R. Wang, and B.J. Choudhury (1981), "Remote sensing of soil moisture content over bare field at 1.4 GHz frequency," *Journal of Geophysical Research*, vol. 86, pp. 5277–5282.

J.R. Wang, P.E. O'Neill, T.J. Jackson, and E.T. Engman (1983), "Multifrequency measurements of the effects of soil moisture, soil texture, and surface roughness," *IEEE Transactions on Geoscience and Remote Sensing*, vol. 21, pp. 44–51.

K.F. Warnick and W.C. Chew (2001), "Numerical Simulation Methods for Rough Surface Scattering," *Waves in Random Media*, vol. 11, issue 1, pp. 1-30.

U. Wegmüller, and C. Mätzler (1999), "Rough bare soil reflectivity model," *IEEE Trans. Geosci. Remote Sensing*, vol. 37, pp. 1391–1395.

J.-P. Wigneron, L. Laguerre, and Y. Kerr (2001), "Simple modeling of the L-band microwave emission from rough agricultural soils," *IEEE Trans. Geosci. Remote Sensing*, vol. 39 no. 8, pp. 1697–1707.

J. -P. Wigneron, , J. -C. Calvet, T. Pellarin, A. Van de Griend, M. Berger, and P. Ferrazzoli (2003), "Retrieving near surface soil moisture from microwave radiometric observations: Current status and future plans" *Remote Sens. Environ.*, vol. 85, pp 489–506.

J.-P. Wigneron , Y. Kerr, P. Waldteufel, K. Saleh, M.-J. Escorihuela, P. Richaume , P. Ferrazzoli, P. de Rosnay, R. Gurney, J.-C. Calvet, J.P. Grant, M. Guglielmetti, B. Hornbuckle, C. Matzler, T. Pellarin, and M. Schwank (2007), "L-band Microwave Emission of the Biosphere (L-MEB) Model: Description and calibration against experimental data sets over crop fields," *Remote Sens. Environ.*, vol. 107, no. 4, pp. 639–655.

J.-P. Wigneron, A. Chanzy, Y. H. Kerr, H. Lawrence, J. Shi, M. J. Escorihuela, V. Mironov, A. Mialon, F. Demontoux, P. de Rosnay, and K. Saleh-Contell (2010), "Evaluating an Improved Parameterization of the Soil Emission in L-MEB", *IEEE Trans. Geosci. Remote Sens*, accepted Sep. 2010

T. T. Wilheit (1978), "Radiative transfer in a plane stratified dielectric," *IEEE Trans. Geosci. Remote Sens.*, vol. 16, no. 2, pp. 138–143.

T.-D. Wu, K.S. Chen, J. Shi, A.K. Fung (2001), "A Transition Model for the Reflection Coefficient in Surface Scattering," *IEEE Trans. Geosci. Remote Sens.*, vol. 39 (9), pp. 2040-2050.

T.-D. Wu, and K.S. Chen (2004), "A reappraisal of the validity of the IEM model for backscattering from rough surfaces," *IEEE Trans. Geosci. Remote Sens.*, vol. 42, no. 4, pp. 743–753.

T.-D. Wu, K.-S. Chen, J. Shi, H.-W. Lee, and A. K. Fung (2008), "A Study of an AIEM Model for Bistatic Scattering From Randomly Rough Surfaces," *IEEE Trans. Geosci. Remote Sens.*, vol. 46 (9), pp. 2584-2598.

H.Ye and Y.Q. Jin (2005), "Parameterization of the tapered incident wave for numerical simulation of electromagnetic scattering from rough surface," *IEEE Trans. Antennas Propag.*, vol. 53, no. 3, pp. 1234-1237.

K. S. Yee (1966), "Numerical solution of initial boundary value problems involving Maxwell's equations in isotropic media," *IEEE Trans. Antennas Propagat.*, vol. AP-14, pp. 302-307.

L. Zhou, L. Tsang, V. Jandhyala, and C.-T. Chen (2001), "Studies on Accuracy of Numerical Simulations of Emission from Rough Ocean-Like Surfaces," *IEEE Trans. Geosci. Remote Sensing*, vol. 39, no. 8, pp. 1757 – 1763.

L. Zhou, L. Tsang, V. Jandhyala, Q. Li, C.H. Chan (2004), "Emissivity Simulations in Passive Microwave Remote Sensing with 3-D Numerical Solutions of Maxwell Equations," *IEEE Trans. Geosci. Remote Sens.*, vol.42, no.8, pp.1739-1748.

M. Zribi, N. Baghdadi, N. Holah, O. Fafin, and C. Guerin (2005), "Evaluation of a rough soil surface description with ASAR-ENVISAT radar data," *Remote Sens. Environ.*, vol. 95, no. 1, pp. 67 – 76.